



<https://theses.gla.ac.uk/>

Theses Digitisation:

<https://www.gla.ac.uk/myglasgow/research/enlighten/theses/digitisation/>

This is a digitised version of the original print thesis.

Copyright and moral rights for this work are retained by the author

A copy can be downloaded for personal non-commercial research or study, without prior permission or charge

This work cannot be reproduced or quoted extensively from without first obtaining permission in writing from the author

The content must not be changed in any way or sold commercially in any format or medium without the formal permission of the author

When referring to this work, full bibliographic details including the author, title, awarding institution and date of the thesis must be given

Enlighten: Theses

<https://theses.gla.ac.uk/>
research-enlighten@glasgow.ac.uk

**Analysis and indicial Modelling of Helicopter
Tail Rotor Orthogonal Blade Vortex Interaction**

David R Suttie

PhD Thesis

February 2006

Department of Aerospace Engineering

**A dissertation submitted for the degree of Doctor of Philosophy
to the Faculty of Engineering at the University of Glasgow**

© David R Suttie 2006

ProQuest Number: 10390551

All rights reserved

INFORMATION TO ALL USERS

The quality of this reproduction is dependent upon the quality of the copy submitted.

In the unlikely event that the author did not send a complete manuscript and there are missing pages, these will be noted. Also, if material had to be removed, a note will indicate the deletion.



ProQuest 10390551

Published by ProQuest LLC (2017). Copyright of the Dissertation is held by the Author.

All rights reserved.

This work is protected against unauthorized copying under Title 17, United States Code
Microform Edition © ProQuest LLC.

ProQuest LLC.
789 East Eisenhower Parkway
P.O. Box 1346
Ann Arbor, MI 48106 – 1346

GLASGOW
UNIVERSITY
LIBRARY:

Abstract

The significant noise produced by helicopters is a well known irritation both in civil and military aviation. This noise generally has two forms: broadband and harmonic. Broadband noise has a wide frequency range, whereas harmonic noise has a small frequency range. As harmonic noise is of a smaller frequency range, this can be heard as a thumping or slapping sound, and is therefore subjectively more irritating than broadband noise. Tail rotor blade vortex interaction has been identified as an interaction that results in irritating harmonic noise, particularly during descent, and has consequently been the subject of research to enable the quieter or stealthier operation of helicopters for civil or military applications respectively. Orthogonal blade vortex interaction is a specific form of tail rotor blade vortex interaction that occurs in climbing flight when the tip vortices from the rear of the main rotor are orthogonal to the tail rotor disc and are cut by the tail rotor blades as the vortices pass downstream.

This study builds on previous experimental investigations of orthogonal tail rotor blade vortex interaction, and investigates semi-empirical modelling of the phenomenon. In the early stages of the work, weaknesses were identified in the published experimental data that limited their use as a modelling correlation source. For this reason, a detailed analysis of data from the experimental study of Wang et al. (2002) was conducted to allow the validation of semi-empirical modelling strategies applied to orthogonal blade vortex interaction.

Indicial modelling was identified as a suitable modelling strategy due to its computational efficiency and also its current use in the helicopter industry. The long-term intention is that the subsequent integration of the orthogonal blade vortex interaction model into a full helicopter aerodynamic model will enable a more complete simulation that considers orthogonal blade vortex interaction during the design stages of a helicopter's development.

A number of modelling strategies were considered during this study. Initial models were based on the Kussner function for an aerofoil encountering an upgust. The orthogonal interaction was captured by representing the axial core flow of the tip vortex as an upgust in the shape of a Lamb vortex that engulfed the entire vortex. This resulted in a markedly greater lift response compared to experimental data because the chordwise distribution of axial velocities due to the interacting tip vortex were not properly represented. The modelling approach was then improved to account for this distribution. This produced good agreement with the experimental data, where the vortex centre interacted with the blade. The predicted response was found to be symmetric about the vortex centre, which was in contrast to the asymmetry found in the experimental data.

The asymmetry was investigated using a two-dimensional panel method simulation of the orthogonal interaction. It was hoped that the asymmetry could be accounted for by the rotational flow of the tip vortex, however, the panel method demonstrated that there was insufficient rotational flow to account for the magnitude of the asymmetry found in the experimental data.

To investigate this asymmetry further a numerical simulation of the wind tunnel experiment was used. This simulation was inviscid and featured a three-dimensional source panel method to represent the wind tunnel walls, a lifting line calculation for the blade of the vortex generator, and a free-wake solution for the wake of the vortex generator. The simulation had previously been found to simulate the experimental wake shape well. The axial velocities predicted by this model at the location of the installed interacting blade were extracted and used as an input into the indicial model. The indicial model then reproduced the asymmetric lift response found in the experimental data; however, the magnitude of the measured lift response was not well represented. This difference may be associated with the inviscid nature of the numerical simulation or flapping of the vortex generator blade observed during the experiment. As a first step towards understanding the difference, the angle of incidence of the vortex generator was reduced in the numerical simulation until the circulation over the interacting blade matched the experimentally measured value. This resulted in a closer

agreement in the magnitude of the blade vortex interaction response for all spanwise locations.

The differences between the prediction based on the prescribed Lamb type axial flow distribution and the indicial prediction based on the horizontal cross flow velocities extracted from the numerical simulation, indicate that the shape of the wake and its corresponding induced flow influence the interaction response. The prescribed indicial prediction features a sharper drop off in lift response compared to the indicial prediction forced by the simulated velocities. This can be attributed to the curved wake shape and the trailing vorticity sheet in the numerical simulation, which represent real features of the experiment.

Comparisons against other studies showed some correlation. Indicial predictions of the data from an earlier feasibility test at the University of Glasgow showed agreement in terms of magnitude but not in form. Comparisons were also made with a computational study conducted by Liu and Marshall (2004). Their viscous, compressible computational method showed some similarity with predictions of the indicial model, however, there were significant differences between the two modelling techniques that led to discrepancies. Significantly, Liu and Marshall demonstrated a linear rate of decrease of axial core flow after the initial stages of the interaction. An inverse indicial method was applied to the experimental data and identified a similar linear rate of decrease. Also, indicial model predictions of a universal lift coefficient derived by Liu and Marshall indicated that the vortex core radius to chord length ratio is directly related to the magnitude of the unsteady blade lift response.

Acknowledgement

I would like to thank Westland Helicopters Limited for their financial sponsorship for this postgraduate study under contract number BG/BGC/151/2001. I would also like to thank the Aerospace Department at Glasgow University in general for their support throughout this PhD.

More specifically, I must convey my most sincere gratitude to my supervisor Prof. Frank Coton for his guidance, support and friendship through this study. I wish him all the best for the future.

I must also thank the comradery of the researchers past and present for their good will and banter. Most notably, the weekly footie that provided a much needed break from studies. Without the companionship of my fellow post graduate researchers the completion of this study would never have been possible. In particular I would like express my gratitude to Xab, Neil, Romi, Dave, Jeremy, Giacinto, Massimo, Francesco, Punit, Josef, Lucy, Adriano and Yoh.

I would also like to my family for their support over the years, and never raising an eyebrow whenever I claimed that I was about to submit for over a year. Finally, I would also like to express my thanks to Pamela for her considerate support.

Table of Contents

Abstract	ii
Acknowledgement	ii
Table of Contents	vi
List of Figures	ix
List of Tables	xiii
Nomenclature	xv
1 Introduction	1
1.1 Operating Environment	1
1.2 Interactional Aerodynamics of Helicopters	4
1.3 Interactions with the Main Rotor Wake	8
1.3.1 Fuselage Interactions	9
1.3.2 Perpendicular Interactions	12
1.3.3 Parallel Interactions	16
1.3.4 Orthogonal Blade Vortex Interaction	23
1.4 Summary of Chapters	44
2 Experimental Studies at Glasgow University	46
2.1 Introduction	46
2.2 Experimental Studies	47
2.3 Summary	62
3 Analysis of Experimental Data	63
3.1 Introduction	63
3.2 Evaluation of Existing Data Analysis	63
3.3 Data Analysis	65
3.4 Digital Filtering	67
3.5 Customised Filtering Using Splines	70
3.6 Discussion	75
3.7 Conclusions	76
4 Indicial Modelling for Helicopter Applications	78
4.1 Introduction	78
4.2 Early Indicial Modelling	79
4.3 Modern Indicial Modelling	80
4.4 Summary	87
5 Indicial Modelling at Vortex Centre	88
5.1 Introduction	88
5.2 Comparison of Indicial Models with Experimental Response at the Vortex Centre	89

5.2.1	Kussner Indicial Lift Response	89
5.2.2	Duhamel Integral	90
5.2.3	Kussner Indicial Lift Response Results	94
5.2.4	Beddoes Indicial Lift Response	97
5.2.5	Beddoes Indicial Lift Response Results	99
5.2.6	Sensitivity to Δt step size and number of Simpson segments	100
5.2.7	Fully Resolved Indicial Response	104
5.2.8	Response at Vortex Centre for Velocities 20, 30, and 50 m/s	105
5.3	Summary	108
6	Two-Dimensional Panel Method	109
6.1	Introduction	109
6.2	Panel Method Theory and Application	109
6.3	Application	111
6.4	Panel Method Used In This Study	112
6.5	Axial Flow Results	113
6.6	Rotational Flow Results	115
6.7	Summary	116
7	Numerical Simulation of the Experimental Flow Field	118
7.1	Introduction	118
7.2	Numerical Simulation	120
7.3	Simplifications	122
7.4	Required Extensions to the Numerical Simulation	123
7.5	The Effect of Multiple Wake on Induced Velocity Convergence	125
7.6	Summary	129
8	Results from Numerical Simulation of Wind Tunnel	131
8.1	Summary	136
9	Comparison of Indicial Model with other Experimental and Computational Sources	138
9.1	Small Wind Tunnel Experimental Data (Anatomy Wind Tunnel, University of Glasgow)	138
9.2	Liu and Marshall Computational Study	142
9.2.1	Investigation of Axial Core Flow Decrease	155
9.3	Summary	164
10	Conclusions and Recommended Future Work	166
	Appendix A: Derivation of the response of a unit step	171
	Appendix B: Measured Data from the Argyll Wind Tunnel Experiment at the University of Glasgow	173
	Appendix C: Wake Comparisons for Numerical Simulations	174
	Appendix D: Comparison of indicial predictions with experimental data	183
	Appendix E: Comparison of indicial predictions with experimental data	192
	Appendix F: Parameters Calculated For B-cases Defined in Liu and Marshall (2004)	201

References	204
------------------	-----

List of Figures

Figure 1.1: Formation of tip vortices (Kuethe and Chow, 1998).....	2
Figure 1.2: Formation of trailing tip vortices	2
Figure 1.3: Dangerous flight conditions in the wake of a larger aircraft due to trailing wing tip vortices	3
Figure 1.4: Rolling up of main rotor blade tip vortices into two discrete trailing vorticity structures,	3
Figure 1.5: Helicopter main rotor blade tip vortices.....	4
Figure 1.6: Perpendicular Interaction	5
Figure 1.7: Parallel and Orthogonal Interactions (Horner et al, 1992)	5
Figure 1.9: Single clean orthogonal blade vortex Interaction	8
Figure 1.10: Configuration used by Liou to capture perpendicular surface vortex Interactions upstream of the main rotor hub (Liou et al, 1989).....	9
Figure 1.11: Pressure signature variation dependent on passage of vortex at different heights (Leishman and Bi, 1990).....	10
Figure 1.12: Typical perpendicular blade vortex interaction configuration. This configuration features a finite span wing as a 'vortex generator'. (Wittmer et al, 1995a).....	13
Figure 1.13: Perpendicular configuration featuring an 'infinite' span 'vortex generator' (Wittmer et al, 1995b)	13
Figure 1.14: Vortex tangential flow results in varying spanwise angle of attack (Wittmer et al, 1995b).....	15
Figure 1.15: Illustration of separation distance Δ (Wittmer et al, 1995b).....	15
Figure 1.16: Visualisation of Convective and Propagative pressure Disturbances (Horner et al, 1996).....	18
Figure 1.18: Illustration of vortex sense of rotation	18
Figure 1.20: PIV shows the splitting of the incident vortex into two (Horner et al, 1996).....	20
Figure 1.21: Comparison of Beddoes indicial model with Navier Stokes calculations for parallel blade vortex interaction (Beddoes, 1989).....	22
Figure 1.22: Cloud of small vortices (Lee et al, 1991).....	23
Figure 1.23: Multiple interactions of main rotor tip vortices with the tall rotor blades [Taken from (Leverton et al, 1977).....	24
Figure 1.24: Variation in impulse peak sound pressure level with forward speed (Leverton et al, 1977).....	25
Figure 1.25: Ahmadi experimental configuration (1986)	29
Figure 1.26: Propeller configuration used by Johnson and Sullivan (1992).....	30
Figure 1.27: Marshall experimental configuration (1994a).....	31
Figure 1.28: Later stages of a Low Impact Parameter Interaction (Krisnamoorthy and Marshall, 1997).....	32
Figure 1.29: High Impact Parameter Interaction (Krisnamoorthy and Marshall, 1997)	33
Figure 1.30: High Thickness Parameter Interaction (Rockwell, 1998).....	34
Figure 1.31: C_L , a universal lift coefficient developed by Liu and Marshall (2004)	35
Figure 1.32: University of Glasgow 'Argyll' wind tunnel configuration for orthogonal blade vortex Interaction (Copland, 1998).....	37

Figure 1.33: Unsteady surface pressure distributions showing the lower surface pressure peak and upper surface suction peak respectively. (Doolan, 2001)	38
Figure 2.1: Copland's experimental configuration installed in the small wind tunnel (Anatomy Tunnel) at Glasgow University (1998)	47
Figure 2.2: Comparison of numerical wake simulation and experimental measurements of wake shape (Doolan, 1999)	51
Figure 2.4: A constant change in normal force is found at all angles of incidence of the interacting blade (Doolan, 1999b)	55
Figure 2.5: Surface pressure measured at leading edge pressure transducer on the upper and lower surfaces respectively (Doolan, 1999b).....	56
Figure 2.6: Preceding blade configuration installed at Glasgow University (Doolan, 2001a).....	57
Figure 2.7: Wind tunnel configuration installed in large wind tunnel (Argyll tunnel) at Glasgow University (Wang, 2002)	59
Figure 3.1: Comparison coefficient of normal force between Time Averaged data blocks and a sample data block	65
Figure 3.2: Diagram of a typical impulsive change in normal force (dC_n).....	66
Figure 3.3: Sample data block from 40 m/s velocity data set at spanwise location where vortex centre passes over blade.....	67
Figure 3.4: Power Spectral Density plot. Zero Hz to (a) Nyquist at 25kHz, and (b) 5kHz respectively	67
Figure 3.5: Frequency response of 10th order Bessel filter with 5 kHz cut off frequency	68
Figure 3.6: Frequency response of 10th order Bessel filter with 500 Hz cut off frequency.....	69
Figure 3.7: Comparison of data block filtered at 500 Hz with original data block.....	69
Figure 3.8: Comparison of splined data with original data	70
Figure 3.9: Illustration of identification of maximum turning point (T.P.). Point B is the T.P., determined by the search through the splined samples. The local maxima must occur between A and C, and is found at D. Diagram showing the identification of local minima and maxima from original data using splined points identifying start and end time	71
Figure 3.10: Comparison of data Above the Vortex Centre and At the Vortex Centre.....	72
Figure 3.11: Example of identification of impulsive dC_n Event for data block at vortex centre.	73
Figure 3.12: Sample data with average time period extended by 2, 5, and 8% stretches	74
Figure 3.13: Variation of dC_n with spanwise location at 40 m/s.....	74
Figure 3.14: Comparison of Time Averaged and Spline Based determination of dC_n	75
Figure 4.1: Beddoes discrete time sampling - Step algorithm.....	83
Figure 4.2: Beddoes discrete time sampling - Ramp algorithm.....	84
Figure 4.3: Comparison of Kussner, Wagner and Beddoes circulatory indicial responses. Note that the Wagner response starts from 0.5 unlike the other responses which start from 0.....	85
Figure 5.1: Sampling of input of a system into a series of steps	91
Figure 5.2: Comparison of Kussner indicial lift response ($d_s=0.25$) to experimental data	95
Figure 5.3: Comparison of Kussner indicial lift response ($d_s=0.125$) to experimental data	96
Figure 5.4: Comparison of axial flow gust profiles and constant gust, respectively.....	96

Figure 5.5: Circulatory and Impulsive Shape Functions.....	99
Figure 5.6: Beddoes lift prediction comparison with experimental data at vortex centre	100
Figure 5.7: Circulatory Lift variation with changes in ds' step size.....	101
Figure 5.8: Impulsive Lift variation with changes in ds' step size.....	101
Figure 5.10: Comparison of 'Step' and 'Ramp' algorithms	102
Figure 5.9: Total Lift variation with changes in ds' step size	102
Figure 5.11: Effect of the number of Simpson segments ($ds' = 0.2\beta^2$). Note that with Simpson segments equal to 90 and 300 and identical response was calculated.....	103
Figure 5.12: Effect of the number of Simpson segments ($ds' = 0.01\beta^2$).....	103
Figure 5.13: Comparison of experimental data with model. ($ds' = 0.01\beta^2$, Velocity = 40 m/s)	105
Figure 5.14: Comparison of experimental data with model. ($ds' = 0.01\beta^2$, Velocity = 20 m/s)	106
Figure 5.15: Comparison of experimental data with model. ($ds' = 0.01\beta^2$, Velocity = 30 m/s)	108
Figure 5.16: Comparison of experimental data with model. ($ds' = 0.01\beta^2$, Velocity = 50 m/s)	107
Figure 6.1: Comparison of 2D vortex panel method with NACA data for NACA 0015.....	113
Figure 6.2: Effect of Axial Core Flow on Lift Coefficient for a blade at zero degrees of incidence.....	114
Figure 6.3: Resultant distribution of rotational velocity.....	115
Figure 6.4: Effect of Rotational Flow on Lift Coefficient for Blade at Two Degrees of Incidence	116
Figure 7.1: Surface pressure plots for upper surface of interacting blade for angle of incidence of 12 degrees. (a) Below, (b) centre, and (c) above.	119
Figure 7.2: Comparison of numerical wake simulation and experimental measurements of wake shape.....	122
Figure 7.3: Comparison of chord locations from Circulatory and Impulsive shape functions.....	124
Figure 7.4: Plan view of wind tunnel contraction and working section showing close proximity of subsequent wakes.	125
Figure 7.5: Comparison of 4th wake with 1st, 2nd and 3rd.	126
Figure 7.6: Comparison of 1st and 3rd wake shape.....	129
Figure 7.7: Comparison of (a) measured experimental response and (b) numerically simulated velocities, above and below the vortex centre	130
Figure 8.1: Simulated Axial Velocity Profile.....	131
Figure 8.2: Indicial Model Response to Simulated Axial Velocity Profile at Vortex Centre	132
Figure 8.3: Indicial Model Response to Simulated Axial Velocity Profile Below the Vortex Centre (One vortex core radius below in the spanwise direction).....	133
Figure 8.4: Indicial Model Response to Simulated Axial Velocity Profile Above the Vortex Centre (One vortex core radius above in the spanwise direction)	133
Figure 8.5: Circulation over Interacting Blade at 40m/s.	134
Figure 8.6: Indicial Response from Simulated Velocity Profile with Vortex Generator Peak Angle of Incidence set to 6 Degrees. Velocity = 40 m/s	136
Figure 8.7: dC_n comparison of experimental data and indicial models across all spanwise locations	137
Figure 9.1: Comparison of small wind tunnel experimental data and the indicial prediction of the experiment using a	

prescribed Lamb type vortex axial velocity profile. The spanwise location of the Interaction is the location where the vortex centre passes.	139
Figure 9.2: Lamb type vortex axial velocity profile	140
Figure 9.3: Figure 9.1 with markings A, B, and C.....	140
Figure 9.4: Comparison of experimental data with indicial prediction using a prescribed vortex core model with a vortex core radius of 0.091m.....	141
Figure 9.5: Comparison of experimental data and indicial model with core radius of 0.1 m, with lift coefficient plotted at 25% of original magnitude.....	141
Figure 9.6: Comparison of coefficient of lift per unit span at the vortex centre calculated by Liu and Marshall with Wang's experimental data (Case B3) (Liu and Marshall, 2004).....	143
Figure 9.7: Comparison of 50 m/s experimental case from Wang, with indicial prediction and Liu and Marshall's computation of this case.....	144
Figure 9.8: Fig 25a from Liu and Marshall (2004). Shows almost linear relationship between $C_{L_{max}}$ and axial core flow.....	146
Figure 9.9: Figure 25b from Liu and Marshall (2004) shows the variation of their new universal lift coefficient (C_L'') with time.....	146
Figure 9.10a: Total, circulatory, and impulsive lift for solution X.....	148
Figure 9.10b: Total, circulatory and impulsive lift for solution Y.....	149
Figure 9.10c: Total, circulatory and impulsive lift for solution Z.....	149
Figure 9.11: Comparison of C_L'' calculated by Liu and Marshall and the indicial model for case B3.	150
Figure 9.12: Indicial prediction of C_L'' using solution X.....	151
Figure 9.13: Indicial prediction of C_L'' using solution Y.....	151
Figure 9.14: Indicial prediction of C_L'' using solution Z.....	152
Figure 9.15: Normalized C_L'' for indicial model and computational cases.....	153
Figure 9.16: Axial flow decrease found by Liu and Marshall (2004). Centre of vortex core reaches leading edge at $t = 0.5$ and reaches the trailing edge at $t=1.0$	156
Figure 9.17: Peak axial velocity profile.....	158
Figure 9.18: Original lift coefficient per unit span response.	159
Figure 9.19: Inversely calculated peak axial velocity profile.....	160
Figure 9.20: Diagram showing experimental data and filtered experimental data.....	160
Figure 9.21: Diagram showing synchronization of the forward indicial calculation with the experiment using the point in time when the regular forward indicial calculation and the experimental data reach the first peak.....	161
Figure 9.22: Calculated peak axial profile required for synchronization as seen in figure 21.....	161
Figure 9.23: Indication of new synchronization of time frames using forward indicial method against experimental data.....	162
Figure 9.24: Inversely calculated peak axial velocity profile for synchronization in figure 9.23.....	163

List of Tables

Table 7.1: Comparison of peak axial velocity measured in all test cases at the spanwise location of the vortex centre.	127
Table 7.2: Comparison of peak axial velocity measured in all test cases at the spanwise location 0.1m above the vortex centre.	128
Table 7.3: Comparison of peak axial velocity measured in all test cases at the spanwise location 0.1m below the vortex centre.	128
Table 8.1: Numerical Simulation d_s' variation with velocity.	131
Table 8.2: Peak Circulation variation with peak vortex generator angle of incidence for freestream velocity of 40m/s. (Experimental Circulation = 1.26 ± 0.25).	135
Table 9.1: Anatomy wind tunnel parameters.	138
Table 9.2: Comparison of Wang's published parameters and the parameters used by Liu and Marshall (2004).	144
Table 9.3: Table 1 from Liu and Marshall detailing the non-dimensional parameters governing the B Cases (2004)	145
Table 9.4: Comparison of potential solutions X, Y, Z, for case B3.	148
Table 9.5: Shows the peak C_L'' in each set of cases, for Liu and Marshall, and for the indicial predictions X, Y, and Z. The normalized C_L'' data is the peak data divided by the maximum peak C_L'' in that set of cases, given in the last row for relevant columns.	152
Table C.1: Comparison of peak axial velocity calculated in all test cases at the spanwise location of the vortex centre. Freestream velocity = 20 m/s.	176
Table C.2: Comparison of peak axial velocity calculated in all test cases at the spanwise location 0.1m above the vortex centre. Freestream velocity = 20 m/s.	176
Table C.3: Comparison of peak axial velocity calculated in all test cases at the spanwise location 0.1m below the vortex centre. Freestream velocity = 20 m/s.	176
Table C.4: Comparison of peak axial velocity calculated in all test cases at the spanwise location of the vortex centre. Freestream velocity = 30 m/s.	178
Table C.5: Comparison of peak axial velocity calculated in all test cases at the spanwise location 0.1m above the vortex centre. Freestream velocity = 30 m/s.	178
Table C.6: Comparison of peak axial velocity calculated in all test cases at the spanwise location 0.1m below the vortex centre. Freestream velocity = 30 m/s.	178
Table C.7: Comparison of peak axial velocity calculated in all test cases at the spanwise location of the vortex centre. Freestream velocity = 40 m/s.	180
Table C.8: Comparison of peak axial velocity calculated in all test cases at the spanwise location 0.1m above the vortex centre. Freestream velocity = 40 m/s.	180
Table C.9: Comparison of peak axial velocity calculated in all test cases at the spanwise location 0.1m below the vortex centre. Freestream velocity = 40 m/s.	180
Table C.10: Comparison of peak axial velocity calculated in all test cases at the spanwise location of the vortex	

centre. Freestream velocity = 50 m/s.	182
Table C.11: Comparison of peak axial velocity calculated in all test cases at the spanwise location 0.1m above the vortex centre. Freestream velocity = 50 m/s.	182
Table C.12: Comparison of peak axial velocity calculated in all test cases at the spanwise location 0.1m below the vortex centre. Freestream velocity = 50 m/s.	182

Nomenclature

a	speed of sound (m/s)
A_1, A_2, A_3	coefficients in indicial method (circulatory)
AFP	Axial Flow Parameter
b_1, b_2, b_3	coefficients of exponential terms in indicial method (circulatory)
c	chord of interacting blade (m)
C_l	lift coefficient per unit span
C_L	lift coefficient
$C_{L\alpha}$	lift curve slope
C_{Li}	impulsive lift coefficient per unit span
C_L''	universal lift coefficient
h	unit impulse
H	Simpson segment size
IP	Impact Parameter
L	lift (N)
L'	lift per unit span (N/m)
M	Mach No.
r	radial distance from centre of vortex (m)
r_c	vortex core radius (m)
R_c	vortex core radius (m)
Re_B	Blade Reynolds Number
Re_V	Vortex Reynolds Number
s	incompressible non-dimensional time in terms of semi-chord lengths
s'	compressible non-dimensional time in terms of semi-chord lengths
t	time (s)
T_1, T_2, T_3	time constants in indicial method (circulatory)
T_I	time constant of impulsive shape function
TP	Thickness Parameter
U	freestream velocity (m/s)
V	freestream velocity (m/s)
V_θ	rotational velocity of vortex (m/s)
w	axial velocity (m/s)
W	axial velocity (m/s)
W_0	peak axial velocity at vortex centre (m/s)
W_{MAX}	peak axial velocity at vortex centre (m/s)
w_g	velocity of upgust (m/s)

w_e	effective gust velocity (m/s)
x	distance from leading edge in chordwise direction (m)
X, Y, Z	deficiency functions of indicial method
y	response of system
α	angle of attack ($^\circ$)
Γ	Circulation (m^2/s)
λ	impulsive shape function
η	circulatory shape function
ρ	density (kg/m^3)
σ	integration variable in indicial method
σ_0	vortex core radius (m)
τ	reference time in convolution sum
θ	angle of rotation from leading edge used in indicial calculations (radians)
ν	kinematic viscosity (m^2/s)
ψ	Kussner indicial lift response

1 Introduction

The significant noise produced by helicopters is well known. Helicopter noise is typically of a broadband nature primarily due to the rotor systems and the engine exhaust. However, helicopter noise has also been identified as containing more discrete components of impulsive noise. These are more noticeable and more irritating than the usual broadband noise and they have been typically named after their sound signature, which include 'bubbling' and 'slapping'. These generated noises normally only become dominant in particular flight modes. Unfortunately, these flight modes are fundamental in helicopter operation and cannot be easily avoided. Therefore, helicopter desirability for use in civil aviation and for stealth activities by the military could be improved with increased knowledge of these noise-generating mechanisms.

This chapter identifies blade vortex interaction as a dominant noise source during helicopter operation, and focuses on developing an understanding of the different types of blade vortex interaction. The particular focus of this work is tail rotor orthogonal blade vortex interaction and the modelling of this interaction. First, however, this interaction and the other blade vortex interactions are examined, together with modelling techniques, to determine an appropriate method to model tail rotor orthogonal blade vortex interaction.

1.1 Operating Environment

The generation of lift by an aerofoil is dependent on the development of a higher pressure on the lower surface than on the upper surface. On a finite span wing, or blade, this pressure distribution must be reconciled in some way at the wing tips. At the tips of a wing of finite span the air's movement is dependent on the greatest pressure gradient and flows from the high pressure on the lower surface to the upper surface by moving around the wing tip. This results in the well-known tip vortices, which exist for every lift generating finite span wing (Figure 1.1).

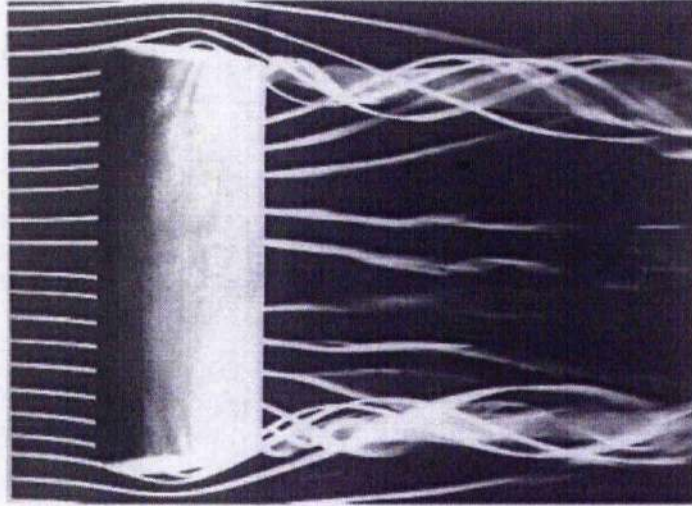


Figure 1.1: Formation of tip vortices (Kuethe and Chow, 1998)

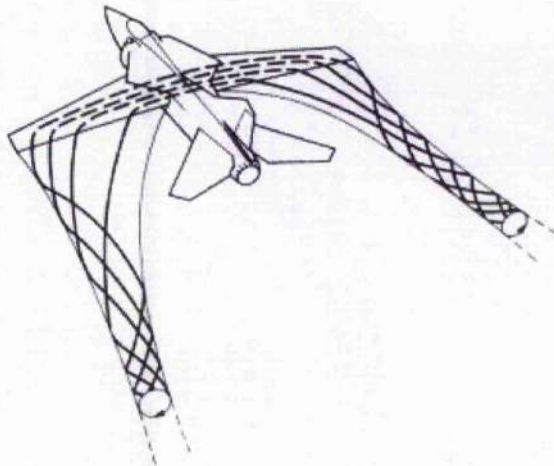


Figure 1.2: Formation of trailing tip vortices

The simplest manifestation of wing tip vortices is their generation by fixed wing aircraft. The two main wings on a typical fixed wing aircraft trail the main dominant pair of vortices (Figure 1.2). These tip vortices are trailed by the wing tips and remain fairly stationary in the flow field as the aircraft continues its forward motion. The tip vortices diffuse over time due to the viscous effects in air. However, these trailing tip vortices can cause serious problems for closely following aircraft particularly at aircraft landing strips. The circulation of the tip vortices is proportional to the lift generated by the wing. Heavier aircraft necessitate higher lift, and therefore generate larger tip vortices. Undesirable circumstances arise when heavy aircraft, travelling at the low velocities necessary for landing, generate a large pair of trailing

tip vortices due to their large lift requirement. A following aircraft descending for landing will not encounter the expected uniform flow but rather a trailed tip vortex that presents potentially dangerous flying conditions, especially for smaller aircraft (Figure 1.3).

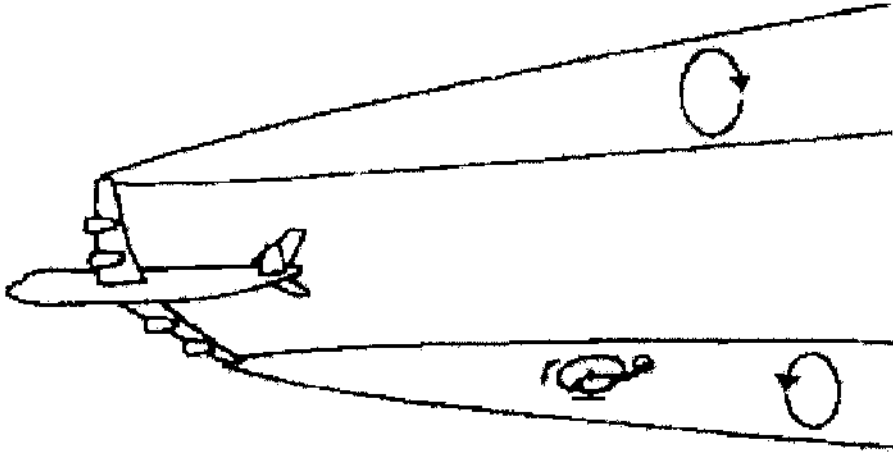


Figure 1.3: Dangerous flight conditions in the wake of a larger aircraft due to trailing wing tip vortices

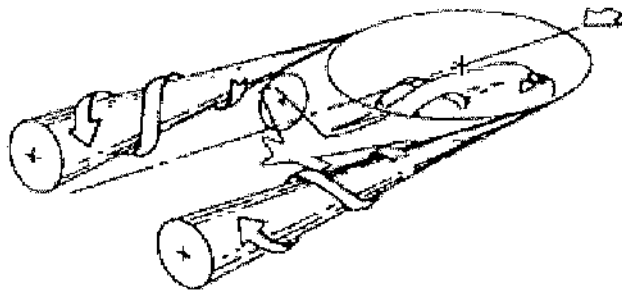


Figure 1.4: Rolling up of main rotor blade tip vortices into two discrete trailing vorticity structures.

Helicopter rotor blades are high aspect ratio wings that are essentially similar to aeroplane wings. Helicopters are also known to generate a pair of trailing tip vortices in their wake when in forward flight (Figure 1.4), however, the focus of this report is the complex flow field in the closer proximity of the helicopter. As each rotor blade is a lifting surface, each blade generates a tip vortex. However, unlike in the fixed wing environment these vortices are trailed in circular paths as the rotor blades rotate (Figure 1.5). Therefore, the flow field is very complex due to the, typically, constant generation of trailed tip vortices by every main and tail rotor blade, at varying locations about the helicopter body. In forward motion, tip

vortices trailed by the main rotor can interact with main rotor blades, tail rotor blades, the tail section, and the helicopter fuselage (Prouty, 1985). These are typically referred to as blade vortex or vortex surface interactions. The particular case examined in this work, i.e. tail rotor orthogonal blade vortex interaction, is the convection of tip vortices generated at the rear of the main rotor disc into the tail rotor disc and tail section.



Figure 1.5: Helicopter main rotor blade tip vortices

1.2 Interactional Aerodynamics of Helicopters

Blade vortex interactions exist in many forms. The three main idealised types are: perpendicular, parallel, and orthogonal (Figures 1.6 and 1.7). Perpendicular and parallel blade vortex interactions are typically only discussed in relation to the interaction of a main rotor blade with a preceding main rotor blade's wake. These are particularly evident on the main rotor blades in forward flight with the detailed interaction geometry depending on subtleties such as the main rotor disc attitude. These interactions are also possible on the tail rotor (Yang, 2004). Since, however, the tail rotor is used to trim the yaw attitude of the helicopter and not solely for the generation of a helicopter's lift, the parallel and perpendicular interactions on the main rotor are more detrimental to helicopter performance.

Parallel and perpendicular interactions both result in noise generation. Similarly, due to the inherently regularly repeating impulsive nature of the orthogonal interaction, it is also considered a significant noise generating mechanism.

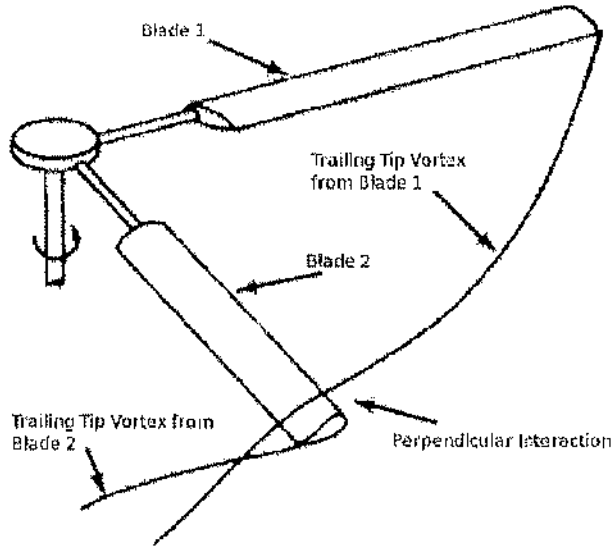


Figure 1.6: Perpendicular Interaction

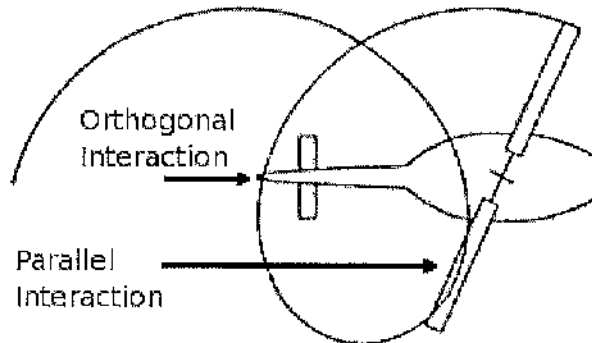


Figure 1.7: Parallel and Orthogonal Interactions (Horner et al, 1992)

Sheridan and Smith (1979) published a comprehensive summary of the problems of interactional aerodynamics in the field of helicopter operation in the late 1970's. They noted that the increased occurrence of interactions at that time was primarily due to a few reasons. Disc loading had increased dramatically resulting in more powerful wakes generated by the main and tail rotors. Smaller, more compact helicopters became more desirable for easier

transportation and for low profile military applications. In addition, the military's tactics were favouring low-level 'nap-of-the-earth' flight manoeuvres resulting in increased interaction of the helicopter with the ground vortex, and increased wake interactions with obstacles on the ground. Also, as a safety measure, increasingly larger tail fins were implemented to prevent the complete loss of yaw control if tail rotor failure occurred.

At that time, the assessment of helicopter interactional aerodynamics was limited to flight-testing. Subsequent adjustments to the helicopter configuration to account for unforeseen performance problems, due to interactional aerodynamics, were expensively carried out at the flight-testing stage. Sheridan and Smith documented the need for increased knowledge in this field to prevent alterations at such a late stage, and suggested the study of the following topics to improve knowledge in the field: the determination of favourable and unfavourable configurations of helicopter components, proper accounting of all interactional phenomena, and the development of methods and models to determine potential problems in the early design stages of a helicopter.

The interactions experienced by a helicopter can result in many different types of flow field responses (Sheridan and Smith, 1979) including flow redirection, separated flow, supersonic flow regions, flow field distortions, surface and vortex impacts, wake impingement, and flow instability between adjacent flows. Sheridan and Smith also reiterated that the interactions are dependent on the sources producing the complex flow field, namely, the main rotor, tail rotor, and the engine exhaust. Typically the interactions in the flow field result in unsteady flow at the location of the interaction and downstream. Of particular relevance to this work, Sheridan and Smith suggested that research focusing on the growth and decay of tip vortices and their interaction with other flows, and particularly the interaction of main rotor tip vortices with main rotor blades and the tail rotor, would be beneficial. They also suggested that analysis of the generation of rotor blade loads in response to interactions was required and the associated noise generation mechanism should be investigated.

Ellin (1994) documented the flight-testing of a Lynx helicopter with the particular intent of measuring the tail rotor disc's response to interactions with main rotor tip vortices in low speed forward flight, and the transition from hover to forward flight. Ellin, similarly to Sheridan and Smith, although considerably more recently, documented the still existent lack of understanding of tail rotor blade vortex interactions. Research (Leverton, 1993, Jacobs, 1997) had been conducted into tail rotor rotational sense, location, and tail rotor parameters to reduce tail rotor noise generation; however, the research had focussed on detailing the gross noise generation rather than identifying the underlying flow field mechanisms.

Ellin used an instrumented tail rotor to measure the change in pressure measured near the tail rotor leading and trailing edges. Ellin observed that the close passage of main rotor tip vortices to the tail rotor disc resulted in a reduction in tail rotor loading in hover and hampered helicopter yaw control. This was due to the orthogonal interaction of the tail rotor with the main rotor wake in hover or forward flight. Yaw control was also reduced in quartering flight (Figure 1.8), where the rolling up of the main rotor tip vortices into a structure similar to a fixed wing aircraft trailed vortex (Figure 1.4), distorts the flow field at the tail rotor. The focus of this work concentrates on the former case of blade vortex interaction where the tail rotor interacts with individual discrete main rotor tip vortices (Figure 1.9), rather than the latter case, where multiple vortices roll up into a larger vorticity structure which interacts with the tail rotor blades during quartering flight for example.

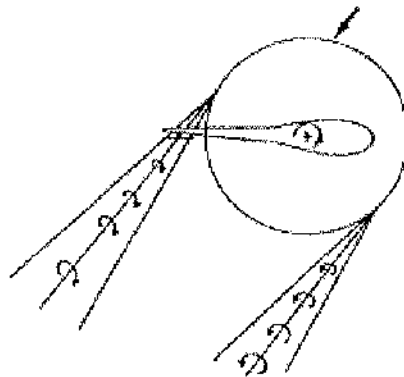


Figure 1.8: Quartering Flight

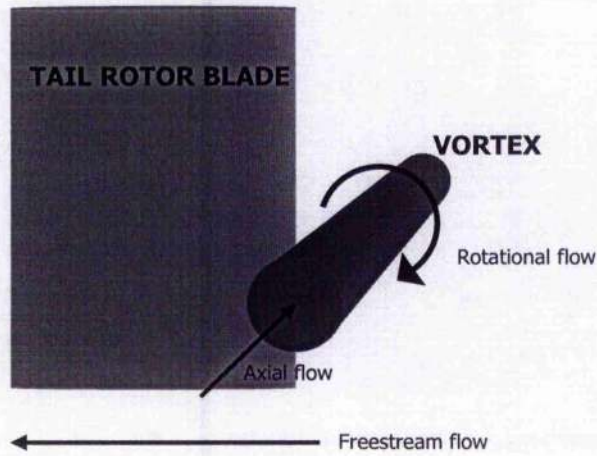


Figure 1.9: Single clean orthogonal blade vortex interaction

1.3 Interactions with the Main Rotor Wake

The different ways in which the main rotor wake interacts with rotor blades or the fuselage are all similar to some degree. Despite the variation in orientation, the interactions typically involve short-term impulsive changes in loading, sound generation and unsteady flow fields. The interaction of the main rotor wake with different bodies results in varying responses, much of which has been thoroughly reviewed by Rockwell (1998).

Given the similarity of the three idealised blade vortex interaction types, the study of all types may yield useful results and methods for analysing orthogonal blade vortex interaction. Therefore, previous work on perpendicular interactions with the fuselage and other blades and the parallel interaction of the main rotor with the main rotor wake will be summarised before looking specifically at orthogonal blade vortex interaction.

1.3.1 Fuselage Interactions

Liou et al. (1989) experimentally investigated the interaction of a two-bladed main rotor wake with a cylinder representing a helicopter fuselage. Pressure measurements, flow visualisations, and velocity measurements (Laser Doppler Velocimetry) were used to examine the behaviour of the tip vortices generated by the main rotor blades upstream of the hub, and their subsequent convection into the cylinder (Figure 1.10), resulting in perpendicular interactions along the top of the cylinder. Liou found that flow stagnation and flow reversal occurred as the tip vortex neared the surface. Negative vorticity was created under the vortex when the vortex was above the cylinder, indicating boundary layer separation due to stagnation and flow reversal near the surface. This negative vorticity moved rapidly around the tip vortex and ended up downstream. Secondary vorticity was also generated when the lower half of the tip vortex interacted with the surface. This vorticity travelled quickly downstream in a manner consistent with image vortex considerations. After the primary impact, pressure measurements on the cylinder surface indicated that, downstream, the flow was dominated by the secondary vorticity.

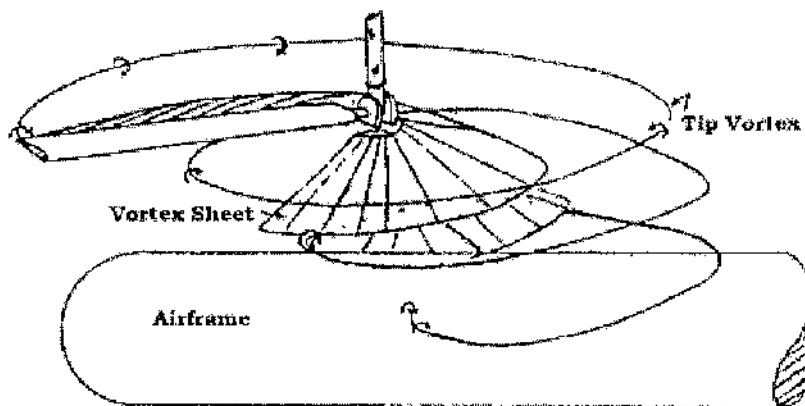


Figure 1.10: Configuration used by Liou to capture perpendicular surface vortex interactions upstream of the main rotor hub (Liou et al, 1989)

Leishman and Bi (1990) experimentally examined fuselage interactions using a similar method to Liou et al. However, Leishman and Bi used a fully articulated main rotor with a body that was more representative of a helicopter fuselage. The fully articulated system allowed the experimental investigation of vortex-fuselage interactions found in typical forward flight, for a scaled down model. The configuration also allowed the investigation of different advance ratios, shaft tilts and rotor thrusts.

Leishman and Bi found that the loads experienced by the fuselage varied primarily with advance ratio, where at an advance ratio of 0.15 and above, the downwash of the main rotor disk on the fuselage was not significant compared to at lower advance ratios. The loading on the fuselage at high advance ratio was therefore similar to that on an isolated fuselage. Leishman and Bi also showed that examination of the pressure signature for an arbitrary point, aft of the main rotor disc on the tail boom, allowed for the identification of the tip vortex interaction occurring at the point. For a direct or very close vortex-surface interaction, the pressure signature contained several impulsive changes in pressure, due to the vortex impingement. As the vortex passed above a point, a characteristic strong 'saw-tooth' pressure signature was found due to the variation of induced velocities from the vortex (Figure 1.11).

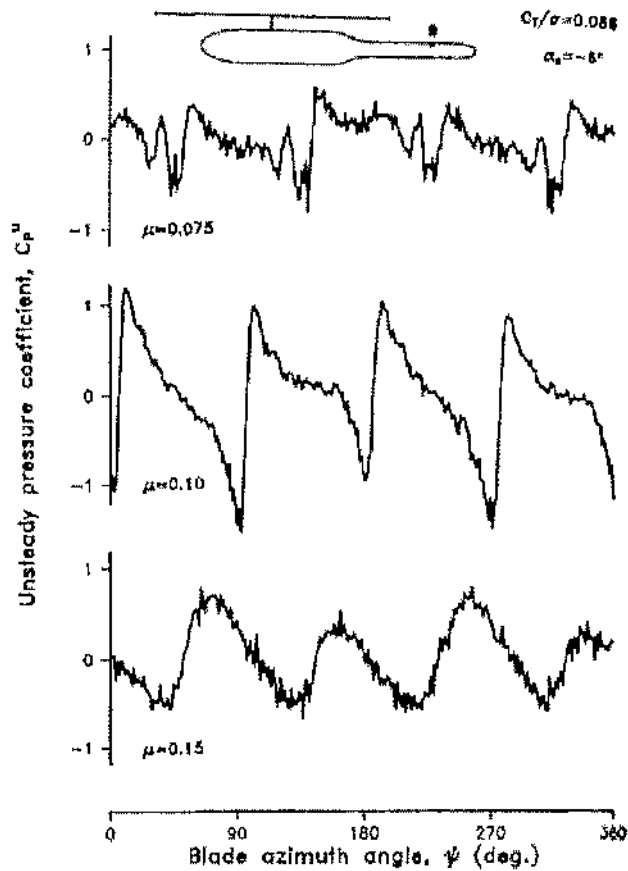


Figure 1.11: Pressure signature variation dependent on passage of vortex at different heights (Leishman and Bi, 1990)

Bi et al (1993), used the same configuration as Leishman and Bi, and also used flow visualisation, together with pressure measurements and vortex trajectory tracking to enable the analysis of the tip vortices as they approached the surface, distorted near the surface, and then impacted on the surface. Bi et al used unsteady potential flow theory to simulate the generated rotor wake by using a prescribed wake shape taken from the vortex trajectory measurements. This three-dimensional simulation enabled the modelling of the approach of the tip vortices to the fuselage surface; however, it failed to predict the impingement and subsequent generation of the secondary vortical structure.

The impingement of the vortex results in high transient loads and a high adverse pressure gradient, which can cause the local separation of the boundary layer. The loads from the interaction are small because the vortex impingement is localised, and is therefore insignificant compared to the total load experienced by the fuselage. Bi et al, similarly to Leishman and Bi, verified that the interactions were limited to hover and low advance ratio forward flight.

A series of subsequent studies by Affes et al (1993a, 1993b, 1998) attempted the modelling of the vortex-fuselage interaction. The model was a three-dimensional potential flow model, which implemented the tip vortex as a single three-dimensional vortex tube and the fuselage as an infinite circular cylinder, with the induced velocity field of the vortex calculated by the Biot-Savart law. The model and experimental data showed agreement before the interaction of the vortex with the cylinder surface. The generation of the suction peak on the surface of the cylinder was predicted in terms of location and magnitude by the model. The adverse pressure gradient that occurs on the fuselage surface was also predicted. This adverse pressure gradient, which typically gives rise to boundary layer separation, was due to the tangential flow in the lower half of the tip vortex opposing the freestream flow near the surface.

The most recent study by Affes et al in 1998 used the three-dimensional boundary layer equations, which were solved by finite difference and Fourier transform methods, to simulate the impingement of the tip vortex. This addition to the existing unsteady potential flow model enabled the viscous modelling of the interaction in the early stages of the generation of the secondary vortical structure, by simulating the reversed flow region and the corresponding adverse pressure gradient as the tip vortex approached the fuselage surface. Affes et al also postulated that the use of a Navier-Stokes solver to model the interaction would be difficult considering the length scales involved, where the size of the tip vortex is very small compared to the flow field of the calculation which includes the two bladed main rotor system and the fuselage.

Further detail on fuselage interactions, in which a cylinder typically represents the fuselage, has been provided by Kim and Komerath (1995) in a review of research into fuselage interactions prior to the viscous modelling of the surface boundary layer by Affes et al in 1998.

1.3.2 Perpendicular Interactions

Perpendicular blade wake interactions contribute to the broadband noise generated by helicopters during forward level flight and gentle climb conditions. This interaction typically occurs on the main rotor's advancing side, where the tip vortex generated by a previous rotor blade interacts with the wake of the subsequent blade. This has primarily been reproduced using simplified experimental configurations in wind tunnels. Wittmer and Devenport (1995a, 1995b, 1999a, 1999b) completed a series of thorough experimental investigations of perpendicular interactions and these are described here.

Figure 1.12 shows the typical experimental wind tunnel configuration used to examine perpendicular interactions of tip vortices with a blade. The configuration features two blades fixed to the wind tunnel walls. The first blade, which is upstream of the second, has a positive angle of attack and therefore generates a streamwise tip vortex. This tip vortex convects downstream and interacts with the 'interacting blade' and its wake.

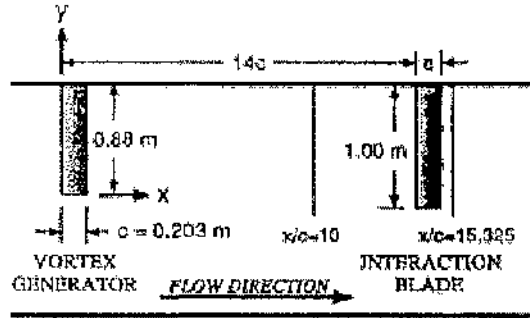


Figure 1.12: Typical perpendicular blade vortex interaction configuration. This configuration features a finite span wing as a 'vortex generator'. (Wittmer et al, 1995a)

Originally the experiment used a finite span interacting blade (Figure 1.12) (Wittmer, 1995a), but due to the mixing of the upstream blade's tip vortex and the interacting blade tip vortex, further tests were conducted with an 'infinite' span interacting blade (Figure 1.13) (Wittmer, 1995b) connected to both sides of the wind tunnel working section. Velocity measurements and flow visualisations were used to examine the close passage of the streamwise vortex over the interacting blade in both cases.

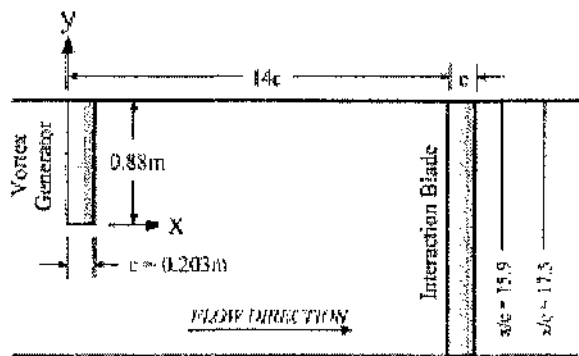


Figure 1.13: Perpendicular configuration featuring an 'infinite' span 'vortex generator' (Wittmer et al, 1995b)

It was found that the upstream tip vortex consisted of a laminar core wrapped in the turbulent blade wake of the vortex generator. Measurement of the high frequency velocity

fluctuations in the vortex core confirmed that they were an order of magnitude less than those in the turbulent wake. The initial passage of the generator's tip vortex over the interacting blade produced no immediate structural response within the vortex. However, the tracking of the tip vortex downstream from the interacting blade indicated that the interaction of the vortex with the interacting blade wake altered the tip vortex structure. This change in vortex structure has its origins in the variation in spanwise blade loading caused by the vortex interaction.

The effect of the induced tangential flow field of the tip vortex on the interacting blade resulted in the generation of negative vorticity at spanwise locations where the local effective angle of attack was decreased (Figure 1.14). This negative vorticity, which is opposite in sense to the positive vorticity in the tip vortex, resulted in the degradation of the tip vortex. The unstable nature of the flow due to the close proximity of the positive vorticity with the negative vorticity caused the vortex core to grow rapidly engulfing the negative vorticity region and reducing circulation in the process. High frequency velocity components in the vortex showed that, at this point, the tip vortex core became turbulent. The interaction of the tip vortex with the negative vorticity on the blade also caused an increase in vortex core radius, a reduction in core circulation, and a decrease in peak tangential velocity and axial core flow.

The development of the tip vortex downstream of the interacting blade was found to be dependent on the vertical separation distance (Figure 1.15). At a separation distance of greater than 0.3 chord lengths, the tip vortex core experienced little change in its structure. If the separation distance was less than 0.3 chord lengths, the core was weakened and increased in size becoming turbulent as it convected downstream. Differences between the suction and pressure sides were found when the separation was less than 0.1c. Typically, the passage of the tip vortex on the pressure side resulted in a more severe interaction. In general, the decay of the tip vortex was faster with a smaller separation. However, if the nominal vortex core path was coincident with the blade stagnation location, then the peak tangential velocity was more severely reduced, and there was a larger increase in core

radius. This response was generally similar to the interaction experienced when the separation distance was less than $0.1c$, where the core circulation was reduced due to the interaction with the negative vorticity shed from the interacting blade.

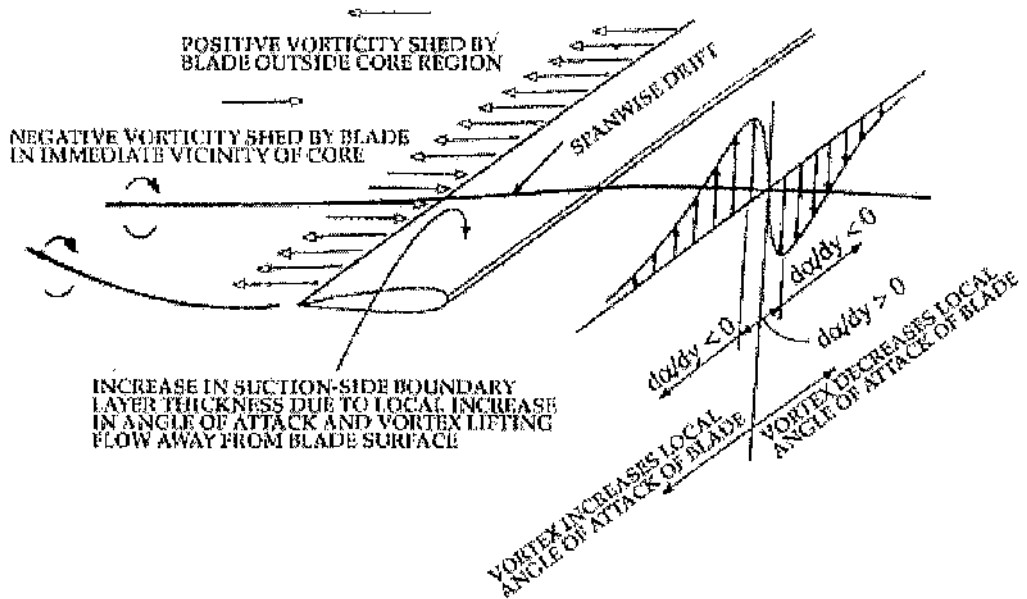


Figure 1.14: Vortex tangential flow results in varying spanwise angle of attack (Wittmer et al, 1995b)

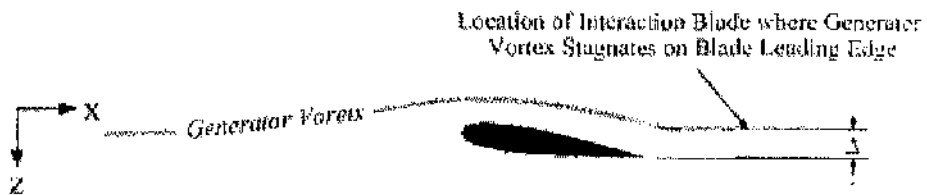


Figure 1.15: Illustration of separation distance Δ (Wittmer et al, 1995b)

Wittmer (1999a, b) also modelled the perpendicular interaction of the tip vortex. By building on the work of Hancock (1970), who estimated the aerodynamic load induced on an aerofoil in forward motion due to a nearby streamwise vortex using Prandtl's lifting line theory, Wittmer was able to predict the resultant distribution of trailed vorticity from the wing under the influence of the streamwise tip vortex. However, this method severely over predicted the experimentally measured circulation distribution. Ham (1975) determined that during the interaction of a returning (self-interacting) tip vortex with an aerofoil, the maximum change in

lift coefficient induced on the blade is limited to a maximum of 0.3 or less due to the occurrence of flow separation. By applying this limit to the maximum change in lift coefficient, Wittmer's lifting line prediction resulted in a reasonably accurate prediction of the interacting blade's shed vorticity sheet strength. However, Wittmer acknowledged that insufficient experimental data was captured with respect to the vortex sheet strength to establish whether the lifting-line model and the maximum change in lift coefficient were valid for varying blade vortex separation distances, vortex strengths, and angles of attack. Wittmer's (1999b) parametric study did, however, again show that the response of the vortex to the interaction was primarily dependent on the separation distance.

Brooks et al. (1989) found that the interaction of a blade with the turbulent wake of a preceding blade dominated the mid-frequency range in forward flight, when strong, parallel blade vortex interactions were avoided. However, Devenport et al (1992) showed, for this condition, that modelling the interaction of a blade, with a blade wake interaction noise prediction scheme (Glegg, 1989), and an undisturbed wake produced lower noise levels than those found experimentally. The work of Wittmer et al (1995) described above found an answer for this discrepancy and enabled accurate prediction by considering the interaction of a turbulent wake from a preceding blade that had already interacted with another blade. The increase in turbulence produced by the initial perpendicular interaction could be sufficient to account for the experimentally observed noise levels.

1.3.3 Parallel Interactions

Parallel blade vortex interactions have been found to produce impulsive, powerful and undesirable noise in rotorcraft flight. Parallel interactions are known to occur in powered descent and during manoeuvring flight. This interaction was observed, for example, in flight tests of a model rotor system (Lorber, 1990), which showed that the most disruptive pressure disturbances are caused by the parallel or near parallel (oblique) blade vortex interactions. This confirmed an observation by Widnall (1971) who showed computationally, using linearised flow theory and transformed sinusoidal gusts to represent the velocity field

of the vortex, that parallel interactions produced the highest amplitude pulse. Generally, (Ziada and Rockwell, 1983; Caradonna et al, 1988) the magnitude of the disturbance from this type of interaction has been found to be dependent on the strength of the vortex, the separation distance between the vortex and the interacting blade, and the angle between the vortex axis and the blade leading edge, i.e. the obliqueness of the interaction.

Surendraiah (1969), Kokkalis et al (1986), Caradonna et al (1988), and Straus et al (1988, 1990), successfully reproduced the parallel or near parallel blade vortex interaction in wind tunnels. Typically, knowledge of the flow field and the blade response increased with each successive study, which primarily focused on the collection of surface pressure data. The integration of the pressure distribution to give force and moment data has enabled comparison with computational predictions of blade vortex interaction. The data show that the vortex induces the growth of the leading edge suction peak on the interacting blade. Also, propagative and convective disturbances on the interacting blade's surface are found, with the convective disturbances correlating to the passage of the vortex in the chordwise direction.

The propagative and convective disturbances are visible in the pressure coefficients measured by Caradonna (1988), and Kokkalis (1986). The propagative disturbance, moving at the speed of sound, can be seen as the reduction in pressure coefficient across the whole blade chord (Figure 1.16), whereas the convective disturbance is visible as the small ridge of pressure coefficient moving across the chord at approximately the freestream velocity.

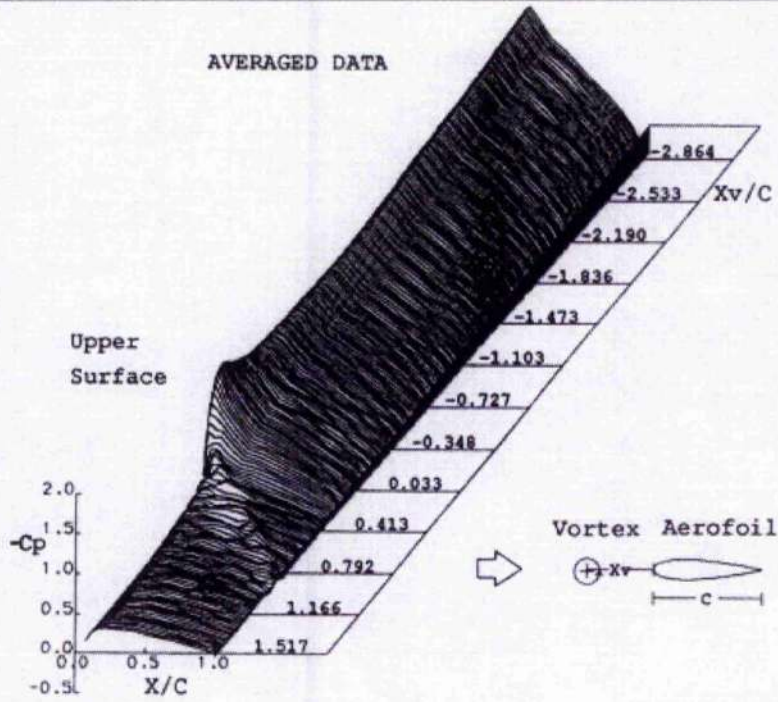


Figure 1.16: Visualisation of Convective and Propagative pressure Disturbances (Horner et al, 1996)

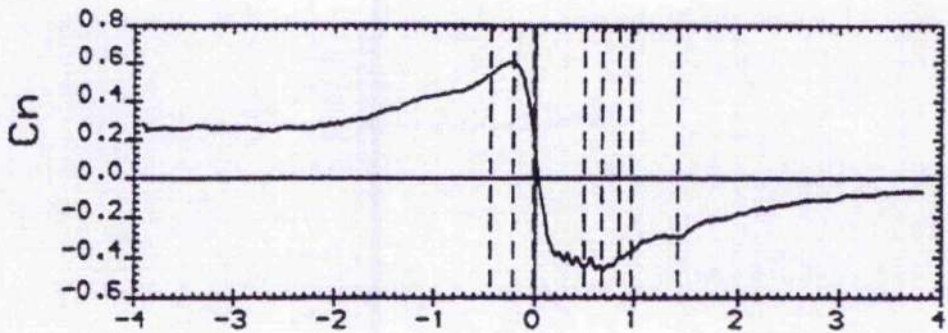


Figure 1.17: Coefficient of normal force response due to parallel blade vortex interaction (Horner et al, 1996)

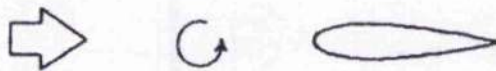


Figure 1.18: Illustration of vortex sense of rotation

In terms of the normal force response (Figure 1.17) to the interaction, both Surendraiah and Kokkalis et al. showed that the parallel interaction is approximately symmetrical about the upper and lower surfaces with respect to the vertical height of the vortex axis in relation to the leading edge of the interacting blade. As the vortex in Figure 1.18 approaches the interacting blade's leading edge it experiences an increase in normal force due to the induced increase in angle of attack. The normal force (Figure 1.17) then drops rapidly coinciding with the dissipation of the leading edge suction peak, and normal force continues to decrease due to the downwash from the interacting vortex as it progresses across the chord. The severity of the drop in normal force is reduced due to enhanced suction on the upper surface from the local increase in velocity due to the interacting vortex as it passes over the upper surface. The interacting blade, set at zero angle of incidence, finally regains lift as the vortex progresses beyond the trailing edge.

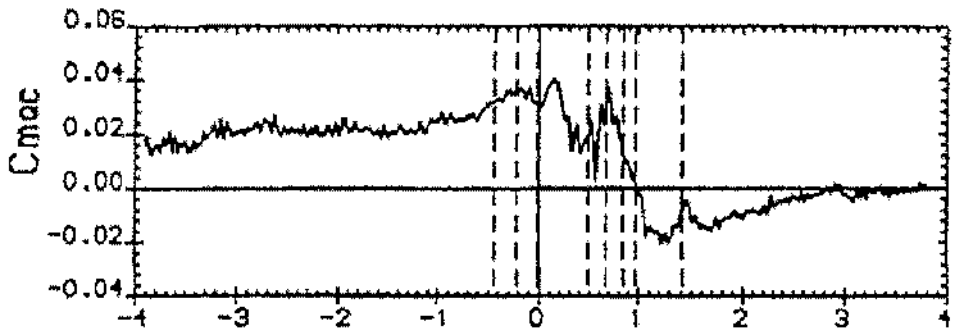


Figure 1.19: Coefficient of moment about aerodynamic centre response due to parallel blade vortex interaction (Horner et al, 1996)

The pitching moment (Figure 1.19) about the interacting blade quarter chord is also dominated by the passage of the vortex across the blade chord. A positive moment is produced as the approaching vortex generates upwash at the leading edge. As the vortex progresses over the blade surface the trailing edge now experiences the upwash and the leading edge now experiences downwash resulting in a negative moment, until the tip vortex moves off the trailing edge. As the vortex moves further downstream the effect of the tip vortex diminishes and the quarter chord pitching moment tends towards the pre-interaction state.

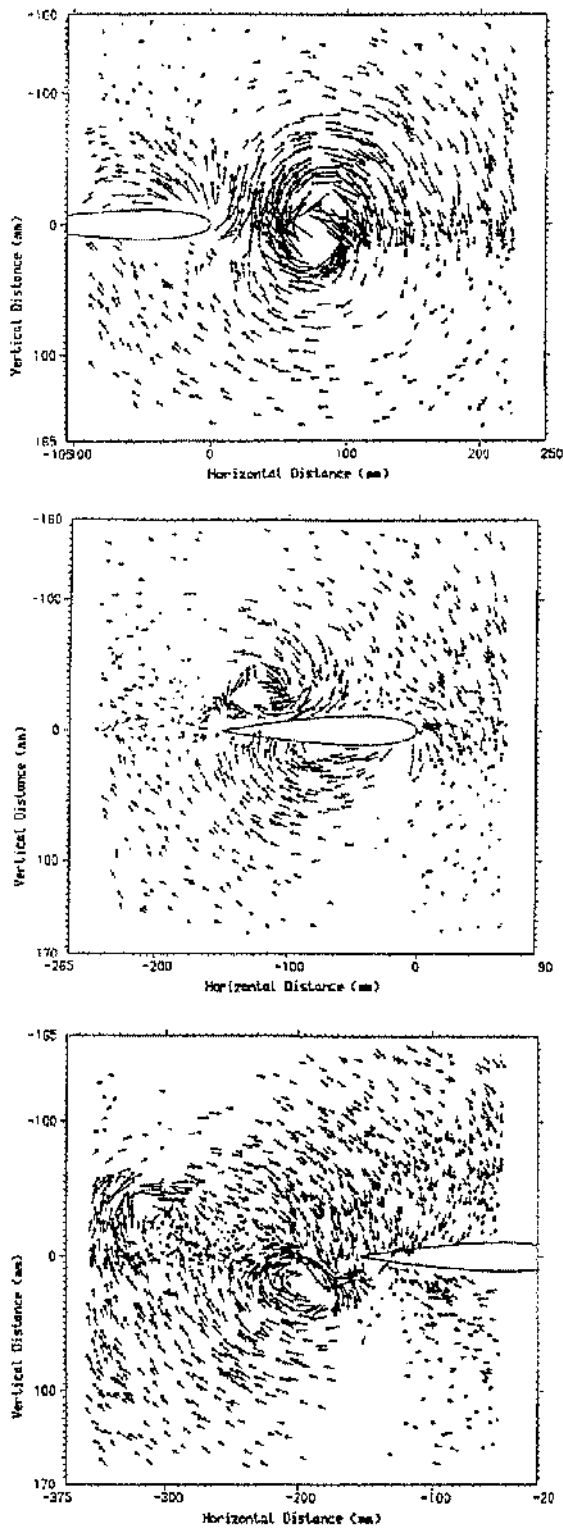


Figure 1.20: PIV shows the splitting of the incident vortex into two (Horner et al, 1996)

A later study by Horner (1996) involved visualisation of the flow using particle image velocimetry (PIV). The visualisation showed that during the direct interaction of the leading edge with the centre of the incident tip vortex, the vortex was split into two separate parts (Figure 1.20). The vortex fragment that passed the lower surface of the blade was stretched about the lower surface, while the upper fragment was only slightly distorted in comparison. The upper vortex fragment convected more quickly, which is consistent with image vortex concepts, and so the two vortical structures were observed leaving the trailing edge. Other significant features observed were the generation of secondary vorticity due to the interaction of the vortex fragments with the blade surface boundary layer, and shed vorticity due to the changes in lift. In this respect, one substantial vortical structure that was observed was a trailing edge vortex that developed above the trailing edge during the early stages of the interaction just after the initial splitting of the incident tip vortex into two fragments.

Various modelling techniques have been employed to model parallel blade vortex

interaction. Caradonna (1988) attempted to model the interaction using the three-dimensional, unsteady, full potential rotor code of the US Army, FPR. The interaction was predicted well even for 'head-on' interactions where vortex deformation, a feature not incorporated into the model, occurred. This code modelled the flow field in three dimensions and produced close comparisons with other experimental and computational data. Caradonna also investigated an alternate, less time consuming, solution where only the inflow at the interacting blade's surfaces was modelled, however, this did not predict the interactions as well as the FPR code with its associated three-dimensional modelling demonstrating the three-dimensionality of the interaction.

To demonstrate how powerful indicial modelling could be, Sears (1969) documented a theoretical example using indicial modelling to simulate the interactions associated with propeller and helicopter noise. This modelling approach is based on classical two-dimensional, incompressible, unsteady aerofoil theory. Beddoes (1989) built on the earlier work of Kussner and Wagner and developed an indicial method for the two-dimensional modelling of parallel blade vortex interaction. Beddoes provided improvements that allowed the separation of the lift response into a propagative impulsive component and a convective circulatory component. Also, Beddoes used thin aerofoil theory to enable the more accurate representation of the chordwise distribution of incident velocities on the interacting blade surface. The resultant indicial model showed good correlation with previous experimental and computational investigations of parallel blade vortex interaction (Figure 1.21). This indicial model, which will later be described in more detail, was used as the basis for the numerical modelling in the present study.

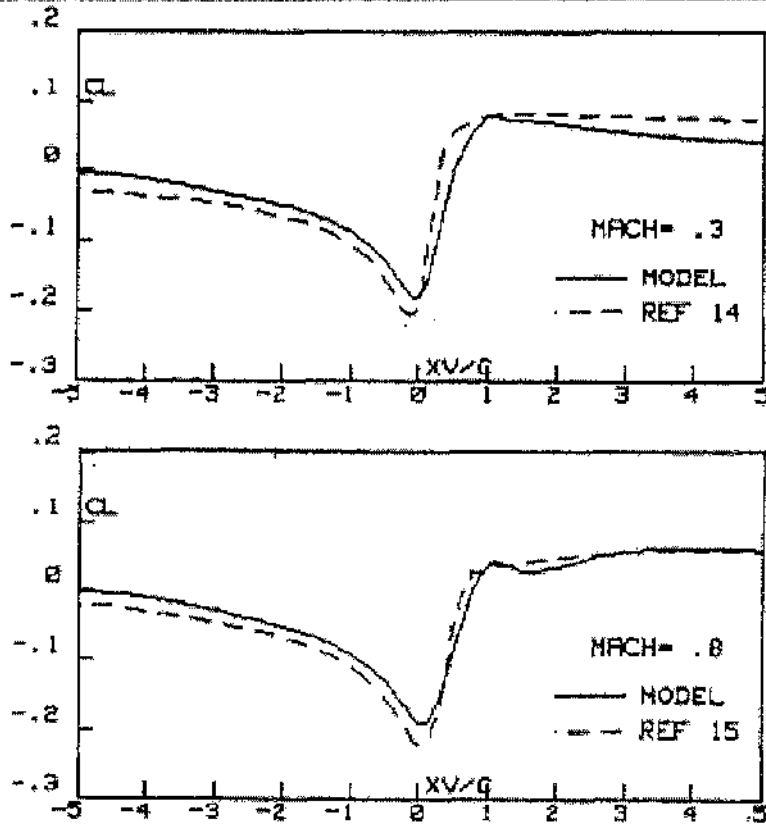


Figure 1.21: Comparison of Beddoes indicial model with Navier Stokes calculations for parallel blade vortex interaction (Beddoes, 1989)

Lee et al (1991) computationally modelled the parallel interaction using a two-dimensional, incompressible, inviscid flow calculation where the vorticity field was represented by many smaller vortices, typically referred to as a "cloud" of vortices (Figure 1.22). The interacting blade was represented by a shifting panel method, which redistributed the panels to retain accuracy and computational efficiency and to follow the vortex as it progressed across the chord. The adaptive panel method and the distributed discrete vortex method allowed the distortion of the vortex to be calculated, a feature commonly not incorporated into other models. The model showed that significant distortion and even splitting occurred for close interactions and that the distortion, the resultant lift response, and the mixing of the vortices with the aerofoil wake, are dependent on the strength and size of the incident vortex. Lee also observed that the unsteady lift generated in the parallel blade vortex interaction is a significant factor in determining the overall lift response of the blade.

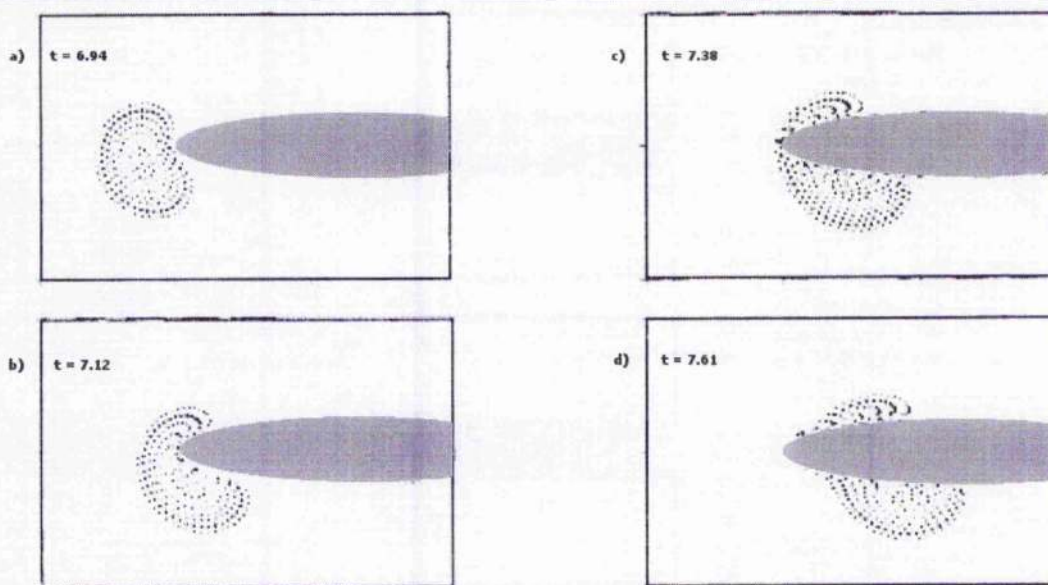


Figure 1.22: Cloud of small vortices (Lee et al, 1991)

In 1991 Renzoni and Mayle, also used a discrete free-vortex method and potential flow theory to model the unsteady parallel blade vortex interaction. Again, they found good agreement demonstrating that inviscid theory, together with a cloud of discrete free-vortices, is adequate to reproduce most parallel blade vortex interactions. However, similarly to Lee et al., the response due to close interactions was still greatly over predicted compared to experimental data (Kokkalis et al, 1986). Renzoni and Mayle found that the total incremental change in lift and moment, was directly proportional to the vortex circulation and inversely proportional to the square root of the initial vertical separation distance.

1.3.4 Orthogonal Blade Vortex Interaction

1.3.4.1 Initial investigations of tail rotor noise

Tail rotor orthogonal blade vortex interaction is challenging to study due to the complexity of the flow field. The measurement of the noise generated by the tail rotor is complicated by the fact that the source is part of the total noise generated by the helicopter. The sound field contains components that result from the main rotor, exhaust, gearbox, and the tail rotor's 'self' interactions. Leverton et al. (1977) detailed an experimental and theoretical study of the

distinctive 'burbling' noise generated by a Lynx helicopter during the orthogonal interaction of the main rotor trailed tip vortices with the tail rotor. In forward flight, due to the relative positions and rotational rates of the main and tail rotors, a main rotor blade tip vortex will interact with four or more tail rotor blades as the tip vortex convects across the tail rotor disc (Figure 1.23). The successive impulsive interaction results in a modulated noise, commonly referred to as 'burbling'.

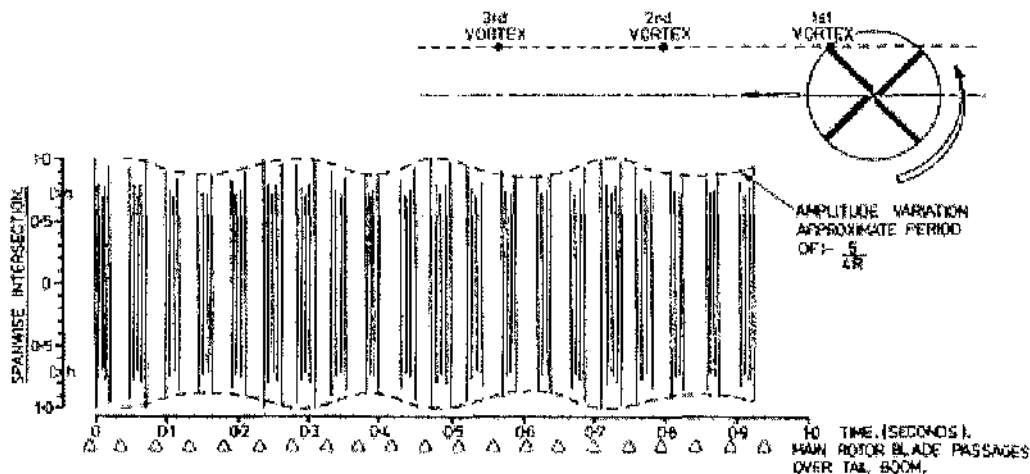


Fig. 1. Tail rotor blade/main rotor vortex intersection points.

Figure 1.23: Multiple interactions of main rotor tip vortices with the tail rotor blades [Taken from (Leverton et al, 1977)]

Leverton et al. (1977) used an array of microphones on the ground and on the helicopter fuselage to record the fly-past of a Lynx helicopter. They managed to isolate the noise source and identify the frequency and amplitude components. Their theoretical analysis confirmed that the generated noise was dependent on the relative rotational frequencies of the main and tail rotors, and forward velocity. They predicted that reversing the direction of tail rotor rotation would reduce the impulsive noise generation of the tail rotor. Reversing the tail rotor rotational sense had the effect that the tail rotor was rotating top aft. This resulted in fewer, and less impulsive peak sound pressures (Figure 1.24). The opposite was true of the original tail rotor rotational sense as the severity of the bottom aft tail rotor resulted in frequently occurring impulsive interactions which were more severe due to the local velocity at the point of interaction. This was confirmed in both the theoretical and experimental studies of Leverton et al. (1977).

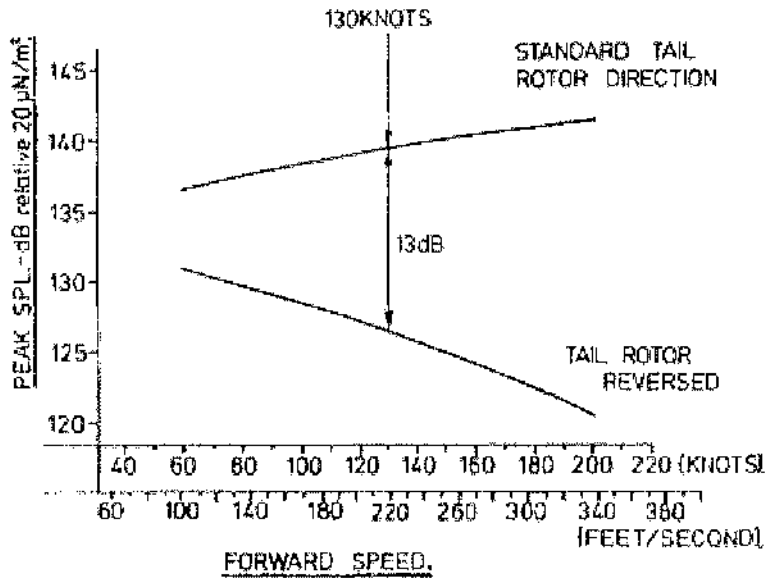


Figure 1.24: Variation in impulse peak sound pressure level with forward speed (Levinton et al, 1977)

By 1979, an increased understanding of the aerodynamic environment in which the tail rotor operates was developing and increases in thrust, a lowering of noise signatures and an extended life span were being achieved. However, Cook (1979) noted that the work up to this point focused on almost ideal conditions. Overall the understanding of tail rotor design for improved yaw control and stability had increased, although this was primarily for the normal operational envelope of helicopters up to cruise speed. Cook suggested that further research into tail rotor noise and its reduction would be needed to increase the performance of the tail rotor.

Early acoustic measurements of blade vortex interaction in wind tunnels (White et al, 1976, Pegg and Shidier, 1978) were confronted with the initial concern that the acoustic field associated with a scaled-down model may not be representative of the full scale. Tadghighi and Cheeseman (1983) sought to understand any discrepancy by comparing the acoustic fields generated by a model in a wind tunnel with full-scale helicopter acoustic fields. To achieve 'clean' acoustic measurements in the wind tunnel, Tadghighi and Cheeseman applied acoustic treatment to restrict the noise generated by the fan reaching the working section. The measured experimental data from the model correlated with full-scale measurements and with various theoretical models (Lowson, 1964, Wright, 1968, Hawkings,

1976). Subsequently, Martin et al (1989) noted that the directivity of noise sources is an important factor in such correlations.

Aside from the early experimental work, acoustic modelling of the orthogonal interaction was conducted by Amiet (1986) whose model was based on the calculation of noise generation by an aerofoil due to unsteady upwash. This work was used by George and Chou (1987), together with Lawson's (1964) moving dipole theory, to establish that the noise generation of a helicopter when tail rotor orthogonal blade vortex interaction was occurring was dependent on the relative phasing and location of the main and tail rotors.

More recently, a particularly comprehensive wind tunnel based study on a full helicopter configuration using both acoustic measurements and surface pressure measurements was conducted by Schultz and Spletstoeser (1992, 1993). They found that the tail rotor noise was more dominant in climb due to the high lift demand on the main rotor and the requirement for a corresponding increase in yaw force to counteract the torque on the fuselage. Typically, the same noise generation mechanisms were found on the tail and main rotors.

They found that the tail rotor produced impulsive noise regardless of the presence of the main rotor. Pressure measurements on the surface of the tail rotor blades indicated that there was little change in pressure distribution in the presence or absence of the main rotor. They did observe small differences in the pressure pulses found in the tail rotor blade pressure histories, which they attributed to the interaction of the main rotor wake with the tail rotor wake. This small difference was the only indication that tail rotor interaction with the main rotor wake occurred. They suggested that the predominant acoustic generation of both rotors was from the interaction with their own wakes. Schultz and Spletstoeser demonstrated a reduction in tail rotor noise by using a more aerodynamically advanced tail rotor blade, which featured a longer chord, reduced thickness and a tapering of the chord towards the blade tip.

Other attempts to reduce the noise generation from tail rotors were documented by Leverton and Pike (1993). The development of a quiet tail rotor was undertaken for the Lynx as the tail rotor was now recognized as a significant noise generation source in Lynx cruise flight. The experimental programme's objective was to reduce the tail rotor noise to a level below that of the main rotor, so that the tail rotor would have a minimal addition to the helicopter on approach.

The main alterations encompassed in the 'quiet tail rotor' study included the change of rotational sense to top-aft, the reduction in tip speed, and alterations to the aerofoil section. Features that were not considered in the study included the blockage caused by the tail fin and the fuselage. The inversion of the rotational sense of the tail rotor was found to remove the 'burble' noise of the Lynx. This was primarily due to the radiation of noise upwards as opposed to downwards, which resulted in lower noise radiation towards the ground. High levels of harmonic noise still existed, however, these were reduced by decreasing the tail rotor rotational rate. Alterations of the aerofoil section primarily involved the lengthening of the chord and the radius, and adding a tip weight. Another study by Sikorsky published by Jacobs et al (1997) also documented the successful reduction of noise levels by similar techniques.

Recently, Yin and Ahmed (2000) used a three-dimensional unsteady panel method with a free wake simulation to represent the main and tail rotor environment. Surface pressures calculated from this simulation were then used to calculate the acoustic characteristics of the interaction of the rotor wakes. Similarly, to Leverton and Pike (1993), they found that the most dominant occurrence of tail rotor orthogonal blade vortex interaction occurred during climb. It was determined that the main rotor had an effect on the tail rotor noise generation affecting the level and directivity of noise. Also, Yin and Ahmed's subsequent modelling of a tail rotor with reversed rotational sense resulted in a change in tonal content and directivity of the noise generated.

1.3.4.2 Studies of Orthogonal Blade Vortex Interaction

Most studies of orthogonal blade vortex interaction have typically focussed on experimental work, however some early modelling enabled the verification of the impulsive nature of the noise due to interaction of the main rotor wake with the tail rotor.

Attempts to isolate the orthogonal blade vortex interaction and examine the fluid mechanics were made first by Schlinker and Amiet (1983). They calculated acoustic spectra, pressure signatures and sound directivity. The modelling of the interaction by George and Chou (1987) with Amiet's (1986) unsteady aerofoil theory and Lawson's (1965) equations for a moving dipole enabled the assertion that the relative phasing and location of the main and tail rotors determined the noise generation. However, experimental visualisation studies (Ahmadi, 1986, Cary, 1987) also allowed a greater understanding of the orthogonal interaction.

All of the early experimental studies used a similar wind tunnel configuration in which a finite span wing was located upstream of a tail rotor. The finite wing trailed a tip vortex which interacted with the tail rotor orientated so that its disc was perpendicular to the freestream flow (Figure 1.25). Using this set-up, Ahmadi observed the generation of impulsive noise that radiated ahead of the rotor blade. Coincident impulsive changes in pressure were also found at the leading edge. Cary used high-speed photography and stroboscopic illumination of oil smoke seeded tip vortices to view the orthogonal interaction. Cary observed that the interaction of the incident tip vortex with the trailed tip vortices generated by the loaded tail rotor blades resulted in the incident tip vortex wrapping around the tip vortices. This resulted in the dissipation of the incident tip vortex on both sides of the interacting tail rotor blades.

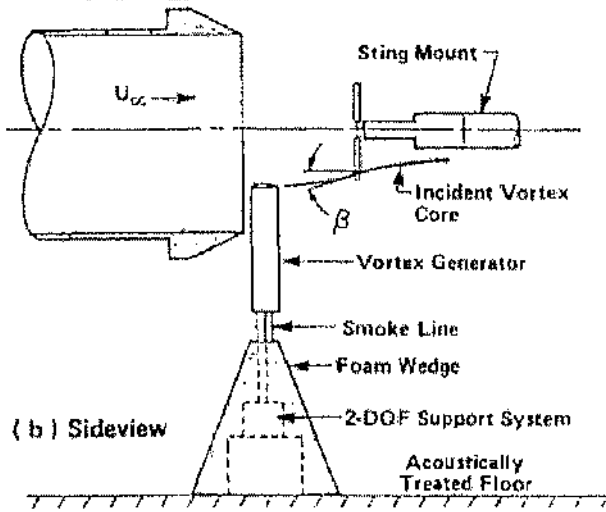


Fig. 1 Experimental setup.

Figure 1.25: Ahmadi experimental configuration (1986)

The orthogonal interaction reproduced by Ahmadi and Cary was, however, unlike the typical helicopter tail rotor interaction because the rotor disc was perpendicular to the freestream flow instead of parallel to it. It was consequently more akin to a propeller interaction. This meant that the 'cutting' interaction that occurred would have been cleaner than the typical helicopter interaction where the orthogonal interaction may be masked by the tail rotor with its own tip vortices. Another difference is that in the propeller configuration, the blades cut different cross-sectional segments of the same vortex filament whereas in the helicopter configuration the blades cut a series of vortex filaments in the same geometrical location on each filament.

A later study by Johnston and Sullivan (1992) used a different propeller type configuration (Figure 1.26) to examine orthogonal blade vortex interactions. This experiment was primarily designed to capture the response of a fixed wing to the wake of an upstream propeller. The experiment was able to capture many unseen effects of the 'cutting' process of the tip vortex because it utilised a higher number of pressure transducers than before. Smoke was also used to mark the propeller tip vortices to enable visualisation of the 'cutting' process.

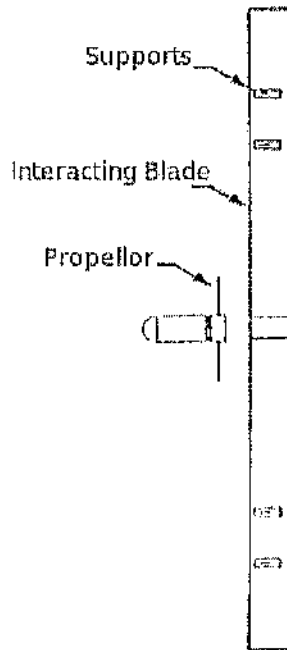


Figure 1.26: Propeller configuration used by Johnson and Sullivan (1992)

Johnston and Sullivan witnessed the deformation of the incident tip vortex before the interaction with the interacting blade. This deformation occurred with respect to inviscid flow considerations prior to the viscous interaction taking place near the blade leading edge. Once the tip vortex had been 'cut', the axial velocity in the tip vortex core caused the vortex to thicken where the axial velocity was directed towards the surface, and to thin where the axial velocity was directed away from the surface.

Corresponding unsteady surface pressure measurements showed transient pressure and suction peaks on either side of the blade during the blade vortex interaction. These were associated with the axial flow along the vortex core. The pressure peak formed on the side of the blade where the axial flow was towards the blade surface leading to compression taking place, and the suction peak was produced on the side where the axial flow was directed away from the blade surface leading to expansion taking place. Also, the combination of flow visualisation and unsteady surface pressure measurements aided in the identification of the spanwise movement of the tip vortex during the interaction. The two

halves of the tip vortex were observed to move in a spanwise direction consistent with the application of an image vortex system at the interacting blade's surfaces.

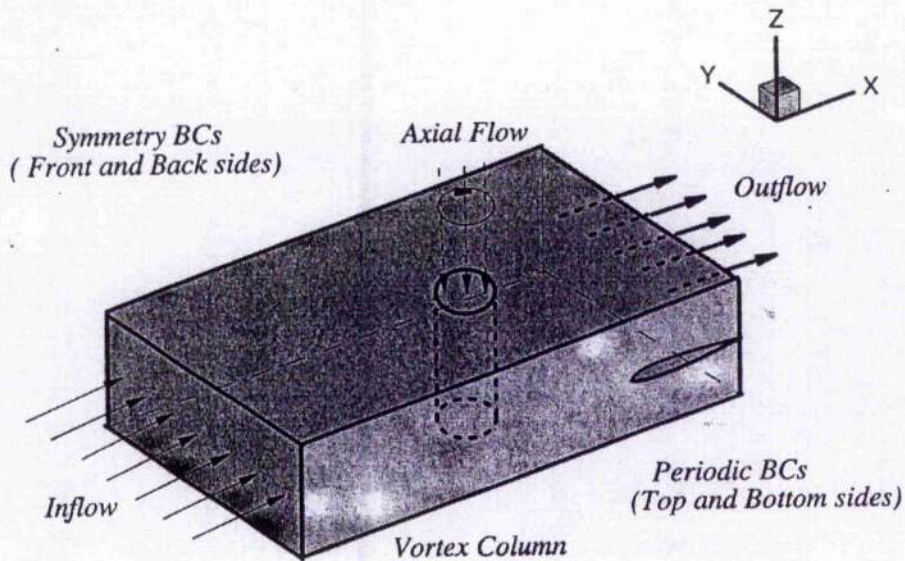


Figure 1.27: Marshall experimental configuration (1994a)

Marshall and his colleagues (1994a, 1994b, 1997, 1998) in particular have been involved in modelling the interaction numerically as well as conducting visualisation experiments using dyes in fluids. Their experimental work used a cylindrical tank within another rectangular tank (Figure 1.27). Water was tangentially pumped into the top of the cylindrical tank, and drained from an outlet at the bottom of the cylindrical tank. Once the flow had stabilized into a steady intake vortex with axial flow downward towards the outlet, a blade was towed across through a small gap in the inner cylindrical tank. Flow visualisation of the blade boundary layer identified that the blade was not significantly affected by the presence of the inner cylindrical tank. This was achieved using a coloured dye emitted from the blade leading edge. A different colour of dye was used to visualise the intake vortex, and therefore by laser illumination they were able to identify the different responses of the blade boundary layer and the interacting vortex.

Through his modelling (1994, 1994b) Marshall has ascertained that the impulsive normal force experienced by the blade is mainly dependent on the ratio of vortex core radii on opposing sides of the blade. Also, Marshall used four parameters to define the type of blade

vortex interaction that occurs: Impact Parameter (IP), Axial Flow Parameter (AFP), Thickness Ratio (TR), and Vortex Reynolds number. The IP takes account of the ratio of freestream velocity to rotational flow (1.1), the AFP: the ratio of the peak axial velocity to rotational flow (1.2), the TR: ratio of the vortex core to the interacting blade thickness (1.3), and the Vortex Reynolds number is the ratio of the vortex circulation to kinematic viscosity (1.4). Marshall and his colleagues' have examined the effect of varying these parameters individually.

$$IP = 2\pi r_c V / \Gamma \quad (1.1)$$

$$AFP = 2\pi r_c w_0 / \Gamma \quad (1.2)$$

$$TP = T / r_c \quad (1.3)$$

$$Re_v = \Gamma / \nu \quad (1.4)$$

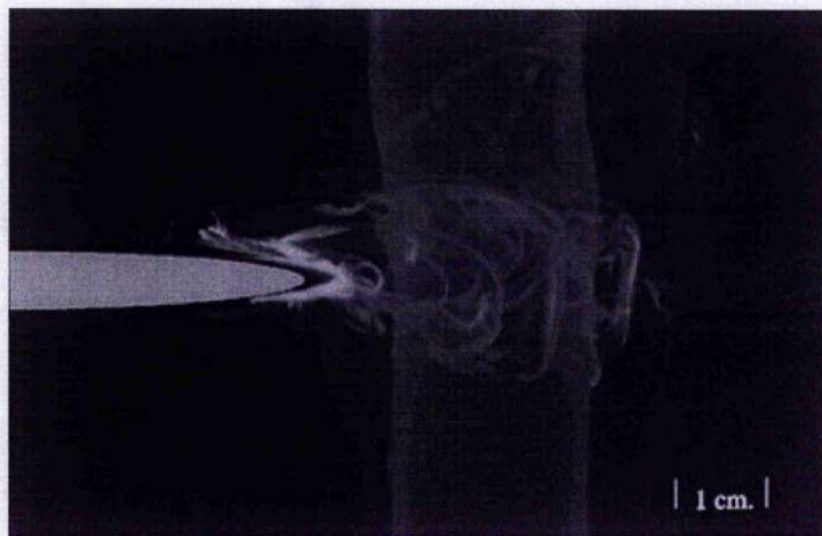


Figure 1.28: Latter stages of a Low Impact Parameter Interaction (Krisnamoorthy and Marshall, 1997)

Krisnamoorthy and Marshall (1997) highlighted two interaction regimes: a 'strong regime' (Figure 1.28) and a 'weak regime' (Figure 1.29). An interaction's regime was determined by

the value of the Impact Parameter (IP). If the IP was below approximately 0.1 it was defined as a 'strong regime' interaction. If the IP was above approximately 0.25 it was defined as an interaction in the 'weak regime'. Secondary vorticity ejections were observed in both regimes, but in the 'strong regime' secondary vorticity ejections were observed to occur before penetration of the interacting blade into the vortex. However, regime transitions occur gradually and there are a wide range of IP values for which penetration of the blade into the vortex and the secondary vorticity ejections occur simultaneously.

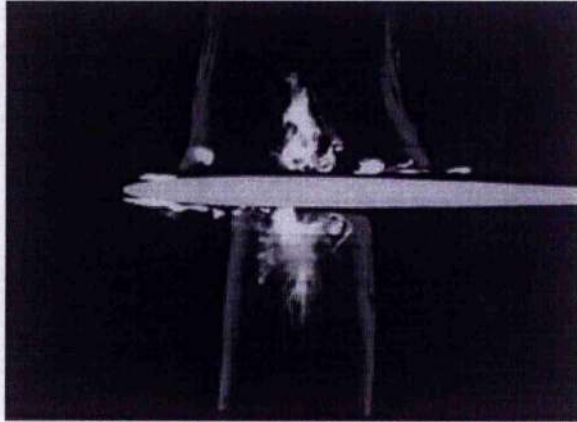


Figure 1.29: High Impact Parameter Interaction (Krisnamoorthy and Marshall, 1997)

These strong and weak regimes were defined for flows where the TR was of order one or less to ensure an impulsive 'cutting' of the vortex occurred. The effect of the AFP parameters was also examined for low thickness ratios. They found that if the AFP was above a critical value of 0.707, then the axial flow was supercritical, and if it was less than 0.707, the axial flow was subcritical. When subcritical axial flow occurs discontinuities in the vortex core radius are visible propagating upstream on the primary vortex from the surface of the blade that has the axial flow directed towards the surface. However, when the axial flow was supercritical, upstream propagating discontinuities in the vortex core radius were not observed to occur due to the stronger axial flow. In this case the vortex spreads out radially on the compression surface of the blade and has the general appearance of a non-swirling jet.

At higher thickness parameter values, the impulsive 'cutting' of the blade does not happen (Figure 1.30). Instead the tip vortex bends around the surface. An example of this type of

interaction is the interaction of a tip vortex with, for example, a cylindrical fuselage body as discussed previously.

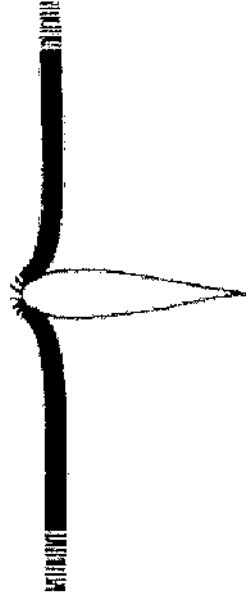


Figure 1.30: High Thickness Parameter Interaction (Rockwell, 1998)

The behaviour of the secondary vorticity depends on the regime. In the 'weak regime' the secondary vorticity becomes entrained into the core, whereas in the 'strong regime' it wraps about the outside of the vortex. The experimental work in Krishnamoorthy & Marshall's (1998) paper focused on the strong regime, showing the impulsive interaction in detail and allowing the behaviour of the secondary vorticity to be identified. As indicated previously, in the 'strong regime' the vortex is strong enough to cause secondary vorticity to be ejected from the blade boundary layer before the impact of the vortex. This was observed to occur earlier for lower IP values. The 'strong regime' wrapping process was observed to have the opposite sense to the vortex, which has subsequently been confirmed by other researchers (Affes and Conlisk, 1993, Affes et al 1993, 1994).

Another feature highlighted by the flow visualisation study was the thinning of the vortex core radius due to the wrapping of the secondary vorticity. This thinning was countered by the self-induced axial core flow which refilled the thinned sections, and the constant process of thinning and refilling resulted in the propagation of two waves with the same cross-sectional area as the core in a direction normal to the interacting blade surface on both surfaces.

Marshall et al (1998) showed that three-dimensional inviscid flow computations also reproduced the secondary vorticity wrapping process. Another experimentally observed feature that Marshall et al. identified was the appearance of secondary vorticity from the blade boundary layer within the tip vortex core as the blade leading edge reached the centre of the tip vortex core. This continued as the vortex passed along the chord filling the vortex core with vorticity from the blade boundary layer. However, helicopter tail rotor blade vortex interactions predominantly occur in the weak regime. This regime features little vortex deformation prior to vortex impact with the interacting blade and little or no boundary layer separation. The force experienced by the interacting blade is primarily due to the 'cutting' of the vortex core.

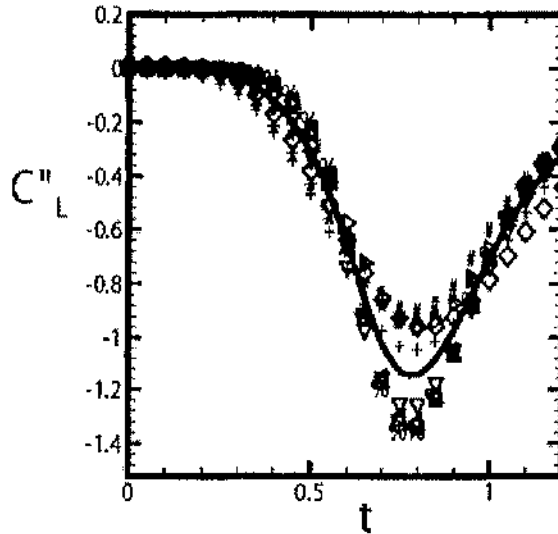


Figure 1.31: C_L'' , a universal lift coefficient developed by Liu and Marshall (2004)

A recent computational study by Liu and Marshall (2004) focussed more on weak regime orthogonal blade vortex interactions. Their viscous, compressible computational fluid dynamics calculations used a dense resolution of points within the vortex core and the interacting blade leading edge to enable the accurate simulation of the interaction. Calculations were completed for tip vortices with and without axial core flow. It was found that the axial core flow resulted in different responses at the two blade surfaces. Similarly to their earlier visualisation studies, on the surface where the axial core flow was directed towards the surface, the vortex core radius increased. On the opposite surface where the

axial core flow was directed away from the surface, the vortex core radius decreased. The computational model predicted the peak normal force during the interaction and compared reasonably well with experimental results. The study showed that the peak normal force experienced by the blade was primarily dependent on axial core flow velocity, and the freestream velocity. An important observation, reported by Liu and Marshall was the development of a single 'universal blade lift coefficient' (Figure 1.31) due to the apparent linear correlation of blade lift with respect to freestream velocity and axial core flow velocity.

As well as the studies at the University of Iowa, documented above, the University of Glasgow has also been investigating tail rotor orthogonal blade vortex interaction in the controlled environment of a wind tunnel. Studies first began with a 'proof of concept' study (Copland et al., 1998), which used a numerical model to investigate the replication of representative, tip vortices using a main rotor configuration in a wind tunnel. Once this was done, two test facilities comprising based on a single-bladed vortex generator (main rotor) and a downstream interacting blade were constructed and used to obtain surface pressures on an interacting blade during blade vortex interactions (Figure 1.32). As the collected data at the University of Glasgow are a primary feature of this work, the details and analysis of the data are presented in the following chapter. However, to complete the current summary section on orthogonal blade vortex interaction a general overview of the key findings of the previous work at Glasgow is given.

Wind tunnel tests were completed in two wind tunnels. Initially, proving tests were conducted in a small wind tunnel of working section cross section 1.15m by 0.85m. Later, these tests were followed by tests in a larger wind tunnel (2.65m by 2.04m) (Wang, 2002) where a higher resolution of surface pressures was obtained. Other measurement techniques employed included particle image velocimetry (PIV) and hot-wire anemometry.

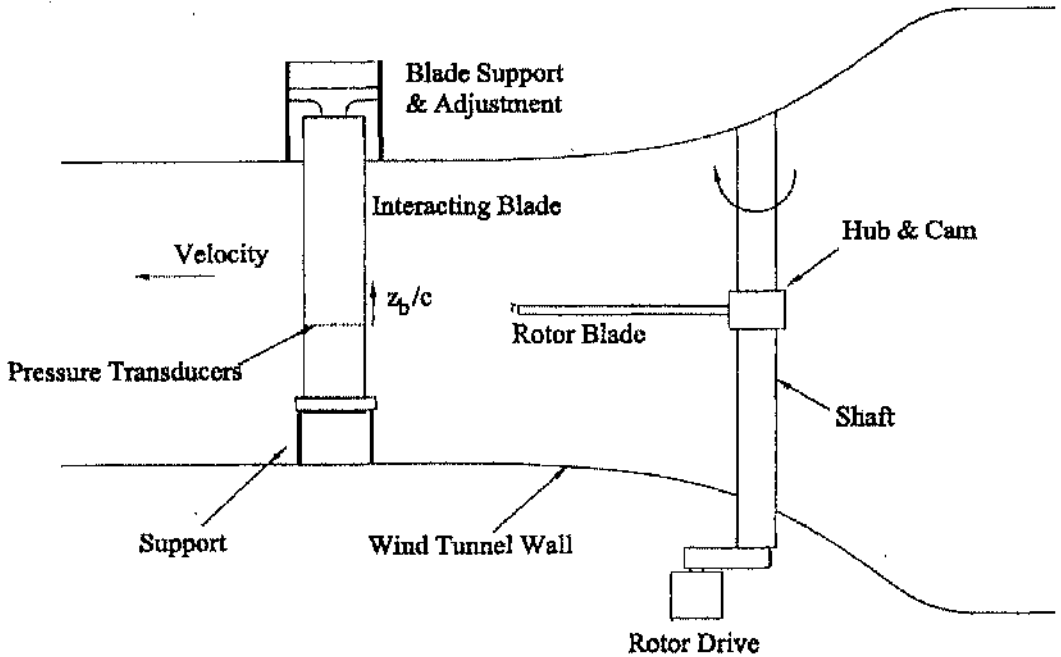


Figure 1.32: University of Glasgow 'Argyll' wind tunnel configuration for orthogonal blade vortex interaction (Copland, 1998)

Surface pressure measurements (Doolan, 2001) on both surfaces of the interaction blade revealed suction and pressure peaks on the lower and upper surfaces respectively (Figure 1.33). This was primarily due to the axial core flow that was directed towards the lower surface and away from the upper surface. These occurred during the early stages of the interaction. The suction peak and pressure peaks diminished after the initial stages of the interaction. The suction peak diminished more rapidly with a weak suction ridge replacing it after the vortex had reached the quarter chord of the interacting blade.

Doolan et al (2001) integrated the surface pressure measurements enabling the calculation of normal force and pitching moment histories. The impulsive blocking of the axial core flow near the leading edge resulted in an impulsive increase in normal force during the initial stages of the interaction, and a nose up pitching moment. The more rapid decrease in the pressure peak on the lower surface in comparison to the suction peak on the upper surface resulted sustained the nose up moment as the tip vortex travelled beyond the quarter chord position. The developing suction peak on the lower surface increased gradually balancing

the suction peak on the upper surface, therefore returning the normal force to the interacting blade's pre-interaction lift.

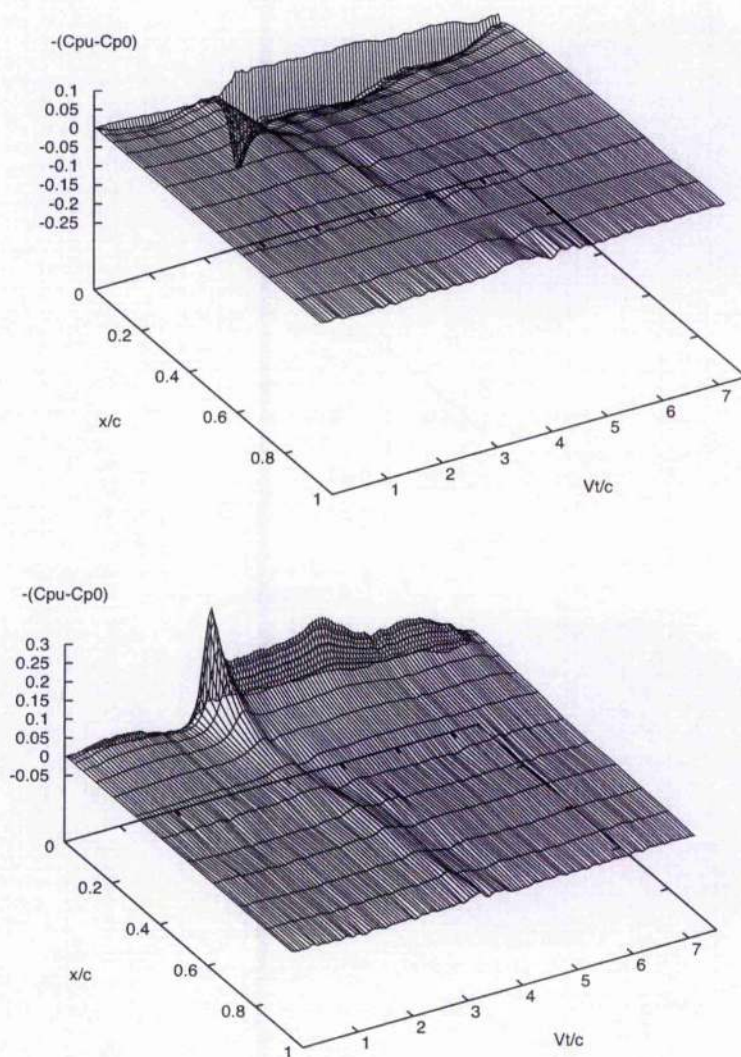


Figure 1.33: Unsteady surface pressure distributions showing the lower surface pressure peak and upper surface suction peak respectively. (Doolan, 2001)

An experimental study with a loaded symmetrical aerofoil was also published by Doolan et al (1999) where the interacting blade angle of incidence was varied between -10 and 10 degrees. As the angle of incidence of the interacting blade increased, the pressure peak on the lower surface reduced in magnitude and the suction peak on the upper surface increased in magnitude. The opposite was found for a decrease in angle of incidence.

However, the magnitude of the impulsive change in normal force resulting from the blockage of the impinging axial core flow remained constant.

Particle Image Velocimetry (PIV) was also used by Doolan et al. (2001) to examine orthogonal blade vortex interaction. This study, however, failed to show flow behavior within the core due to the high number of 'wild vectors'. Green et al. (2000) developed an enhanced PIV image processing system that allowed the removal of rogue vectors in the measured flow field. With this technique a clearer visualization of activity within and around the vortex core was achieved. In particular, radial out-flow was observed on the surface of the blade to which the axial flow was directed. This outflow was matched by inflow on the suction side of the blade in response to the impulsive blocking of the core flow. As the distance from the blade surface increased, these flows diminished. Early et al. (2002) also used PIV, and investigated the redirection of the axial core flow due to its impingement on the surface. Radial outflow was found on the lower surface and radial inflow on the upper surface. This radial outflow caused the redistribution of vorticity from the axial core flow as the vortex passed downstream along the interacting blade's chord.

Wang et al. (2002) presented preliminary analysis of data collected from the larger wind tunnel. As expected pressure and suction peaks were found on the lower and upper surfaces respectively, dependent on the direction of axial core flow normal to the respective surface. A variation in blade response with spanwise distance from the centre of the vortex core was found. The normal force response of the blade decreased in magnitude as spanwise distance from the vortex centre increased. The response was also found not to be symmetric on either side of the vortex. The data collected by Wang et al (2002) will be used in this study as the basis for indicial model comparisons.

A more recent study conducted by Coton et al (2004) collected pressure data from an instrumented rotating full tail rotor system. Surface pressure measurements exhibited the same basic features as those observed on the static interacting blade. Consequently, it is appropriate to use the higher resolution static blade data for the numerical modelling

comparisons as they are representative of the interactions experienced on a tail rotor whilst providing greater detail than the measurements made on the model tail rotor.

1.3.4.3 Summary of Modelling of Blade Vortex Interaction

There are many different ways in which the modelling of blade vortex interaction has been attempted. Most of the earlier models focussed on simulating the noise generation characteristics of various interactions. Some formulations considered the interaction with arbitrary turbulence, others more directly with concentrated vorticity. The principal source of noise radiated due to the interaction of a blade with atmospheric turbulence or concentrated vorticity, for example from a preceding rotor blade, is the force exerted on the fluid in reaction to the unsteady lift response.

Substantial early work was contributed by Lawson (1964), which followed on from the derivation of equations representing the sound generation from standard aerodynamic equations by Lighthill (1952). These investigations and the later work of Ffowcs Williams and Hawkings (Glegg, 1987) enabled the calculation of the noise generated by unsteady fluctuations in loading. Some substantial reviews of the work relating to acoustic prediction have been published (Boxwell et al, 1987; Tadghighi and Cheeseman, 1983), however, the recent modelling of blade vortex interaction has focussed on the modelling of the fluid mechanics.

Researchers (Tadghighi and Cheeseman, 1983; Quackenbush et al, 1989; Schultz and Spletstoesser, 1992; Yin and Ahmed, 2000) have shown that the loading of a rotor blade was directly associated with noise generation. Recent studies have therefore focussed on understanding the underlying fluid mechanics associated with noise generation. Most of these techniques have already been mentioned in passing above, however, as a route to justification of the validity of using indicial modelling in this work, the achievements and shortcomings of other modelling techniques are detailed below.

A potential flow discrete free-vortex method was used by Lee et al (1991) and Renzoni and Mayle (1991) to model parallel blade vortex interaction. Particularly acceptable comparisons with linear theory and experimental data were achieved when a distributed vorticity method was used where the incident vortex was separated into a cluster of multiple smaller vorticity elements, commonly referred to as a "vortex cloud". This work built on earlier simulations of a point source moving past an aerofoil at a fixed separation distance, progressing to more representative flow whereby the point source was convected with respect to the induced flow field. Other methods employed finite vortex core models which avoided the singularity at the centre of the point source. However, the "vortex cloud" method allowed the simulation of tip vortex distortion and also the alteration of the vortex trajectory due to the interaction with the aerofoil.

For orthogonal interaction, the plug-flow model developed by Lundgren and Ashurst (1989) enabled the calculation of area-varying waves propagating along the primary vortex. They demonstrated that the production of these area varying waves was dependent on a subcritical axial flow parameter, and observed the similarity of the interaction to a non-swirling jet impinging on a surface when the axial flow parameter was supercritical. However, Lundgren and Ashurst's plug flow model did require a uniform axial velocity profile, uniform vorticity field, and a circular core. These conditions are stringent; nevertheless, important insights were made into the basic flow response to the interaction.

Recently, the use of computational fluid dynamics to model orthogonal blade vortex interaction has been undertaken. These studies have progressively provided more detailed simulations of the blade vortex interaction. Marshall and Krisnamoorthy (1997) published results from the numerical solution of the Euler equations for a blade interacting with an axisymmetric inviscid vortex with axial flow. The computational model reproduced the experimentally observed increase in core radius on the blade surface experiencing compression, and a decrease in core radius on the blade surface experiencing expansion. Also, like Lundgren and Ashurst, propagating area-varying waves were found on the vortex

on both sides of the blade for subcritical axial flow parameters. For a supercritical axial flow parameter, only downstream propagating area-varying waves were found.

A later study by Sheikh and Hillier (2001) documented an Euler solution for a compressible orthogonal interaction of a vortex-jet combination, and a pure-jet, without rotational flow. Sheikh and Hillier found upstream propagating disturbances when the axial flow was supercritical, which is in contrast to the inviscid study by Marshall and Krisnamoorthy. However, Sheikh and Hillier noted that the inclusion of compressibility resulted in a local decrease in axial velocity and therefore a reduction in the local axial flow parameter. This possibly explains why upstream propagating disturbances could exist for cases where the axial flow parameter was apparently supercritical. Sheikh and Hillier also reported that, as the axial flow parameter increased, the flow was similar to the pure jet interaction.

Computational fluid dynamic studies have proven capable of modelling many features of the orthogonal blade vortex interaction. However, the calculations still require extensive resources. An example of the demanding nature of the blade vortex interaction and the computational fluid dynamic modelling of helicopter flows was presented by Yang et al (2004). Yang used unsteady Euler and aeroacoustic codes to simulate the various combinations of main and tail rotor interactions, and their noise production. Yang's calculations reproduced experimental results, however, the computational resources required were extensive.

Recently, a particularly relevant computational fluid dynamic study by Liu and Marshall (2004) investigated orthogonal blade vortex interaction. This study examined cases of high impact parameter where ejection of vorticity from the blade boundary layer prior to the interaction of the vortex core with the interacting blade was not found. As stated previously, high impact parameter orthogonal interactions are indicative of orthogonal blade vortex interactions found in 'real' helicopter flight.

The study also found that non-zero axial flow resulted in lift generation by the interacting blade due to the impulsive blocking of the axial core flow. The lift force increased with impact parameter and axial flow parameter. For the range of vortex Reynolds numbers considered, there was no significant change in lift force magnitude effect resulting from variation in vortex Reynolds number. However, the rate of change in lift force was increased for higher vortex Reynolds numbers.

1.3.4.4 Indicial Modelling

At the present time a viscous compressible Navier-Stokes solution would enable a full understanding of the flow field physics during orthogonal blade vortex interaction. This would be possible for a small-scale simulation involving only the localized flow field of an orthogonal blade vortex interaction. However, the impetus for this work is the creation of a technique that would enable orthogonal blade vortex interactions to be included into a full simulation of a helicopter's flow field. For such a case the prediction of the impulsive loading is most important but resolution of the detailed flow behaviour is not necessary. The simulation of a full helicopter flow field by a Navier-Stokes calculation that resolves all the required length scales is extremely computationally demanding and beyond current capabilities. For this reason, industry has developed aerodynamic performance models of the full helicopter flow field (Beddoes, 1987) into which an indicial solution for orthogonal blade vortex interaction could easily be integrated.

Indicial modelling has already been used to predict the flows for various idealised interactions; for example, the calculation of wing lift due to an encounter with an up gust (Kussner, 1936) or an angle of attack change (Wagner, 1925). Indicial techniques are inviscid approximations that can accommodate some viscous effects. Features such as the existence of circulation, the Kutta-Joukowski condition, and the shedding of vorticity from the trailing edge of wings or blades in response to changes in lift (Sears, 1969) can all be represented in indicial models.

More recently, Beddoes and Leishman have extended the earlier work of Kussner and Wagner separately and in collaboration with others (1978, 1983, 1986, 1989, 1993). The most relevant piece of indicial modelling was the simulation of parallel blade vortex interaction by Beddoes (1989), which also included a compressibility correction. Previous indicial models only allowed for global effects, for example, a large gust completely engulfing a wing. Beddoes developed a method of accounting for the localised flow conditions on the surface of the blade due to the flowfield associated with the close proximity of a vortex. Beddoes also demonstrated that the indicial method provided a reasonably accurate correlation with experimental and computational results.

Other recent uses of indicial modelling include the development of an indicial model to simulate the lift and pitching moment behaviour of fighter aircraft (Reisenthal, 1996, 1999).

Indicial modelling is a flexible technique that provides a means of obtaining a fast and reasonably accurate linear approximation of an essentially non-linear system. As such, it is an ideal technique for providing a local solution for an interactional event within a more global flow field calculation. The application of indicial modelling to orthogonal blade vortex interaction provides the focus for the present work.

1.4 Summary of Chapters

Chapter 2 describes the experiments conducted at Glasgow University to measure tail rotor orthogonal blade vortex interaction and summarizes the main features of the measured response. Chapter 3 details analysis of the data for the purposes of validating indicial models in subsequent chapters. Chapter 4 provides an introduction to the indicial method and existing models. In chapter 5, the indicial models of the orthogonal interaction are examined, and weaknesses are identified in the indicial model's ability to predict the measured blade response at spanwise locations away from the location where the vortex centre interacts with the blade. Chapter 6 uses a two dimensional panel method to show that the measured response away from the vortex centre cannot be reproduced by considering

only the axial and rotational flow of a tip vortex based on a Lamb-type vortex at the blade surface. Chapters 7 and 8 detail the use of a numerical simulation to investigate the flow field that existed in the wind tunnel and demonstrates that an indicial model based on this flow field can produce more accurate predictions of the orthogonal blade vortex interaction. Chapter 9 then documents indicial modelling of other experimental and computational datasets before the main conclusions of the work are presented and recommendations are made for future work.

2 Experimental Studies at Glasgow University

2.1 Introduction

Over the last 10 years the University of Glasgow has been focusing on the experimental investigation of orthogonal tall rotor vortex interaction. A logical way of reproducing this in the controlled environment of a laboratory was a facility where the tip vortex was generated by a rotating blade similar to an actual main rotor. At Glasgow University the design of such a facility was started by Copland et al (1995).

Copland conceptually designed an experimental facility to fit an existing wind tunnel at the University of Glasgow; the Anatomy wind tunnel [1.15m x 0.85m]. The experimental configuration featured a stationary blade mounted vertically in the working section of the wind tunnel, and a main rotor system installed upstream in the contraction of the wind tunnel generating tip vortices.

Copland's design (Figure 2.1) had two specific features that resulted in clean, strong tip vortices being produced. The first was limiting the number of blades of the main rotor system to one. This single bladed rotor will subsequently be referred to as the vortex generator. The second feature was constraining the azimuthal pitch incidence around the cycle in such a way that the generation of tip vortices by the vortex generator was limited to the downwind pass of the cycle. By preventing the generation of tip vortices on the upwind pass, the complexity of the vortex generator wake was greatly reduced and the spacing between sequential tip vortices increased.

Thus, the vortex generator produced an idealised flow field that still replicated the essential features of a helicopter rotor wake. Copland's design was validated by hot wire velocity measurements, surface pressure measurements and particle image velocimetry demonstrating that it was an effective means of generating representative tip vortices, with

their associated axial flow, and that their subsequent orthogonal impact on a stationary blade could be measured.

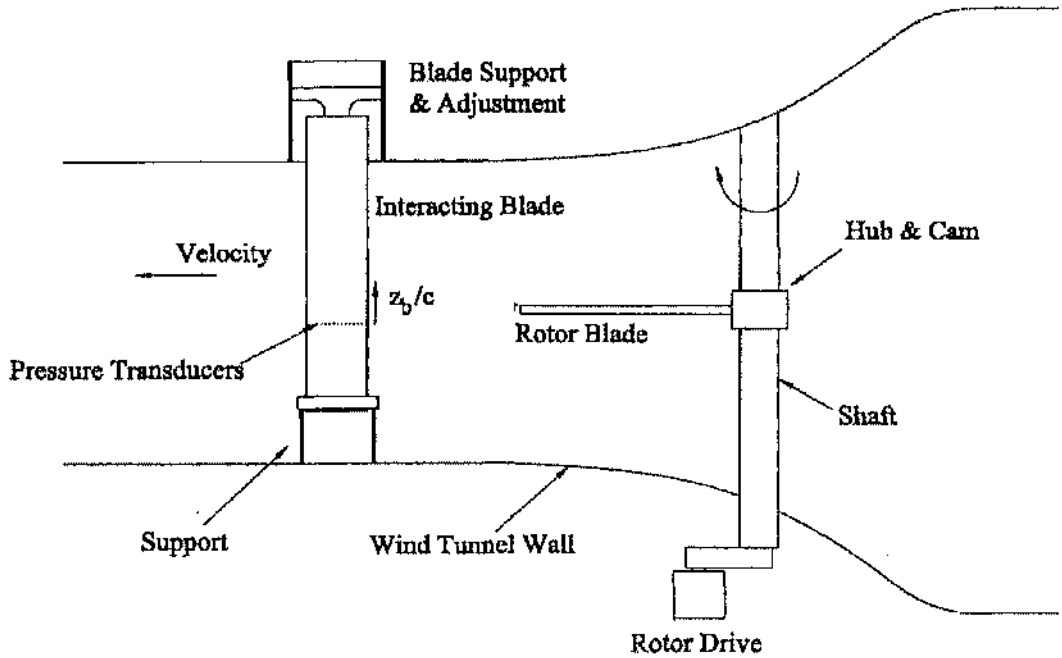


Figure 2.1: Copland's experimental configuration installed in the small wind tunnel (Anatomy Tunnel) at Glasgow University (1998)

2.2 Experimental Studies

Copland developed a numerical model (1995, 1997) that enabled the investigation of potential test configurations before the installation of either the stationary interacting blade or the main rotor system. The numerical model predicted the wake generated by the vortex generator and the surrounding fluid within the existing wind tunnel. In 1998, Copland published (1998) the results from the successful wind tunnel configuration detailing the parametric study conducted using this numerical model.

Modelling the flow field in a wind tunnel is complicated by the contraction and associated acceleration of the flow field between the settling chamber and the working section. The

velocity gradient has the effect of distorting any fluid structure, such as a tip vortex, generated upstream of the working section. To predict this effect, Copland extended a technique developed by Hess & Smith (1964) who successfully demonstrated the capabilities of a source panel implementation to represent three-dimensional non-lifting bodies.

Copland made use of this three-dimensional source panel implementation to represent the wind tunnel walls, and coupled it with classical lifting line theory, which represented the lifting behaviour of the vortex generator and the associated change in circulation due to changes in pitch incidence. In Copland's method, the vortex generator blade was split into 10 blade segments and at each time step the pitch incidence was re-evaluated and shed and trailed vorticity was generated in the form of a series of free vortex elements. The convection of this lattice of vortex elements was then dependent on the local velocity calculated from the result of velocity contributions from: the other vortex elements previously generated, the velocity contributions of the vortex generator, and the velocity contributions from the three-dimensional source panel method capturing the empty wind tunnel flow field.

The model was purely inviscid, aside from the inclusion of a finite viscous vortex core. This addition was necessary as the inviscid model of a vortex core features an infinite velocity at the vortex centre, which would produce spurious results and can cause numerical instability. Also, the model did not include any dissipation or strength variations as the free vortex wake structure was deformed when travelling to the working section.

Copland originally considered two vortex generator operating regimes to generate clear, stable tip vortices. The first regime, which was considered to be optimal, was a single rotation of the vortex generator producing a single, clean tip vortex structure. However, the calculated actuation loads required to accelerate and decelerate the vortex generator to perform this single azimuthal rotation were extremely high, and could not have been achieved within the budget of his original project.

The second operating regime that Copland considered featured the vortex generator operating at a constant rotational rate, and following an azimuthal pitch profile that prevented the generation of tip vortices on the upwind pass, whilst promoting a strong, clean tip vortex on the downwind pass. This operating regime was preferred for its operational simplicity and lower implementation costs.

Preliminary analysis of potential experimental configurations using the numerical model demonstrated that the location of the vortex generator hub, the wind tunnel velocity, and the vortex generator's rotational rate were the key parameters in determining the vortex shape. These parameters characterised the wake's curvature, elongation, skewing, and also the separation between consecutive wakes.

Installation of the vortex generator in the working section was not feasible for two reasons. First, the size of a vortex generator, with a suitable chord and radius capable of generating a significant tip vortex, prevented installation in the working section. Also, if the vortex generator were installed in the working section, the location at which an orthogonal blade interaction occurred would be directly downstream of the vortex generator hub's wake. The accelerating effect of the contraction of the wind tunnel was essential to ensure a clean orthogonal interaction away from the vortex generator hub's wake, even although the wake structure would be slightly deformed. Consequently, the vortex generator was installed as close as possible to the working section, in the contraction, to minimize deformation.

The numerical model suggested the use of a 10-degree pitch incidence on the downwind pass, a freestream velocity of 20 m/s, a vortex generator chord of 0.1 m, vortex generator radius from the hub of 0.75, and a rotational speed of 500 rpm would produce a clear tip vortex structure at the interaction location that would be orthogonal to the stationary blade. The azimuthal pitch profile was split into 4 segments of 90 degrees. For the most downstream segment, the pitch incidence was set to 10 degrees, whilst the most upstream segment was set to 0 degrees. The other two intermediate segments facilitated the change in incidence increasing the incidence from 0 degrees to 10 degrees on the retreating

segment of rotation, and decreasing the incidence from 10 degrees to 0 degrees on the advancing segment. This test configuration was used for all testing in this wind tunnel.

The predicted location of the generated tip vortex was verified by the measurement of freestream and vertical cross flow velocities in the working section with a hot wire probe. The maximum vertical cross flow velocity from the rotational component of the tip vortex was used as an indicator of the passage of the vortex centre. The change in freestream velocity due to positive and negative reinforcement by the vortex's rotational component also helped to indicate the location of the tip vortex centre.

Further to Copland's work, Doolan et al (1999) undertook a more rigorous investigation of the quality of the tip vortex structure. Doolan recorded more hot wire velocity measurements in the working section to try and obtain a more detailed picture of the structure of the tip vortex. Doolan discovered that the measured vortex axial velocity matched very well with the axial velocity profile predicted by a Lamb-type vortex in regions outside and close to the vortex core. Measurements of the axial velocity within the core did not show much agreement which suggested that the hot wire probe interacted with the tip vortex core. Also, frequent changing from positive to negative reinforcement of the freestream velocity, by the rotational flow of the vortex, showed that vortex wandering occurred.

Probe Interference effects of convecting vortices have been documented by other researchers such as Ziada & Rockwell (1983). Although they were not investigating the orthogonal interaction, they did observe the self induced movement of the vortex upon approaching a rotor blade. In Ziada & Rockwell's case a wedge, simulating a blade's leading edge, was orientated such that the wake tip vortex core axis was parallel and in plane with the leading edge of the blade. As the vortex approached the leading edge, the vortex was drawn towards the lower surface due to the self-induced pressure gradient. Another possible interference mechanism that could occur is the 'bulging' or 'thinning' of the vortex core due to the probe blocking the axial core flow. This has been demonstrated to occur when a solid

surface interacts orthogonally with the vortex core flow (Marshall and Krisnamoorthy (1997) , Lundgren and Ashurst (1989), Lee et al (1987)).

Despite these mechanisms potentially resulting in inaccurate measurement of velocity at the core, a critical validation of the overall wake shape predicted by the numerical wake model was successfully completed using hot wire measurements. The shape of the tip vortex was mapped by measuring the time between the passage of the tip vortex past two hot-wire probes located at different lateral positions in the wind tunnel. One probe remained fixed while the other traversed across the width of the wind tunnel working section. As the wind tunnel velocity was known, the shape of the tip vortex could be plotted according to the product of the freestream velocity and the time difference, together with the horizontal distance from the fixed probe. This resulted in a close match in predicted and measured wake shape (Figure 2.2) demonstrating the wake code's ability to replicate the wind tunnel experimental configuration fairly accurately despite its inviscid nature.

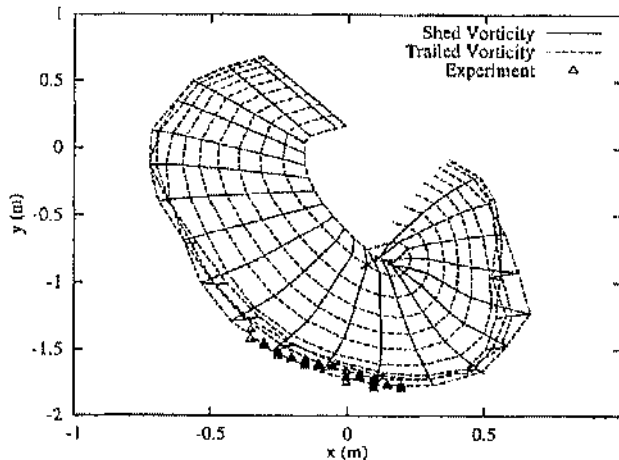


Figure 2.2: Comparison of numerical wake simulation and experimental measurements of wake shape (Doolan, 1999)

Doolan et al (1999) also conducted surface pressure measurements during orthogonal blade vortex interaction. In their experiments an array of pressure transducers was mounted on the upper and lower surfaces of a symmetrical interacting blade. This stationary blade was installed at a position downstream of the hub where Copland's wake code predicted a fully orthogonal blade vortex interaction would occur. This location was on the retreating side of

the vortex generator's rotation, 225 mm from the centre of the wind tunnel and 2 m downstream of the vortex generator's hub.

The pressure history of the orthogonal blade vortex interaction featured a strong suction peak on the upper surface at the height coincident with the vortex centre. This suction peak diminished slowly after the initial interaction as the vortex travelled along the interacting blade's chord. At the vortex centre height on the lower surface, a strong pressure peak formed which rapidly decreased as the vortex travelled over approximately the first quarter of the blade chord. Aft of the quarter chord point a weak suction ridge developed which, subsequently, slowly reduced in magnitude towards the trailing edge. This behaviour on the lower surface can be explained in terms of the vortex response. The initial blocking of the axial flow produces the pressure rise experienced by the blade leading edge. With the subsequent stagnation of the axial flow the low pressure associated with the vortex rotation becomes dominant and persists to the trailing edge. This transformation from pressure peak to suction peak has been verified by the studies of Marshall & Krisnamoorthy (1998) in which the entrainment of the boundary layer on both the upper and lower surfaces into the vortex core was observed.

As mentioned previously, Marshall and Krisnamoorthy (1997, 1998) have also identified three parameters of importance in orthogonal blade vortex interaction: the Impact Parameter (IP), Axial Flow Parameter (AFP), and the Thickness Parameter (TP). For Doolan's experiment, the calculated IP and AFP were 2.16 and 0.89 respectively. The IP value indicates that the severity of the vortex response to the 'cutting' process is 'weak' where no boundary layer separation occurs prior to the vortex core's interaction with the stationary blade's leading edge. The AFP value is supercritical ($AFP > 0.707$) indicating that only downstream area waves can be supported on the vortex core, meaning that a jet-like incompressible flow develops on the stationary blade's lower surface with a resulting vortex core thickening, together with vortex thinning on the upper surface.

Doolan et al also examined the blade response above and below the vortex core. On the upper surface, at a spanwise location one vortex core radius above the vortex centre height, the suction peak was less severe and diminished before the trailing edge. A weaker effect was also found on the lower surface where the pressure peak was slight compared to the response at the vortex centre. Also, the suction ridge that previously developed on the lower surface at the vortex centre after the quarter chord point was almost undetectable.

At a spanwise location one vortex core radius below the vortex centre, a very weak suction peak formed on the upper surface and deteriorated before the trailing edge. On the lower surface, a pressure peak developed that rapidly transformed after the quarter chord to a suction ridge of increasing strength as the vortex travelled along the chord to the trailing edge.

As indicated above, the gross characteristics of this behaviour can be understood by considering the effect of the axial core flow of the tip vortex. The impulsive blocking of the vortex core results in the increased pressure on the lower surface where the axial flow is towards the surface and decreased pressure on the upper surface where the axial flow is away from the surface. The weaker response one core radius either side of the vortex centre demonstrates the strong influence that the axial flow has on determining the response.

In Doolan et al's study, the pressures measured at the transducers were integrated to calculate normal force and pitching moment histories. Doolan et al documented the data acquisition system that made use of automatic gain adjustment that enabled measurements to be taken using the maximum resolution of the system. The uncertainty in the measurement of the pressure coefficients was estimated to be around 0.5%, and the corresponding inaccuracy in the normal force coefficients, due to the approximation of numerical integration, was estimated to be around 2%.

To obtain the normal force and pitching moment plots (Figure 2.3), data were ensemble averaged. This introduced spatial and temporal attenuation in to the data due to the vortex

wandering. The vortex wandering was measured to be approximately 19% of the stationary blade chord.

The normal force exhibited an impulsive increase during the initial stages of the interaction in response to the impulsive blocking of the axial core flow. After this, the normal force slowly decreased in magnitude as the vortex core moved along the chord.

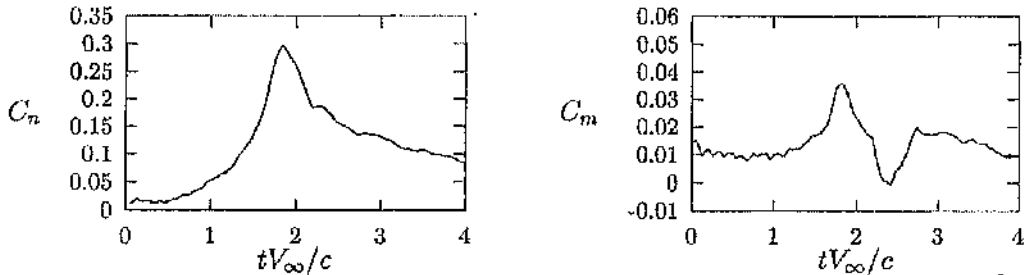


Figure 2.3: Normal force and pitching moment data (Doolan, 1999a)

The pitching moment sharply increased as the vortex approached the leading edge. As the vortex progressed to the quarter chord, the pressure peak on the lower surface diminished at a faster rate than the suction peak on the upper surface. Consequently, the pitching moment decreased rapidly. During the later stages of the interaction, the magnitude of the suction ridge on the lower surface increased in magnitude, compensating for the suction ridge on the upper surface and returning the pitching moment to its pre-interaction value.

In a later study, Doolan et al (1999b) also investigated the effect of blade incidence on orthogonal blade vortex interaction. Using exactly the same experimental setup described above, the interacting blade was placed 225 mm from the tunnel centre on the retreating side but this time the blade incidence was varied between -10 and $+10$ degrees.

Doolan observed that an increasing angle of incidence resulted in increased suction on the upper surface and decreased pressure on the lower surface during the interaction. The opposite was observed for decreasing angles of incidence. The most important observation from this investigation was the consistent behaviour of the unsteady normal force. In

particular, the magnitude of the impulsive change in normal force associated with the blockage of the axial core flow was found to be constant across all blade incidences (Figure 2.4).

Doolan et al (1999b) analysed the pressure response at the leading edge of the blade for different blade angles of incidence. Analysis of the responses of the transducers closest to leading edge on the upper and lower surfaces revealed that the peak suction and peak pressure recorded varied monotonically in the range ± 5 degrees (Figure 2.5). It was found that the suction peak on the upper surface increased in magnitude with increasing angle of incidence until approximately 5 degrees, after which, it began to decrease. The pressure peak on the lower surface behaved in a similar manner, increasing in magnitude as the angle of incidence decreased until about 5 degrees.

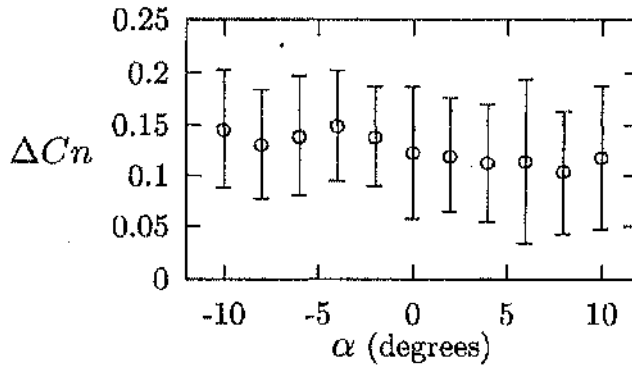


Figure 2.4: A constant change in normal force is found at all angles of incidence of the interacting blade (Doolan, 1999b)

Another observation made from the pressure measurements on the lower surface was the appearance of a suction ridge behind the pressure peak at the leading edge during the early stages of the interaction. This peak grew as the pressure peak diminished and became visible after the quarter chord location when the pressure peak had completely diminished. Doolan postulated that this suction ridge could be attributed to the generation of secondary vorticity due to the interaction of the tangential velocity components of the vortex with the boundary layer leading to a small region of localized separation. This is consistent with work

of Marshall and Krishnamoorthy (1997, 1998) who observed secondary vorticity generated in a weak regime interaction such as this.

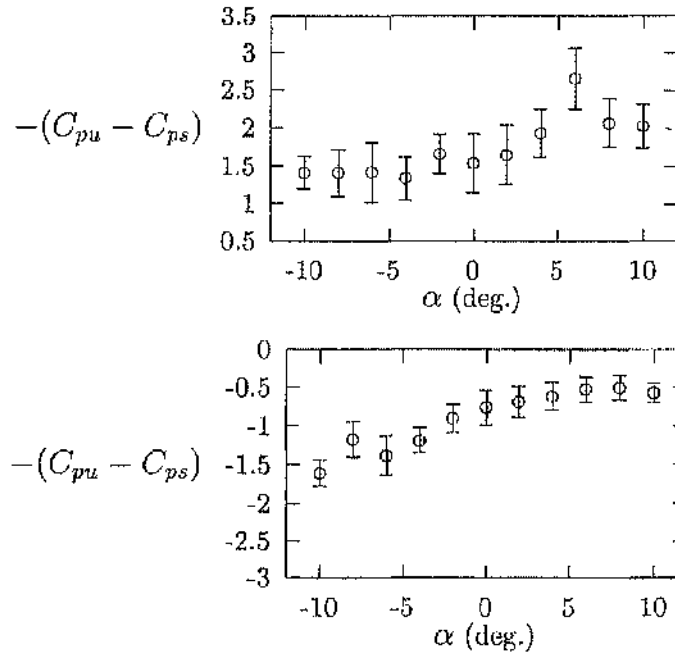


Figure 2.5: Surface pressure measured at leading edge pressure transducer on the upper and lower surfaces respectively (Doolan, 1999b)

Following this, Doolan et al (2001a) investigated the aerodynamic response on an instrumented blade due to vortex interaction after the vortex had been 'cut' upstream by an identical stationary blade (Figure 2.6). The upstream blade was located was one chord length upstream of the downstream, instrumented blade.

Doolan observed that the upstream blade removed some axial momentum from the tip vortex, and although the general form of the response exhibited by the blade was similar to the clean interaction, the magnitude of the normal force response was approximately halved. The strong suction ridge that was previously found on the upper surface was intermittent between successive vortices and was of generally smaller magnitude when present. This suggests that some form of vortex reconnection exists after the initial cut, although the tip vortex may still be in the process of reconnection when cut by the downstream blade. This may explain the intermittent presence of the upper surface suction peak.

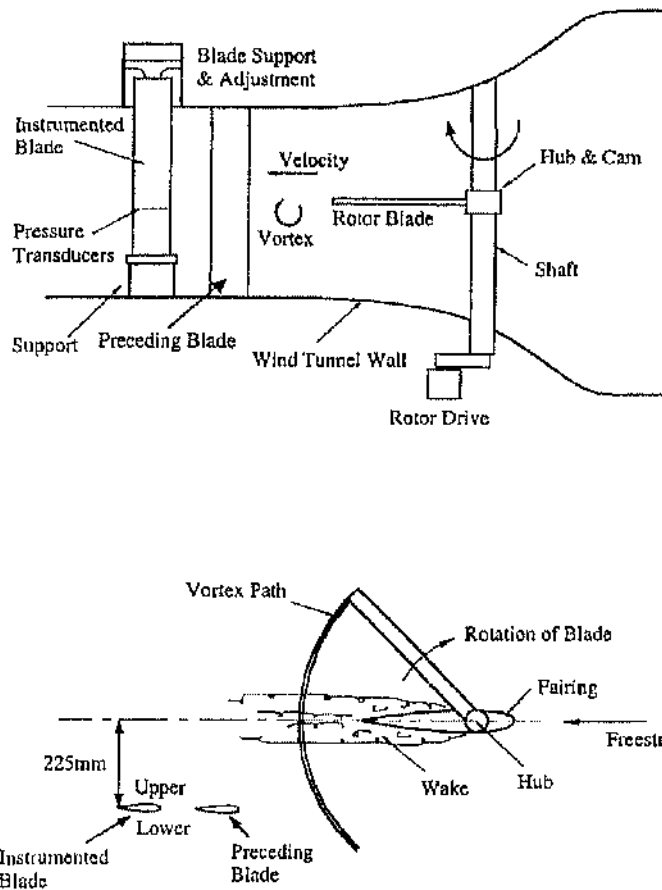


Figure 2.6: Preceding blade configuration installed at Glasgow University (Doolan, 2001a)

The main conclusion that can be drawn from this work on the effect of a preceding blade is that repeated orthogonal 'cutting' of the same tip vortex can generate a significant unsteady aerodynamic response. This inevitably adds to the complexity of the loading experienced by a helicopter tail rotor.

In addition to making surface pressure measurements, Doolan et al (2001b) also used PIV (particle image velocimetry) to interrogate the interaction flow field. In this method, the flow is illuminated by a laser sheet and seeded with small particles of oil smoke. Placing the laser sheet close to the surface, Doolan was able to measure the velocity of the particles in this region. The wind tunnel configuration was consistent with the previous work where the wind tunnel velocity was 20 m/s, the rotational speed of the vortex generator was 500 rpm and the

stationary blade was located 2 metres downstream of the vortex generator hub. Once again the stationary blade was positioned 225mm from the centre of the wind tunnel on the retreating side of the vortex generator hub.

Doolan revealed that while PIV was proficient at calculating the circulation of the interaction vortex, it was hampered by poor resolution in the vortex core. The PIV technique was able to measure the circulation more accurately than the hot-wire probe as it was unaffected by vortex wander. The potential error in measurement of the circulation was reduced by 50%.

Green et al (2000) documented a technique to improve the poor resolution of the particle velocities within the tip vortex core by implementing a vector validation scheme. This validation scheme allowed the extraction of data from the vortex core which is typically barren of smoke particles as particles spiral out of the core region. The technique used two cameras each with their own laser sheet. Polarizing filters prevented cross contamination of light from the other camera's laser. The filters also prevented the confusion of solid surface reflections of light from the other camera. This dual laser and camera technique, together with the vector validation technique, allowed the analysis of flow within the vortex core.

Green et al established the presence of radial outflow and inflow close to the lower and upper surfaces respectively. The radial outflow was identified as originating from the vortex axial core flow impulsive blocking which was only observed close to the lower blade surface. Green noted that the superposition of a vortex and a source would reproduce the flow field found close to the surface. This observation was also verified in Marshall and Krisnamoorthy's work (1997).

Early et al (2002) also used PIV to investigate the orthogonal blade vortex interaction. Early observed the reduction in peak vorticity levels close to the lower surface in comparison to the constant peak vorticity levels close to the upper surface. The drop in vorticity is consistent with the radial outflow when the axial flow impinges on the lower surface.

Early also used divergence calculations to evaluate the change in velocity of flow in the out of plane direction from the two dimensional PIV images. The divergence calculation, based on continuity theory, allowed the determination of flow deceleration on the lower surface due to the impulsively blocked axial core flow. Beyond the trailing edge of the interacting blade, Early found zero divergence after tip vortex had progressed beyond the trailing edge suggesting that reconnection of the core flow could have occurred.

The research described so far in this chapter was carried out in the small low-speed wind tunnel (Anatomy) at the University of Glasgow where the dimensions of the wind tunnel are 1.15m by 0.85m. Wang et al (2002) used a similar test configuration in the larger wind tunnel (2.65m by 2.04m) to study orthogonal blade vortex interaction. This facility was designed to allow the extraction of pressure data at higher spatial resolution compared to the small wind tunnel. Tests were conducted in the larger wind tunnel for a range of freestream velocities and angles of incidence of the interacting blade.

The experimental setup consisted of a single main rotor blade, rotating in the contraction of the wind tunnel, upstream of a stationary blade, the 'interacting blade', located in the working section of the wind tunnel. The single main rotor together with its hub is typically referred to

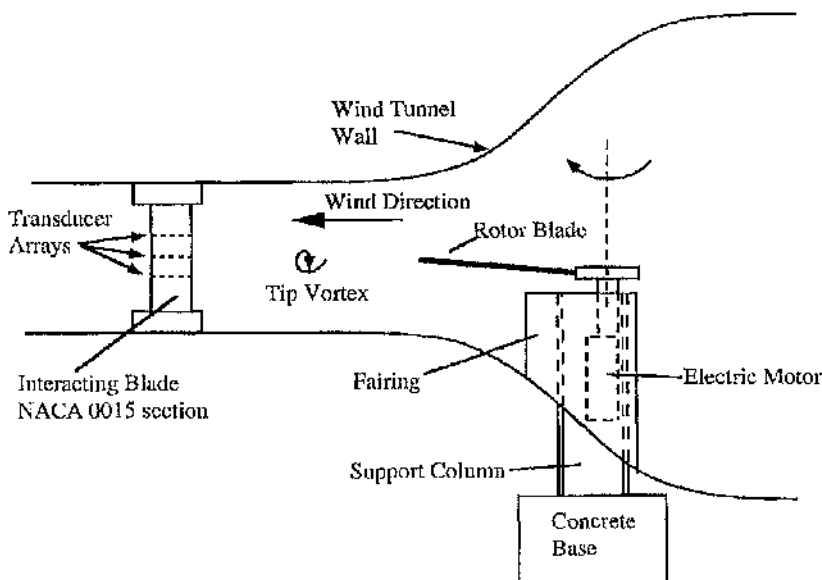


Figure 2.7: Wind tunnel configuration installed in large wind tunnel (Argyll tunnel) at Glasgow University (Wang, 2002)

in Doolan (1999) and Wang (2002) publications as the 'vortex generator'. The term will also be used here to maintain continuity with their work.

The interacting blade was aligned so that the chord line was parallel with the direction of freestream flow and aligned orthogonally to the vortex generator rotation plane (Figure 2.7). The vortex generator was a symmetrical aerofoil of NACA 0015 profile, which simplified the generation of tip vortices to non-zero angles of attack. To ensure the generation of tip vortices by the vortex generator it was pitched to an angle of incidence of 10 degrees in the most downstream quarter of azimuthal rotation, and to an incidence of zero degrees for the most upstream quarter of rotation (Figure 2.8). The intermediate quarters of rotation allowed for the corresponding smooth ramp up and ramp down of the angle of incidence. To maintain the correct azimuthal pitch profile a custom made hard-chromed cam-plate and fully articulated hub were used. This fully articulated hub incorporated cantilevered flap springs and lag dampers. The tip vortices produced by the downwind pass of the hub by the vortex generator blade convected downstream and interacted orthogonally with the interacting blade.

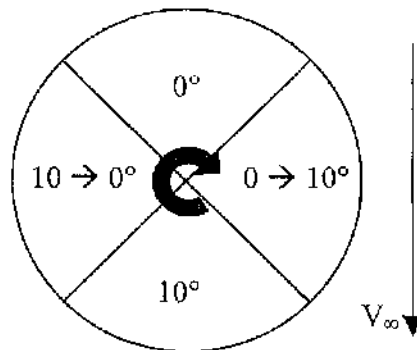


Figure 2.8: Angle of incidence variation with azimuthal position

The interacting blade, also a NACA 0015, was located horizontally off centre from the tunnel's symmetry axis, on the side of the wind tunnel where the vortex generator blade was retreating. The off centre location of the interacting blade was necessary for two reasons. Firstly, the wake of the vortex generator's hub and associated assembly would contaminate any experimental data collected close to the centre of the wind tunnel. Secondly, the manner in which the vortex generator wake convects is such that the wake is only orthogonal to the

interacting blade at locations away from tunnel centre line. Copland's wake code was used in the design of this enlarged configuration to identify appropriate locations for the vortex generator and the interacting blade. In the tests the interacting blade (chord = 0.275m) was located 0.37m from vortex centre line, and the leading edge of the interacting blade was 4 metres downstream of the vortex generator hub. This suitability of this location was verified by hot-wire measurements of the flow field.

During testing flow velocities were varied from 20 to 50 metres per second in steps of ten. For each freestream velocity the wake code was used to predict an optimal rotational rate ensuring a clean orthogonal interaction at each velocity. Blade incidence was also varied between -12 and 12 degrees in steps of two degrees.

The blade response characteristics measured in this larger wind tunnel were different to those from the smaller wind tunnel for many reasons. The tip vortex had a larger vortex core radius with respect to the interacting blade chord meaning that the interaction would be less localised on the surface of the blade. However, the ratio of the vortex axial velocity to the freestream velocity was much lower than in the small tunnel at every freestream velocity used in the large wind tunnel. Thus, despite the larger vortex core radius, the magnitude of the interaction response was less due to the relatively lower axial velocity.

Despite these differences, the orthogonal interactions measured in both wind tunnels were strictly within the weak regime, commonly known to be the dominant interaction experienced by helicopter tail rotors. The tests in the large wind tunnel did, however, produce a variation in the Axial Flow Parameter (AFP) such that both subcritical and supercritical interactions were recorded.

The data recorded in the large wind tunnel also benefited from a considerable reduction in vortex wander. The wander was estimated to be approximately 5 mm, or 1.8% of the interacting chord. As a result, the data showed high levels of repeatability and so provided

an ideal basis on which to develop the indicial model that provides the focus for the present study.

2.3 Summary

High resolution pressure data have been collected by Wang (2002) from a large wind tunnel at the University of Glasgow. The vortex generation method used in this study resulted in the creation of tip vortices with little wander in their travel along the wind tunnel, which demonstrated improved repeatability compared to previous studies in the smaller wind tunnel. Wang's data is therefore an important validation source for indicial models of the interaction. The next chapter details analysis of the data for this purpose.

3 Analysis of Experimental Data

3.1 Introduction

The work presented in this chapter begins by summarising the data collection method and the data reduction methods applied to (Wang et al., 2002) the data collected in the large wind tunnel.

Indicial models reproduce the effect of shed vorticity as a blade experiences changes in lift, therefore, an accurate determination of the normal force response from the experimental data is vital for the validation of any indicial model. It is shown that the data published in the previous papers are useful for visualising the general form of the interaction, however, there was spatial and temporal attenuation present in these data. To enable the valid correlation of the experimental data with indicial models, or any mathematical model, the effect of the attenuation should be removed by a more detailed analysis of the experimental data.

The analysis of the normal force data from the large wind tunnel will focus mainly on the 40 m/s data set. From an initial appraisal of this data set, it appears to feature the most stable and reliable orthogonal blade vortex interactions. Data from the other velocity data sets, 20, 30, and 50 m/s, will, however, also be presented. In addition, the only angle of incidence that will be examined in this report is the zero degree angle of incidence. The previous research documented here suggested that the zero degree blade response will exhibit the essential features of the other angle of attack cases.

3.2 Evaluation of Existing Data Analysis

In the tests conducted in the 2.64m x 2.04m wind tunnel, the data acquisition system collected data from three parallel pressure transducer arrays mounted flush with the surface

3 Analysis of Experimental Data

of the interacting blade. For each vortex that passed over the interacting blade a block of data was collected by each transducer array. Each block contained 2000 data samples, sampled at a rate of 50 kHz, at each transducer location enclosing the time frame within which the vortex passed over the blade's surface. A spanwise distance of 68.75 mm separated the three transducer arrays and by shifting the location of the interacting blade in the vertical plane by increments of 20 mm, data blocks were recorded at heights relative to the vortex centre's path at 0 mm of: -108.75, -88.75, -68.75, -60, -48.75, -40, -28.75, -20, 0, 20, 28.75, 40, 48.75, 60, 68.75, 88.75 and 108.75 millimetres.

Sixteen blocks of data were captured by each transducer array at each of the vertical locations relative to the vortex centre. This process was repeated for the four different freestream velocities (20, 30, 40, 50 m/s) and thirteen different angles of incidence from -12 degrees to 12 degrees in increments of 2 degrees. As discussed previously, the vertical height of the vortex centre at each of the freestream velocities was determined by hot wire anemometry as detailed by Doolan (1999c) and Wang (2002).

The coefficient of normal force was calculated from the pressure measurements captured in the data blocks. Once each of the normal force coefficient histories had been calculated for each of the sixteen blocks, the data were time averaged across each of the sixteen blocks. The triggering of the collection of each data block was dependent on the azimuthal location of the vortex generator blade. Although the data collection was triggered automatically, attenuation occurred due to random disturbances in the flow and the small amount of vortex wander that occurred. Therefore, every block will capture an orthogonal blade vortex interaction, which features a different response.

When the data from this experiment was published (Wang, 2002), plots of the time-averaged coefficient of normal force were shown for each ensemble of 16 data blocks. However, due to the spatial and temporal attenuation that was present, these plots do not accurately show the severity of the blade response in terms of the impulsive peak in normal force attained, or the sharpness of the impulsive increase in normal force (Figure 3.1). The following analysis

focuses on establishing an accurate measurement of the impulsive peak, and directly comparing this to the time-averaged data. Therefore providing a valid correlation source for the indicial modelling of the interacting blade experiencing orthogonal blade vortex interaction.

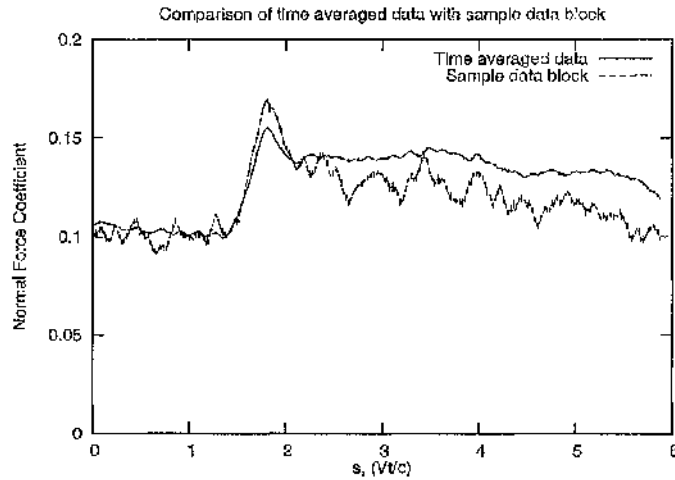


Figure 3.1: Comparison coefficient of normal force between Time Averaged data blocks and a sample data block

3.3 Data Analysis

Before discussing the impulsive change in normal force found during orthogonal blade vortex interaction, the interaction itself needs to be characterised. Figure 3.2 shows a simplified interpretation of an ideal interaction at the spanwise location where vortex centre passed over the interacting blade's chord. The normal force experienced by the interacting blade temporarily increases in magnitude for a short period of time before decreasing slowly back to the pre-interaction normal force magnitude. It is also evident from a closer inspection of the normal force response, that there is a small dip in normal force before the steep impulsive increase in normal force, perhaps due to a local increase in dynamic pressure from the rotational component of the approaching tip vortex near the leading edge. Therefore, a simple algorithm that can search for minimum turning points followed by maximum turning points will find the impulsive change in normal force coefficient (dC_n) in each data block. Due to the large number of data blocks, a simple programmed search

algorithm is preferable. However, a simple algorithm will only be able to search through a simple block of data.

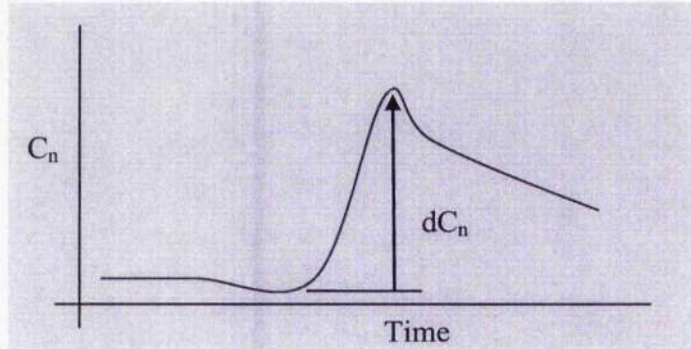


Figure 3.2: Diagram of a typical impulsive change in normal force (dC_n)

Initial data analysis will be conducted on data blocks from the 40 m/s data set because it contains the most clearly defined interactions. The 20 m/s data set features very high magnitude random freestream disturbances when compared to the other velocity data sets and therefore might require more rigorous processing. This is due to the pressure transducer measurement sensitivity. The magnitude of the changes in pressure during the interaction are smaller at 20 m/s and the corresponding signal to noise ratio is poorer. The 30 m/s data set is the only set that features a subcritical axial flow parameter and may show unusual results when compared to a typical representative helicopter tip vortex interaction which is considered (Krisnamoorthy and Marshall, 1998) to typically feature a supercritical axial flow parameter. During the testing process there were concerns about excessive flapping of the blade for the 50 m/s data set due to the high vortex generator rotational rate. Therefore, the 40 m/s data set features the most favourable characteristics.

It is apparent, from a brief examination of any data block in the forty metres per second data set (Figure 3.3), that each data block features high frequency background 'noise', and naturally occurring high frequency random turbulence in the freestream. Therefore, filtering was attempted to simplify the data blocks to enable a simple search algorithm to find the impulsive change in the coefficient in normal force due to orthogonal blade vortex interaction.

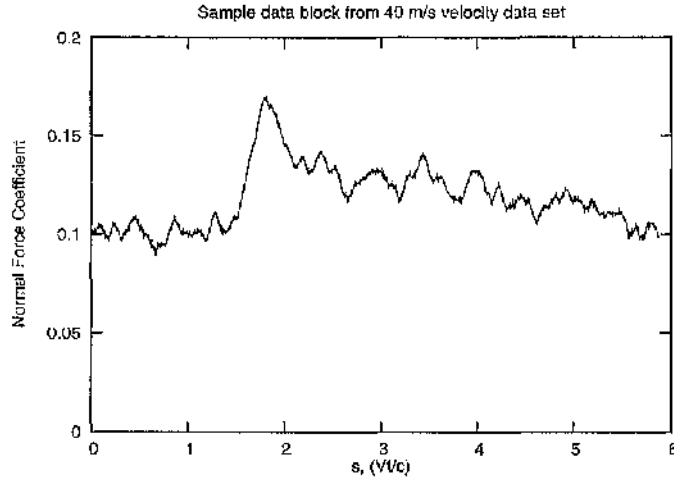


Figure 3.3: Sample data block from 40 m/s velocity data set at spanwise location where vortex centre passes over blade.

3.4 Digital Filtering

Typically, the preferred technique for removing unwanted high frequency interference in a signal is the use of a low band pass digital filter. PV-WAVE was the preferred data processing software available which featured a built in digital filter function. Figures 3.4a and 3.4b show the power spectral density plots of a sample data block from the span location where the vortex centre passes over the chord. The power spectral density shows that the signal features minor high frequency interference, with the bulk of the frequency response concentrated in the lower frequency range below 500 Hz.

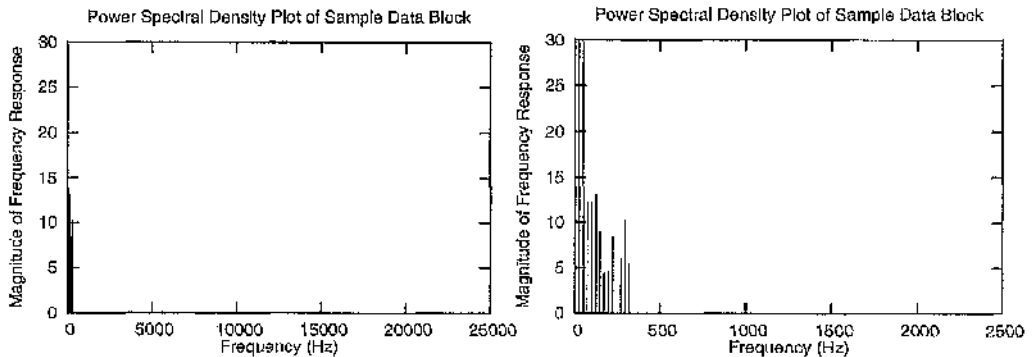


Figure 3.4: Power Spectral Density plot. Zero Hz to (a) Nyquist at 25kHz, and (b) 5kHz respectively

3 Analysis of Experimental Data

PV-WAVE's digital filter function uses a Bessel filter. The Bessel filter features a shallow roll off in its frequency response, which meant that it was difficult to filter the very low frequencies present in the signal. Figure 3.5 shows a sample Bessel filter with the cut off frequency set at 5 kHz. This shows that due to the slow roll off in the frequency response frequencies as low as 8 kHz are filtered to some extent. When the cut off frequency is dropped to nearer the low frequencies found in the power spectral density, at around 500 Hz, the frequency response (Figure 3.6) shows that nearly all frequencies are filtered to some extent which means that the desired signal of the impulsive blade vortex interaction is therefore also filtered. Figure 3.7 shows the resultant digitally filtered samples after applying the built in Bessel digital filter with a cut off frequency of 500 Hz.

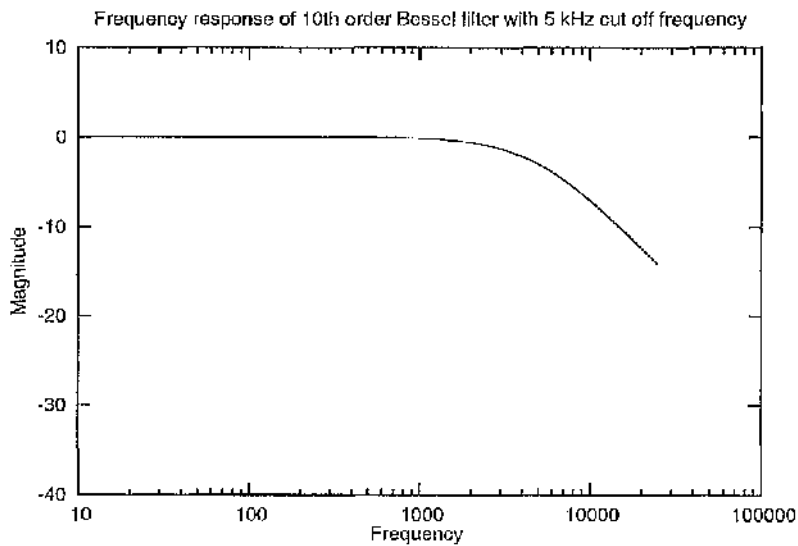


Figure 3.5: Frequency response of 10th order Bessel filter with 5 kHz cut off frequency

The magnitude of the impulsive response is decreased due to attenuation when the cut off frequency is reduced to 500 Hz. This demonstrates that the desired signal of the impulsive blade vortex interaction is filtered as well as the undesirable interference and background noise. The Bessel filter simplifies the data blocks, however, the magnitude of the impulsive response is attenuated in the filtered data. Phase shifting and or attenuation in the filtered sample data block are expected in digital filtering, however, in this case the magnitude of the response is the critical feature and consequently, the attenuation of the magnitude of the normal force response make PV-WAVE's filter unsuitable in this situation. Due to the small

3 Analysis of Experimental Data

range of low frequencies in the data block, it is not possible to filter the data block with a Bessel filter as the roll off in the frequency response is too shallow to allow the selective filtering of only some of the frequencies found in the power spectral density.

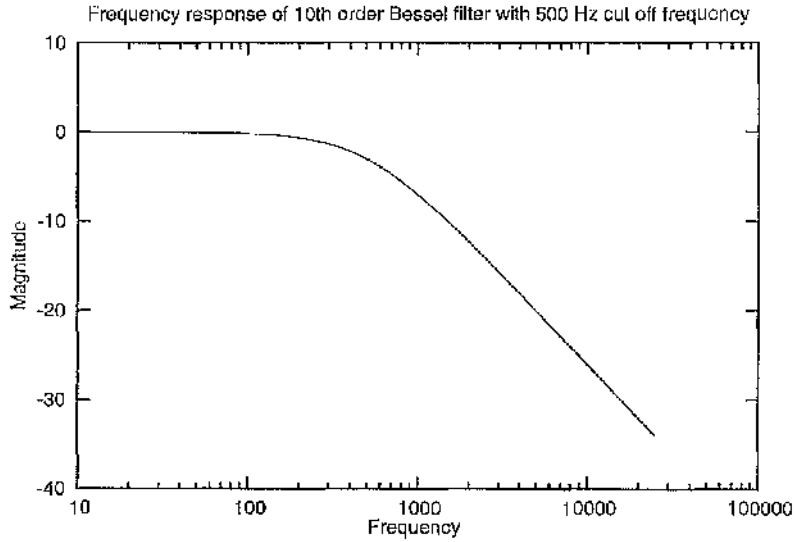


Figure 3.6: Frequency response of 10th order Bessel filter with 500 Hz cut off frequency

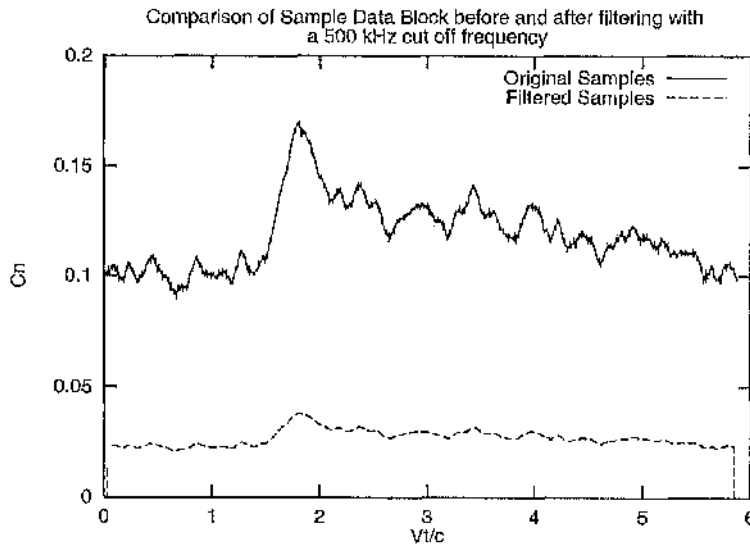


Figure 3.7: Comparison of data block filtered at 500 Hz with original data block

Digital filtering is not the only solution for filtering the data, particularly as the purpose of the filtering was to simplify the data enabling a search algorithm to easily find the impulsive interactions. Therefore a splining routine was used to filter the data.

3.5 Customised Filtering Using Splines

The cubic spline interpolation function in PV-WAVE reduces the number of the samples in each data block and fits a cubic spline fit through each of the splined data samples. By severely reducing the samples in the sample data block from 2000 to 100, only every twentieth sample is used by the spline function to fit the cubic spline. Figure 3.8 shows a comparison between the original data and splined data samples.

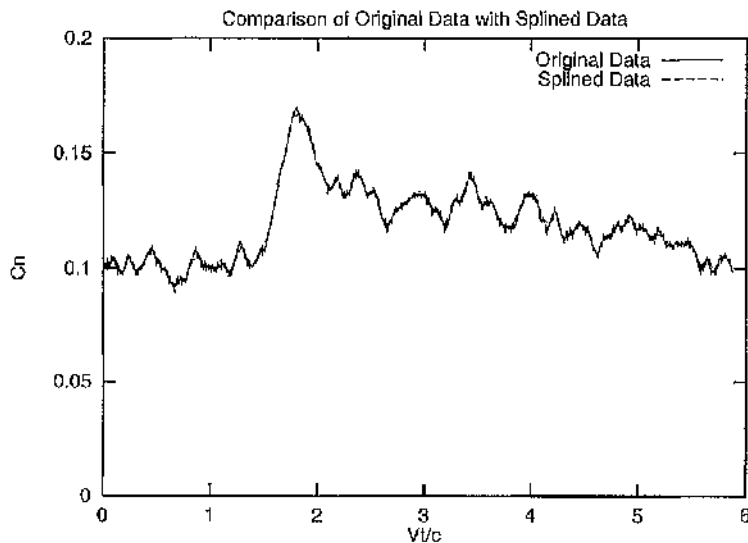


Figure 3.8: Comparison of splined data with original data

An algorithm searched through each data block finding each minimum turning point and the immediately following maximum turning point in the 100 splined samples. Typically, the largest change in the coefficient of normal force between minimum turning point and following maximum turning point identified the impulsive increase in normal force due to the orthogonal blade vortex interaction. Once the largest impulsive increase in normal force was identified the start and end time of the impulsive increase were mapped back to the original data block.

The magnitude of this impulsive interaction was taken from the local minima and maxima found in the original data block at the minimum and maximum turning point respectively. By local minima and maxima, this means the original data samples occurring within the time

3 Analysis of Experimental Data

frame from the splined data sample immediately before and after the identified splined data sample for both the minimum and maximum turning points respectively (Figure 3.9).

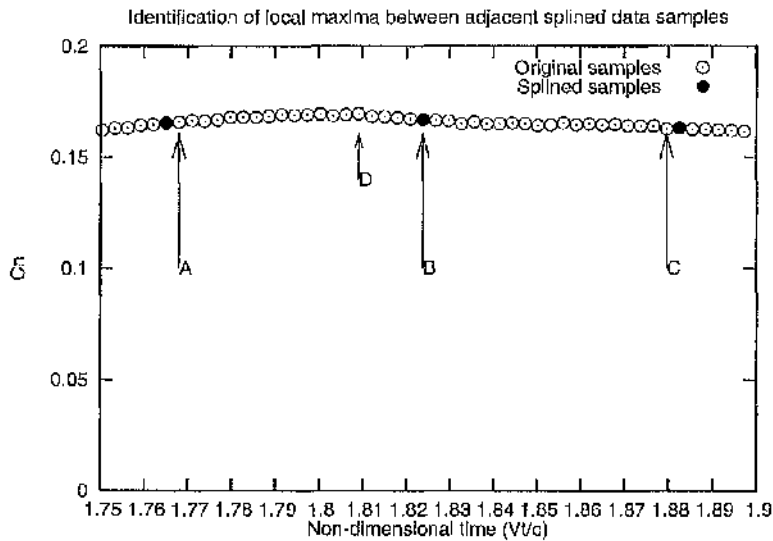


Figure 3.9: Illustration of identification of maximum turning point (T.P.). Point B is the T.P. determined by the search through the splined samples. The local maxima must occur between A and C, and is found at D. Diagram showing the identification of local minima and maxima from original data using splined points identifying start and end time

Typically, it was simple to identify the largest change in C_n , however, in some data blocks the largest dC_n occurred outside the timeframe within which the other data blocks from the same spanwise location experienced their largest dC_n . Also, at spanwise locations above the vortex centre the form of the interacting blade's response to the orthogonal interaction is different. The response is a gradual slow build in normal force, as opposed to the sharper, impulsive increase at spanwise locations near the vortex centre and below. Consequently, due to the magnitude of random freestream disturbances there exists multiple similar magnitude dC_n events across a much longer timeframe when compared to more impulsive spanwise locations (Figure 3.10).

To resolve these problems, an average minimum and maximum turning point was calculated from the data blocks where impulsive interactions occurred, and then within this average time period each data block was reduced again for the greatest impulsive interaction (dC_n). Obviously, by taking the average some interactions will start before the average start time and some will end after the average end time and, therefore, the start time and end time will

split many of the impulsive interactions. To capture every impulsive interaction the average time period must be extended in some way.

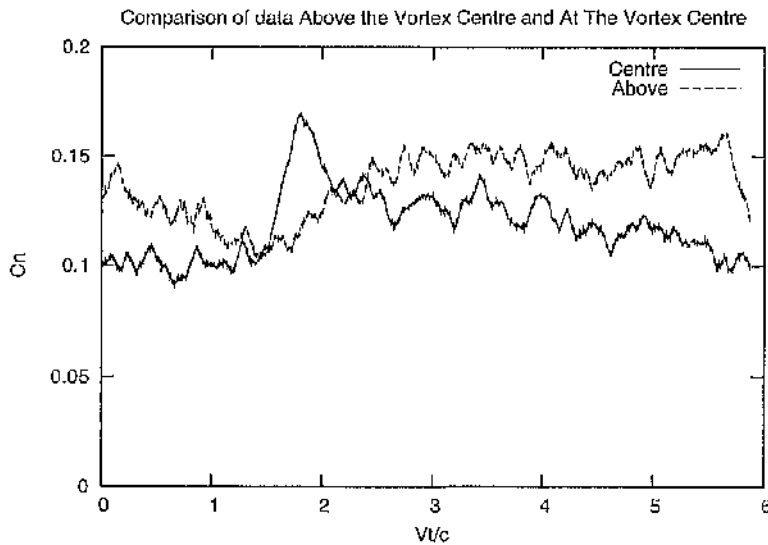


Figure 3.10: Comparison of data Above the Vortex Centre and At the Vortex Centre

The average time period will not inherently include many of the impulsive interactions. However, if the average time period is equally stretched in length at both ends then degrees of 'generous fits' are achieved. Ideally, searching for the impulsive interaction between the earliest start time and the latest end time would find all impulsive interactions. But, as previously stated, there is no guarantee that the earliest start time and latest end time would give a sensible time frame as some of the largest changes in normal force occur due to random freestream disturbances at earlier or later time frames typically in data blocks where the magnitude of the impulsive response due to the orthogonal blade vortex interaction is small compared to the disturbances.

By stretching the average time period by 5% of the total time period of the data block, an agreeable selection of the impulsive interaction was made by the search algorithm in every data block. In data blocks where an impulsive interaction was not found, for example, at spanwise locations above the vortex centre, poor agreement was found more often. At other span locations the agreement was, in general, excellent.

3 Analysis of Experimental Data

Before any further evaluation of this algorithm is presented, it is important at this time to explain how an 'agreeable selection' of impulsive interaction was verified. Typically, the algorithm runs through each of the blocks where an impulsive interaction is expected to occur, the average start and end time of these data blocks is calculated, and every data block is processed again this time looking only within the average time period with the percentage stretch applied. Once the algorithm has found the dC_n due to the impulsive interaction, the data block is plotted with vertical lines indicating the dC_n 's start and end, and also the average time period with the percentage stretch applied to enable visual verification of the each block's impulsive response (Figure 3.11).

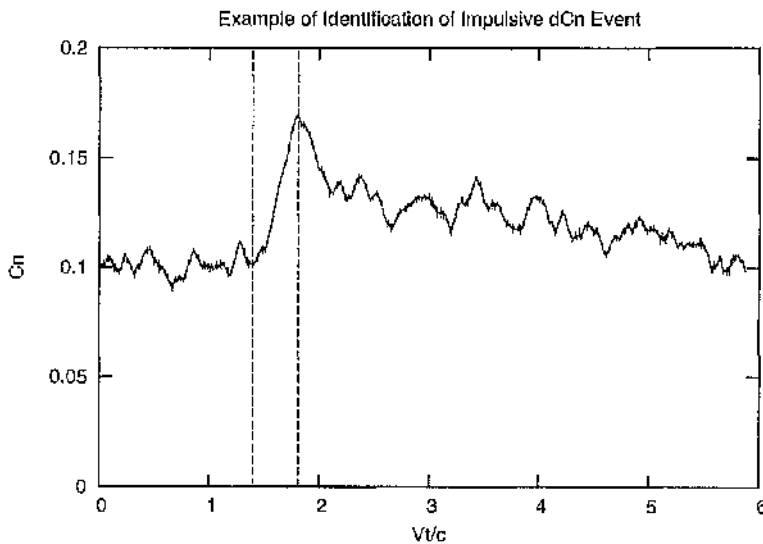


Figure 3.11: Example of identification of Impulsive dC_n Event for data block at vortex centre.

To establish a level of confidence in the results different stretches were used to give pessimistic and optimistic estimates of the change in normal force. An 8% stretch of the average time period provided a generous fit where the stretched time period allowed for more wander and potentially could have resulted in the identification of an impulsive change in normal force which was not due to the orthogonal vortex interaction, In the more pessimistic case, with the time period stretched by 2 %, the search is confined to a smaller time frame. This will therefore not allow for as much wander. Figure 3.12 illustrates the extent that the stretches have on the average time period relative to the total time frame.

3 Analysis of Experimental Data

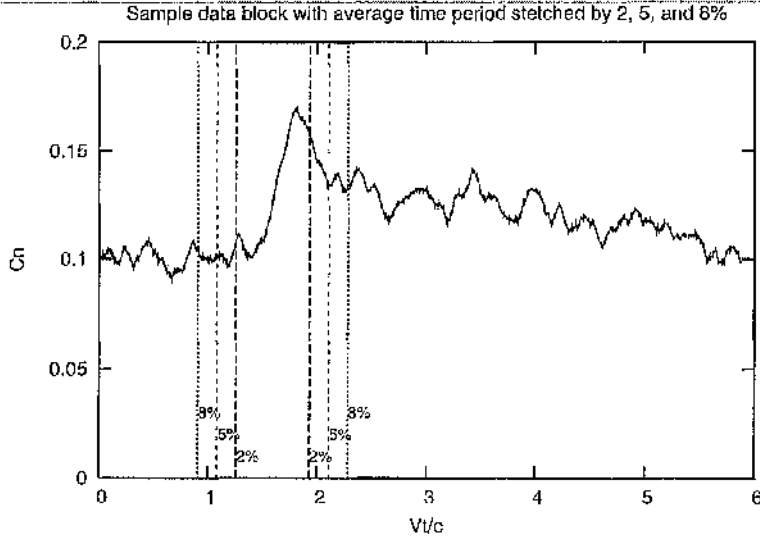


Figure 3.12: Sample data with average time period extended by 2, 5, and 8% stretches

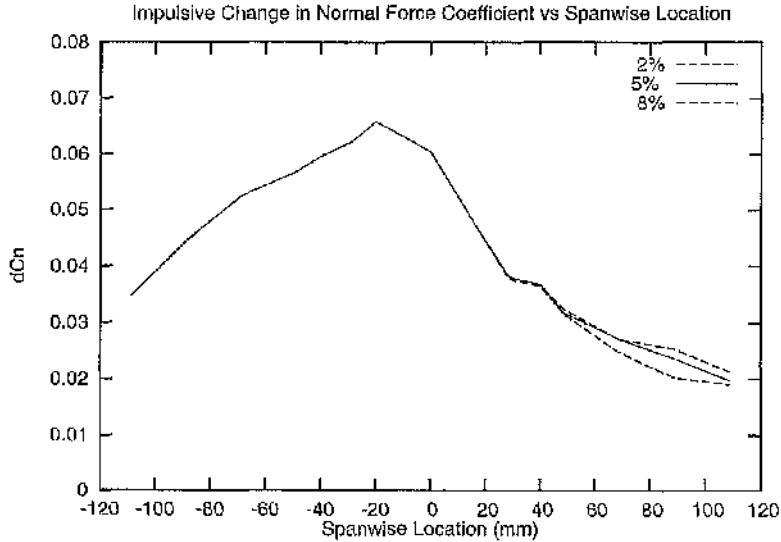


Figure 3.13: Variation of dC_n with spanwise location at 40 m/s

Figure 3.13 demonstrates the level of confidence that can be achieved by using percentage stretches of the average time period. The solid line indicates the 5% stretch match, while dotted lower and upper lines indicate the pessimistic 2% and the optimistic 8% results respectively. It is evident that for the spanwise locations near the vortex centre and below the vortex centre, that it is simple to identify the magnitude of the impulsive change in normal force as indicated by the lack of visible dotted lines.

Conversely, the variation in dC_n between the 2, 5, and 8 % results for spanwise locations above the vortex centre indicate that the impulsive interaction cannot be easily identified at these locations. Indeed, when the data blocks are individually examined 'by eye' there is no clear, obvious short-term impulsive interaction in many cases. This is primarily due to the different type of interaction that can be observed to occur at spanwise locations above the vortex centre.

3.6 Discussion

Individually processing each data block, rather than time-averaging each set of 16 data blocks, has resulted in a more accurate calculation of the change in normal force (dC_n) with respect to spanwise location relative to the vortex centre. Figure 3.14 shows that time averaging under predicted the severity of the impulsive interaction. The customized filtering detailed above also highlighted the contrast between the response at spanwise locations above the vortex centre and at other spanwise locations.

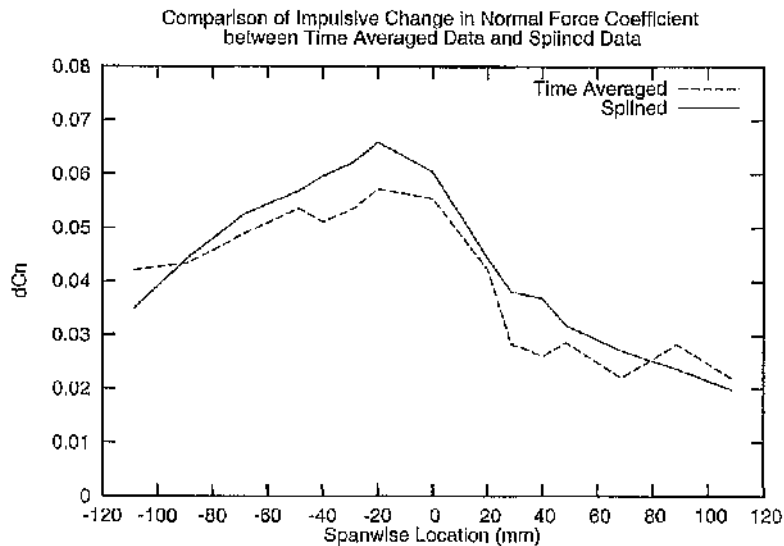


Figure 3.14: Comparison of Time Averaged and Spline Based determination of dC_n

Figure 3.13 showed that there is a clear impulsive change in normal force for spanwise locations near and below the vortex centre. Whereas the larger error bars for spanwise locations above the vortex centre aid in demonstrating that there is a different form of normal

force response on the interacting blade above the vortex centre which cannot simply be characterised by a single short-term impulsive increase in normal force.

The increasing differences between the 2, 5, and 8 % results for spanwise locations above the vortex centre are the result of the software algorithm failing to find a consistent impulsive change in normal force with different percentage stretches of the average time period. However, even on visual inspection of the data blocks at these locations it is difficult to objectively select the impulsive interaction. There is a different form of blade response at spanwise locations above the vortex centre. The response above the vortex centre reaches a comparable peak change in normal force, however the change is more gradual, as the time period over which the change in normal force occurs is much longer. Therefore, the average time period, which is calculated for spanwise locations near and below the vortex centre is not relevant for above the vortex centre.

3.7 Conclusions

Time averaging did enable the general form of orthogonal blade vortex interaction to be seen. However, the severity of the interaction was 'masked' by the spatial and temporal attenuation introduced by time averaging. By individually examining each data block using splines, a more accurate calculation of the impulsive change in normal force is found. Within the vortex core ($< 76\text{mm}$), the splining analysis determined an increased magnitude of dC_n . This is particularly evident at spanwise locations near the centre and just below where a clear impulsive interaction can be identified.

The impulsive responses near and below the vortex centre enabled the identification of a time frame when an impulsive interaction was expected to occur for all spanwise locations on the interacting blade. This time frame, when applied to the spanwise locations above the vortex centre, applies a constraint on the magnitude of the response found. This allows a

value to be given to the impulsive change in normal force for these locations in the given time frame. Its validity is questionable, however, due to the extended slow build in normal force found above the vortex centre which is longer than the average time period even with the 8% stretch. The most important point that must be taken from the spanwise locations above the vortex centre is that the blade response is not impulsive.

The strongest response is found near the spanwise position where the vortex centre travels along the chord. This is due to the axial core flow that is most dominant at the centre of a tip vortex core. As previously noted, there is also an asymmetry in the blade response between spanwise locations above and below the vortex centre. The next two chapters deal with indicial modelling and its application to predicting the response of the interacting blade to the vortex axial core flow.

4 Indicial Modelling for Helicopter Applications

4.1 Introduction

An indicial function is the response to a step change in forcing. By definition, this step change in forcing is instantaneously applied and remains constant. The indicial response is then modelled by an indicial function, which exponentially asymptotes to the steady state response established by the applied forcing. However, in unsteady aerodynamics the aerodynamic forcing is rarely constant. Even so, by using a single indicial function or a combination of functions combined through Duhamel's principle of superposition, indicial modelling is capable of predicting unsteady aerodynamics by sampling the time history into a series of step functions.

The development of indicial models for unsteady aerodynamics has advanced steadily since the first documented method in the 1920s. More recently, within the last 30 years, Beddoes and Leishman have almost solely expanded the development of indicial models for helicopter aerodynamics.

The indicial method has been the preferred modelling technique for investigating the inherently complex helicopter rotor environment. This environment is characterised by large variations in velocity dependent on the radial distance, the azimuthal position, and the mode of flight. Ideally, exact frequency domain solutions are derived to solve for aerodynamic loads. However, the reduced frequency, the common independent timescale variable in frequency domain solutions becomes ambiguous in this environment. Consequently, time domain solutions are more common and can be easily applied as the azimuthal travel of a rotor can be sampled in a time dependent manner. This time dependent sampling is also consistent with some existing rotor load and aeroelastic calculations.

Indicial solutions in the time domain simplify the indicial model whilst retaining the indicial technique's ability to model arbitrary flows. Wagner, Kussner, von Karman and Sears developed early time domain dependent indicial models for idealised flows, and through experimental and other numerical modelling comparisons, Beddoes and Leishman have built upon the early indicial models enabling their potential use as a predictive tool for unsteady rotor aerodynamics.

4.2 Early Indicial Modelling

Unsteady aerodynamics typically concerns flows where the response to velocity perturbations in the flow field results in significant changes in forces or moments over a short timescale. Typically, modelling of the unsteady aerodynamics of rotors captures both the attached flow conditions and the separated flow conditions including those associated with dynamic stall. These models are derived from experimental data and generally feature discrete attached and separated flow models. The attached flow models are particularly relevant to this work on tail rotor orthogonal blade vortex interaction where large-scale unsteady flow separation typically does not occur.

Early indicial models were formed to predict the response to changes in flow conditions of idealised forms with solutions in both the frequency and time domains. Theodorsen (1935) and Sears (1940) developed frequency domain solutions to calculate the indicial lift response to harmonic changes in angle of attack and a non-uniform gust field respectively.

These frequency domain solutions were useful for fixed wing and some aspects of rotary wing aerodynamics where the reduced frequency is still a useful parameter. However, as previously mentioned, velocities in the rotor environment are rarely constant around the cycle and also feature a variation in velocity along the spanwise direction. In these

circumstances solutions in the time domain rather than the frequency domain are more practical.

In the time domain Kussner and Wagner developed two indicial lift solutions. Wagner (1925) obtained a solution for a thin aerofoil's indicial response to a step change in angle of attack, and Kussner (1936) determined the indicial response for an aerofoil entering a sharp edged gust.

Unlike frequency domain solutions, the time domain indicial response is typically found numerically as opposed to analytically. Despite the requirement of numerical solution, the time domain indicial functions are powerful and robust enabling the modelling of arbitrary unsteady rotor aerodynamics. Due to their numerical nature, time domain Indicial methods are typically subject to large correlation studies to establish confidence. Full analytical solutions are cumbersome and time consuming to solve, therefore accurate exponential approximations have been developed. Jones (1940) and Sears & Sparks (1941) derived exponential approximations to the Wagner and Kussner functions respectively.

A time domain solution is typically expressed as the solution of the quasi-steady state response minus some combination of deficiency functions that decay exponentially with time. By using the principle of superposition and the Duhamel integral, the indicial response is constructed through the combination of the quasi-steady state and corresponding deficiency functions for the particular unsteady aerodynamic interaction being investigated. In this way, the indicial method captures Kelvin's Circulation Theory. The quasi-steady response is gradually attained as the influence of the vorticity shed in to the freestream has less effect as the aerofoil continues away from the shed vorticity at the freestream velocity.

4.3 Modern Indicial Modelling

In 1976, Beddoes (1976) developed an indicial model capable of reconstructing unsteady aerodynamic loads for use in rotor calculations. The model was composed of two parts: an attached flow model, and a dynamic stall model. The combination of these two elements was implemented using a set of conditions that determine which particular part of the model was used at any particular moment. The attached flow model is the only part of the model used in this work, and consequently further details of the separated flow model can be found in the associated references.

The attached flow model is based on the incompressible Wagner solution for the indicial lift in responding to changes in angle of attack. However, Prandtl-Glauert (Katz and Plotkin, 2001) compressibility effects were also included by the scaling of the time scale by $(1-M^2)$ and the result of the Wagner function by $(\sqrt{1-M^2})$. Close agreement with experimental data from a variety of sources was found except during the very early stages of aerofoil response. In general, Beddoes' first generation computational model modelled experimental and flight test data well showing that there was potential for using indicial modelling as an effective tool for helicopter aerodynamic performance estimation. [comment on the fact that Beddoes indicial model starts from 0 and not 0.5 like Wagner function does – a sketch of the Wagner, Kussner, Beddoes.]

In 1983, Beddoes (1983) identified weaknesses in his first generation model and focused on developing the indicial model's ability to predict the high Mach number flows found in helicopter forward flight. Also, Beddoes noted that the existing first generation model captured different types of stall with varying levels of success. Beddoes noted that the level of agreement with different aerofoil sections could be classified dependent on the type of static stall associated with that aerofoil. The dynamic stall behaviour of aerofoils statically stalling due to leading edge stall were predicted well and conversely, aerofoils exhibiting trailing edge separation at static stall were not.

Beddoes augmented the first generation model by incorporating the modelling of trailing edge stall and leading edge stall together with shock induced stall, where appropriate, all via

simple calculations based on empirical data. This indicial model retained the computational efficiency of the original with the additional benefit of more accurately predicting the different forms of dynamic stall.

Beddoes (1984) demonstrated that the indicial formulation fulfilled the two-dimensional computational requirements for the calculation of rotor aerodynamic loads incorporating unsteady flow. Beddoes demonstrated good agreement between the indicial formulation and a compressible, time-dependent Navier-Stokes calculation for an abrupt motion. He also demonstrated the ability of the indicial formulation to model any arbitrary flow, including separated flow, and emphasised its computational efficiency.

A key feature of the indicial model was that the indicial response was separated into two components: the circulatory and the impulsive responses. The circulatory component, due to induced effects of the shed wake and its movement relative to the aerofoil, featured an exponentially decreasing deficiency function for the shed wake effect added to the quasi-steady lift response. The impulsive component is analogous to an acoustic wave similar to piston theory (Bisplinghoff, 1962). The fluid is instantaneously accelerated by the aerofoil, creating a pressure wave that propagates at the speed of sound. The instantaneous value then decays exponentially with time.

The circulatory and impulsive components of the indicial lift response depend on different time scales. For this reason, Beddoes investigated the effect of different time sampling strategies on the predicted response. In particular, he examined two strategies. The first, the 'step' algorithm, is dependent on the sampling rate. The second, the 'ramp' algorithm, is dependent on the rate of a ramp motion.

Beddoes observed that using the 'step' sampling strategy for both the circulatory and impulsive calculation resulted in different problems. For example, if the 'step' algorithm was used to sample both the circulatory and the impulsive inputs, a phase lag would develop in the circulatory response whereas the impulsive response decreased in amplitude. Similar

problems were also found when using the 'ramp' algorithm for both components. Typically, these disparities were manifest in the form of poor peak prediction and the shifting of peaks due to phase lag.

Lowering the sampling rate resulted in poor agreement with experimental results for both the 'step' and 'ramp' algorithms. However, Beddoes found for the circulatory calculation that a lower sampling rate could be used for the circulatory calculation using the 'step' algorithm. Similarly, a lower sampling rate could be used for the impulsive calculation when using the 'ramp' algorithm.

Lowering the sampling rate of the 'step' algorithm (Figure 4.1) affected the impulsive response more severely, the impulsive response lost more prediction accuracy compared to the circulatory response for the 'step' algorithm. For the same approximate sampling rate, the 'ramp' algorithm (Figure 4.2) predicted a more accurate impulsive response. Therefore, if only a limited sampling rate is possible, the 'ramp' algorithm should be used to help resolve inaccuracies in the impulsive prediction. However, the 'step' algorithm is sufficient to model the impulsive component provided the sampling rate of the 'step' algorithm is high enough.

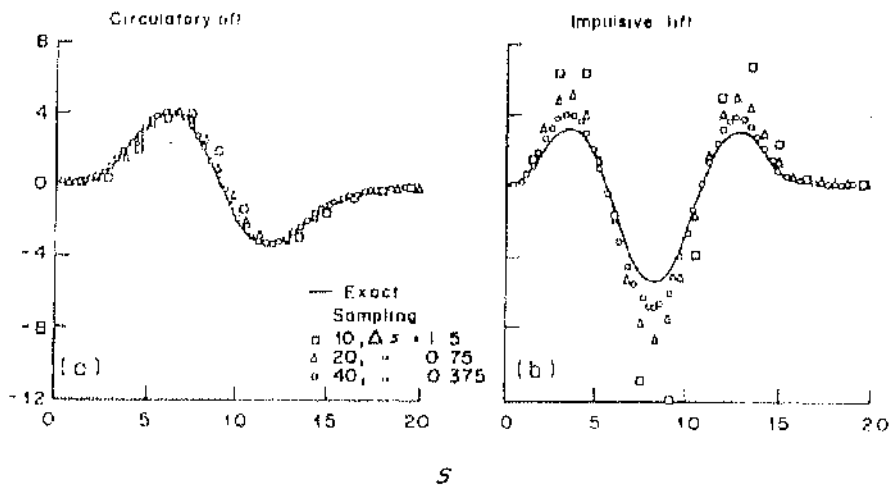


Figure 4.1: Beddoes discrete time sampling - Step algorithm

Computational efficiency was the primary concern for Beddoes in 1984 and this was why he developed the 'ramp' algorithm. This work is predominantly interested in accuracy and

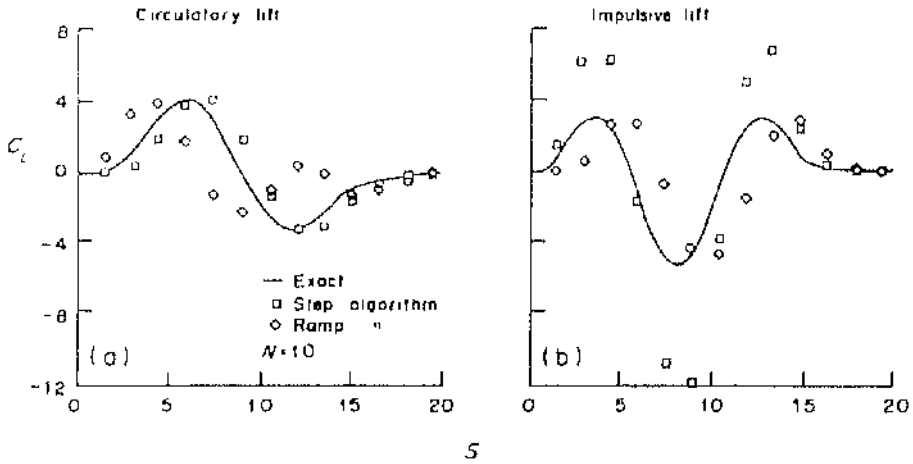


Figure 4.2: Beddoes discrete time sampling - Ramp algorithm

therefore the extra computational time required to solve both the circulatory and impulsive components using the 'step' algorithm was acceptable in this case.

Beddoes and Leishman, both working for Westland Helicopters Ltd, presented comparisons of their indicial model with experimental data for ramp and oscillatory generation of dynamic stall, at the American Helicopter Society Annual Forum in 1986 (Leishman and Beddoes, 1986). Of particular relevance to the current work was the demonstration that the indicial model was capable of predicting the response for arbitrary rotor blades. This was shown by the good agreement with the NACA 0012 aerofoil and two rotor blades, the Hughes HH-02 and the Sikorsky SC-1095. The particularly strong agreement under attached flow conditions was vital validation for the potential use of indicial modelling in the modelling of the attached flow found during orthogonal blade vortex interaction.

A few years later in 1989, Beddoes (1989) added more improvements to the indicial method (Figure 4.3). In addition to the two deficiency functions used to model the circulatory indicial response, Beddoes introduced a third deficiency function. This function was developed from the realisation that the circulatory component of the response is dependent on the decay of the initially strong response of the impulsive component. The timescale of this third deficiency function is related to the decay time constant of the impulsive component.

Beddoes also documented the use of 'shape functions' based on thin aerofoil theory to capture the chordal distribution of velocities found in blade vortex interaction. The shape functions integrate the effect of the incident velocity distribution along the chord. In this way, the effect of the circulatory loading and impulsive loading are shaped to allow for irregularities normally found at the leading and trailing edge. These irregularities, in previous versions of the indicial model, led to excessive forces at the leading edge and trailing edges. The 'shape functions' addressed the lack of accurate modelling at chordal locations near the leading and trailing edge, and consequently more accurately predicted the passage of a disturbance across the chord.

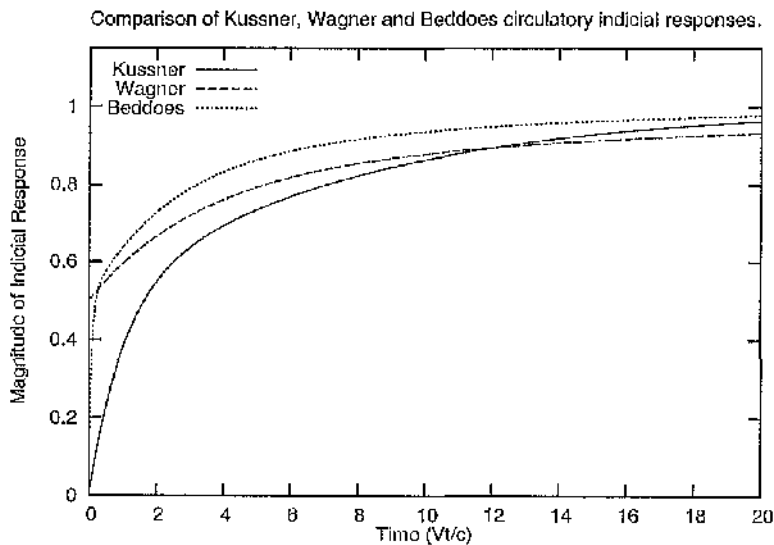


Figure 4.3: Comparison of Kussner, Wagner and Beddoes circulatory indicial responses. Note that the Wagner response starts from 0.5 unlike the other responses which start from 0.

The indicial method was rigorously verified by validation against experimental data and other numerical representations. Comparisons with fully resolved indicial calculations, without the use of exponential approximations, are also possible, even although they are not commonly found. Wagner (1925) calculated some incompressible solutions, whilst Mazelsky (1951) updated the solutions for compressible flow. The calculations are summarized in Bisplinghoff (1955), where pitch and plunge motions are modelled. Beddoes' indicial model predicted accurately both the lift and pitching moment. Agreement with a high Mach number Euler solution was also found to be acceptable particularly for the initial few chord lengths of the response.

Importantly, this paper also documented Beddoes attempt to model parallel blade vortex interaction. The aerodynamics of a rotor blade depend on its own wake and also the wakes generated by other blades. Beddoes idealised the parallel blade vortex interaction into 2 dimensions, and therefore simplified the highly variable spanwise distribution of wake effects. Also, in this case, the vortex travelled parallel to the spanwise direction and the chordal plane. The indicial model normal force coefficient response for this case compared well to Navier-Stokes calculations completed by NASA (Srinivasan, 1986) for a low ($M=0.3$) and a high ($M=0.8$) Mach number flow.

Beddoes also developed a three-dimensional indicial formulation to calculate spanwise loadings on rotor blades. In the present study only two dimensional calculations are performed and so Beddoes 3-D model will not be considered here.

In 1993, Leishman derived the indicial response for parallel blade vortex interaction in the frequency domain from available experimental data. This was typically for aerofoils undergoing angle of attack changes and pitch changes, during parallel blade vortex interaction. Leishman showed that the availability of suitable data was the key factor to determining an accurate derivation of the indicial response from experimental data.

Two problems existed with the experimental data. Frequently, the experimental data were of insufficient quantity, or not available over a broad enough range of conditions to allow the accurate derivation of the indicial response. It was also noted that experimental data collected for the same aerofoil under the same conditions exhibited a different response depending on the source of the data. These problems, limited the accuracy with which the indicial response could be derived.

Leishman, however, did observe that the key to determining an accurate indicial response were the accurate modelling of compressibility and the unsteady aerodynamic response. Leishman detailed the use of simplifying techniques including increasing the vortex core

radius, in existing techniques to account for compressibility. Whilst this approach provided acceptable results, future models will need to represent the effects of compressibility in a rigorous manner.

In 1994, van der Wall and Leishman developed a general indicial model that took account of a combination of pitching, plunging and fore-aft motion. They demonstrated the limitations of existing techniques and their assumptions in predicting of aerofoil response to arbitrary motion. They demonstrated through comparisons with modern Euler CFD calculations, and also comparisons with the exact solutions, that the indicial response derived by their method was superior to any other in terms of quality.

4.4 Summary

The derivation of indicial responses to various simple prescribed motions have been around for a long time. In application to helicopter rotor interactional aerodynamics and their associated flow fields, solution has only been attempted for the parallel blade vortex interaction on the main rotor. This study concentrates on applying the indicial methods to the orthogonal blade vortex interaction. In the following chapter a range of indicial modelling strategies will be investigated.

5 Indicial Modelling at Vortex Centre

5.1 Introduction

This chapter will examine the application of the different indicial prediction methods to orthogonal blade vortex interaction. Firstly the unsteady lift response predicted by the basic Kussner function will be examined before the more sophisticated Beddoes model is applied to the flow. These two indicial lift predictions will be directly compared with an experimental base line case, which is the 40 m/s case at the spanwise location where the centre of the vortex passes along the chord. Following this in a later Chapter, comparisons are made with other orthogonal blade vortex interaction computations documented by Liu and Marshall (2004) and experimental data from a smaller wind tunnel at the University of Glasgow (2001b).

A previous chapter documented the analysis of the experimental data. It was found that the dominant response was at the spanwise location coincident with the vortex centre, and at spanwise locations below the vortex centre. The main cause of the blade response at the vortex centre is the axial core flow, and therefore, initial indicial modelling will focus on characterising the response due to the tip vortex axial core flow.

There are different types of vortex axial core flow models. These will be discussed later, however, they are all very similar and typically feature a peak axial velocity at the vortex centre with some form of decay of the axial velocity dependent on radial distance from the centre. Therefore, because the dominant velocity exists at the vortex centre, this chapter will concentrate on indicially predicting the blade response at the spanwise location where the vortex centre passes along the chord. After analysing the response at the vortex centre, the chapter will also briefly examine the predicted blade response at spanwise locations away from the vortex centre based only on the axial core flow.

5.2 Comparison of Indicial Models with Experimental Response at the Vortex Centre

Theodorsen, Sears, Wagner and Kussner developed the first indicial models, which represented responses to typically simple step functions. The Wagner and Kussner indicial lift responses calculate the change in lift due to changes in angle of attack and due to an encounter with a sharp-edged gust respectively. The axial velocity profile from the vortex core can be modelled as a sharp-edged gust field, and therefore the ability of Kussner's indicial function to predict orthogonal blade vortex interaction was initially investigated.

5.2.1 Kussner Indicial Lift Response

The indicial lift response for a sharp-edged gust is given by:

$$C_l(t) = \frac{2\pi}{V} \left[w_g(0) \psi(s) + \int_0^s \frac{dw_g}{dt} \psi(s - \sigma) d\sigma \right] \quad (5.1)$$

For a thin aerofoil the lift curve slope, m_α , can be approximated as 2π , i.e.:

$$C_l = 2\pi\alpha \quad (5.2)$$

Assuming the indicial step change is small, the angle of attack can be simplified with the small angle approximation:

$$\frac{w_g}{V} = \tan \alpha \approx \alpha \quad , \quad C_l \approx 2\pi \frac{w_g}{V} \quad (5.3)$$

On this basis it can be seen that the indicial lift response dynamically predicts the effect of the vertical gust field for a thin aerofoil undergoing small angle of attack changes. The

unsteady changes in the vertical gust w_g are captured by the square bracketed term in equation (5.1), which is a Duhamel Integral.

5.2.2 Duhamel Integral

Linear systems, either continuous or discrete time systems, possess an important property called superposition. If an input consists of several weighted inputs the corresponding output is the weighted sum, or superposition, of each input's respective output. Due to this superposition property of linear systems any output signal can be reproduced by superposition. The sum of these responses is called the convolution sum for discrete (i.e. sampled) systems, and the convolution Integral for continuous time systems.

In aerodynamics, the convolution sum or integral is commonly referred to as the Duhamel integral, and it is this term that is typically associated with indicial modelling. Aerodynamics, like many fields, is non-linear in nature. However, linear representations of non-linear systems are possible in some particular cases, allowing more complex non-linear aerodynamics to be accurately approximated, in certain particular circumstances, by simple linear approximations.

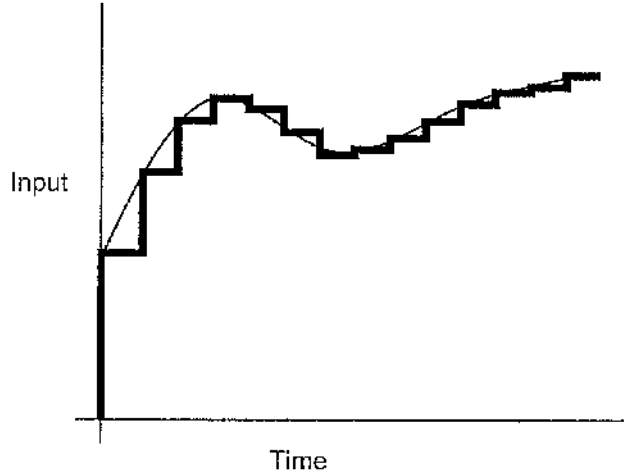


Figure 5.1: Sampling of input of a system into a series of steps

As previously stated, if the input of a system is discretized into a series of steps (Figure 5.1) then the solution for the output signal is logically the superposition of the response to each shifted steps. Therefore, the convolution sum is the product of each shifted unit step ($h[t-\tau]$) multiplied by a weighting factor ($x[t]$), where $t-\tau$ is the shift for each unit step h :

$$y[n] = \sum_{\tau=-\infty}^{+\infty} x[t]h[t-\tau] \quad (5.4)$$

The convolution integral is identical except that the unit impulses are infinitesimal in width:

$$y(t) = \int_{-\infty}^{\infty} x(\tau)h(t-\tau)d\tau \quad (5.5)$$

However, in this application the system is discretely sampled and therefore the convolution sum will be used. If the system is assumed to be a simple linear first order system of the form:

$$\frac{dy(t)}{dt} + ay(t) = x(t), \text{ where } y(0) = y_0 \quad (5.6)$$

The response to a unit step is given by:

$$y(t) = 1 - e^{-at} \quad (5.7)$$

The derivation of this is given in Appendix A.

This response to a unit step can now be used to approximate the response of a non-linear system, which in this case is the unsteady lift response of an aerofoil to a sharp-edged gust or changes in angle of attack. Since the response to a single step is now known, the input signal can be discretized into a series of steps and the response of any system can be reproduced by the linear superposition of the responses to the steps. This is, in essence, the result of the bracketed term in equation (5.1).

Unfortunately, to complete the calculation involving the Duhamel integral would require calculation of all outputs for all of the discretized time steps and consequently requires the storage of a large amount of data to calculate the final response. However, exponential approximations to the solution of the Duhamel integral have been obtained for the Kussner and Wagner indicial lift expressions. The exponential approximations are of the form of equation (5.7) for the response to a linear system given by (5.6). These exponential approximations are implemented into a recursive formula where the calculation of the current time step's indicial lift response is only dependent on the previous time steps' output. This greatly reduces the volume of data required to be stored between time steps and also the number of calculations in each time step.

Leishman (2001) provided a review of modelling of unsteady aerodynamics, where he documented the Kussner indicial lift, the numerical solution of the Duhamel integral, and the recursive solution of the Duhamel integral using exponential approximations. By assuming that the non-linear aerodynamic response of the aerofoil can be adequately modelled by the combination of two step responses, the indicial lift response can be represented by a two-

term exponential indicial function. Therefore, the response of the system can be approximated by:

$$\psi(s) = 1 - A_1 e^{-b_1 s} - A_2 e^{-b_2 s} \quad (5.8)$$

Where s is non-dimensional time, in terms of semi-chords of travel:

$$s = 2Vt / c \quad (5.9)$$

Due to the previously discussed superposition principle of linear systems, the response of a system can logically be represented by the superposition of multiple, in this case two, linear responses. This is true as long as the sum of the coefficients of the exponentials ($\sum A_n$) equals one, ensuring that the initial output from the system at time $s=0$ is zero. If this is not true then the superposition principle will not hold, as the system will no longer be linear.

A two-term exponential approximation of the Kussner lift function was calculated by Sears & Sparks (Leishman, 2002):

$$\psi(s) \approx 1 - 0.5e^{-0.13s} - 0.5e^{-1.0s} \quad (5.10)$$

By substituting the two-term exponential response function into the Duhamel integral and neglecting short-term transients, the effective magnitude of the vortical upgust calculated in the Kussner lift response is:

$$\begin{aligned} w_e(s) &= w(0)\psi(s) + \int_0^s \frac{dw}{ds} \psi(s-\sigma) d\sigma \\ w_e(s) &= w(0)(1 - A_1 e^{-b_1 s} - A_2 e^{-b_2 s}) + \int_0^s \frac{dw}{ds} (1 - A_1 e^{-b_1(s-\sigma)} - A_2 e^{-b_2(s-\sigma)}) d\sigma \\ w(0) &= 0 \\ w_e(s) &= \int_0^s dw(s) - \int_0^s \frac{dw}{ds} A_1 e^{-b_1(s-\sigma)} - \int_0^s \frac{dw}{ds} A_2 e^{-b_2(s-\sigma)} \\ w_e(s) &= w(s) - X(s) - Y(s) \end{aligned} \quad (5.11)$$

Where the indicial lift response equals:

$$C_l = 2\pi \frac{w_e(s)}{V} \quad (5.12)$$

By assuming a continuously sampled system, the following 3 recursive solutions give progressively more accurate solutions for X and Y.

$$X(s) = X(s - \Delta s)e^{-b_1\Delta s} + A_1\Delta w_g \quad (5.13)$$

$$X(s) = X(s - \Delta s)e^{-b_1\Delta s} + A_1\Delta w_g e^{-b_1\Delta s/2} \quad (5.14)$$

$$X(s) = X(s - \Delta s)e^{-b_1\Delta s} + \frac{A_1}{6}\Delta w_g \left(1 + 4e^{-b_1\Delta s/2} + e^{-b_1\Delta s}\right) \quad (5.15)$$

The three recursive solutions are the original solution (5.13), the mid-point solution (5.14) (or half-step lead, as documented by Beddoes (1989)), and the solution based on Simpson's rule (5.15). The mid-point solution and Simpson solution result in approximations that are within 1% and 0.05% respectively. In this study indicial models were coded in C++ and in this particular case, for the Kussner indicial lift response, used the mid-point solution.

5.2.3 Kussner Indicial Lift Response Results

For all future comparisons of the experimental data against indicial models, a sample C_n plot was taken from the selection of sixteen data blocks available at the centre spanwise location. Effort has been made to select a 'representative' C_n plot from the selection of sixteen, which features a 'typical' interaction. This was done by selecting a data block that featured a dC_n of similar magnitude to the average dC_n magnitude determined in the previous chapter. The gust velocity used in the calculation corresponded to the peak axial velocity measured by Wang (2004) for the 40m/s interaction case.

As mentioned earlier in the introduction of this chapter, there are different core models used to represent the axial velocity distribution of a tip vortex. Kaufman (or Scully), Rankine, and Lamb are but a few. However, these formulations all result in very similar axial velocity profiles (Bhagwat and Leishman, 2002). Therefore the selection of one model over another will not significantly affect the result of any indicial modelling. The Lamb-type vortex model was chosen due to its simplicity to implement where Lamb's equation (5.16) calculates the axial velocity w , dependent on the peak velocity (W_{MAX}) at the vortex centre, the radius of the core r_c , and the radial distance from the vortex centre. All subsequent indicial models feature a prescribed axial velocity profile determined by Lamb's axial velocity profile formulation:

$$W = W_{MAX} \left(e^{-\frac{r^2}{r_c^2}} \right) \quad (5.16)$$

The comparison of the Kussner indicial lift response with the experimental data at the vortex centre location is plotted in Figure 5.2. The Kussner function over predicts the magnitude of the initial response peak. However, the gradient of the impulsive increase to the initial peak is well represented. Due to the over prediction of the initial peak, it is difficult to evaluate the effectiveness of the Kussner function in predicting the decay of the lift coefficient after the initial stages of the interaction. The experimental data do feature a rapid decay in lift

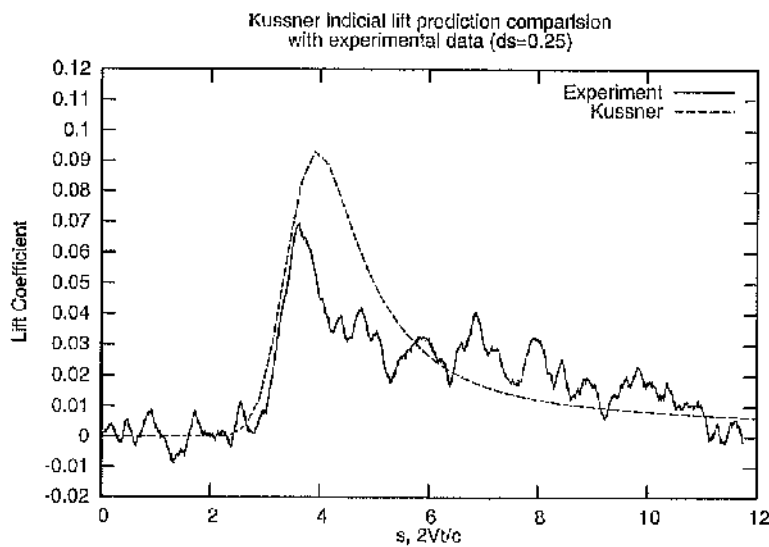


Figure 5.2: Comparison of Kussner indicial lift response ($ds=0.25$) to experimental data coefficient after the initial peak, which is then followed by a more gradual decay. The indicial

prediction, however, only features an exponential decay. Also, the indicial prediction has a slightly 'jagged' appearance near the peak, demonstrating that the time scale resolution is too coarse.

Figure 5.3 shows the same plot comparison as Figure 5.2, but in this case the time step has been halved and so the initial peak is more rounded than before. The increased temporal resolution of the Kussner function does slightly increase the magnitude of the initial peak but the general form of the response remains the same.

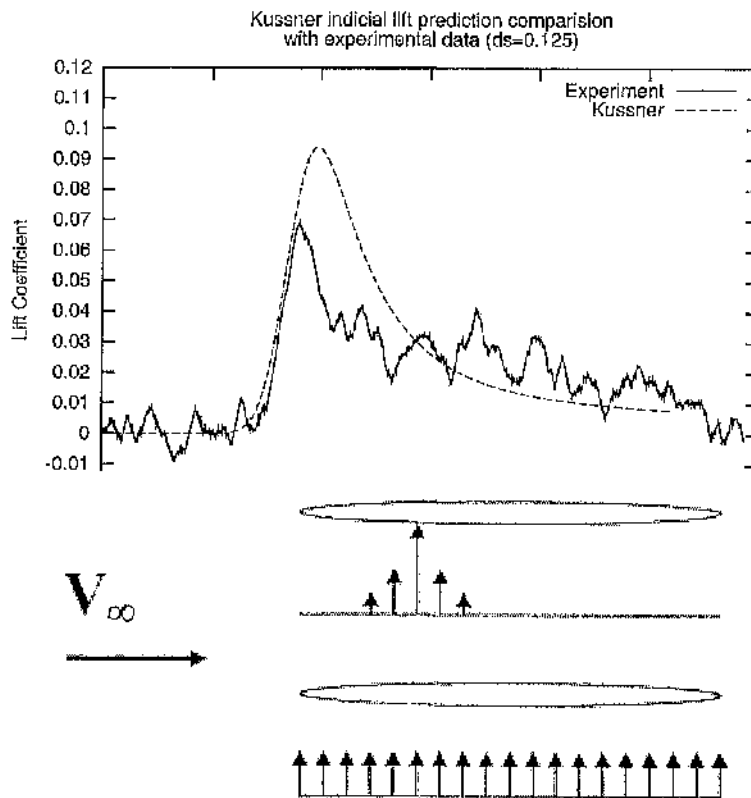


Figure 5.4: Comparison of axial flow gust profiles and constant gust, respectively

The Kussner function was designed to calculate the unsteady lift response to a sharp-edged gust for a thin aerofoil. Typically, this would be the interaction of an aerofoil with a gust of constant magnitude (Figure 5.4). Before the aerofoil interacts with the gust the upgust experienced by the aerofoil is zero m/s. After the gust has reached the leading edge the aerofoil experiences continuous gust of constant magnitude w_0 across the chord.

However, in orthogonal blade vortex interaction, the vertical gust field varies dramatically across the chord due to the radial distribution of axial core flow (Figure 5.4). Consequently, the orthogonal blade vortex interaction gust field is different to the idealised sharp-edged gust field. The over prediction of the initial peak in the response is due to the calculation assuming that the whole chord of the blade is engulfed in a gust of constant magnitude equal to the vortex axial velocity measured in the experiment.

The Kussner function incorrectly calculates the velocity distribution for any non-uniform sharp-edged gust field. The relative size of the vortex core to the length of the chord ensures that the loading due to the axial core flow will always be localized and therefore a calculation that assumes a uniform velocity sharp-edged gust field will not be suitable. To improve the calculation of the indicial lift prediction for orthogonal blade vortex interaction, a representation of the chordal distribution of the axial core flow must be incorporated.

5.2.4 Beddoes Indicial Lift Response

In 1989, Beddoes published a paper detailing an updated indicial technique with potential application to the orthogonal blade vortex interaction. Beddoes first separated the indicial lift response into two components: a circulatory component and an impulsive component. Also, Beddoes allowed for the integration of the effect of a varying chordal distribution of vertical upgust velocities typically found in blade vortex interaction.

The circulatory component is:

$$C_{lC} = C_{l\alpha} \Delta \eta_i \left(1 - A_1 e^{-s'/T1} - A_2 e^{-s'/T2} - A_3 e^{-s'/T3} \right) \quad (5.17)$$

Where $A_1=0.165$, $A_2=0.335$, $A_3=0.5$, $T1=20$, $T2=4.5$, $T3=1.25M$, M = Mach No, s' = non-dimensional time in terms of semi-chords of travel with Prandtl-Glauert compressibility correction.

The Impulsive component is:

$$C_{II} = \Delta\lambda_i \frac{4}{M} e^{-\pi\Gamma} \quad (5.18)$$

Where $\Gamma = (c/a) \left(\frac{1+3M}{4} \right)$, a = speed of sound, c = chord, M = Mach No.

The $\Delta\eta$ and $\Delta\lambda$ components represent the resultant effect of the chordal distribution of axial core flow for the circulatory and impulsive components respectively. The $\Delta\eta$ and $\Delta\lambda$ are evaluated as the difference between the calculated η and λ for the current time step minus the calculated η and λ from the previous time step. η and λ are the integrals of the axial core flow distribution across the blade chord, for the circulatory and impulsive components respectively:

$$\eta_i = \frac{1}{\pi V} \int_0^\pi w(\theta)(1 - \cos \theta).d\theta \quad (5.19)$$

$$\lambda_i = \frac{1}{V} \int_0^1 w(\theta) \sin \theta.d\left(\frac{x}{c}\right) \quad (5.20)$$

Where:

$$\theta = \cos^{-1}(1 - 2x/c) \quad (5.21)$$

Figure 5.5 shows how the shaping affects the distribution of the vortex axial core velocity. In the case of the circulatory component, η , the flow after the mid chord location is accentuated whilst the flow is damped over the first half chord. The impulsive component, λ , is accentuated at the mid chord and damped for the leading and trailing edges. Consequently, the maximum η is obtained as the centre of the vortex moves between the three quarter

chord location and the trailing edge, and the maximum λ is obtained when the centre of the vortex is at the mid chord location.

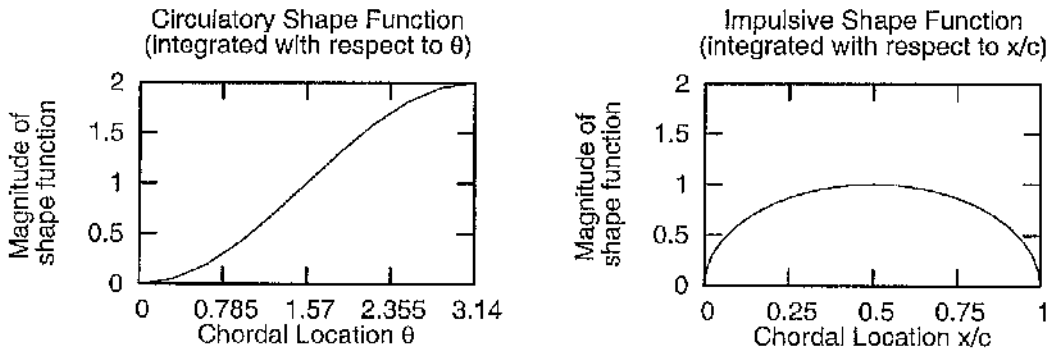


Figure 5.5: Circulatory and Impulsive Shape Functions

To evaluate the integral in a computer program numerical integration is required. Simpson's rule is commonly regarded as the most accurate numerical integration method. Therefore, a function was programmed to calculate the Simpson's rule for arbitrary input data. Beddoes documents the use of thirty Simpson segments providing enough accuracy to calculate the indicial lift response for the parallel blade vortex interaction. Thirty segments were also used here in the indicial lift calculations.

One other improvement that was documented by Beddoes was the inclusion of compressibility by using the Prandtl-Glauert compressibility correction (β) (Mazelsky, 1951, Anderson, 2001). This is simply implemented by scaling the non-dimensional time by $(1-M^2)$, and the lift coefficient by $(1/(1-M^2))^{1/2}$. Therefore the compressible non-dimensional time is:

$$s' = \frac{2Vt}{c} (1 - M^2) \quad (5.21)$$

Beddoes recommended that the size of the time step be kept to $Vt/c = 0.1$ in order to fully resolve the indicial response.

5.2.5 Beddoes Indicial Lift Response Results

Figure 5.6 shows a comparison between the experiment and the indicial response calculated using the Beddoes model with thirty Simpson segments, and a step size $Vt/c = 0.1$ which is equivalent to $ds' = 0.2\beta^2$ (where $\beta = \sqrt{1-M^2}$).

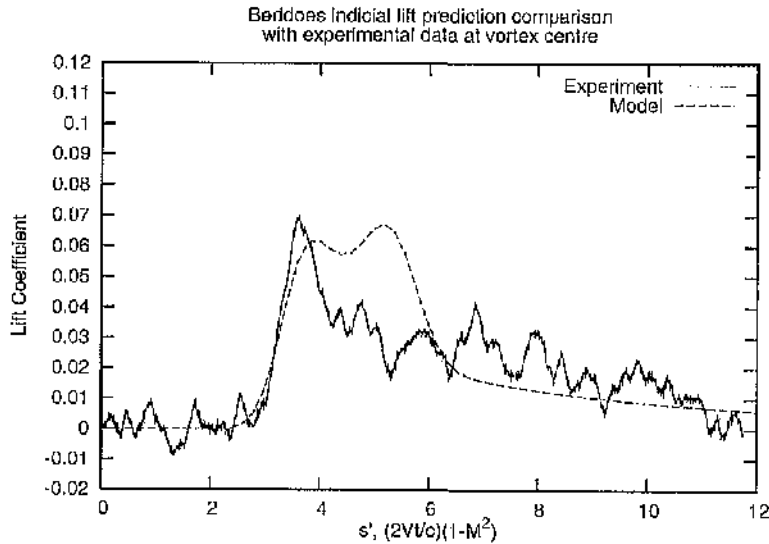


Figure 5.6: Beddoes lift prediction comparison with experimental data at vortex centre

The predicted peak now more accurately matches the impulsive peak found in the experimental data. However, the gradient of the impulsive increase in the indicial response is slightly less steep, and the indicial response also shows a second peak that is not present in the experimental data. Also, after the secondary peak the indicial response decays more quickly than the experimental data. Furthermore, it can be seen that the indicial response is slightly 'jagged' near the peaks indicating a similar lack of temporal resolution found with the Kussner indicial lift prediction, again the ds' step size was too large.

5.2.6 Sensitivity to ds' step size and number of Simpson segments

Figures 5.7 - 5.9 shows the effect of reducing the ds' step size for the circulatory, impulsive and total lift, respectively. The impulsive component can be further resolved by reducing the step size, and consequently, this results in a different shape for the total lift prediction. Figure 5.9 shows that the secondary peak previously found is reduced in magnitude and the

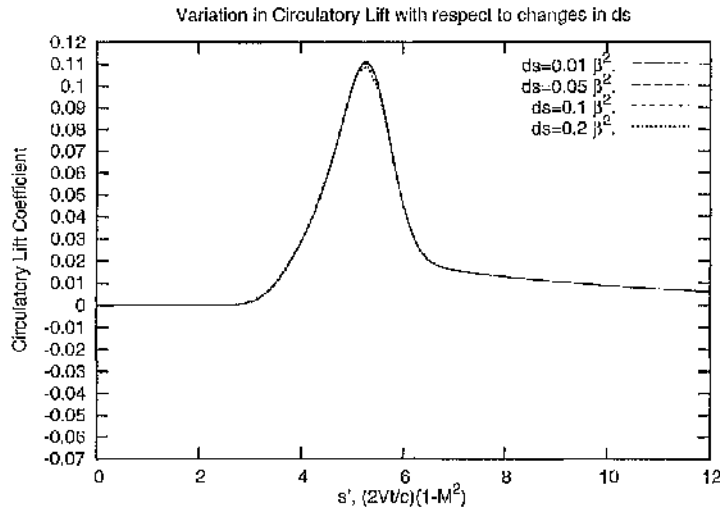


Figure 5.7: Circulatory Lift variation with changes in ds' step size

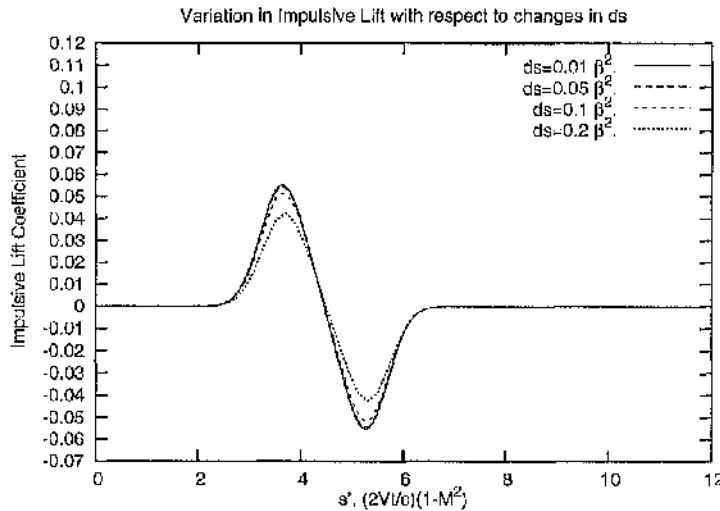


Figure 5.8: Impulsive Lift variation with changes in ds' step size

gradient of the initial peak, and its magnitude, are now accentuated if the step size is decreased. With a ds' step size equal to $0.01\beta^2$ the form and magnitude of the indicial lift prediction produces a significantly better agreement with the experimental base line case for the initial stages of the interaction.

As documented earlier in this chapter, Beddoes stated that the 'step' algorithm, used here so far, might not adequately represent the impulsive component when V/c equals 0.1. Beddoes recommended the use of the 'ramp' algorithm if an excessive decrease in the size of time steps was required to fully resolve the impulsive component

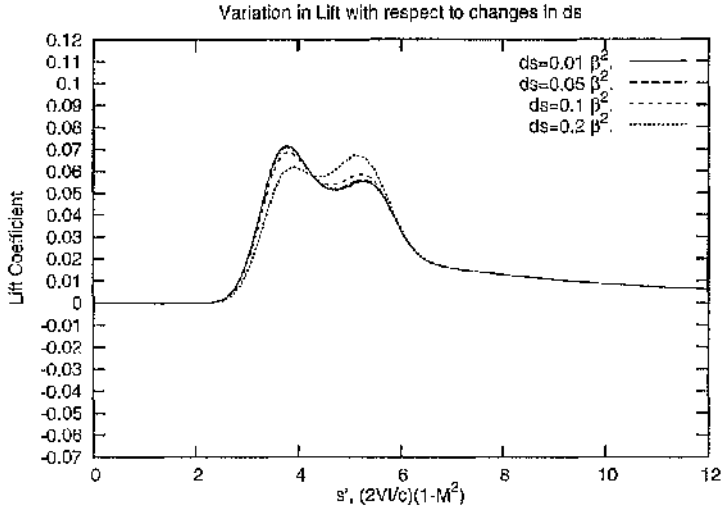


Figure 5.9: Total Lift variation with changes in ds' step size

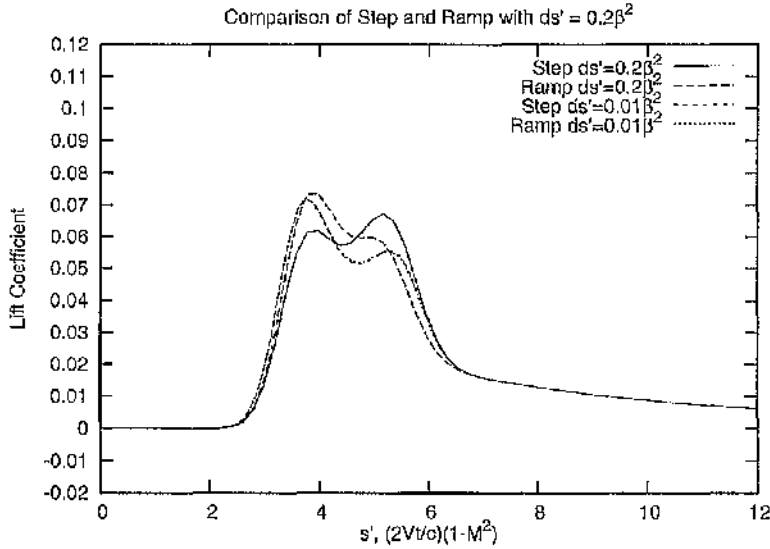


Figure 5.10: Comparison of 'Step' and 'Ramp' algorithms

The effect of using the ramp algorithm may be observed in Figure 5.10. First, it accurately predicts the fully resolved impulsive component with $ds' = 0.2\beta^2$ but the prediction is 'jagged'

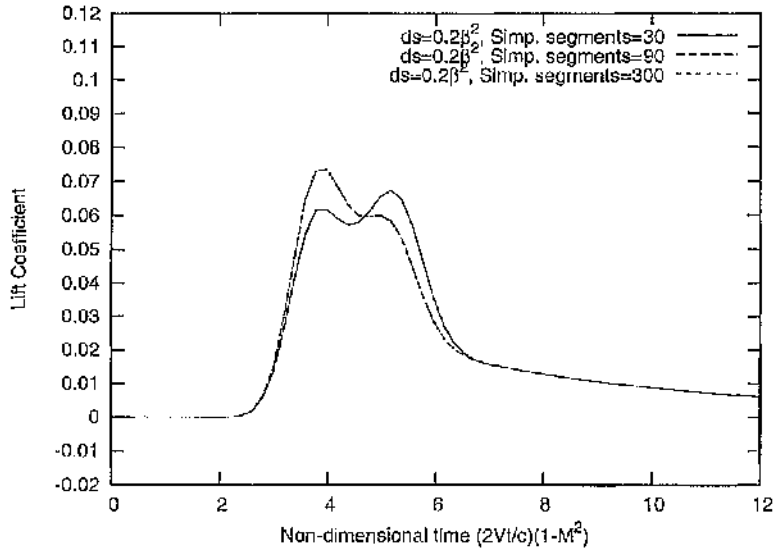


Figure 5.11: Effect of the number of Simpson segments ($ds' = 0.2\beta^2$). Note that with Simpson segments equal to 90 and 300 and identical response was calculated.

in appearance indicating that the prediction could be further resolved by decreasing the ds' step size. However, on decreasing the ds' step size to $0.01\beta^2$ the 'jagged' appearance is still evident suggesting that the 'ramp' algorithm is not as well refined as the 'step' but nevertheless provides a suitable solution when increased computational efficiency is required. The fully resolved total lift 'step' prediction has a more agreeable form, since it does not feature the 'jagged' peaks of the 'ramp' prediction. Therefore, since the form of the

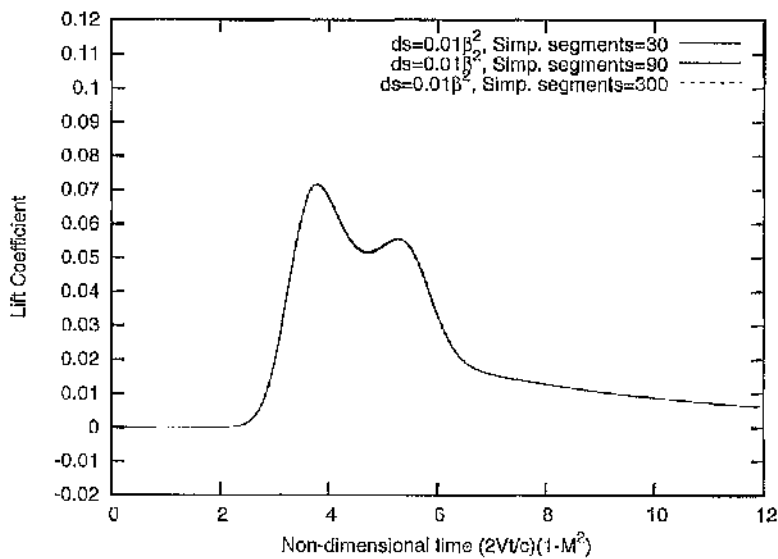


Figure 5.12: Effect of the number of Simpson segments ($ds' = 0.01\beta^2$)

'step' calculation is more agreeable, the 'step' calculation is favoured over the 'ramp' calculation. Also, the relative increase in computational time required when the ds' step size is reduced to $0.01\beta^2$ for the 'step' algorithm is not seen as limiting factor in this study, as the total running time of the calculation is still negligible.

A small sensitivity of Beddoes indicial lift prediction to the number of Simpson segments was found. Figure 5.11 shows that increasing the number of Simpson segments does produce a better prediction when $ds' = 0.2\beta^2$ and when there are 90 or 300 segments, however, the shape is still not as smooth as the $ds' = 0.01\beta^2$ with 30 segments. No such improvement is found with the 'fully resolved' case where $ds' = 0.01\beta^2$ (Figure 5.12).

5.2.7 Fully Resolved Indicial Response

Comparison of the experimental data with the indicial model, where $ds' = 0.01\beta^2$ and the number of Simpson segments is 30, results in a much more favourable agreement in form and magnitude (Figure 5.13). The model accurately predicts the initial impulsive rise in the lift coefficient present in the experimental data. Also, the gradient of the impulsive rise is more accurately predicted. The later stages of the interaction are relatively poorly predicted by the indicial model. So far, experimental data from the 40 m/s base line case have been considered. Now, comparisons of the Beddoes indicial lift prediction with experimental data at velocities of 20, 30, and 50 metres per second are made to demonstrate the robustness of the modelling procedure.

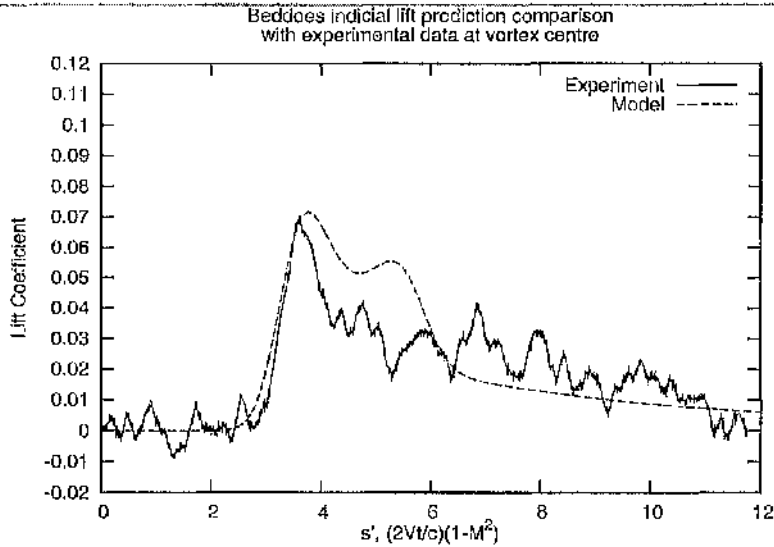


Figure 5.13: Comparison of experimental data with model. ($ds' = 0.01\beta^2$, Velocity = 40 m/s)

5.2.8 Response at Vortex Centre for Velocities 20, 30, and 50 m/s

Again, the experimental data set at each velocity for the spanwise location of the vortex centre contains sixteen data blocks, with each block capturing a single orthogonal blade vortex interaction. Each block was visually compared against the other fifteen comprising the set, and a 'representative' data block was selected based on a subjective evaluation of what comprised the mean(/average) response. The responses in each of the sixteen blocks were generally of fairly similar nature, and selecting a 'representative' block was straightforward.

Figures 5.14 - 5.16 demonstrate that the Beddoes indicial lift prediction model is capable of predicting the initial impulsive rise and peak fairly adequately for all cases, demonstrating a robust capability to predict the initial peak in terms of magnitude and gradient.

5 Indicial Modelling at Vortex Centre

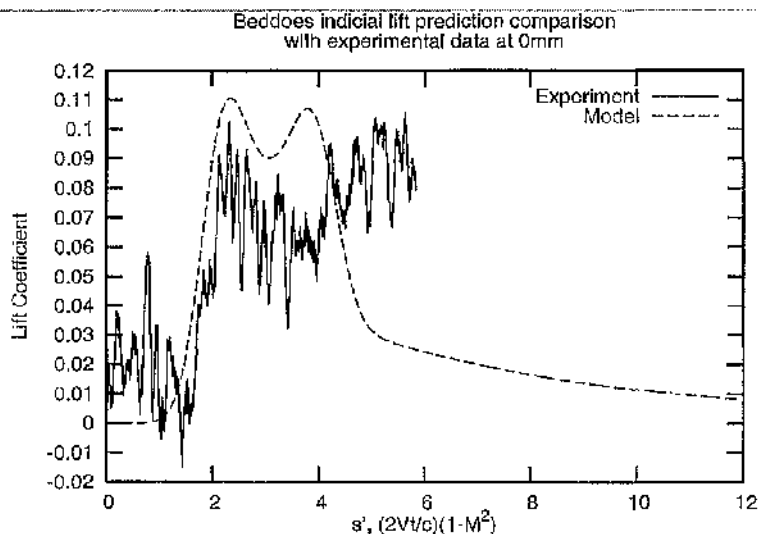


Figure 5.14: Comparison of experimental data with model. ($ds' = 0.01\beta^2$, Velocity = 20 m/s)

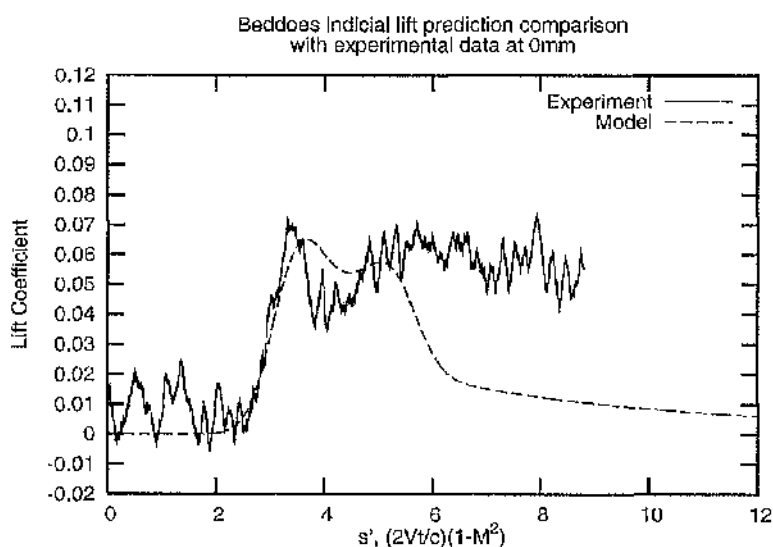


Figure 5.15: Comparison of experimental data with model. ($ds' = 0.01\beta^2$, Velocity = 30 m/s)

However, similar to the base line forty metres per second case, the predictions at the other velocities fail to reproduce the trends in the experimental data after the initial stages of orthogonal blade vortex interaction. Appendix B shows the configuration settings for the 4 different velocities. The 4 cases feature a large variation in freestream velocity, although not such a dramatic variation in vortex core radius or maximum axial velocity. Therefore, the results characterise vastly different types of interaction as indicated by the variations in Impact Parameter (IP), Axial Flow Parameter (AFP) and Thickness Parameter (TP).

5 Indicial Modelling at Vortex Centre

As previously discussed in the background reading on orthogonal blade vortex interaction, Marshall and Krisnamoorthy (1997, 1998), from the University of Iowa, developed these three main parameters to determine the type of vortex interaction that would occur during orthogonal blade vortex interaction. Marshall also documented critical values of these parameters about which the type of flow is determined.

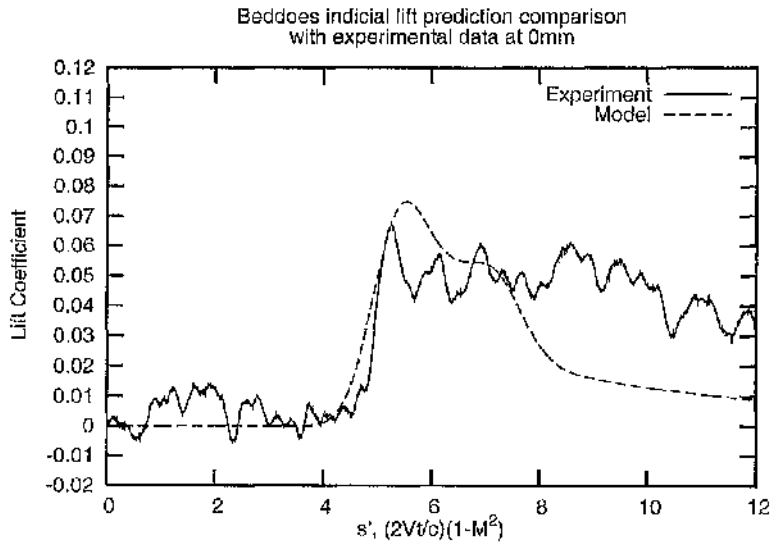


Figure 5.16: Comparison of experimental data with model. ($ds' = 0.01\beta^2$, Velocity = 50 m/s)

The most relevant of the parameters for these data sets, are the Impact Parameter and the Axial Flow Parameter. The IP in each case characterises a 'weak regime' interaction where the breakdown of the tip vortex core does not occur until the vortex core is 'cut' by the blade. The AFP is supercritical for all cases except 30 m/s where the AFP is subcritical. In this case the axial core flow is not strong enough to block the propagation of vorticity generated at the blade surface travelling against the axial core flow. This therefore poses a potentially different case compared to the subcritical case where the flow is typically compared to a jet-like flow impacting on a normal surface. Despite the large variation in freestream velocities compared to the relative small variations of the vortex core radius and axial velocity, only one of Marshall's four parameters, which characterise an orthogonal blade vortex interaction, cross a critical boundary. However, the variation in the Axial Flow Parameter across its critical boundary at 0.707 has not led to any inconsistencies in the prediction of lift

during the initial stages of orthogonal blade vortex interaction. The later stages of all interactions are poorly predicted. This will be discussed in more detail later.

5.3 Summary

This chapter demonstrated that the indicial models based on the Kussner function are incapable of indicial modelling the orthogonal interaction accurately. However, it has been found that by using an indicial model that takes into account the chordwise distribution of axial velocities due to the interaction, that an accurate prediction of the initial stages of the interaction is predicted. The peak magnitude of the lift response predicted by the indicial model is similar to the magnitude found by the detailed analysis of the experimental data in Chapter 3 at the vortex centre.

Also, the detailed analysis in chapter 3 identified a non-symmetric peak lift response about the spanwise location where the vortex centre interacted with the blade. However, the indicial models presented in this chapter are dependent on the axial velocity profile alone, and would result in a symmetrical peak lift response about the vortex centre. Potentially, the rotational flow about the interacting tip vortex may account for the asymmetry. A panel method study is used in the next chapter to investigate this.

6 Two-Dimensional Panel Method

6.1 Introduction

The use of numerical panel methods has become commonplace in aerodynamics since the introduction of computers to industry. The technique involves solving the flow around a body by discretising its surface into a series of panels. Singularities are located at the centre of each panel and their strengths adjusted until the series of connecting panels forms a streamline of the flow coincident with the body's surface.

Panel solutions have been formed in both two and three dimensions, and a three-dimensional panel method is documented in a subsequent chapter. However, this chapter focuses on using a two-dimensional panel method to calculate the resultant quasi-steady change in lift on a symmetric aerofoil, due to orthogonal blade vortex interaction.

6.2 Panel Method Theory and Application

The panel method is based on the principle of superposition of flows. Superposition of flows is possible when the equations governing the flow field can be reduced to linear equations. This occurs when incompressible, irrotational flows are considered. Obviously, this limits the application of the panel method to basic inviscid flows, where the Mach number is limited to subsonic values of less than approximately 0.3.

Once the linearity of the flow field is established, the superposition of elementary flows is possible and basic flow fields around some bodies can be calculated. For example the streamlines of flow past a cliff can be synthesised by the addition of a uniform flow and point source, or the flow around elliptical bodies, and cylinders, can be replicated by the use of a

source-sink pair (doublet). The panel method extends the idea of representing body shapes by elementary flows by placing singularities on the surface of the desired body shape, and then determining the flow conditions due to the distribution of singularities, and the uniform flow or other external flow conditions.

Panel modelling different types of bodies requires different types of singularities. For non-lifting bodies, such as solid surfaces like walls or an aircraft fuselage, source singularities are used. For lifting bodies, like aerofoils and blades, the circulation around the blade must be accounted for by the use of vortex singularities. Once, the type of singularity has been decided, the efficient distribution of panels to cover the body's surface must be determined.

The way in which singularities are distributed about a body's surface is determined by dividing up the surface into a series of panels. Typically, at the centre of each panel, usually called the collocation point, a singularity is placed. Where changes in the flow are relatively small, a high number of panels require additional computational time for a less than marked increase in accuracy. Therefore, panels are more densely packed in regions where more severe flow changes are likely. For example, for an aerofoil a larger number of panels may be located at the leading and trailing edge compared to mid-chord locations.

Whilst the distribution and the number of panels used to represent a body's surface can be customized to a particular case, the way in which the singularity strength varies can also be altered. Low order panel singularity solutions usually resolve each panel's strength as a constant strength across the panel's length, and therefore, for a typical aerofoil, discontinuities in panel strength will exist at the boundaries of each panel leading to some inaccuracies in the subsequent calculation of forces and moments. However, higher order linearly or quadratically varying strength panels result in smooth transitions in singularity strength at panel boundaries. These higher order panel methods require more computational time, and still require the distribution of the panels to be tuned to each particular case.

6.3 Application

The panel method solution is obtained by identifying influence coefficients that represent the influence of each panel on all others and then routinely solving for the n unknown panel singularity strengths corresponding to the n panels, dependent on external flow conditions. This is accomplished by determining the flow conditions that must exist at each collocation point. To establish a body's surface as a streamline of the flow the panel method ensures that all flow is tangential at the body's surface by ensuring zero normal flow incident at the surface. Once the singularity strengths have been determined, by solving the n simultaneous equations, the body's surface forms a streamline of the flow.

Flow tangency at each collocation point can be enforced in two ways: either by the Neumann boundary condition or the Dirichlet boundary condition. Both boundary conditions effectively result in the same solution, although the application of one may be simpler in a particular case. The Neumann boundary condition enforces the streamline by specifying zero velocity normal to the panel surface at the location of the singularity, and the Dirichlet boundary condition implies the same condition only in terms of a velocity potential boundary.

When solving the panel method for a lifting body the Kutta condition must also be satisfied. This is usually achieved by making an assumption about the strength of the vortex panel on the upper surface and the vortex panel on the lower surface at the trailing edge. They are assumed to have equal strength but opposite sense, resulting in flow leaving the trailing edge in the same direction as the bisector at the trailing edge and therefore simulating a sharp trailing edge. To solve for a lifting body, vortex panels must be used to capture the circulation and, hence, the lift generated by the body.

The panel method is free from the typical constraints found in other potential flow solutions where bodies are restricted to particular shapes or flow conditions. The effectiveness of the panel method is only limited by the ability of the panel designer to appropriately implement panels to effectively capture the body shape. The efficiency of the panel method is better

than other computational methods, which typically require the discretizing of the flow field around the body, rather than solely the body's surface as in the panel method, and consequently the panel method is many orders of magnitude more efficient. However, the panel method is limited to the incompressible domain, or circumstances where assumptions of incompressibility are valid.

6.4 Panel Method Used In This Study

In 1988, Coton documented a Fortran code capable of reproducing low speed flow over arbitrary aerofoils. The code was capable of solving the flow in two dimensions calculating the pressure distribution over both the upper and lower surface and subsequently calculating the lift and pitching moment associated with a given aerofoil. The panel method used linearly-varying vortex singularities to solve for the lifting body, and the Neumann boundary condition enforced zero normal velocity on the surface of the body. This chapter documents the application of this vortex panel method to calculate the lift generated by an interacting blade experiencing orthogonal blade vortex interaction under the same conditions as in the experiments.

The blade was modelled by 496 evenly distributed vortex panels. A high number of panels was required to capture the highly localised flow found during blade vortex interaction where the vortex core of a tip vortex is typically smaller than the chord length of the blade. An even distribution of panels was employed as opposed to the more commonplace denser distribution of panels at the leading and trailing edges. This is also necessary in this application as it was essential to capture the effect of the localized flow conditions due to the vortex core as it travelled over the chord.

In the cases studied here, the blade was fixed at zero degree of incidence, and the cross flow, caused by the tip vortex axial core flow resulted in a distribution of local angle of attack along the chord.

The accuracy of the vortex panel method calculation is validated in the following figure (Figure 6.1). The lift coefficient was calculated for varying angles of incidence from 0 to 20 degrees and compared with 3 separate sets of test data for the NACA 0015 aerofoil. The figure shows a good comparison for low angles of incidence, particularly angles less than 5 degrees which are most important for the work presented here.

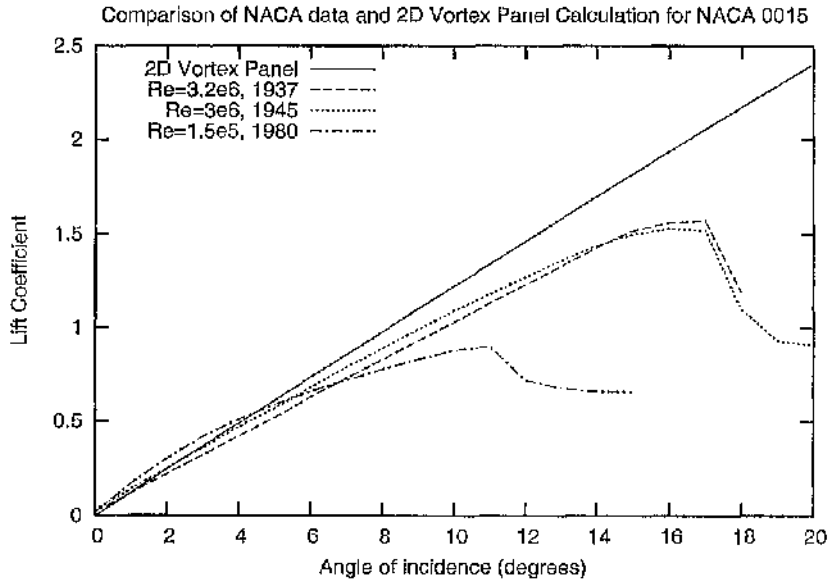


Figure 6.1: Comparison of 2D vortex panel method with NACA data for NACA 0015

To accommodate the introduction of localised flow conditions on the surfaces of the blade, some alterations were made to the vortex panel method. First, the normal velocity at each of the vortex panels was changed to account for the axial velocities associated with an orthogonal tip vortex. Second, the vortex panel method was placed inside a standard looping structure, where the axial and rotational velocities input into the vortex panel method were varied to simulate the passage of an orthogonal tip vortex along the aerofoil's chord.

6.5 Axial Flow Results

The two-dimensional panel method was subjected to the axial velocity distribution of a Lamb-type vortex. The axial velocity profile is defined according to Lamb's equation (6.1).

$$W = W_{MAX} \left(e^{-\frac{r^2}{r_c^2}} \right) \quad (6.1)$$

The vortex centre started off two chord lengths ahead of the leading edge of the blade and was moved towards and across the aerofoil until it was two chord lengths downstream of the trailing edge, therefore travelling a total of 5 chord lengths.

Figure 6.2 shows how the lift coefficient changes as the vortex moves along the blade chord for an incidence of zero degrees for a range of spanwise positions relative to the vortex centre line. The maximum lift is generated at the spanwise location where the vortex centre travels along the chord. The lift coefficient symmetrically decreases about the central spanwise location due to the symmetrical axial velocity distribution that varies solely as a function of radial distance.

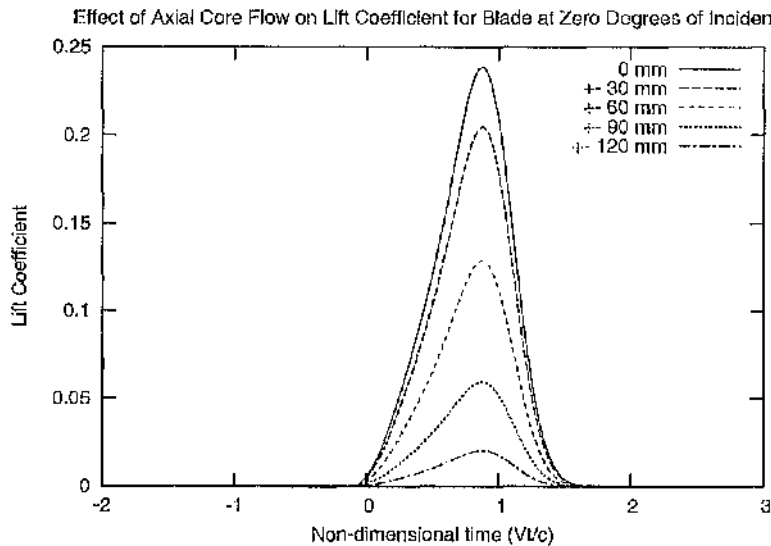


Figure 6.2: Effect of Axial Core Flow on Lift Coefficient for a blade at zero degrees of incidence

At all spanwise positions, the lift increases to a maximum as the vortex core approaches the trailing edge. From this point on the main vortex axial flow of the vortex core is leaving the chord and consequently the lift decreases dramatically. Of note, is that the axial flow imposed on the aerofoil is the equivalent to the axial flow taken from the experimental measurements. The maximum lift coefficient from this quasi-steady state response is

approximately 0.24, which is roughly four times the magnitude found in the experimental data (0.06). This demonstrates that the blade vortex interaction response is highly unsteady, and therefore a quasi-steady state calculation is not a suitable way in which to predict it.

6.6 Rotational Flow Results

It was anticipated that the axial flow calculation would not yield reasonable predictions of the blade vortex interaction response. However, the primary reason for using the 2D vortex panel method was to get a feel for how the lift response was augmented by the vortex rotation. This is now examined.

Again, the equation governing the rotational flow about the vortex centre was determined by Lamb's equation:

$$V_{\theta} = \frac{\Gamma}{r \cdot 2\pi} \left(1 - e^{-\frac{r^2}{r_c^2}} \right) \quad (6.2)$$

The resultant distribution of rotational velocity is given in Figure 6.3. As a symmetrical

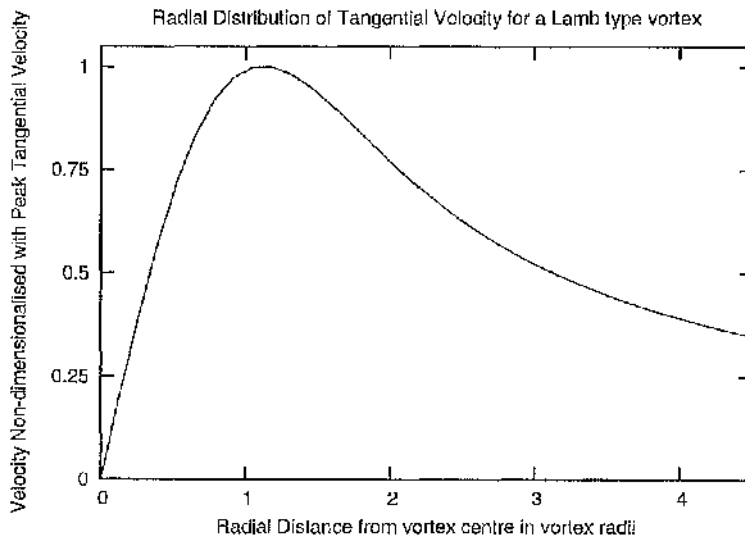


Figure 6.3: Resultant distribution of rotational velocity

aerofoil produces zero lift at zero degrees incidence, the rotational flow will not result in a change in lift for this condition. Therefore, to examine the effect of the rotational flow, the blade was set to two degrees. This angle was chosen, as it would approximate the maximum angle of attack that could possibly be achieved as a result of the upwash from the axial velocity distribution, and consequently the response due to the local dynamic pressure changes produced by the rotational flow would be maximised.

The maximum change in local velocity due to the vortex is approximately ± 3 m/s at ± 76 mm from the vortex centre height. Indeed, it can be seen (Figure 6.4) that the resultant change in the lift coefficient is also small. The maximum change in lift coefficient is only approximately 4%. This is too small to account for the experimentally observed variations in spanwise loading during the orthogonal interaction (Figure 3.14).

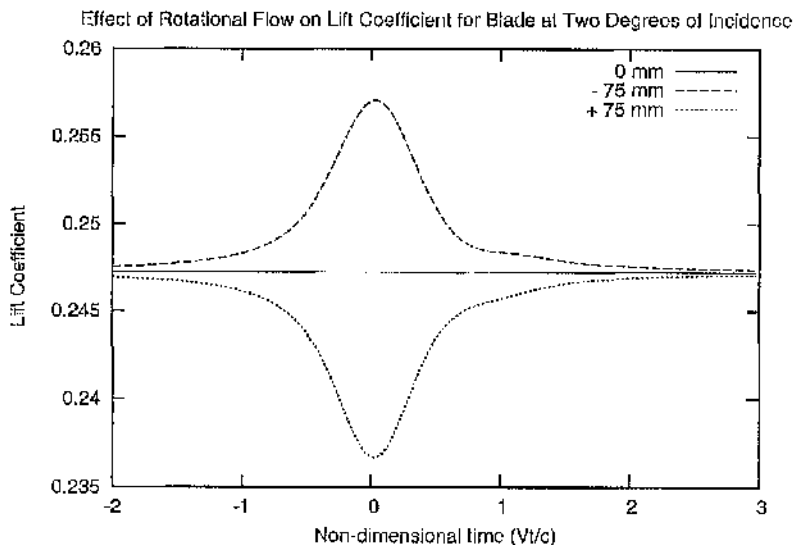


Figure 6.4: Effect of Rotational Flow on Lift Coefficient for Blade at Two Degrees of Incidence

6.7 Summary

Using the two-dimensional panel method, it has been demonstrated that rotational flow has an almost negligible effect on the total lift of the aerofoil during the interaction. In the

experimental data, there is a large variation in the blade response with spanwise location relative to the path of the vortex centre. The panel method has shown that the rotational flow is not responsible for this effect. Therefore another cause must be considered.

The panel method has also been used to demonstrate the dynamic nature of the blade vortex interaction. The calculated maximum lift during the blade vortex interaction was around four times the experimentally observed maximum lift because the unsteady effects were not accounted for in the panel method calculation.

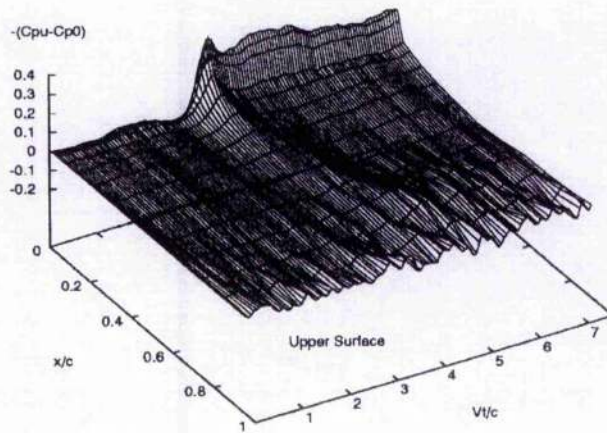
7 Numerical Simulation of the Experimental Flow Field

7.1 Introduction

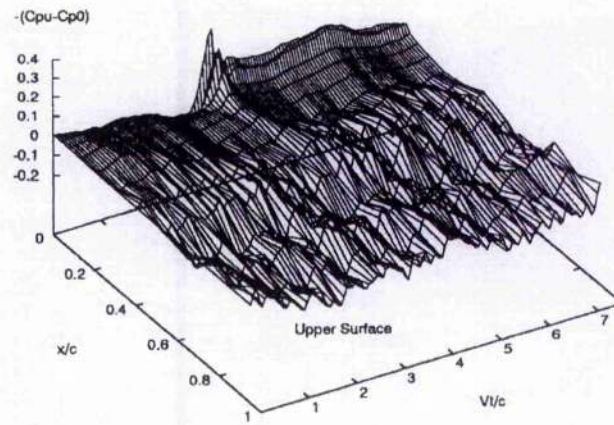
In the previous chapters, the axial core flow of an orthogonally interacting tip vortex has been identified as the major contributor to the normal force response of the interacting blade at the spanwise location where the centre of the vortex core travels along the chord. From the analysis in chapter 3 it is evident that the magnitude of the impulsive change in normal force is not symmetric about the spanwise location of the vortex centre. Potentially the rotational flow of the tip vortex may have been responsible for the asymmetry of the interacting blade's normal force response. However, the previous chapter demonstrated through the use of a two-dimensional panel method that the magnitude of the rotational component of the tip vortex was insufficient to generate the necessary asymmetric blade response at spanwise locations away from the vortex centre.

Upon examination of the upper surface pressure histories of the blade, previously published by Wang (2002) (Figure 7.1), it becomes clear that there is a large scale spanwise effect experienced by the blade. Figure 7.1 shows the pressure response of the blade at spanwise locations below the vortex centre, at the vortex centre, and above the vortex centre. The three-dimensional plots show very varied responses. The blade in these plots has a fixed angle of incidence of 12 degrees. At the spanwise location below the vortex centre, the progress of the vortex along the chord can be clearly identified as the suction peak and subsequent ridge. There is little or no separation present. At the vortex centre, a suction peak and ridge are also present, but separated flow is present from approximately 40% of the chord to the trailing edge. At the spanwise location above the vortex centre, the upper surface pressure history features full separated flow over the entire chord, with no obvious localised interaction indicating the vortex. This progressive forward movement of trailing edge separation, suggests that the blade is experiencing a progressively increasing angle of attack from below to above the vortex. A large scale cross flow effect in the experiment

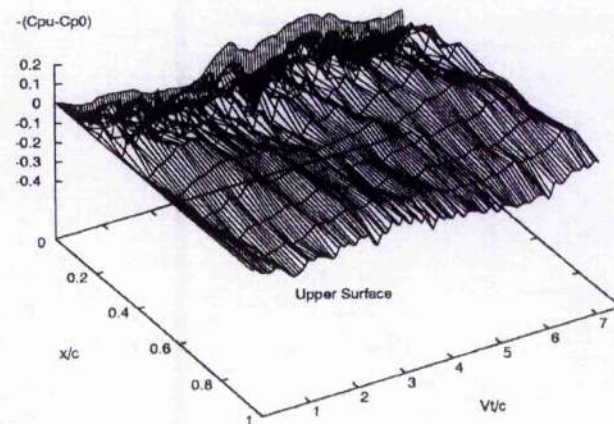
would be required to produce this spanwise variation in angle of attack rather than much smaller localised changes as expected.



a) $z/c = -0.25$



b) $z/c = 0$



c) $z/c = 0.25$

Figure 7.1: Surface pressure plots for upper surface of interacting blade for angle of incidence of 12 degrees. (a) Below, (b) centre, and (c) above.

To investigate this effect, the numerical model developed by Copland, and used in the design of the experiment was used to calculate induced flow at the blade. As indicated previously, this numerical model consisted of a three-dimensional source panel method to represent the wind tunnel walls, a lifting line calculation for the vortex generator blade, and a free wake solution to model the convection of the generated wake downstream into the wind tunnel working section.

This chapter explores the use of the numerical simulation to extract the cross from the locations in the wind tunnel where pressure transducer arrays measured the orthogonal blade vortex interaction. The Beddoes indicial model is then used to calculate the coefficient of normal force in response to the numerically simulated cross flow.

7.2 Numerical Simulation

The use of panel methods to solve flow problems has already been discussed in the previous chapter. Copland's numerical simulation extended the work of Hess & Smith (1964) who documented the use of a three-dimensional source panel method for calculating flow around non-lifting bodies. Copland also made use of the Gauss-Seidel method documented by Hess & Smith as an efficient means of solving the simultaneous equations required to calculate each source panel's influence coefficient.

Source panels were used to represent a significant portion of the wind tunnel geometry including, the working section, the contraction, and part of the settling chamber. The wind tunnel walls were discretized into a lattice of quadrilateral source panels with constant strength singularities at each panel's control point. The accuracy of the panel method depends on the number of panels, the type of singularity distribution, and an appropriate density of panels in areas of interest. However, increased accuracy incurs a higher computational cost.

Initially, the corner points of the quadrilateral panels are defined using an input file containing the wind tunnel geometry. The control point of each panel is then determined as the intersection of panel's diagonals. The matrix of influence coefficients is then calculated by summing the induced effects of all panels at each control point. Again in this case, as in the two-dimensional panel method, the boundary condition imposed at each control point is the Neumann boundary condition, which enforces zero normal velocity on the body's surface. The ambient flow conditions are then applied to give the total onset velocity at each panel's control point due to the freestream. This is calculated from conservation of mass applied to each cross section of the wind tunnel based on a given working section velocity. This results in a set of simultaneous linear equations, which are then solved for the source strength at each panel's control point.

The vortex generator blade is modelled using lifting line theory, with the lifting line located at the quarter chord of the blade. The blade is discretized into multiple sections and the bound vorticity for each section is determined from two-dimensional lift curve data. The generation of trailed vorticity in the wake of the vortex generator results from calculating the differences in bound vorticity between adjacent blade sections and the differences in bound vorticity at each blade section from one time step to the next produce the shed vorticity. A free vortex wake from the vortex generator is built up by the blade trailing and shedding vortex elements at each time step.

The convection of these wake elements is then dependent on the free wake analysis. This allows the 'natural' convection of every element dependent only on the local flow conditions. The local flow conditions are calculated the onset freestream velocity, the induced velocity from the source panel distribution and the induced velocity from every vortex element in the wake and on the blade. The induced velocity from the free wake lattice is calculated by applying the Biot-Savart equation repeatedly to assess the contribution of every vortex element at every control point in the wake. Therefore, the total number of computations required to resolve the induced velocity at a point increases with every time step iteration of

the model. The displacement of every wake element at each time step is determined by a second order Adams-Bashforth multi-step integration (Coton et al, 1994)

The strengths of the sources representing the wind tunnel walls require re-calculation at each time step as the onset velocity at each control point will be affected by the induced flow from the vortex generator and the free wake lattice of shed and trailed vorticity.

7.3 Simplifications

Copland's implementation of the numerical simulation featured some simplifications to reduce the computational time required to calculate the wake simulation. A fully coupled simulation would have required an iterative calculation of the effect on each panel of every wall panel and each vorticity element at every time step. Copland, however, only solved the 3D source panel distribution at the first time step before the creation of any vorticity nodes and re-used the same source strength distribution for all future time steps. Copland assessed that this shortcut would not significantly affect the predictive qualities of numerical simulation and demonstrated this via the tip vortex shape prediction already presented (shown again in Figure 7.2).

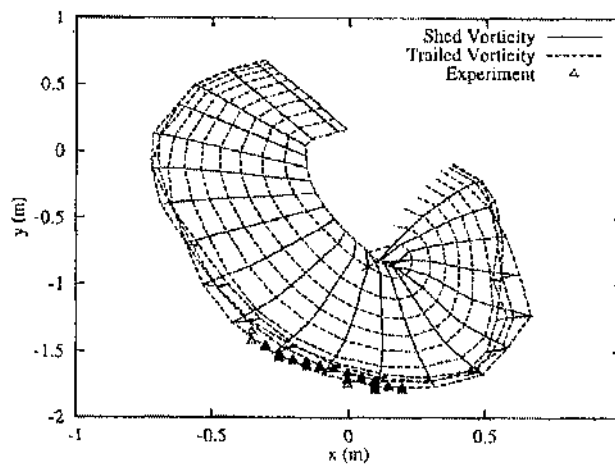


Figure 7.2: Comparison of numerical wake simulation and experimental measurements of wake shape

The other simplification implemented by Copland, was a reduction in the number of calculations to establish the induced velocity at any wake node. As stated previously, the velocity is dependent on all the other vorticity elements and each of the source panels. However, the induced velocity varies with the inverse of the square of the distance between the element and the velocity evaluation point. The induced velocity due to a far away element is minimal compared to that from a closer element. Copland, therefore, established a separation limit that prevented the calculation of the induced velocity from a vortex element if it was too far away from the evaluation point. Copland experimented with this limit until it was possible to significantly reduce the number of calculations required without affecting the accuracy of the numerical simulation (Copland, 1995, Copland, 1997).

7.4 Required Extensions to the Numerical Simulation

The numerical simulation simulates the generation of vorticity by a rotating blade in the settling chamber, and the convection of the vorticity from the wind tunnel contraction to the working section. The simulation does not feature the interacting blade in the working section. To use the numerical simulation with the Beddoes indicial model, the horizontal cross flow velocities at the blade from the numerical simulation must be extracted to drive the indicial model predictions of the resultant normal force response of the interacting blade.

As the indicial model shape functions are built on thin-aerofoil theory, a single line of points coincident with the interacting blade's chord replaced the interacting blade. At each of these points, the local flow velocity can be calculated in exactly the same way as for each of the vorticity nodes in the free wake. The total velocity will be the sum of the contributions from each of the wind tunnel wall source panels, and the Biot-Savart calculations of the flow from each vortex element.

The number of points required to accurately calculate the velocities needed for the indicial model is determined by the number of Simpson segments in the indicial calculation. To

accommodate the different distribution of points along the chord line used for the circulatory and impulsive shape functions, the number of points along the chord line at which induced velocity was evaluated was equal to approximately twice the number of Simpson segments. For 30 Simpson segments, 31×2 points are required along the chord line. Figure 7.3 shows a simplified comparison of a blade with 11 points, and the locations of the points as defined by the circulatory shape function and 11 points as defined by the impulsive shape functions, for 10 Simpson segments.

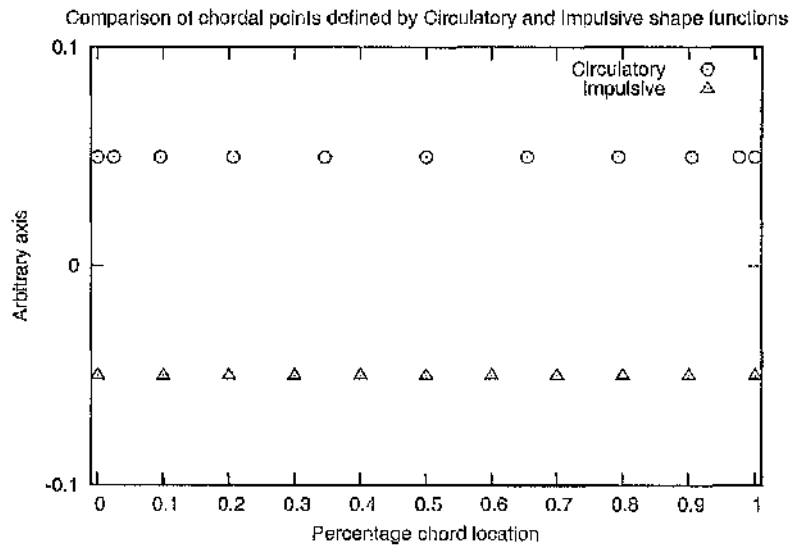


Figure 7.3: Comparison of chord locations from Circulatory and Impulsive shape functions

It should be noted here that in this form the simulation does not calculate the impact of the interacting blade on the induced flow field. This simulation should, nevertheless, provide a good approximation to the cross flow experienced by the blade.

One other adjustment that had to be made to the numerical model was the extension of the wall constraint beyond the wind tunnel's working section length. Doolan et al. (1999) (Figure 7.2) documented the close agreement of the numerical simulation's predicted wake shape to experimental measurements, however, this was only for the first wake generated by the vortex generator. It is clear from plots of the vortex wake shape (Figure 7.4) that the second wake is close behind the first wake and may experience an induced velocity component from the first wake and consequently the second wake may more accurately capture the horizontal cross flow velocities experienced by the interacting blade in the experiment.

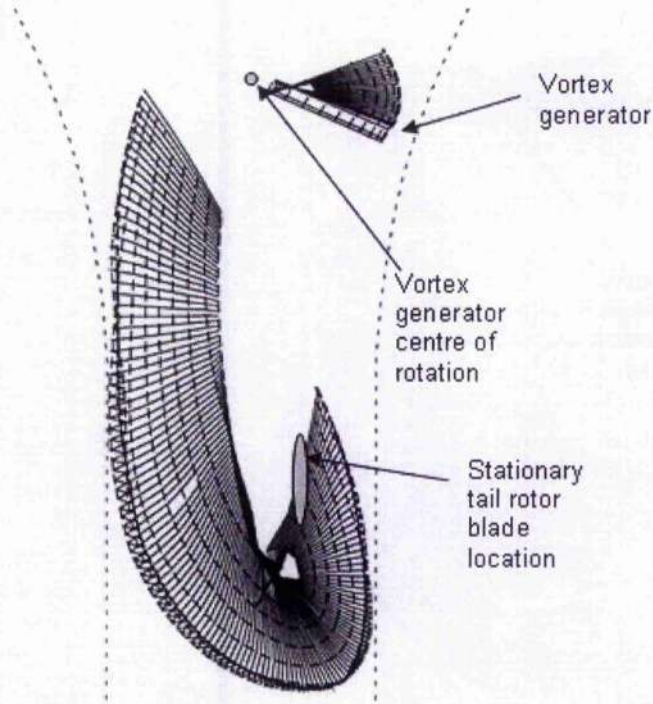


Figure 7.4: Plan view of wind tunnel contraction and working section showing close proximity of subsequent wakes.

Before using the horizontal cross flow velocities predicted by the method as input to the indicial model, the convergence characteristics of the method and a sensitivity study of the temporal resolution was carried out.

7.5 The Effect of Multiple Wake on Induced Velocity

Convergence

To investigate the response of the interacting blade to the wakes produced by the second, third, fourth and fifth rotations of the vortex generator, an extension to the length of the simulated wind tunnel was required. The numerical simulation required that every vorticity node be located within the start and end of the wind tunnel source panel representation. Therefore, additional panel co-ordinates were used to extend the length of the working section. An incremental increase in the wind tunnel length was employed until the induced velocity variation on the blade due to the passage of a tip vortex system had converged.

It was found that by extending the wind tunnel section to allow the wake produced by the third rotation of the vortex generator pass the location of the interacting blade, convergence of the induced horizontal cross flow velocity was achieved. Figure 7.5 shows the difference in simulated horizontal cross flow velocities between the passage of the fourth wake and the first, second and third wakes.

Figure 7.5 is from the numerical simulation data set where the azimuthal step size was 1 degree. This is the smallest azimuthal step size used in these tests. The other azimuthal step sizes that were investigated were 8, 4, and 2 degrees. Appendix C (Velocity 40 m/s section) shows that, regardless of which step size was chosen, the third wake was the first to reach a converged state.

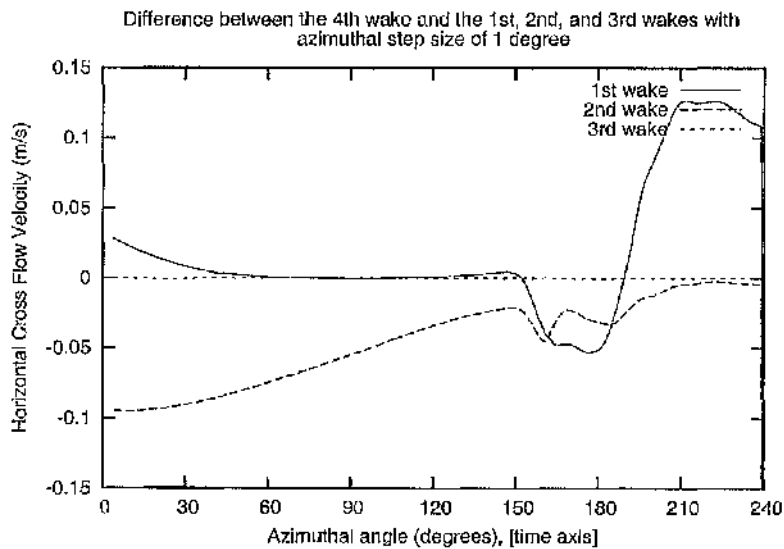


Figure 7.5: Comparison of 4th wake with 1st, 2nd and 3rd.

The default step size defined in the original code was a time step size of 0.01, which was equivalent to just over 2 degrees azimuthal step size. Larger azimuthal step sizes were attempted to potentially reduce the running time of the numerical simulation. The extended wind tunnel uses more panels and, due to the extended length, more time steps. The increase in the number of time steps means that the number of vorticity elements in the wind tunnel will also increase, and the number of calculations required to determine the induced velocity for each of these vorticity elements exponentially increased with each time step.

Therefore in the later stages of the simulation the calculation time for each time can be very long in comparison to time steps earlier in the simulation.

The generation of four wakes with a one-degree azimuthal step size required a considerable time to complete. Decreasing the azimuthal step size below one degree would have required more than doubling the total computational time to complete the numerical simulation. For this reason, a one-degree azimuthal step size was set as a lower limit to ensure that simulations could be completed in an acceptable time frame.

One of the typical ways to identify the location of a tip vortex in a flow is to either measure the rotational or the axial velocities. In this case, the effect of temporal resolution on the axial velocity at the location of the interacting blade leading edge was used as the indicator that a suitable time step was being used.

	1st wake	2nd wake	3rd wake	4th wake
8 deg.	1.1334	1.1651	1.1168	1.1164
4 deg.	1.1947	1.2414	1.1799	1.18
2 deg.	1.2499	1.2839	1.2364	1.2362
1 deg.	1.28	1.3187	1.267	1.2689

Table 7.1: Comparison of peak axial velocity measured in all test cases at the spanwise location of the vortex centre.

Table 7.1 shows the maximum measured axial velocity for a range of time step sizes and wake passages. By examining the peak axial velocity measured for each of the passages it is clear that the peak velocity is increased with increased temporal resolution. This indicates a potentially more accurate simulation could be achieved by increasing the temporal resolution further by decreasing the azimuthal step size. It is interesting to note, however, that progressive halving of the time step produces progressively smaller changes in peak axial velocity. The magnitude of the increase in peak axial velocity is likely to continue to decrease with increasing temporal resolution, and will probably slowly asymptote to a fully resolved value.

7 Numerical Simulation of the Experimental Flow Field

	1st wake	2nd wake	3rd wake	4th wake
8 deg	0.9446	0.973	0.9791	0.979
4 deg	0.922	0.9518	0.9593	0.9593
2 deg	0.9198	0.9547	0.9642	0.9641
1 deg	0.9151	0.9526	0.9617	0.9616

Table 7.2: Comparison of peak axial velocity measured in all test cases at the spanwise location 0.1m above the vortex centre

Further comparisons demonstrating the effect of azimuthal step size are shown in Tables 7.2 and 7.3. These comparisons also show that an increasingly accurate numerical solution can be obtained by increasing the temporal resolution. However, as noted above, the extension in the computational time is not warranted as the inviscid numerical simulation is a limited approximation that will never fully resolve the detailed structure of the local cross-flow.

The main focus of the indicial model comparisons with the experimental data has predominantly been the forty metres per second case. However, the twenty, thirty, and fifty metres per second cases have also been examined. A similar analysis of the effect of extending the numerical wind tunnel to accommodate the wake from four rotations of the vortex generator altering the temporal resolution was also completed for these cases. Appendix C shows comparisons of the induced velocity from the fourth wake with that of the first, second and third wakes, and the variation of peak axial velocity for the twenty, thirty and fifty metres per second cases for a range of azimuthal step sizes.

	1st wake	2nd wake	3rd wake	4th wake
8 deg	0.8209	0.8373	0.8571	0.8572
4 deg	0.9618	0.9638	1.0026	1.0023
2 deg	0.9952	1.0045	1.0398	1.0397
1 deg	0.9882	1.002	1.0352	1.0351

Table 7.3: Comparison of peak axial velocity measured in all test cases at the spanwise location 0.1m below the vortex centre

The conclusions that were drawn for the forty metres per second case can also be drawn for the twenty, thirty and fifty metres per second cases. An increasingly more resolved simulation is achieved by decreasing the azimuthal step size. This was identified, as before, by examining the peak axial velocity found at the location that would be occupied by the interacting blade's leading edge at a spanwise location where the vortex centre of the wake passes. The increase in the magnitude of the peak maximum axial velocity achieved by

reducing the time step is small. Potentially, smaller incremental improvements could be found by increasing the temporal resolution further, however, as the numerical simulation will, at best, only be representative due to its inviscid nature, the increase in computational time is not justified as it will not significantly improve the accuracy of the simulation. Also, as with the forty metres per second case, the induced velocity during the passage of the fourth and third wakes are almost identical, indicating that the wake produced by the third rotation of the vortex generator is the first steady wake generated by the numerical simulation. Therefore, to keep the computational time required to complete the numerical simulation to an acceptable time frame, the 2 degree azimuthal step size and the 3rd wake were chosen for the full simulation cases.

A final important observation is that the wake shapes produced by the first and third rotations of the vortex generator are very similar (Figure 7.6). The difference in the velocities measured at the location of the interacting blade results from the induced effect of the additional wake vorticity fore and aft of the cycle passing the interaction location.

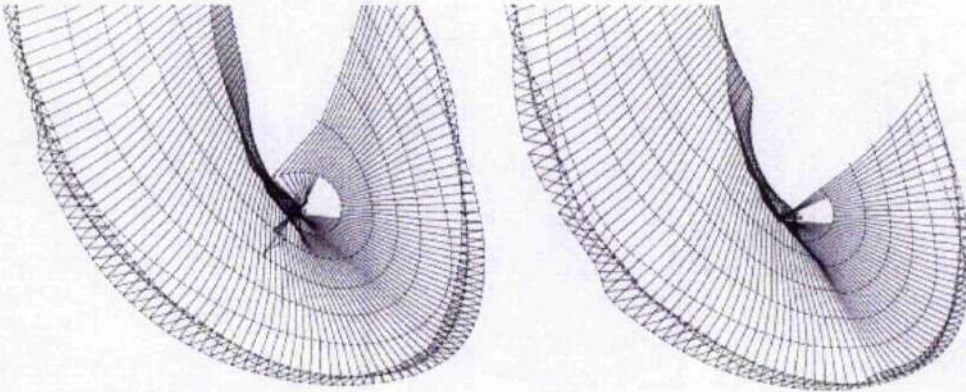


Figure 7.6: Comparison of 1st and 3rd wake shape

7.6 Summary

This chapter's focus was the identification of horizontal cross flow at spanwise locations away from the vortex centre. Figure 7.7a, b show the calculated values of the horizontal

cross flow for the 40m/s case and it is already possible to see similar trends to those observed in the normal force data. There is a sharp increase in axial flow at spanwise locations near the centre and below (-0.1 m), and also a more gentle, slow build in axial flow above the vortex centre (0.1 m). This is an important observation and suggests that indicial modelling based on this calculated axial flow may improve the modelling of the normal force response. The following chapter details the indicial modelling using the simulated horizontal cross flow velocities extracted from the numerical simulation.

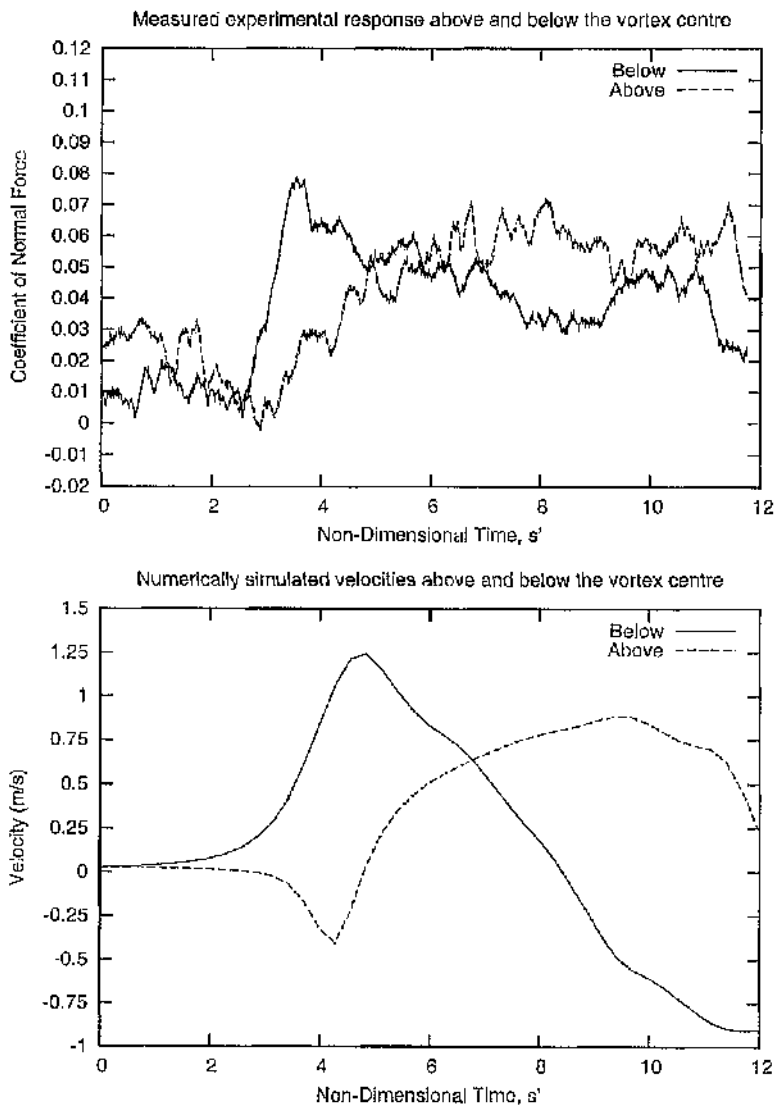


Figure 7.7: Comparison of (a) measured experimental response and (b) numerically simulated velocities, above and below the vortex centre

8 Results from Numerical Simulation of Wind Tunnel

It has been shown that by using the wake produced by the third rotation of the vortex generator and an azimuthal step size of 2 degrees, the numerical simulation output, in terms of maximum measured horizontal cross flow velocity, is satisfactory. This temporal resolution is considerably less than that used in the indicial model based on the Lamb type vortex. This is due to the sharp nature of the axial velocity profile in the prescribed vortex model compared to the velocity profile extracted from the numerical simulation (Figure 8.1). Therefore the time step size can be decreased when modelling the response to the horizontal cross flow velocities because the velocity profile is considerably less impulsive.

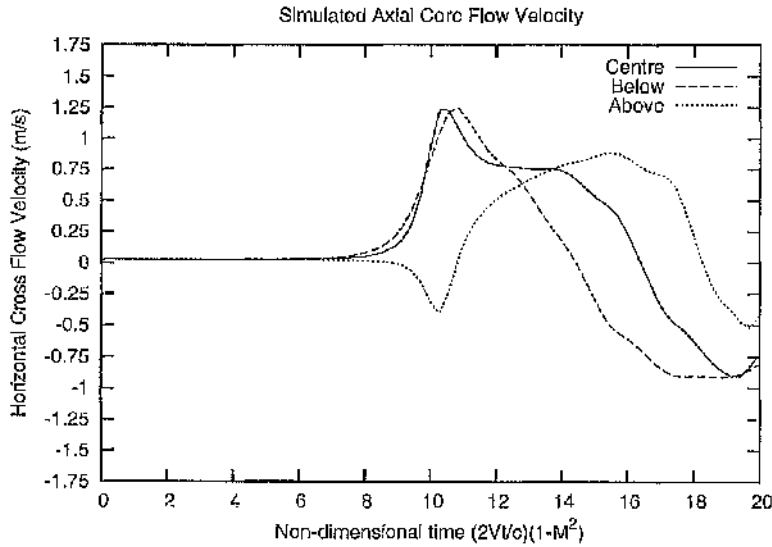


Figure 8.1: Simulated Axial Velocity Profile

Velocity	dt	ds'
20	0.001984	0.287602
30	0.001323	0.286353
40	0.000992	0.284606
50	0.000794	0.282359

Table 8.1: Numerical Simulation ds' variation with velocity

Table 8.1 above shows the respective time steps (dt) for each velocity case. The corresponding non-dimensional time step (ds') is approximately $0.285\beta^2$ at each velocity. Therefore sampling the data at $0.01\beta^2$ as in the prescribed velocity case is unnecessarily time consuming. It was found that by sampling at $0.1\beta^2$ a fully resolved indicial prediction is

calculated. This is still a higher sampling rate than the input data, the numerical simulation velocity data in this case, and therefore simple linear interpolation was employed to find the horizontal cross flow required by the indicial model sampling rate.

Figure 8.1 shows the axial velocity history, for the 40m/s case, from the numerical simulation calculated at the vortex centre, at one vortex core radius below the vortex centre, and at one vortex core radius above the vortex centre. The horizontal cross flow velocity profile calculated by the numerical simulation, at one core radius below the vortex centre, features a similar peak to that at the vortex centre. This would explain the similar magnitude of dC_n response found at and below the vortex centre. Also, the decrease in axial velocity after the impulsive peak is slower than the initial increase in both these locations. This differs from the symmetric prescribed axial core of the Lamb type vortex.

Figures 8.2, 8.3, and 8.4 show the comparisons of experimental data against the predicted lift response, for freestream velocity of 40m/s, at the vortex centre, below, and above respectively for the corresponding cross flow velocity profiles shown in Figure 8.1. A full series of the predicted responses for each spanwise location together with their respective experimental comparisons is present in Appendix D. This includes the comparisons for 20, 30 and 50 m/s. An artificial time shift has been applied to bring the indicial lift response

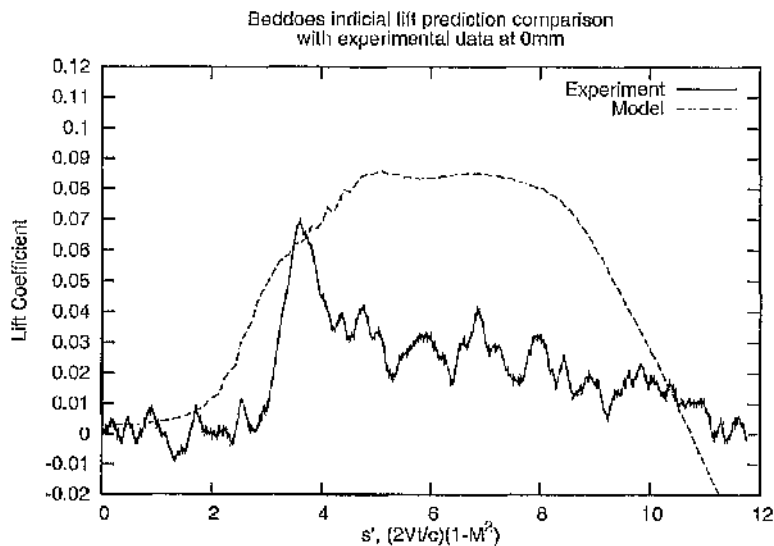


Figure 8.2: Indicial Model Response to Simulated Axial Velocity Profile at Vortex Centre

peaks, on average across the fifteen figures, in line with the corresponding peaks in the experimental data for each separate freestream velocity. Also, the experimental data and indicial predictions are shifted down so that each data block's impulsive interaction starts approximately from zero.

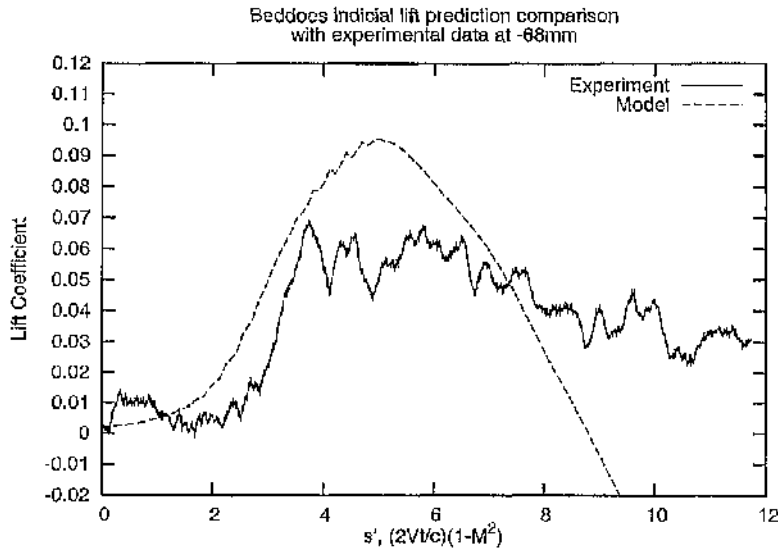


Figure 8.3: Indicial Model Response to Simulated Axial Velocity Profile Below the Vortex Centre (One vortex core radius below in the spanwise direction)

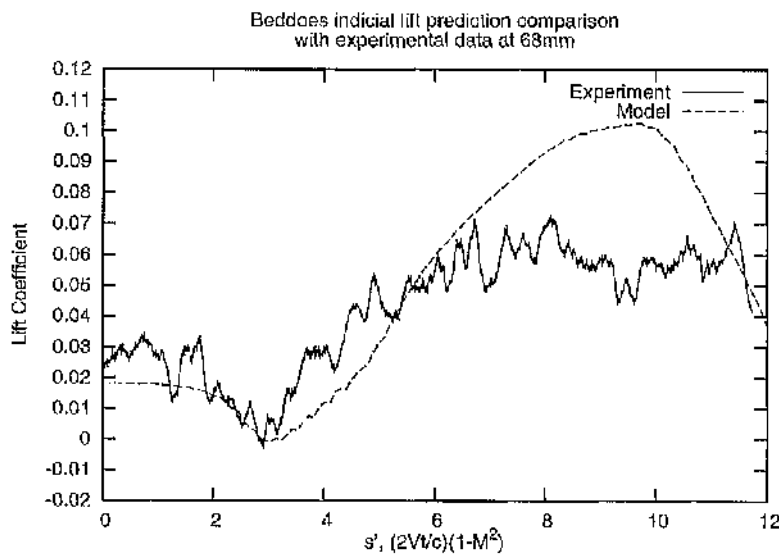


Figure 8.4: Indicial Model Response to Simulated Axial Velocity Profile Above the Vortex Centre (One vortex core radius above in the spanwise direction)

The most significant observation that can be made from the Figures 8.2, 8.3, and 8.4 is the shape of the cross flow velocity profile in Figure 8.4 at one vortex core radius above the vortex centre. This shows smaller and more gradual variations in cross-flow velocity than at

the vortex centre and below. This variation is consistent with the measured blade response for the spanwise location one core radius above the vortex centre.

In general the indicial predictions reproduce the approximate magnitude of the experimental data at all spanwise locations. However, the sharpness of the impulsive rise at the vortex height and below has not been captured as well as with the prescribed indicial prediction, and also, the magnitude of all responses is generally higher than the experimental data at all spanwise locations.

The lack of agreement in the sharpness of the increase in normal force may partially be explained by the lack of resolution in the free wake code near the vortex centre. The axial core velocity rise in the experiment happens over a length scale which is much shorter than the vortex spacing in the free wake code.

The over prediction of the magnitude of the impulsive interaction at all locations may be due to the inviscid incompressible nature of the numerical simulation. Using the numerically simulated velocity data it was possible to calculate the tip vortex circulation strength at the interacting blade location during the interaction. Figure 8.5 shows the variation in circulation

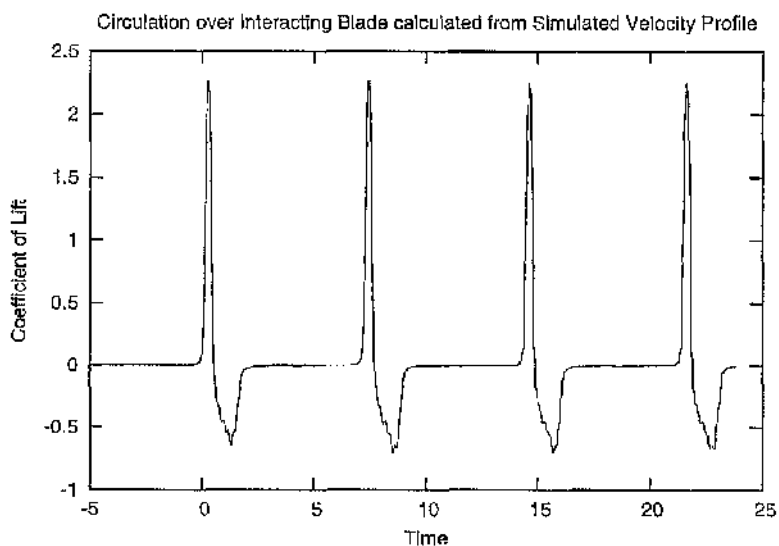


Figure 8.5: Circulation over Interacting Blade at 40m/s.

calculated from the numerical simulation. This figure shows that the peak circulation

calculated at the blade location is approximately $2.26\text{m}^2/\text{s}$ for the 40m/s case. This is substantially higher than the experimentally measured value of $1.26\text{m}^2/\text{s}$.

During the collection of the experimental data, it was observed that blade flapping may have occurred at the high rotational rate required for the wind tunnel velocity set at 50m/s . Potentially, some degree of blade flapping may also have occurred at 40m/s . This may have resulted in the blade experiencing a lower angle of attack than intended. In addition, the inviscid model does not allow for vortex dissipation or viscous flow separation on the vortex generator blade. All of these factors may have contributed to the experimentally measured vortex strength being lower than that predicted by the model.

To investigate this, the peak vortex generator angle was reduced so that the circulation of the generated tip vortex was reduced. Table 8.2 shows the peak calculated circulation of the tip vortex at the interacting blade for different peak angles of incidence of the vortex generator blade. A reduction of the peak angle to 6 degrees results in the simulated peak circulation closely approximating the experimentally measured circulation.

Peak Vortex generator angle (degrees)	Circulatory (m^2/s)
10	2.26
8	1.85
6	1.39

Table 8.2: Peak Circulation variation with peak vortex generator angle of incidence for freestream velocity of 40m/s . (Experimental Circulation = 1.26 ± 0.25)

Appendix E shows that using this case as input to the indicial calculation the magnitude of the normal force response is reduced as expected at all spanwise locations. In line with previous calculations, the sharpness of the impulsive response is also not as sharp as the experimental data. The indicially predicted responses at spanwise locations above the vortex centre at a distance of one core radius (76mm) or more are now more accurately predicted with a close agreement in shape and magnitude as shown in Figure 8.6. Appendix E also contains calculations of circulation strengths for the other freestream velocity cases of 20 , 30 and 50m/s . In all cases, the use of blade incidence values that produce circulation strengths close to those measured in the experiment improve the level of agreement between the indicial predictions and the experiment.

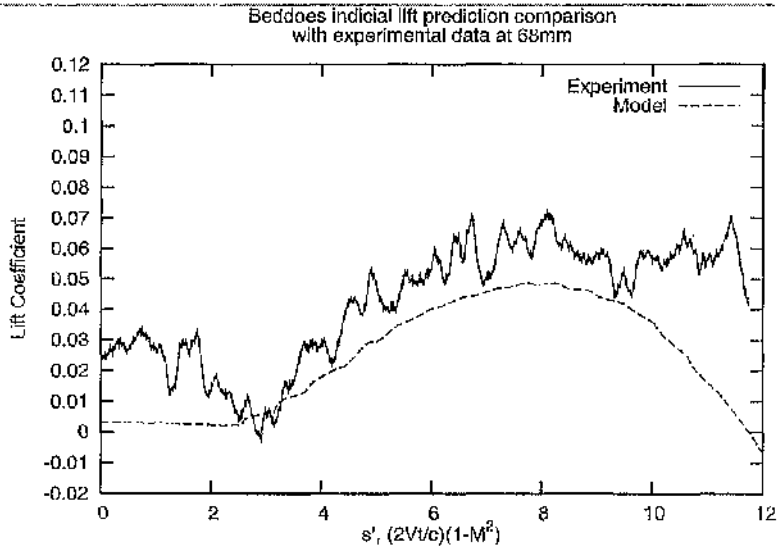


Figure 8.6: Indicial Response from Simulated Velocity Profile with Vortex Generator Peak Angle of Incidence set to 6 Degrees. Velocity = 40 m/s

8.1 Summary

Numerical predictions based on the horizontal cross flow extracted from a numerical simulation of the experiment reproduce the asymmetry found in the experimental data. This is particularly evident at spanwise locations above the vortex centre where a more gradual slow build in blade response is found. In general, the predicted response found was excessive at all spanwise locations compared to the experimental data. The over-predicted response may have been due to the inviscid, incompressible nature of the numerical simulation, or a degree of blade flapping observed to occur in the experimental data for high rotational speeds of the vortex generator.

Circulation calculations for the tip vortex in the model indicated that a vortex of greater circulation was present in the numerical simulation. A crude technique, whereby the strength of the vortex was decreased by decreasing the angle of incidence of the vortex generator until the strength of the vortex was closer to the experimentally measured magnitude, resulted in more accurate indicial predictions in terms of the magnitude of blade response.

Figure 8.7 shows the average change in normal force for all spanwise locations extracted from the experimental data, the indicial predictions based on the Lamb-type vortex, the indicial predictions based on the horizontal cross flow extracted from the numerical simulation, and the indicial predictions based on the horizontal cross flow extracted from the numerical simulation with a reduced angle of incidence of the vortex generator so that the circulation is equivalent to the experimentally measured circulation. The figure shows that the indicial predictions based on the prescribed Lamb-type vortex, unlike the experimental data, are symmetric away from the vortex centre, whereas, the indicial predictions based on the horizontal cross flow exhibit the same basic trend with spanwise location as the experimental data although the magnitudes are different.

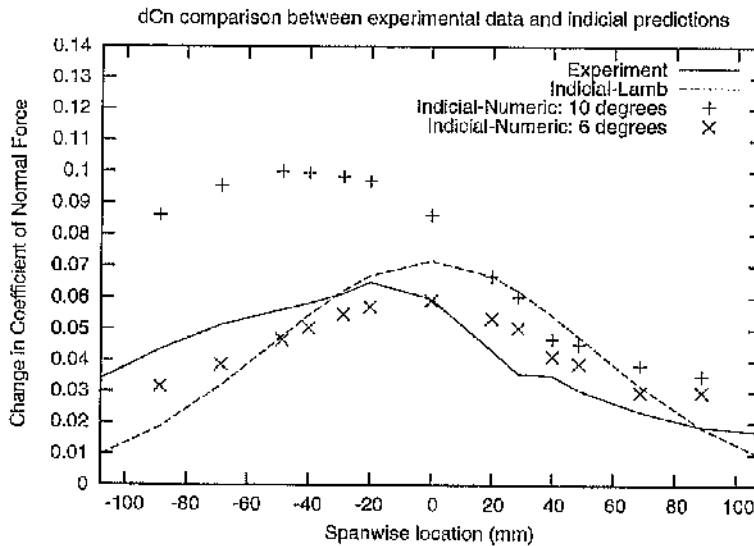


Figure 8.7: dC_n comparison of experimental data and indicial models across all spanwise locations

The over prediction below the vortex centre when the generator blade was set at 10° is eliminated when the blade incidence is reduced to 6° . For this case the level of agreement with the experimental data above the vortex centre is also improved. Looking, however, at the difference between the two blade settings, it appears likely that a blade setting of somewhere between 6 and 10 degrees would yield better agreement overall.

9 Comparison of Indicial Model with other Experimental and Computational Sources

Previous chapters have demonstrated the ability of indicial modelling to reproduce the trends in the experimental data from the large wind tunnel at the University of Glasgow. This chapter presents comparisons with other experimental and computational sources. As previously discussed data were also collected during an earlier feasibility test in a smaller wind tunnel at the University of Glasgow. Indicial predictions of the orthogonal interaction in the small wind tunnel are now presented.

9.1 Small Wind Tunnel Experimental Data (Anatomy Wind Tunnel, University of Glasgow)

Vortex Generator Radius (m)	0.75
Vortex Generator Chord (m)	0.1
Aerofoil profiles	NACA 0015
Distance from vortex generator hub to interacting blade leading edge (m)	2
Vortex Generator rotational rate (rpm)	500
Interacting blade Reynolds number	200000
Vortex Core Radius (m)	0.066 ± 0.031
Ratio of Axial Velocity to Freestream Velocity	0.4 ± 0.12
Freestream velocity (m/s)	20

Table 9.1: Anatomy wind tunnel parameters

Table 9.1 details the parameters governing the wind tunnel configuration and the measured incident tip vortex for the tests in the small wind tunnel.

Figure 9.1 shows a comparison between the experimentally measured normal force response of the interacting blade and the indicial prediction of the interaction using a prescribed Lamb-type vortex with parameters matching those in Table 9.1. An approximate synchronization is applied as there was no information detailing the progress of the vortex, from the experiment data, in the timeframe that was recorded for each interaction. However, generally the timeframes are synchronized using the initial peak in normal force as a reference point.

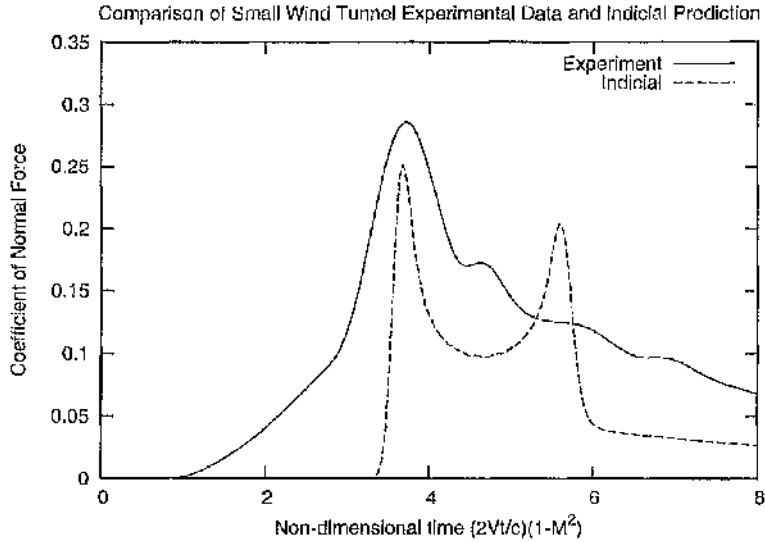


Figure 9.1: Comparison of small wind tunnel experimental data and the indicial prediction of the experiment using a prescribed Lamb type vortex axial velocity profile. The spanwise location of the interaction is the location where the vortex centre passes.

A similar magnitude of response is obtained although the indicial response features two significantly sharper peaks in normal force compared to the single peak found in the experimental data. The two peaks in the indicial prediction are due to the impulsive and circulatory responses respectively. Due to the smaller ratio of vortex core size to interacting blade chord, and the low freestream velocity, the impulsive and circulatory responses produce a combined output with two distinct peaks. The sharpness of the circulatory and impulsive responses can be understood by examining the difference in the initial peak simulated by the indicial prediction and the peak in the experimental data.

The indicial model was 'forced' by the shaping function and ultimately by the axial velocity distribution. Figure 9.2 shows the axial velocity profile of the Lamb-type vortex. The axial velocity varied inversely with radial distance from the vortex centre. At approximately two vortex core radii from the vortex centre, the axial velocity has reduced to approximately zero. Therefore, the Indicial model will predict zero normal force until the vortex centre is within two core radii of the interacting blade leading edge.

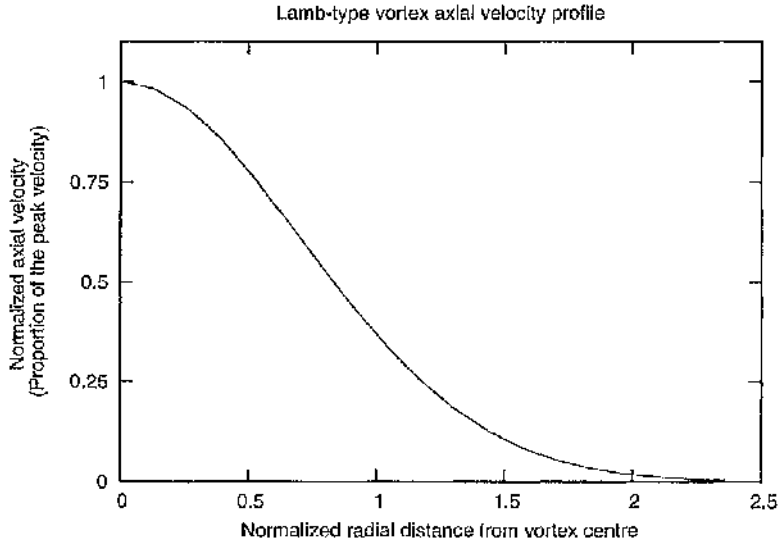


Figure 9.2: Lamb type vortex axial velocity profile

Approximate time points have been added to Figure 9.3, which is a copy of the original comparison in Figure 9.1. Position A indicates the predicted point in time when the vortex centre interacted with the leading edge of the interacting blade. Position B indicates the point in time two-vortex core radii of travel before this according to the parameters in Table 1. However, the normal force in the experimental data begins to increase in magnitude much earlier. This potentially indicates that the two-vortex core radii position B should actually be closer to position C.

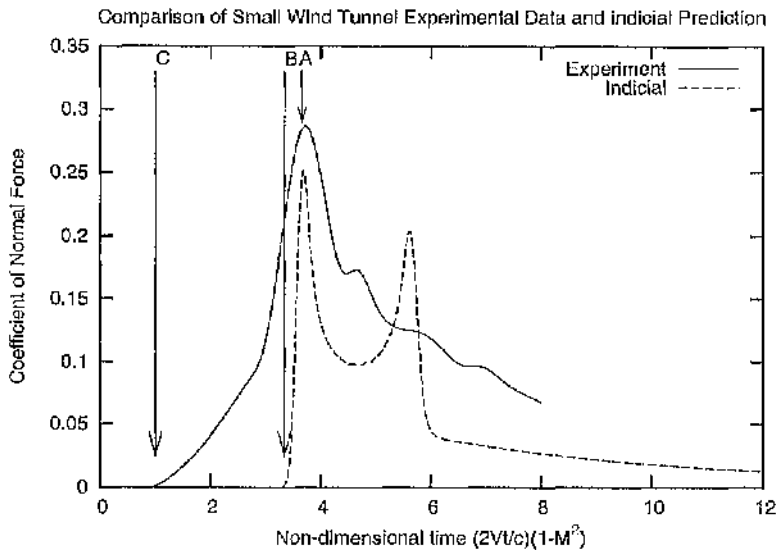


Figure 9.3: Figure 9.1 with markings A, B, and C.

Figure 9.4 shows the indicial prediction based on a two-vortex core radii parameter determined from position C. This results in a vortex core radius of 0.091m that is approximately 10 times larger than the experimentally measured value. The peak normal force magnitude is now approximately four times the magnitude of the peak normal force in the experimental data. In Figure 9.5 the magnitude of the response has been scaled down by 25% to allow a comparison of form. This shows that the shape of the response with the larger vortex core radius is now much more similar to the experimental data.

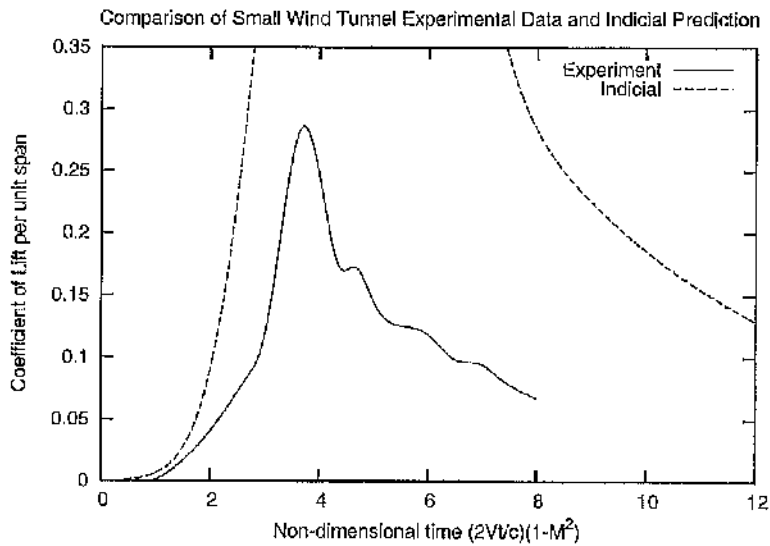


Figure 9.4: Comparison of experimental data with indicial prediction using a prescribed vortex core model with a vortex core radius of 0.091m

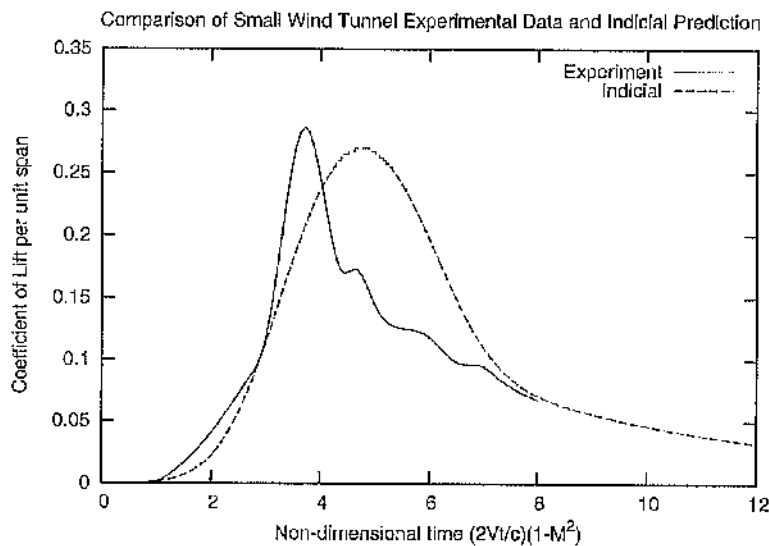


Figure 9.5: Comparison of experimental data and indicial model with core radius of 0.1 m, with lift coefficient plotted at 25% of original magnitude.

Doolan et al (2001) collected the experimental data in the small wind tunnel primarily from pressure transducers on the surface of the interacting blade. The samples were examined for representative data and it is the selected 'representative data' that were presented in the publication. The selection of representative data samples was necessary due to the large tip vortex wander that occurred in the tunnel. The wander was measured at approximately 19% of the interacting chord, approximately 0.028956m. Therefore the magnitude of the measured wander is very large in comparison to the measured vortex core radius of 0.009906m. Consequently, the selection of representative data would have been problematic. A possible explanation for the disparity between the indicial prediction and data may be found in the experimental configuration, for which a detailed description of the configuration is given by Copland (Copland, 1995(dept report), Copland, 1995b (thesis)). The main problem associated with the small wind tunnel configuration was that the spring used to enforce the pitch profile was prone to failure. This factor, combined with the problems associated with vortex wander, may have contributed to poor data quality and repeatability. Given the trends exhibited in Figures 9.3 - 9.5 it is likely that a good fit with the experimental data could have been achieved by further variations in the vortex core radius and axial flow velocity in the indicial model. Whilst this is interesting, it merely suggests that this set is unreliable and has little value as a validation source.

It is also worth noting that no account has been taken of induced cross-flow in the wind tunnel. As seen previously for the large wind tunnel, this can be influential away from the vortex centre. It is also possible that it may have had an influence at the vortex centre height in this experiment.

9.2 Liu and Marshall Computational Study

Liu and Marshall (2004) conducted a computational study that investigated the orthogonal blade vortex interaction with an initially columnar vortex in a viscous fluid. The study

investigated the interaction of vortices with and without axial core flow for high impact parameter interactions where secondary vorticity is not ejected from the blade boundary layer before the vortex core impacts on the blade leading edge. The study investigated a large variation of axial core flow magnitudes.

Liu and Marshall compared their calculation with the experimental data of Wang (2002) (Figure 9.6), which is the primary experimental data source used in this work. All parameters were given in non-dimensionalized form by Liu and Marshall, and therefore required conversion into dimensional values for the existing indicjal model. The experimental parameters taken from Wang by Liu and Marshall are from the fifty metres per second case. The selection of freestream velocity equal to 50 m/s and chord equal to 0.275m, as per Wang, resulted in the following dimensionalized parameters (Table 9.2).

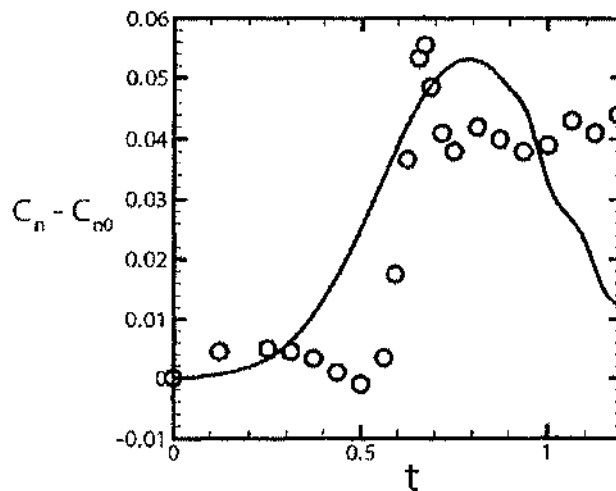


Figure 9.6: Comparison of coefficient of lift per unit span at the vortex centre calculated by Liu and Marshall with Wang's experimental data (Case B3) (Liu and Marshall, 2004).

The parameters chosen by Liu and Marshall are within the limits of measured experimental parameters. The one potential anomaly is the kinematic viscosity. Standard atmospheric kinematic viscosity is $0.0000145\text{m}^2/\text{s}$, which is considerably lower than the value determined by Liu and Marshall's non-dimensionalized parameters. However, for the purposes of prediction of the blade response, the indicjal model requires only the freestream velocity, the peak axial velocity, the blade chord, and the vortex core radius. Figure 9.7 shows a

comparison of the coefficient of lift per unit span between Wang's experimental data, Liu and Marshall's computation, and the indicial prediction.

Case	B3 (Liu & Marshall)	B3 (Wang)
IP	41	36.84
TP	0.42	0.457
Re _v	44	-
AFP	1.8	1.62
Re _g	1000	-
Kinematic Viscosity	0.1375	-
Freestream velocity (m/s)	50	50
Chord (m)	0.275	0.275
Peak Axial Velocity (m/s)	2.195122	2.2 ± 0.2
Vortex Core Radius (m)	0.078571	0.09030 ± 0.04932
Circulation (m ² /s)	0.60204	0.77 ± 0.27

Table 9.2: Comparison of Wang's published parameters and the parameters used by Liu and Marshall (2004)

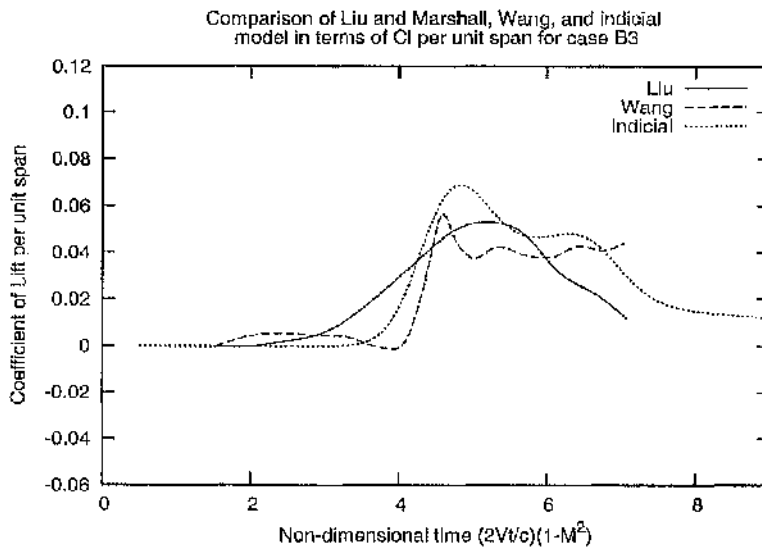


Figure 9.7: Comparison of 50 m/s experimental case from Wang, with indicial prediction and Liu and Marshall's computation of this case.

The Liu and Marshall computation predicts a similar magnitude when compared to the experimental data. However, the indicial model provides a better comparison, capturing the sharpness of the initial response more accurately. Both computations fail to capture the interaction after the initial impulsive increase in lift, however, it was demonstrated in the previous chapter that this was potentially due to differences in the tip vortex shape and or the presence of the trailing vortex sheet.

Liu and Marshall created a set of cases to allow them to gain an understanding of the influence of Impact Parameter, Axial Flow Parameter, Vortex Reynolds Number, and the Thickness Parameter. These cases were enumerated from B1 to B10 (Table 9.3).

Case	IP	TP	Re _v	AFP	Re _b
B1	4	0.78	488	0.51	2000
B2	10	0.56	45	0.85	1000
B3	41	0.42	44	1.8	1000
B4	4	0.78	488	3.8	2000
B5	4	0.78	245	3.8	1000
B6	4	0.78	73	3.8	300
B7	4	0.78	488	3	2000
B8	16	0.37 (0.78)	250 (488)	3	2000
B9	33	0.37 (0.78)	125 (488)	3	2000
B10	4	0.39 (0.38)	968 (488)	3.8	2000

Table 9.3: Table 1 from Liu and Marshall detailing the non-dimensional parameters governing the B Cases (2004)

The array of cases calculated by Liu and Marshall demonstrated an almost linear relationship between axial flow parameter and total non-dimensional lift evaluated across the span of the blade (Figure 9.8). They and showed that when also a new universal lift coefficient was plotted against non-dimensional time (Figure 9.9) all of the results collapsed onto one curve. The new universal lift coefficient is:

$$C_L'' = L / \pi \rho U w_0 \sigma_0^2 \quad (9.1)$$

The cases where axial flow was present in the Liu and Marshall calculations were calculated using the Beddoes indicjal model with a prescribed Lamb type vortex distribution for axial velocity. The parameters governing the calculations are given in Table 9.3. In some cells in Table 9.3 there are also figures in brackets. The figures without brackets indicate the correct parameters, while the figures in brackets, where present, indicate erroneous data published in Liu and Marshall (2004). The authors updated the published values with corrected values after an inconsistency was identified.

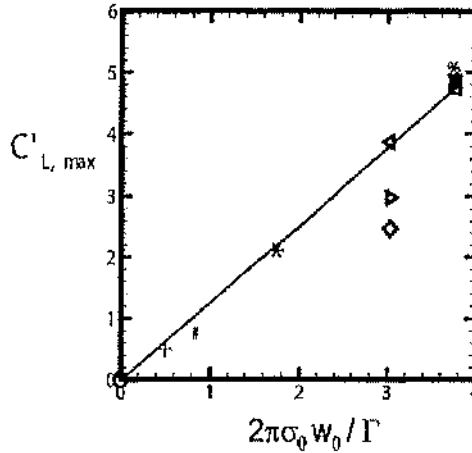


Figure 9.8: Fig 25a from Liu and Marshall (2004). Shows almost linear relationship between $C'_{L, \max}$ and axial core flow

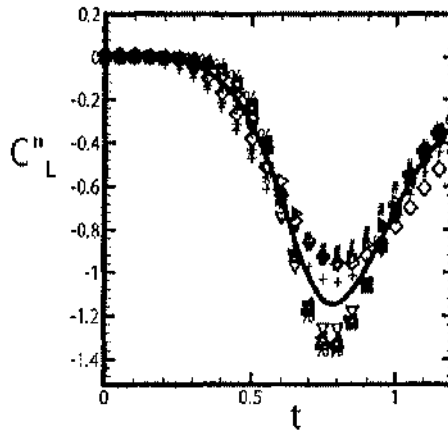


Figure 9.9: Figure 25b from Liu and Marshall (2004) shows the variation of their new universal lift coefficient (C''_L) with time

The indicial predictions of the total spanwise lift across the interacting blade in Liu and Marshall Cases B1-10 required the spanwise integration of the lift per unit span predictions produced by the indicial method. The lift across the span was calculated by numerical integration using Simpson's rule. This was achieved by reusing the subroutine used previously to evaluate the shape functions, except in this case the subroutine numerically integrated the lift per unit span to give the total lift of the blade.

The relatively large changes in lift in the small region of the vortex centre meant that it was necessary to have a large number of spanwise locations in the integration to enable the accurate calculation of the spanwise lift coefficient. The large number of spanwise locations

coupled with the large number of time steps resulted in a substantially longer calculation time. Therefore, for spanwise locations greater than two vortex core radii, where the axial flow was zero according to the Lamb model, the coefficient of lift per unit span was assumed to be zero.

The process for calculating the spanwise lift was:

1. The blade was divided into equal parts in the spanwise direction enabling the evaluation of the Simpson's rule at a later stage.
2. Coefficients of lift per unit span were calculated for each spanwise location using the indicial model.
3. Coefficients of lift per unit span were multiplied by $\frac{1}{2}\rho V^2 c$ resulting in values for lift per unit span.
4. The lift per unit span was then integrated across the span by the Simpson's rule resulting in total Lift.

Step 2 of the process detailed above was only completed for spanwise locations where axial flow was present.

For the previously examined case, B3, experimental data existed which allowed the determination of the dimensional parameters required for the indicial model. The freestream velocity and interacting blade chord were taken from the experimental data and the rest of the dimensional parameters were calculated. However, for the other cases where experimental data do not exist, the magnitudes of the calculated parameters for the indicial model are dependent on the three parameters: the freestream velocity, the blade chord, and the kinematic viscosity.

In the comparison with case B3 above, the freestream velocity and the blade chord were fixed. However, any combination of two fixed parameters from the three yields a valid solution. The three combinations are:

- X. Freestream velocity and blade chord fixed, kinematic viscosity varies,

- Y. Freestream velocity and kinematic viscosity fixed, blade chord varies, and
- Z. Blade chord and kinematic viscosity fixed, freestream velocity varies.

Case	Kinematic Viscosity	Freestream Velocity [m/s]	Chord [m]	Peak Axial Velocity [m/s]	Vortex Core Radius [m]	Circulation [m ² /s]
B3 - X	0.01375	50	0.275	2.195122	0.078571	0.602047
B3 - Y	1.45e-5	50	0.00029	2.195122	8.28571E-05	0.000635
B3 - Z	1.45e-5	0.0527	0.275	0.0023	0.078571	0.0006349

Table 9.4: Comparison of potential solutions X, Y, Z, for case B3

Table 9.4 shows a comparison of the three potential solutions and the resultant dimensional parameters for case B3. Figures 9.10a, b and c show comparisons of the resultant coefficient of lift per unit span C_l , circulatory lift coefficient per unit span, and impulsive lift coefficient per unit span. In Figure 9.10, the response is of a positive magnitude. This is in contrast to the negative magnitude responses found by Liu and Marshall as shown in Figure 9.9. The reason for this difference is explained by the difference in orientation of the axial core flow. The indicjal models remain consistent with previous models where the axial flow is directed towards the lower surface, whereas in Liu and Marshall's case the axial flow is directed towards the upper surface. Therefore, when comparing the indicjal predictions and results of Liu and Marshall the absolute magnitude is considered.

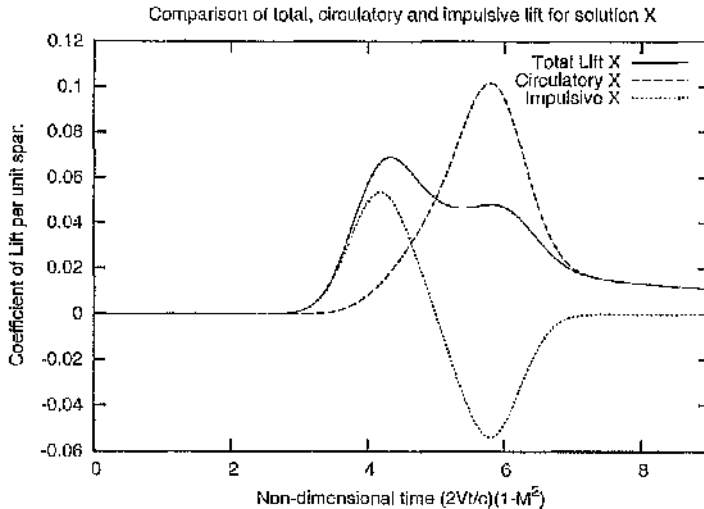


Figure 9.10a: Total, circulatory, and impulsive lift for solution X

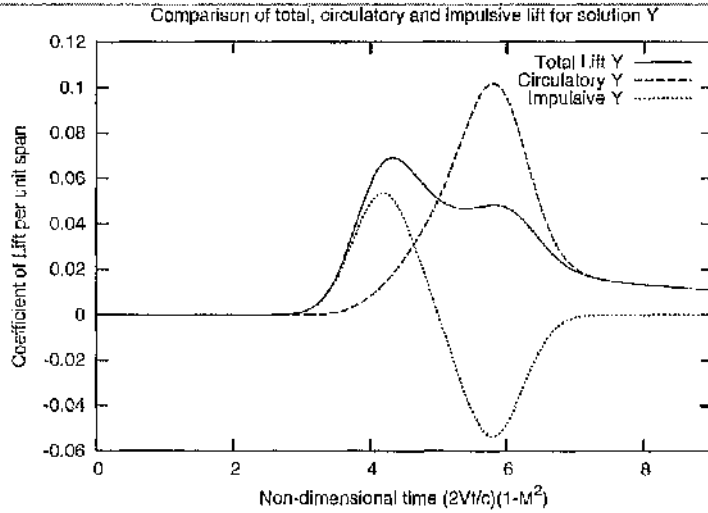


Figure 9.10b: Total, circulatory and impulsive lift for solution Y

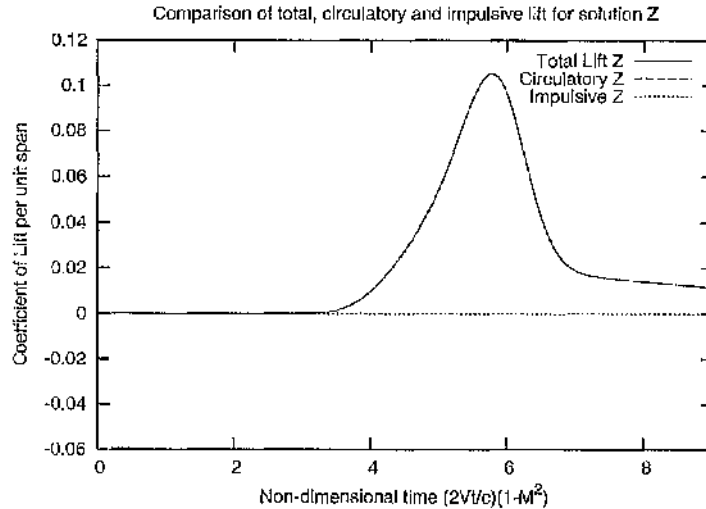


Figure 9.10c: Total, circulatory and impulsive lift for solution Z

Due to the impulsive component's dependence on Mach No, and therefore freestream velocity, the magnitude of the impulsive component decreased when the decreased freestream velocity was reduced. The circulatory response is identical in each solution when the compressibility correction is taken into account; therefore, the differences between each solution are dependent on the magnitude of the impulsive component due to the different freestream velocity. Figure 9.11 shows the calculated C_L'' in a comparison with the C_L'' figure taken from Liu and Marshall (2004) for each of the three potential solutions. The form of the response is identical for the solutions where the freestream velocity is fifty. The magnitude of the peak is approximately of the same magnitude as the experiment. However,

the indicjal prediction still features two peaks unlike the computational data. For the solution where the freestream velocity is not fixed (Solution Z), the resultant lift is equal to the circulatory lift as the velocity is very small. For Solution Z the form of the circulatory response is the total lift response and consequently is very similar in form to the computational data, but of much greater peak magnitude.

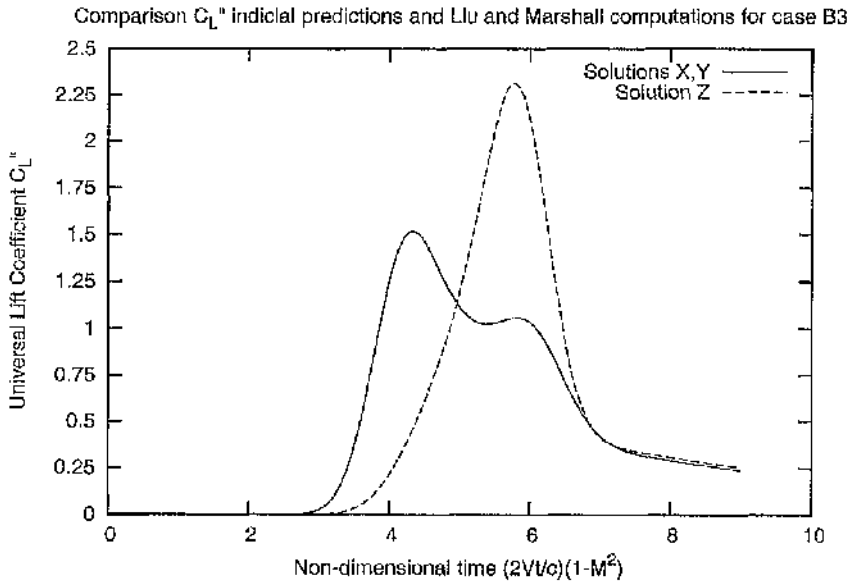


Figure 9.11: Comparison of C_L'' calculated by Liu and Marshall and the indicjal model for case B3.

A similar comparison is made for every other B case from Liu and Marshall. Tables in Appendix F tabulate the three solutions (X, Y, and Z) for each case. Figures 9.12, 9.13, and 9.14 show the resultant C_L'' for each case for solutions X, Y, and Z respectively. As expected the solution where the freestream velocity is very low is identical in form to the circulatory response.

From Figures 9.12-9.14 and Table 9.3 it is apparent that the peak magnitude of C_L'' is dependent on the thickness parameter. A similar trend is also apparent in some of the data presented in Figure 25b (Figure 9.8) in Liu and Marshall (2004), however, the correlation is inconsistent. Figure 9.15 shows the correlation of solutions X, Y, and Z with the computational data by plotting a normalized C_L'' against thickness parameter. The line indicates the potential correlation between thickness parameter and normalized C_L'' . The normalized C_L'' is C_L'' divided by the peak C_L'' for each set of case. For example, the peak

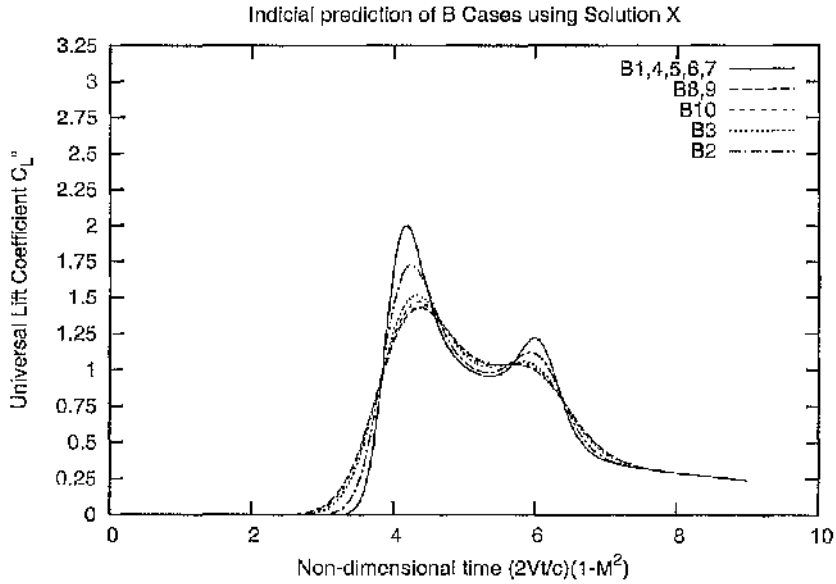


Figure 9.12: Indicjal prediction of C_L'' using solution X

values of C_L'' for Liu and Marshall's computations were divided by the maximum C_L'' in their set of cases, and the peak C_L'' for each of the indicjal predictions was divided by the maximum C_L'' found in Figure 9.12 (See Table 9.5). From Figure 9.15, it appears that two of the values calculated by Liu and Marshall do not fit the trend in normalized C_L'' with thickness parameter produced by the indicjal method. The reason for this is unclear but it is interesting to note that, if the thickness parameters associated with the two anomalous cases were swapped over, the points would fit the correlation.

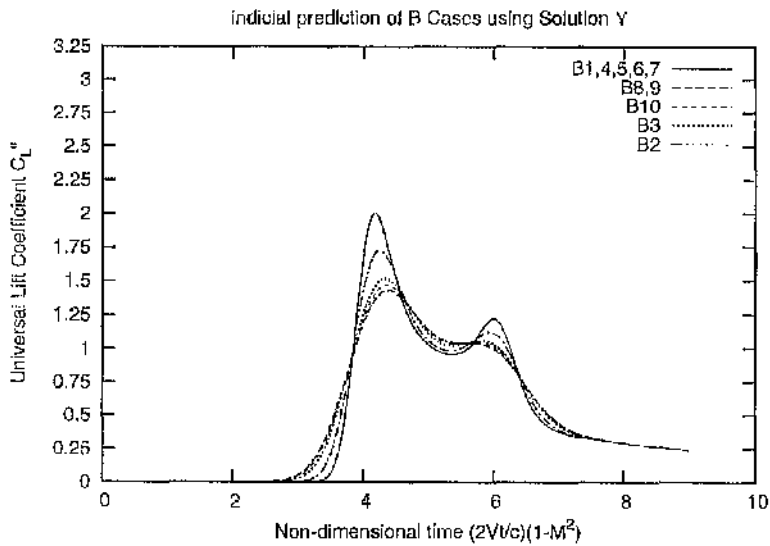


Figure 9.13: Indicjal prediction of C_L'' using solution Y

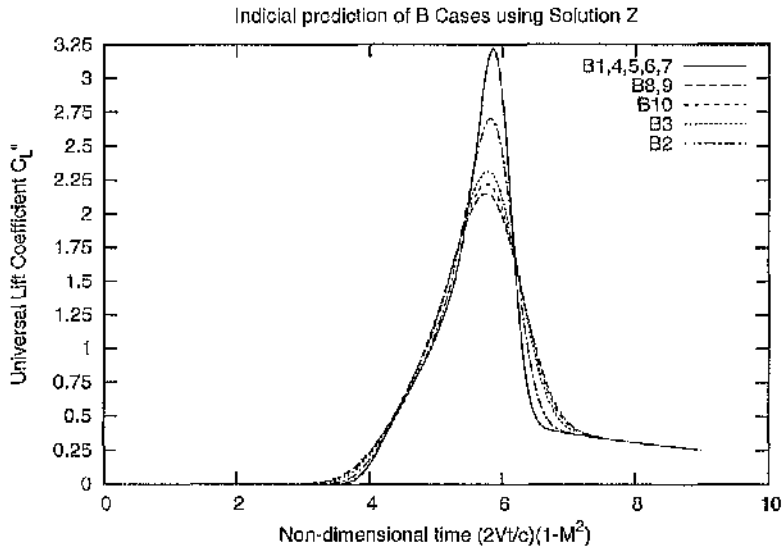


Figure 9.14: Indicjal prediction of C_L'' using solution Z

Case	TP	Peak C_L'' Liu/Marshall	Normalized Liu/Marshall	Peak C_L'' X,Y	Normalized X,Y	Peak C_L'' Z	Normalized Z
B1	0.78	1.04	0.76	2.01	1.00	3.22	1.00
B2	0.56	0.9	0.66	1.73	0.86	2.70	0.84
B3	0.42	0.94	0.69	1.52	0.76	2.31	0.72
B4	0.78	1.34	0.99	2.01	1.00	3.22	1.00
B5	0.78	-	-	2.01	1.00	3.22	1.00
B6	0.78	1.26	0.93	2.01	1.00	3.22	1.00
B7	0.78	1.32	0.97	2.01	1.00	3.22	1.00
B8	0.38	0.92	0.66	1.43	0.71	2.15	0.67
B9	0.38	0.96	0.71	1.43	0.71	2.15	0.67
B10	0.39	1.36	1.00	1.47	0.73	2.22	0.69
		1.36		2.01		3.22	

Table 9.5: Shows the peak C_L'' in each set of cases, for Liu and Marshall, and for the indicjal predictions X, Y, and Z. The normalized C_L'' data is the peak data divided by the maximum peak in that set of cases, given in the last row for relevant columns.

However, there is one problem with the analysis above. The indicjal model calculates the lift due to the interaction by evaluating the effect of the axial velocity profile of the incident vortex along the chord line of the interacting blade. The indicjal technique does not take account of blade thickness and therefore the observed variation in C_L'' with thickness parameter must be due to some other factor.

In the case of orthogonal blade vortex interaction the angle of attack will vary with respect to the ratio of the vortex core to the chord length. This simply results from the weighting of the portion of the chord subject to the vortex cross flow and the portion with no cross flow to give

an average cross flow across the chord. It should be noted that this is a steady flow effect and should not be confused with the significance of the vortex/chord ratio discussed below in relation to the unsteady response. Therefore, in steady flow, the representative angle of attack will be a function of this ratio, and the ratio of the axial and freestream velocities.

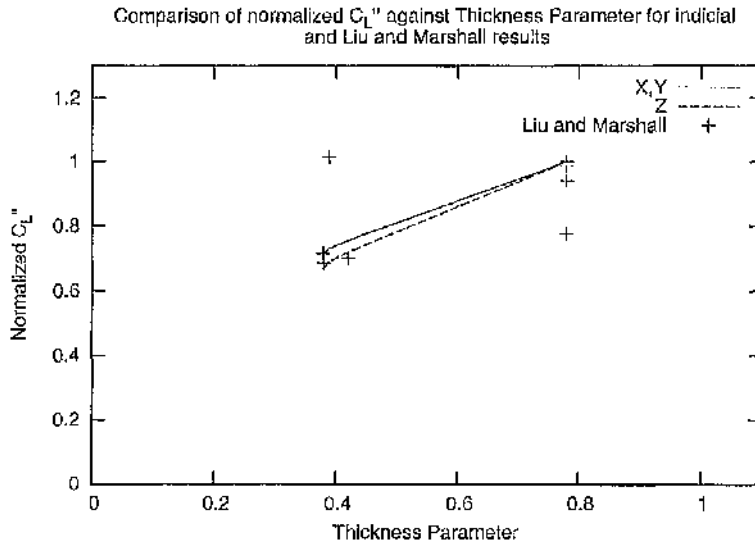


Figure 9.15: Normalized C_L'' for indicial model and computational cases

Liu and Marshall used a NACA 0012 in all cases. This therefore defines a symmetrical aerofoil of fixed thickness to chord length ratio of 12%. It is clear that the apparent effect of the thickness parameter in these cases is not due to the thickness ratio, which does not feature in the indicial calculation, but rather the ratio of the vortex core radius to the chord. The reason why C_L'' should vary with this ratio can be more readily understood by first considering a derivation of Liu and Marshall's C_L'' .

Liu and Marshall's C_L'' can be derived by considering the standard equation for lift per unit span and the simplifications for angle of attack. Considering that lift per unit span equals:

$$L' = \frac{1}{2} \rho V^2 c C_l \tag{9.2}$$

The coefficient of lift can also be approximated by assuming lift curve slope of 2π for small angles of attack (α):

$$C_l = 2\pi\alpha \quad (9.3)$$

Also, for small angles of attack, the angle can be simplified to the axial velocity (w) divided by the freestream velocity (V):

$$\alpha = \tan^{-1}\left(\frac{w}{V}\right) \approx \frac{w}{V} \quad (9.4)$$

In the case of orthogonal blade vortex interaction the angle of attack will vary with respect to the ratio of the vortex core to the chord length. Therefore the representative angle of attack will be a function of this ratio, and the ratio of the axial and freestream velocities:

$$\alpha = f\left(\frac{r_c w}{c V}\right) \quad (9.5)$$


Therefore lift per unit span equals:

$$L' = f(\pi\rho V w r_c) \quad (9.6)$$

This is very similar to the C_L'' derived by Liu and Marshall. The lift for the whole blade is made up from the lift on the spanwise sections involved in the vortex interaction and the lift from the sections outside of the interaction region. Since the latter is zero, the total lift is dependent on the spanwise extent of the vortex. Therefore, the total lift may be expressed as:

$$L = f(\pi\rho V w r_c^2) \quad (9.7)$$

Liu and Marshall's new universal lift coefficient, C_L'' is therefore defined as the coefficient that satisfies the relationship in equation 9.7 assuming that the relationship is linear. However, since no attempt has been made to include unsteady effects, equation 9.7 represents only the steady state response of the blade. Therefore, the observed variation of C_L'' may be due to some aspect of the unsteady response of the blade.

For a given flow speed, the unsteady response depends on the rate at which the vortex core is blocked by the blade and the extent of the interacting blade that is subject to the vortex cross flow as the core is blocked. Three simple scenarios can be used to illustrate this effect. Consider first the interaction of a blade with a vortex which has a core size that is the same size as the blade chord. In this case, the blade will only block the core for an instant and the blade will experience a smoothly varying cross flow. In this , the lift will vary progressively throughout the interaction. Now consider a case where the vortex core size is extremely small in comparison to the chord. In this case, the vortex is blocked impulsively by the blade and remains blocked as the vortex traverses the chord. In this case, the initial interaction is highly impulsive and unsteady but the circulatory lift subsequently has time to asymptote to the steady state. In the final scenario, the vortex core size is around 10% of the chord length. In this case, the initial interaction is more gradual than the previous case but the flow has relatively little time to reach a steady state value before the front edge of the vortex crosses the trailing edge. On this basis, it would be expected that the second scenario would provide the closest approximation to a steady state maximum lift coefficient whereas the others would fail to reach this value.

Looking again at Table 9.5, and remembering that TP varies inversely with the ratio of the vortex core to the blade chord, it may be observed that the cases with the lowest core radius/chord ratio produce the highest values of C_L^* . This is entirely consistent with the argument developed above.

9.2.1 Investigation of Axial Core Flow Decrease

Another feature observed by Liu and Marshall (2004) in their computational study was the decrease in the axial flow rate after the initial stages of the interaction. Figure 9.16 taken from Liu and Marshall (2004), shows an almost linear decrease in axial flow rate as the interaction progresses. This phenomenon was investigated in the present study using indicial modelling to quantify the axial flow rate decrease in the experimental data. This

comparison, however, could only be made at the vortex centre due to the variation in axial velocity away from the vortex centre in the spanwise direction as discussed in the previous chapter. An inverse indicjal technique provided the basis for the investigation of the change in magnitude of the vortex axial core flow during the orthogonal interaction with the stationary blade.

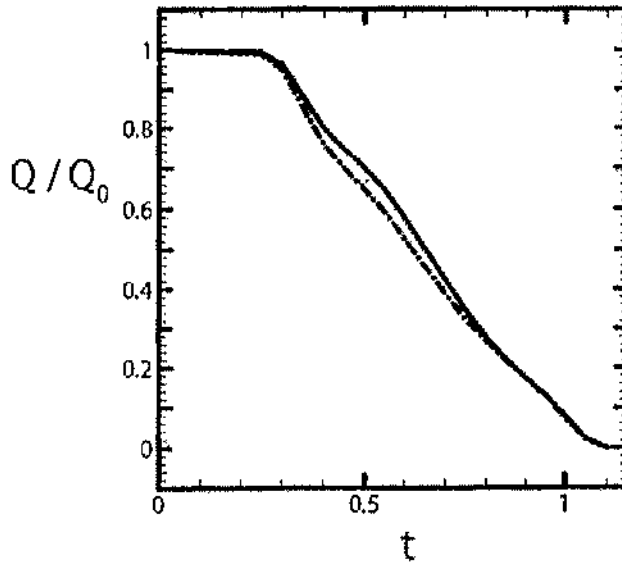


Figure 9.16: Axial flow decrease found by Liu and Marshall (2004). Centre of vortex core reaches leading edge at $t = 0.5$ and reaches the trailing edge at $t=1.0$

The first step in the process of the inversion of the indicjal model requires the sampling of the desired lift coefficient output from the system. The lift coefficient is then converted from a compressible to an incompressible lift coefficient:

$$C_l = C_l^{Compressible} \sqrt{(1 - M^2)} \tag{9.8}$$

The lift coefficient is equal to the sum of both the circulatory and impulsive parts, where n is the current iteration of the calculation:

$$C_l = C_{l_c} + C_{l_i} \tag{9.9}$$

$$C_l = 2\pi(\eta_n - X_n - Y_n - Z_n) + \frac{4}{M}(H_n) \tag{9.10}$$

$$C_l = 2\pi \begin{pmatrix} \eta_n - X_{n-1} e^{\frac{-ds}{T_1}} - A_1 e^{\frac{-ds}{2T_1}} (\eta_n - \eta_{n-1}) \\ -Y_{n-1} e^{\frac{-ds}{T_2}} - A_2 e^{\frac{-ds}{2T_2}} (\eta_n - \eta_{n-1}) \\ -Z_{n-1} e^{\frac{-ds}{T_3}} - A_3 e^{\frac{-ds}{2T_3}} (\eta_n - \eta_{n-1}) \end{pmatrix} + \frac{4}{M} \left(H_{n-1} e^{\frac{dt}{T_1}} + e^{\frac{-dt}{2T_1}} (\lambda_n - \lambda_{n-1}) \right) \quad (9.11)$$

In the complete equation given in 9.11, η_n and λ_n are the only unknown values in the equation. All other values can be easily calculated or exist from a previous iteration of the calculation. Obviously, the values from the previous time step only exist after the first time step and therefore default values that are commonly used for the first time step of the regular 'forward' indicial model were used.

The calculation of η_n and λ_n is the solution of the shape functions from Beddoes (1989). They are given below with the numerical integration summation by Simpson's rule for thirty segments:

$$\eta_n = \frac{1}{\pi V} \int_0^\pi \left(w_0 e^{\frac{-r^2}{r_c^2}} (1 - \cos \theta) \right) d\theta = \frac{w_0}{\pi V} \sum_{i=0}^{i=30} \left(e^{\frac{-r_i^2}{r_c^2}} (1 - \cos \theta_i) \right) \quad \text{SIMPSON} \quad (9.12)$$

$$\lambda_n = \frac{1}{V} \int_0^1 \left(w_0 e^{\frac{-r^2}{r_c^2}} \sin \theta \right) d\left(\frac{x}{c}\right) = \frac{w_0}{V} \sum_{i=0}^{i=30} \left(e^{\frac{-r_i^2}{r_c^2}} \sin \theta_i \right) \quad \text{SIMPSON} \quad (9.13)$$

Where:

$$\sum_{i=0}^{i=k} (x_i) \text{SIMPSON} = (x_0 + 4x_1 + 2x_2 + 4x_3 + \dots + 4x_{k-1} + x_k) \left(\frac{H}{3} \right) \quad (9.14)$$

The calculation of the peak axial velocity is straight forward as the peak axial velocity variable, w_0 , can be moved outside of the integration.

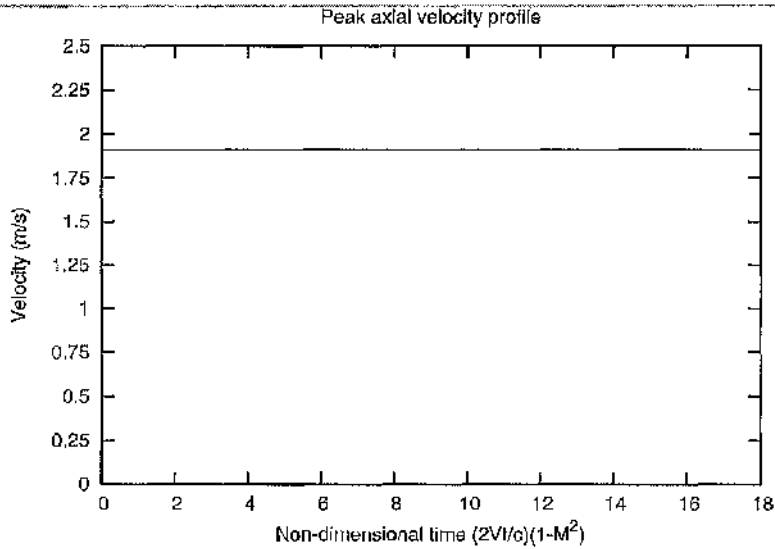


Figure 9.17: Peak axial velocity profile

To test the method, the prescribed indicial prediction of the large wind tunnel experiment at forty metres per second was examined first. The peak axial velocity for the regular 'forward' indicial model was set to 1.91m/s. Figures 9.17 and 9.18 show the variation of the peak axial velocity with time, and the corresponding indicial prediction of the lift coefficient respectively.

Figure 9.19 shows the calculated peak axial velocity profile using the inverse indicial prediction. The inverse indicial method predicts the correct peak axial velocity profile correctly up until a non-dimensional time value of approximately of 11.6. This point coincides with the time that the vortex centre has reached approximately two-vortex core radii beyond the trailing edge. At this point there is effectively no influence of the vortex on the interacting blade, and consequently there are an infinite range of solutions for the peak axial velocity after this point. Therefore, there is a finite range over which the calculation will find 'realistic' solutions. For the location two vortex core radii in front of the leading edge there is a solution as the lift coefficient gradually increases from this point. The initialisation of the inverse indicial model requires an initial peak axial velocity to start the calculation, and as the correct value is known in this case, the method produces the correct peak axial velocity profile. In general, the calculation of the peak axial velocity by the inverse indicial model is indeterminate when the vortex centre is greater than approximately two vortex core radii fore or aft of the leading or trailing edge. These limits are imposed by the axial velocity

distribution associated with a Lamb-type vortex that reduces to zero at core radii from the vortex centre. Other axial velocity profiles for the vortex core have similar limits and therefore this is not only a limitation of the Lamb type vortex. However, the direct correlation between the Figure 9.19 and Figure 9.17 over the determinate time frame demonstrates the integrity of the inverse indicial method. The inverse method is now applied to experimental data.

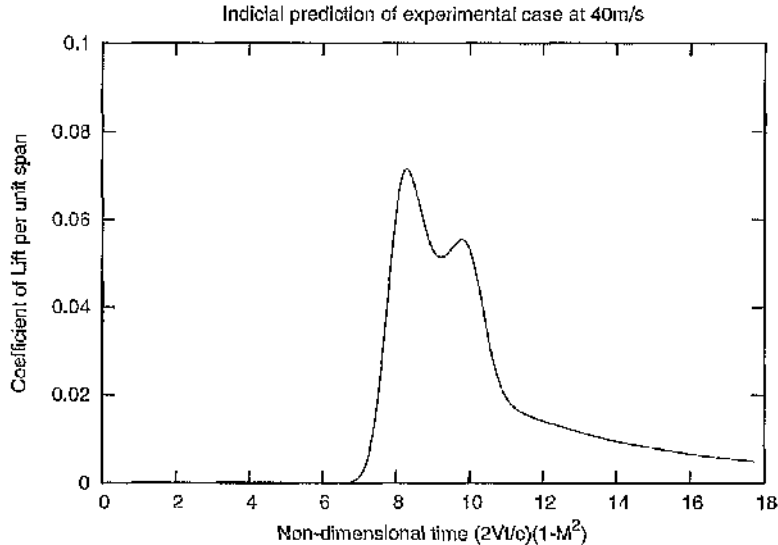


Figure 9.18: Original lift coefficient per unit span response.

Figure 9.20 shows experimental data for the forty metres per second case at the spanwise location where the vortex centre passed over the chord. Also in Figure 9.20 is a simplified version of the experimental data, which was created by curve fitting to the data after the initial interaction and removing the fluctuations before and aft of the main interaction. The simplified experimental data were then used as input to the inverse indicial model to avoid rapid, impulsive changes in peak axial velocity being predicted in response to what is really flow turbulence. The purpose of this analysis is to calculate the variation of peak axial velocity with time that would result in the general response found. The part of the response that is of interest is the initial peak in lift coefficient followed by the gradual decrease. The other smaller scale fluctuations are not of interest in this analysis.

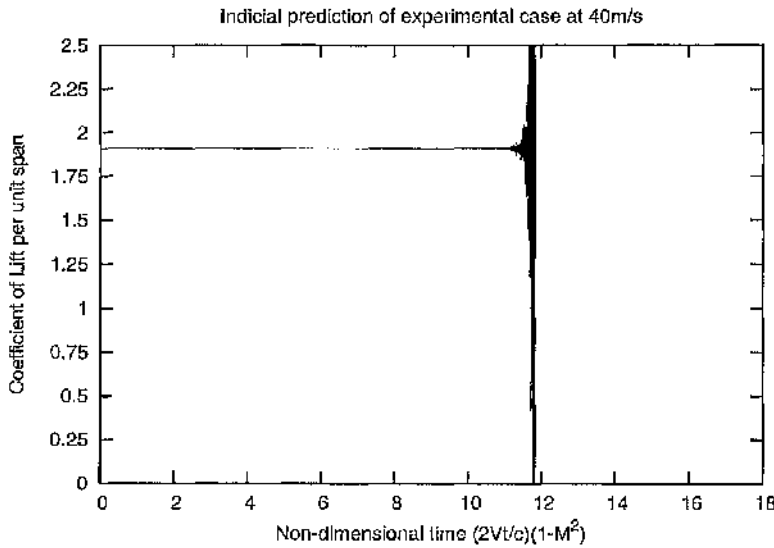


Figure 9.19: Inversely calculated peak axial velocity profile

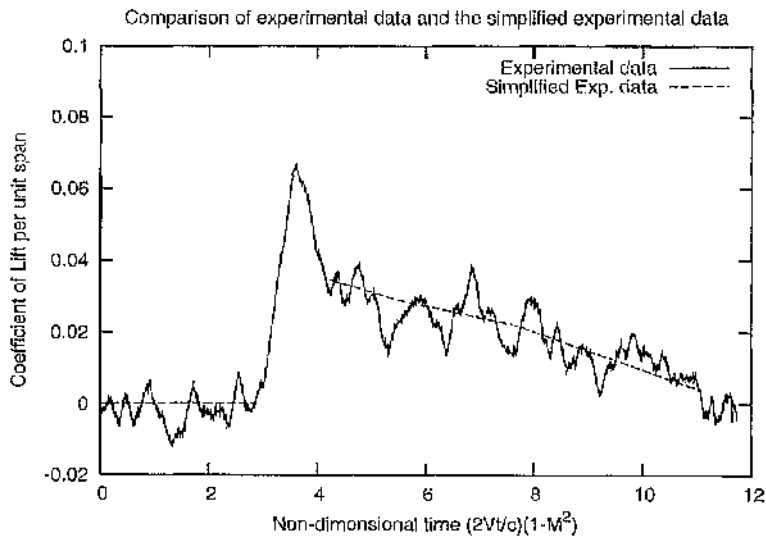


Figure 9.20: Diagram showing experimental data and filtered experimental data

A specific problem associated with the inverse indicjal modelling of the experimental data is making sure that the timing of the interaction in the experimental data matches that in the indicjal model. Figure 9.21 shows a preliminary attempt to synchronize the two time frames based on matching the time point at which the peak normal force is achieved in both the experiment and a conventional forward indicjal simulation. The timing of the movement of the vortex across the blade chord is then extracted from this forward indicjal simulation to provide an input into the inverse method. The corresponding peak axial velocity variation calculated by the inverse method is plotted against non-dimensional time in Figure 9.22. The

determinate time frame is the region between the dotted lines on Figure 9.22. As indicated previously, at times outside this time frame it is not possible to determine a realistic solution.

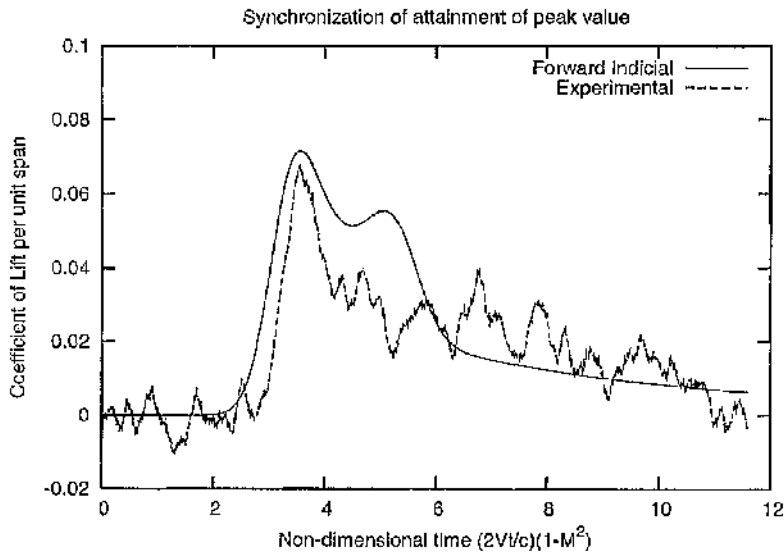


Figure 9.21: Diagram showing synchronization of the forward indicial calculation with the experiment using the point in time when the regular forward indicial calculation and the experimental data reach the first peak.

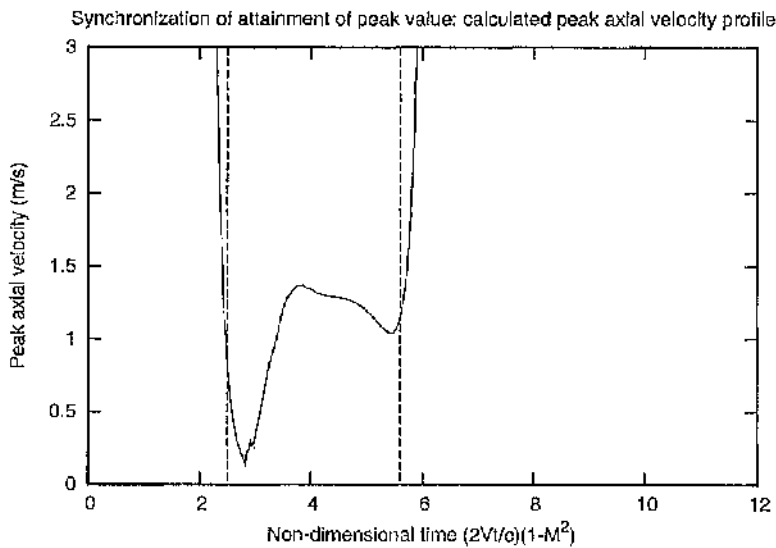


Figure 9.22: Calculated peak axial profile required for synchronization as seen in figure 21

Within the determinate time frame there is an increase in peak axial velocity to a maximum followed by an almost linear decrease. The maximum velocity calculated is approximately 1.38 m/s, which is significantly lower than the experimentally measured 1.91 m/s. The general form of the variation in peak axial velocity after the maximum value is similar to the axial volume flow decrease found by Liu and Marshall (Figure 9.16). One feature that is

different from Liu and Marshall is the initially low peak axial velocity. This can be explained in this case by the fact that, as shown in Figure 9.21, the lift coefficient rise starts too early in the indicial prediction and the initial increase is shallower compared to the experimental data.

Therefore, perhaps a more reasonable synchronization of the experimental and indicial time frames is the synchronization of the initial impulsive increase in lift coefficient (Figure 9.23). As shown in Figure 9.23 this produces an overshoot in the forward indicial simulation. Interestingly, Liu and Marshall (2004) found that the axial volume flow rate decrease began before the vortex core had reached the leading edge. The overshoot in the forward indicial simulation may be due to a failure to account for this effect.

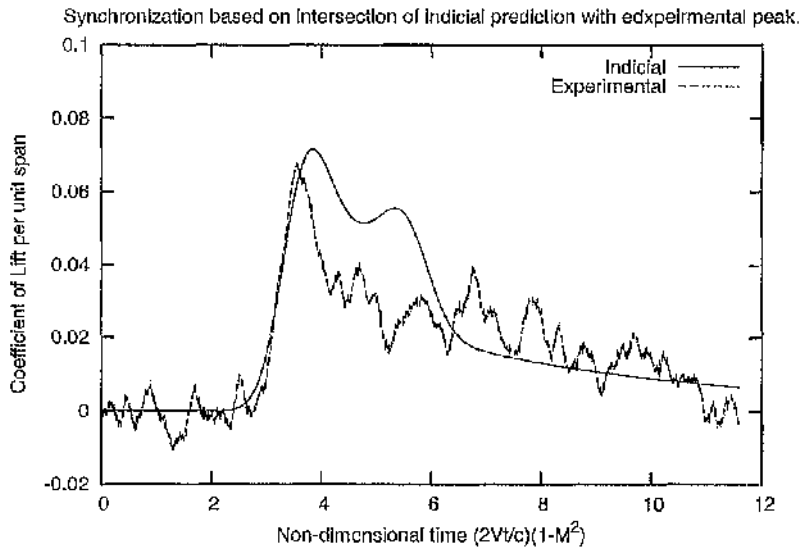


Figure 9.23: Indication of new synchronization of time frames using forward indicial method against experimental data

Figure 9.24 shows the inversely calculated peak axial velocity variation that corresponds to the time frame synchronization shown in Figure 9.23. The peak axial velocity now reaches a maximum of around 1.87 m/s, which is just below the experimentally measured peak axial velocity of 1.91 m/s. Again, there is an initially lower peak axial velocity due to the shallower increase in lift coefficient in the indicial prediction. After the initial impact of the interaction there is a greater, almost linear, decrease in the peak axial velocity as the vortex progresses downstream.

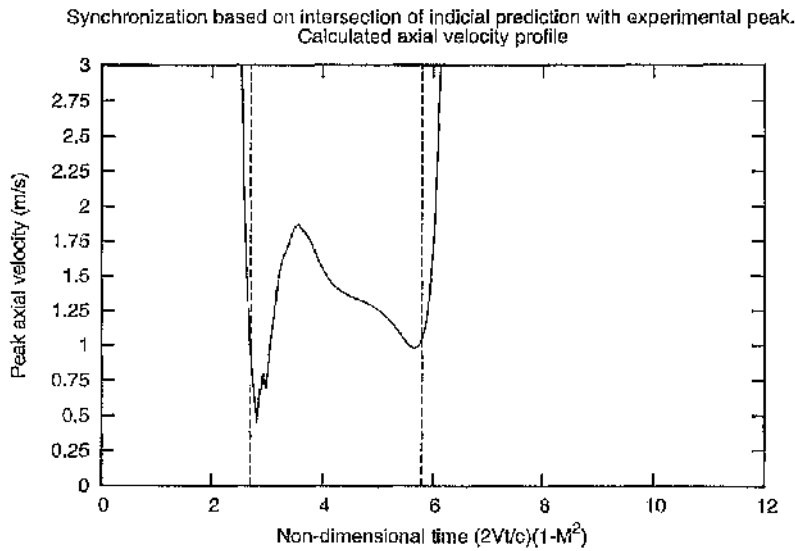


Figure 9.24: Inversely calculated peak axial velocity profile for synchronization in figure 9.23

At first glance, the rate of decrease in axial velocity in the vortex predicted by the inverse indicial model after the initial interaction is not as severe as the rate of decrease in volume flow rate found by Liu and Marshall. However, this comparison is not straightforward. There are major differences between the two computational methods. The computational method used by Liu and Marshall (2004) modelled the interaction in viscous, compressible flow. The indicial method is an inviscid calculation with a compressibility correction factor. The calculation of volume flow rate by the inverse indicial model assumes a constant vortex core radius, and therefore volume flow rate is dependent only on the axial velocity profile. In comparison, the calculation of Liu and Marshall allows for the variation of both the vortex core radius and the axial velocity. The other significant difference between the two models is the type of interaction. The experimental data that the inverse indicial model is forced to follow has been shown in a previous chapter to be affected by the shape of the rotor wake and its associated induced flow. The experimental lift coefficient response is from a representative rotor wake, whereas the calculations of Liu and Marshall assume an initially columnar tip vortex. These differences therefore make it difficult to directly compare the rate of axial flow decrease calculated by Liu and Marshall and by the inverse indicial model.

Nevertheless the same general trend, of an almost linear decrease in the axial core flow after the initial interaction, is predicted by the two methods.

9.3 Summary

The comparisons of the indicial model predictions with other experimental and computational datasets have provided a greater insight into the datasets. The first case examined was the experimental data collected from the 'proof of concept' orthogonal blade vortex interaction rig in the small wind tunnel of the University of Glasgow (Doolan, 2001). The indicial model, using a prescribed Lamb type vortex, approximately reproduced the peak lift coefficient for this case, but the form of the response was not well modelled. It was shown that, by increasing the core radius in the indicial model, the form of the response could be more closely reproduced. For this case features of the experiment were highlighted as possibly contributing to the differences between the predictions and the experiment.

The second comparison made was with the computational study of Liu and Marshall (2004). Liu and Marshall derived a new universal lift coefficient C_L'' . Indicial prediction of this lift coefficient resulted in some similarities with the results of Liu and Marshall. In general, the C_L'' values predicted by the indicial model were slightly higher than those of Liu and Marshall. However, the trend of the peak C_L'' found in the indicial predictions showed that the peak C_L'' is dependent on the thickness parameter. However, the thickness parameter, for the set of cases presented by Liu and Marshall, also determines the vortex core radius to chord ratio. It was shown that it is, in fact, this ratio and not TP that influences the unsteady lift response and is not accounted for by C_L'' . This is true for most of the results predicted by Liu and Marshall but there are two anomalous cases. The reasons for the anomalies are not clear at present.

The third comparison made was with the decrease in axial volume flow rate predicted by Liu and Marshall for the latter stages of the orthogonal interaction. An inverse indicial method

was used to determine the variation in the peak axial velocity of the interacting vortex during the interaction. In a manner that was consistent with the linear decrease in volume flow rate predicted by Liu and Marshall, the peak axial velocity was found to decrease almost linearly after the initial phases of the interaction using inverse indicial calculations based on the experimental data. The rate of decrease found using the inverse indicial method, was of lower magnitude than that found by Liu and Marshall. This was attributed to, significant differences between the two studies.

10 Conclusions and Recommended Future Work

Experimental studies and flight tests have shown that tail rotor orthogonal blade vortex interaction can have a significant effect on helicopter performance. The orthogonal interaction of main rotor tip vortices with the tail rotor disc results in noise generation, control degradation and structural fatigue. Industry is keen to develop techniques for modelling the interaction to reduce development costs and to improve the performance of helicopters for both civil and military applications. Industry requires accurate yet, computationally efficient modelling of the interaction. Full flow field modelling, typically by computational fluid dynamics, offers the most accurate modelling method, however, industry requires techniques that can be used for rapid prediction during development stages. Consequently, computational fluid dynamics is generally not used due to the computational time required to simulate the complex helicopter flow field. Therefore, other modelling techniques that are both efficient and can be applied locally are preferred by industry. Indicial modelling is one such technique that has been applied by industry to other aspects of helicopter unsteady aerodynamics. It is, therefore, an appropriate technique to apply to the modelling of orthogonal blade vortex interaction as the resulting method can be easily integrated with existing codes.

Typically, modelling requires validation through correlation with experimental studies. In this study, data from an experimental study of orthogonal blade vortex interaction at the University of Glasgow was used for this purpose. In the experiment, representative main rotor tip vortices were generated upstream of a stationary blade, referred to as the 'interacting blade', on which surface pressure data were captured. The tip vortex generation method produced steady, stable vortices that featured little wander in their path down the wind tunnel. However, in the current work it has been shown that ensemble averaging of the collected data is not an effective method for analysis of the interaction. Despite the small wander that was present in the experiment there is still spatial and temporal attenuation produced by the averaging process. Another analysis technique was therefore considered.

The general response of the interaction is characterised by an impulsive increase in lift coefficient of the interacting blade up to a peak, followed by a slower decrease back to the pre-interaction lift coefficient. A more detailed analysis whereby the magnitude of each impulsive peak in lift coefficient was measured and compared to averaged data revealed the extent of the attenuation. An automated analysis method was developed to extract more accurate estimates of the impulsive response and to provide a basis for the subsequent validation of the indicial model.

Initial indicial modelling of the interaction revealed that a simplistic approach based on the Kussner function, did not adequately model the chordwise distribution of velocities due to the interacting vortex, and consequently over predicted the blade loading. The use of a model that did represent the chordwise distribution of axial velocities of the incident tip vortex, resulted in the accurate prediction of the interacting blade lift coefficient for the initial stages of the interaction. However, accuracy was only found at the spanwise location where the vortex centre travelled across the chord. Here both the gradient and magnitude of the peak of the initial impulsive increase in lift coefficient was well represented by the model.

The indicial model, which was based purely on axial core flow, predicted a symmetric blade response about the vortex centre. However, the experimental data demonstrated a clear asymmetry. Inviscid, quasi-steady state two-dimensional panel method simulations of the experiment showed that the interaction was asymmetric if the local increase in dynamic pressure due to the rotational flow of the tip vortex was considered. The magnitude of the asymmetry found in the experimental data could not be reproduced by considering the experimentally measured rotational flow alone.

To examine this disparity further, an inviscid, incompressible numerical simulation was used to simulate the main rotor wake inside the wind tunnel. The numerical simulation consisted of a three-dimensional panel method, a lifting line calculation, and a free wake model. The wake shape predicted by the numerical simulation was accurate when compared with the shape of the experimental measured wake despite its inviscid, incompressible nature.

Therefore the simulation provided a means to analyse the effect of the wake shape on induced flow at the interacting blade.

Horizontal cross flow velocities were extracted from the numerical simulation at locations which coincided with the pressure measurements made on the surface of the interacting blade. These velocities were used as the 'forcing function' for the indicial model, instead of the previously used prescribed vortex axial flow. The resulting prediction featured an asymmetric response about the vortex centre consistent with the experimental data. Of particular significance was the agreement in form of the response at spanwise locations above the vortex centre where a less impulsive, slow build in normal force was found compared to the more impulsive response found at the vortex centre and below.

In general, the indicial predictions that used the horizontal cross flow as a forcing function resulted in a response of greater magnitude than the experimental data. During the capture of the experimental data, it was witnessed that main rotor blade flapping had occurred at the highest velocity investigated in the tests. Also, calculations of the peak circulation in the vortex generator tip vortex predicted by the numerical simulation showed that much greater circulation was present compared to the experimentally measured value. This difference could possibly be explained by a combination of the inviscid, incompressible nature of the numerical simulation and blade flapping in the experiment.

To investigate the effect of the circulation strength, the angle of incidence of the vortex generator blade in the numerical simulation was reduced until the circulation calculated closely matched the experimentally measured value. This resulted in a closer match in terms of the magnitude of the international response for all spanwise locations, and particularly close agreement in form at spanwise locations above the vortex centre. Agreement in form was not very close at other spanwise locations, but this could potentially be explained by the limitations of the numerical simulation.

The indicial model was also compared with other datasets. Data from a previous test configuration at the University of Glasgow in a smaller wind tunnel showed agreement in terms of the peak response found but not in form. The indicial model with the prescribed axial flow predicted a much more severe impulsive increase in normal force compared to the experimental data. Reasons for the difference between the model and these test data were discussed.

Liu and Marshall (2004) completed viscous, compressible computational fluid dynamic simulations of orthogonal blade vortex interaction of an initially columnar vortex. Indicial prediction of the cases calculated by Liu and Marshall showed general agreement with their solutions in terms of approximate magnitude and form. The predictions were then transformed into the form of a new universal lift coefficient, C_L'' , suggested by Liu and Marshall. It was established however that, far from being universal, C_L'' varied with the thickness parameter. A more detailed investigation showed that the thickness parameter actually determined the vortex core radius to chord ratio in the set of cases presented by Liu and Marshall, and it was this second parameter that determined the magnitude of C_L'' . It was shown that the expression for C_L'' captured the steady state lift response, but did not represent the unsteady lift response. The unsteady lift response was shown to depend on the vortex core radius to chord ratio in a manner consistent with physical expectations. This relationship was found in all indicial predictions but was not present in all of the computational solutions of Liu and Marshall. The reason for this difference remains to be resolved.

Liu and Marshall also calculated a linear rate of decrease of the axial core flow during the interaction. A similar linear rate of decrease was also found using inverse indicial simulations of the experimental data; however, it was of a less severe nature. This difference was attributed to differences in the modelling techniques used and the fact that the Glasgow University experimental data were complicated by the induced effect of the vortex generator wake.

Future work should include the integration of the indicial model of tail rotor orthogonal blade vortex interaction into a full helicopter simulation to enable the evaluation of changes in tail rotor lift/thrust due to the interaction. The inviscid numerical simulation of the wind tunnel was unable to reproduce all of the features found in the experimental data. A viscous, compressible simulation of the experiment may enable a greater understanding of the way in which the full wake structure influences the local interaction.

Also, the experimental validation of the indicial model is only for low Mach number orthogonal interactions. High Mach number experimental data for orthogonal interactions is not available and consequently comparisons could not be made. Indicial modelling has shown good agreement with experimental data for both low and high Mach No flows for parallel blade vortex interactions. This suggests that the indicial model may well replicate High Mach number data for orthogonal blade vortex interactions but this should be properly verified.

Appendix A: Derivation of the response of a unit step

System assumed to be a simple linear first order system of the form:

$$\frac{dy(t)}{dt} + ay(t) = x(t), \text{ where } y(0) = y_0$$

Then a solution for the system exists:

$$e^{at} \frac{dy(t)}{dt} - ae^{at} y(t) = x(t)e^{at}$$

$$\int_0^t \frac{d}{d\tau} (e^{a\tau} y(\tau)) d\tau = \int_0^t e^{a\tau} x(\tau) d\tau$$

$$e^{at} y(t) - x(0)e^0 = \int_0^t e^{a\tau} x(\tau) d\tau$$

For a discrete system:

$$y[n] - ay[n-1] = x[n]$$

$$y[n] = x[n] + ay[n-1]$$

For n = 0: $n = 0 : y[0] = x[0] + ay[-1] = 1(\text{unit_step_impulse}) + 0 = 1$

For n=1: $n = 1 : y[1] = x[1] + ay[0] = 0(\text{no_input}) + a.1 = a$

For n=2: $n = 2 : y[2] = x[2] + ay[1] = 0 + a.a = a^2$

The response of a discrete time (DT) linear time invariant (LTI) system is the first difference of its step response; a.

Therefore solution of the linear system is:

$$y(t) = e^{-at} \int_0^t e^{a\tau} x(\tau) d\tau = a.e^{-at} \int_0^t e^{a\tau} d\tau$$

$$y(t) = a.e^{-at} \frac{[e^{at} - 1]}{a} = 1 - e^{-at}$$

Appendix B: Measured Data from the Argyll Wind Tunnel Experiment at the University of Glasgow

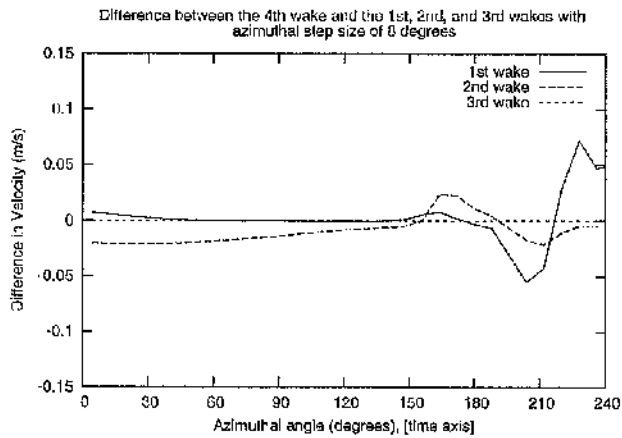
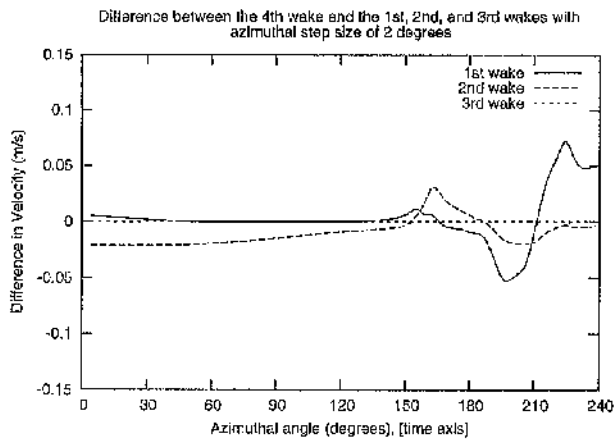
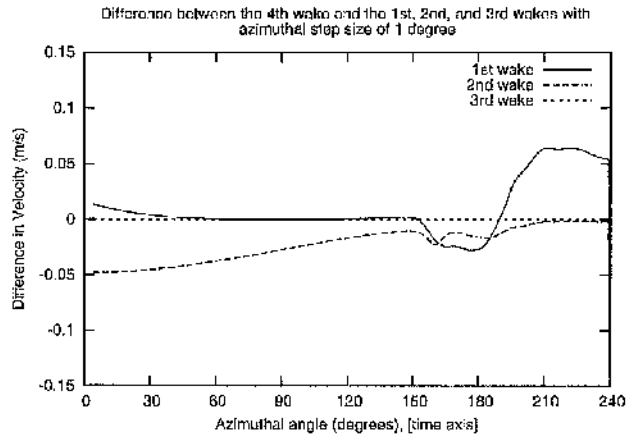
Blade aerofoil section: NACA 0015

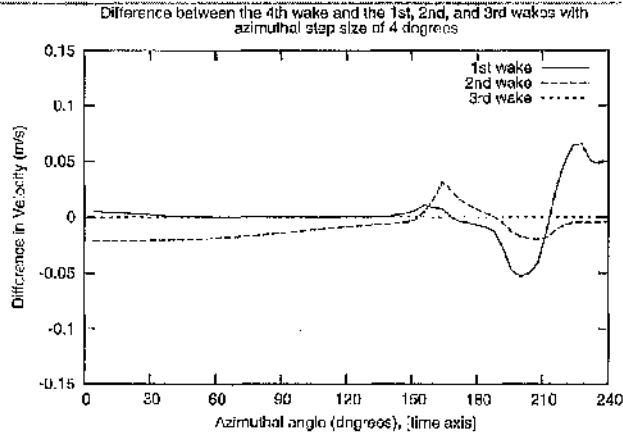
Velocity (m/s)	20	30	40	50
Rotor Speed (rpm)	168	252	336	420
Vortex Height (mm)	980	960	920	900
Vortex Core Radius [Rc] (mm)	74.18 ± 16.35	84.83 ± 33.31	76.3 ± 10.24	90.3 ± 49.32
Peak Rotational Velocity [V _θ] (m/s)	2.77 ± 0.35	3.2 ± 0.45	3.17 ± 0.38	1.72 ± 0.41
Peak Axial Velocity [W _θ] (m/s)	1.62 ± 0.23	1.27 ± 0.23	1.91 ± 0.25	2.2 ± 0.2
Peak Circulation [Γ] (m ² /s)	0.9 ± 0.25	1.26 ± 0.41	1.26 ± 0.25	0.77 ± 0.27
Thickness Parameter -T/r _c	0.556	0.486	0.541	0.457
Impact Parameter - 2πr _c V/Γ	10.36	12.69	15.22	36.84
Axial Flow Parameter - 2πr _c W _θ /Γ	0.84	0.54	0.73	1.62

Appendix C: Wake Comparisons for Numerical Simulations

The appendix is referenced in the chapter discussing the numerical simulation of the wind tunnel configuration (Chapter 7). Figure 7.5 in chapter 7 shows that the third wake is the first repeating wake. This is shown by the comparison of the horizontal cross flow velocity for a point corresponding to interacting blade's location in the wind tunnel. Figure 7.5 was the result obtained when the azimuthal step size of the vortex generator in the numerical simulation was one degree per time step for a freestream velocity of 40 m/s. However, results were also obtained for azimuthal step sizes of 2, 4, and 8 degrees at a freestream velocity of 40 m/s. Comparisons of the cross flow velocities were also obtained for 20, 30, and 50 m/s for each of the previously used azimuthal step sizes. All results are shown below.

Velocity 20m/s





	1st wake	2nd wake	3rd wake	4th wake
8 deg.	0.5771	0.5933	0.5696	0.5696
4 deg.	0.6115	0.6349	0.6039	0.6039
2 deg.	0.6352	0.6566	0.6292	0.6292
1 deg.	0.6537	0.6728	0.6479	6.48E-01

Table C.1: Comparison of peak axial velocity calculated in all test cases at the spanwise location of the vortex centre. Freestream velocity = 20 m/s.

	1st wake	2nd wake	3rd wake	4th wake
8 deg.	0.4815	0.4945	0.4973	0.4972
4 deg.	0.4692	0.4827	0.4865	0.4864
2 deg.	0.4691	0.4849	0.4896	0.4895
1 deg.	0.4667	0.4837	0.4884	0.4883

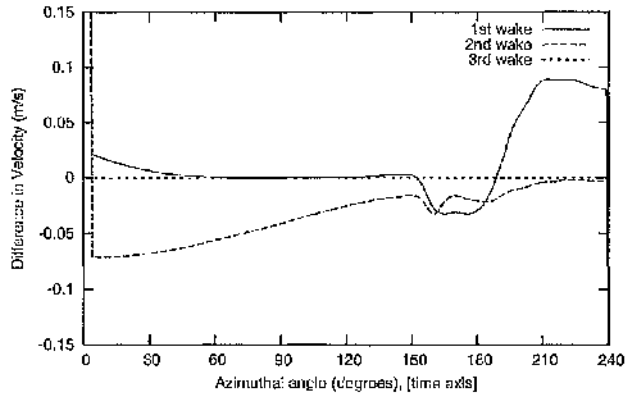
Table C.2: Comparison of peak axial velocity calculated in all test cases at the spanwise location 0.1m above the vortex centre. Freestream velocity = 20 m/s.

	1st wake	2nd wake	3rd wake	4th wake
8 deg.	0.414	0.4232	0.4334	0.4333
4 deg.	0.4863	0.4874	0.5071	0.507
2 deg.	0.5048	0.5096	0.5275	0.5275
1 deg.	0.5018	0.5091	0.5258	0.5257

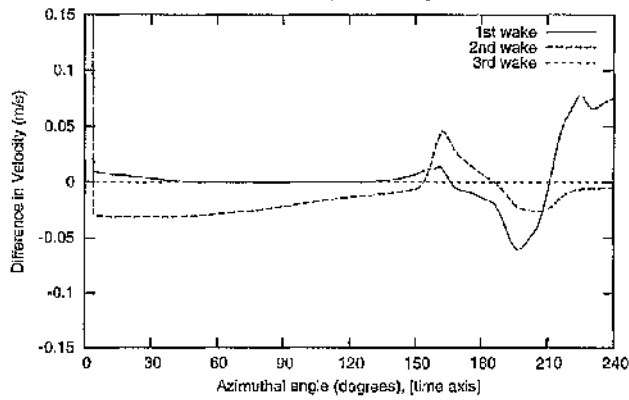
Table C.3: Comparison of peak axial velocity calculated in all test cases at the spanwise location 0.1m below the vortex centre. Freestream velocity = 20 m/s.

Velocity 30m/s

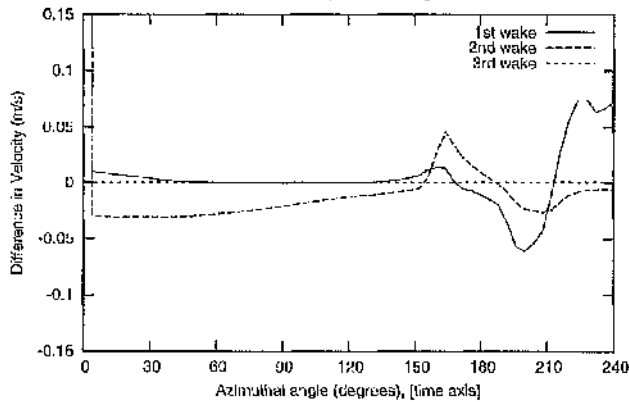
Difference between the 4th wake and the 1st, 2nd, and 3rd wakes with azimuthal step size of 1 degree

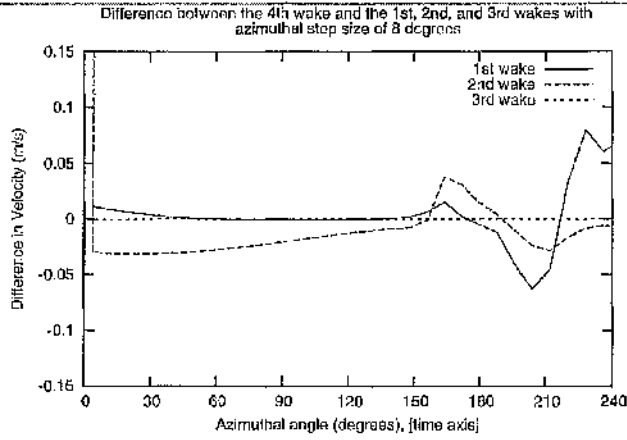


Difference between the 4th wake and the 1st, 2nd, and 3rd wakes with azimuthal step size of 2 degrees



Difference between the 4th wake and the 1st, 2nd, and 3rd wakes with azimuthal step size of 4 degrees





	1st wake	2nd wake	3rd wake	4th wake
8 deg.	0.7914	0.8141	0.7762	0.7761
4 deg.	0.8154	0.848	0.802	0.802
2 deg.	0.8777	0.901	0.8645	0.8645
1 deg.	0.8885	0.9171	0.8755	0.8755

Table C.4: Comparison of peak axial velocity calculated in all test cases at the spanwise location of the vortex centre. Freestream velocity = 30 m/s.

	1st wake	2nd wake	3rd wake	4th wake
8 deg.	0.657	0.6836	0.6893	0.6892
4 deg.	0.6533	0.6732	0.6795	0.6795
2 deg.	0.6542	0.6709	0.6782	0.6782
1 deg.	0.6539	0.6724	0.677	0.6769

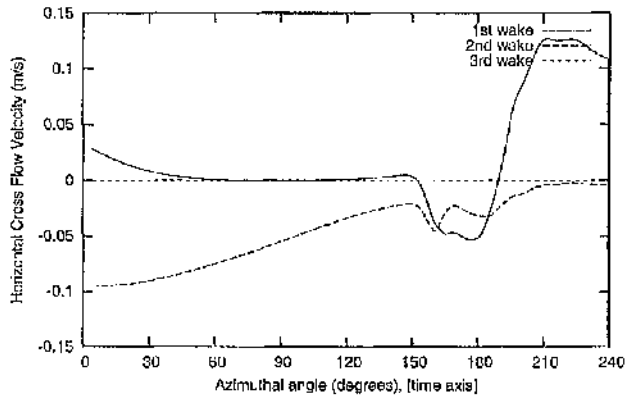
Table C.5: Comparison of peak axial velocity calculated in all test cases at the spanwise location 0.1m above the vortex centre. Freestream velocity = 30 m/s.

	1st wake	2nd wake	3rd wake	4th wake
8 deg.	0.6108	0.6087	0.6353	0.6352
4 deg.	0.6929	0.8948	0.7228	0.7227
2 deg.	0.7083	0.7141	0.7395	0.7394
1 deg.	0.7047	0.7094	0.7359	0.7358

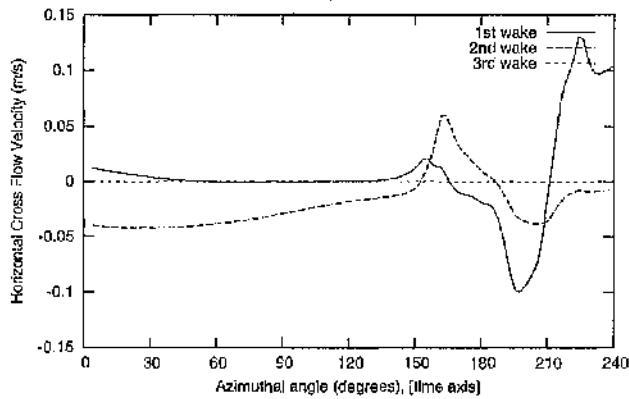
Table C.6: Comparison of peak axial velocity calculated in all test cases at the spanwise location 0.1m below the vortex centre. Freestream velocity = 30 m/s.

Velocity 40m/s

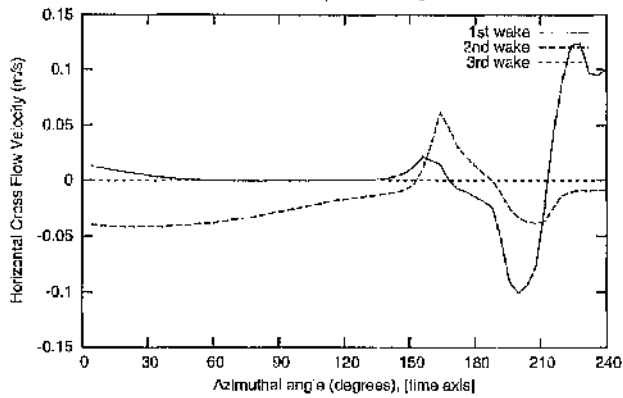
Difference between the 4th wake and the 1st, 2nd, and 3rd wakes with azimuthal step size of 1 degree

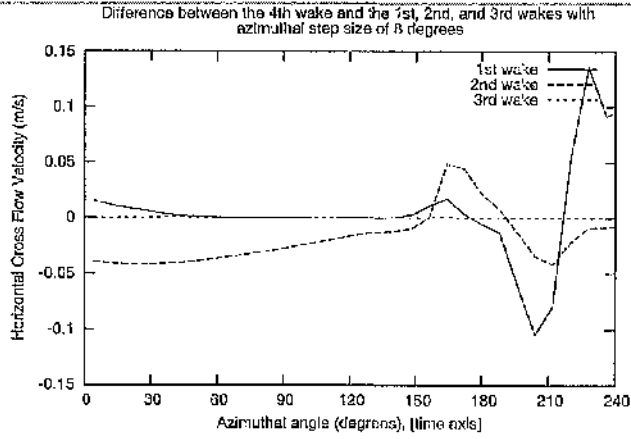


Difference between the 4th wake and the 1st, 2nd, and 3rd wakes with azimuthal step size of 2 degrees



Difference between the 4th wake and the 1st, 2nd, and 3rd wakes with azimuthal step size of 4 degrees





	1st wake	2nd wake	3rd wake	4th wake
8 deg.	1.1334	1.1651	1.1168	1.1164
4 deg.	1.1947	1.2414	1.1799	1.18
2 deg.	1.2499	1.2839	1.2364	1.2362
1 deg.	1.28	1.3187	1.267	1.2669

Table C.7: Comparison of peak axial velocity calculated in all test cases at the spanwise location of the vortex centre. Freestream velocity = 40 m/s.

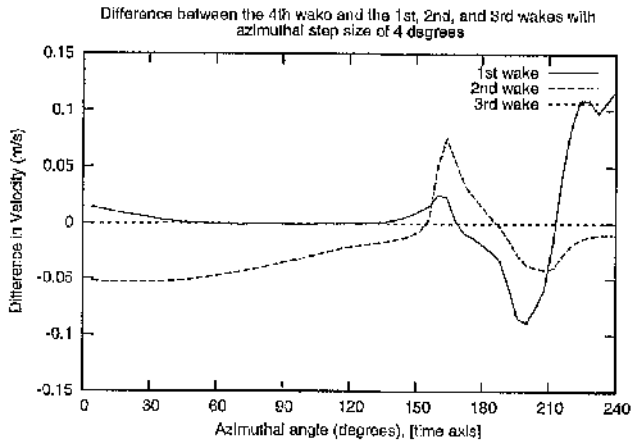
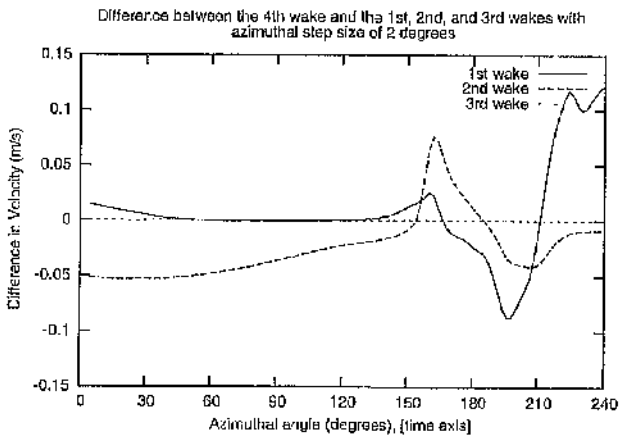
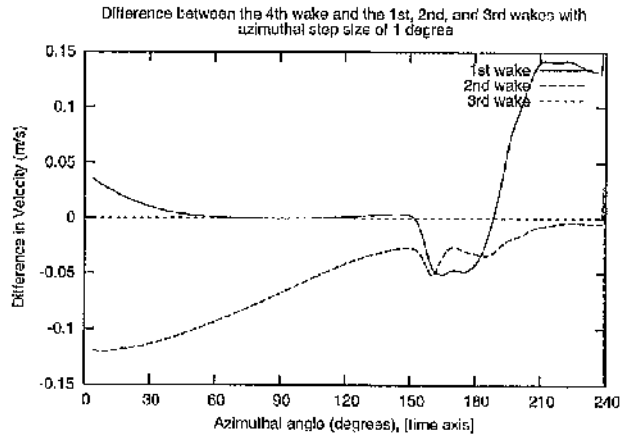
	1st wake	2nd wake	3rd wake	4th wake
8 deg	0.9446	0.973	0.9791	0.979
4 deg	0.922	0.9518	0.9593	0.9593
2 deg	0.9196	0.9547	0.9642	0.9641
1 deg	0.9151	0.9526	0.9617	0.9616

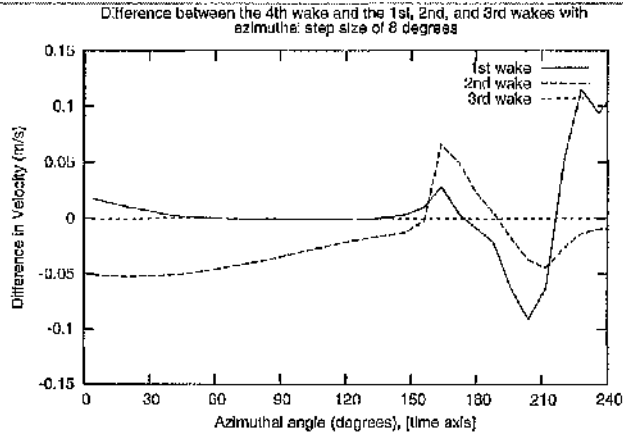
Table C.8: Comparison of peak axial velocity calculated in all test cases at the spanwise location 0.1m above the vortex centre. Freestream velocity = 40 m/s.

	1st wake	2nd wake	3rd wake	4th wake
8 deg	0.8209	0.8373	0.8571	0.8572
4 deg	0.9618	0.9638	1.0026	1.0023
2 deg	0.9952	1.0045	1.0398	1.0397
1 deg	0.9882	1.002	1.0352	1.0351

Table C.9: Comparison of peak axial velocity calculated in all test cases at the spanwise location 0.1m below the vortex centre. Freestream velocity = 40 m/s.

Velocity 50m/s





	1st wake	2nd wake	3rd wake	4th wake
8 deg.	1.2415	1.2791	1.2134	1.2133
4 deg.	1.2971	1.3492	1.2736	1.2736
2 deg.	1.3802	1.4191	1.3548	1.3547
1 deg.	1.3989	1.4451	1.3747	1.3747

Table C.10: Comparison of peak axial velocity calculated in all test cases at the spanwise location of the vortex centre. Freestream velocity = 50 m/s.

	1st wake	2nd wake	3rd wake	4th wake
8 deg.	1.052	1.0928	1.1033	1.1033
4 deg.	1.0584	1.0858	1.0916	1.0915
2 deg.	1.0597	1.0904	1.0848	1.0847
1 deg.	1.0592	1.0923	1.0847	1.0846

Table C.11: Comparison of peak axial velocity calculated in all test cases at the spanwise location 0.1m above the vortex centre. Freestream velocity = 50 m/s.

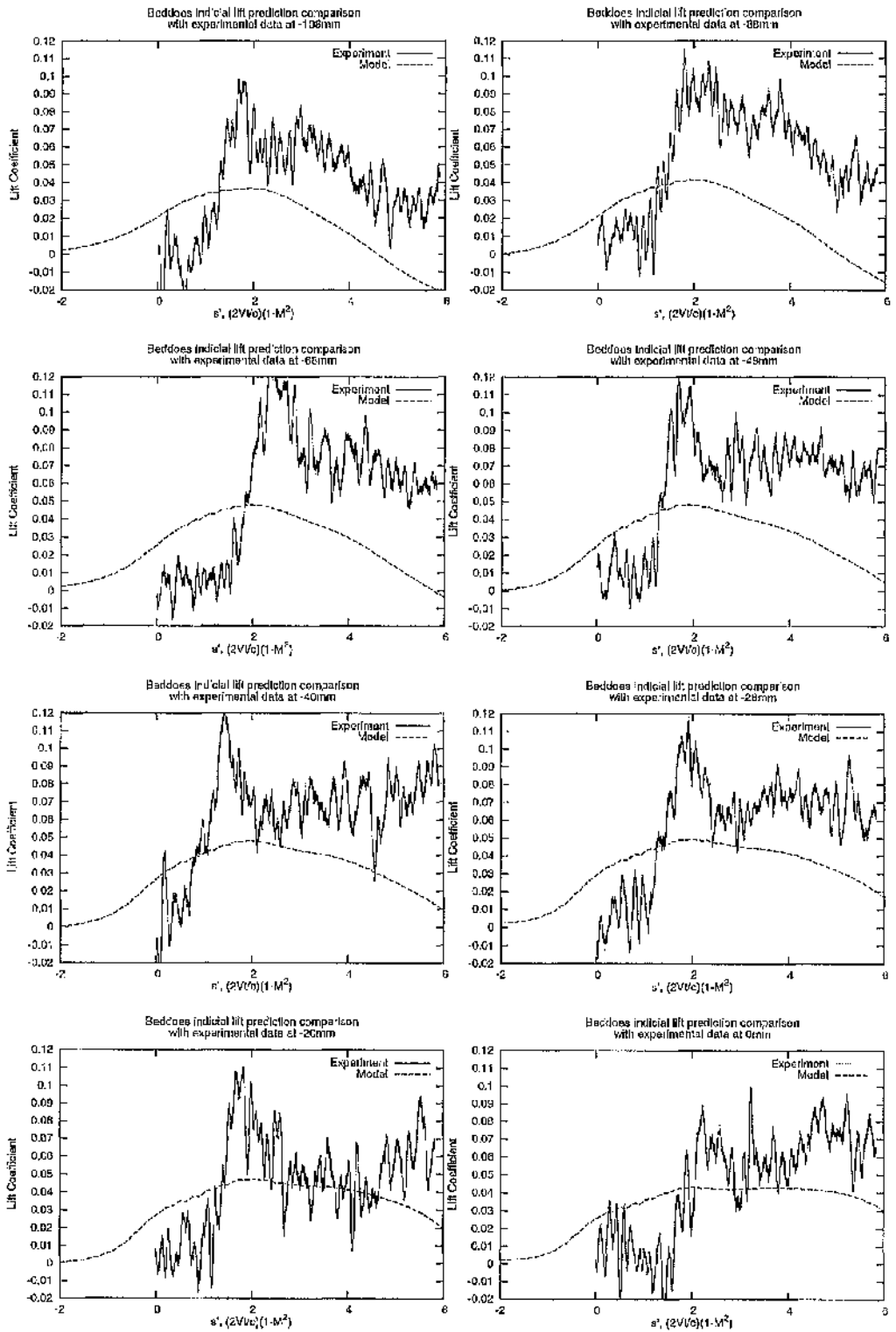
	1st wake	2nd wake	3rd wake	4th wake
8 deg.	1.0045	1.0017	1.0437	1.0436
4 deg.	1.1248	1.1281	1.1728	1.1726
2 deg.	1.1424	1.151	1.1916	1.1914
1 deg.	1.1371	1.1437	1.1864	1.1863

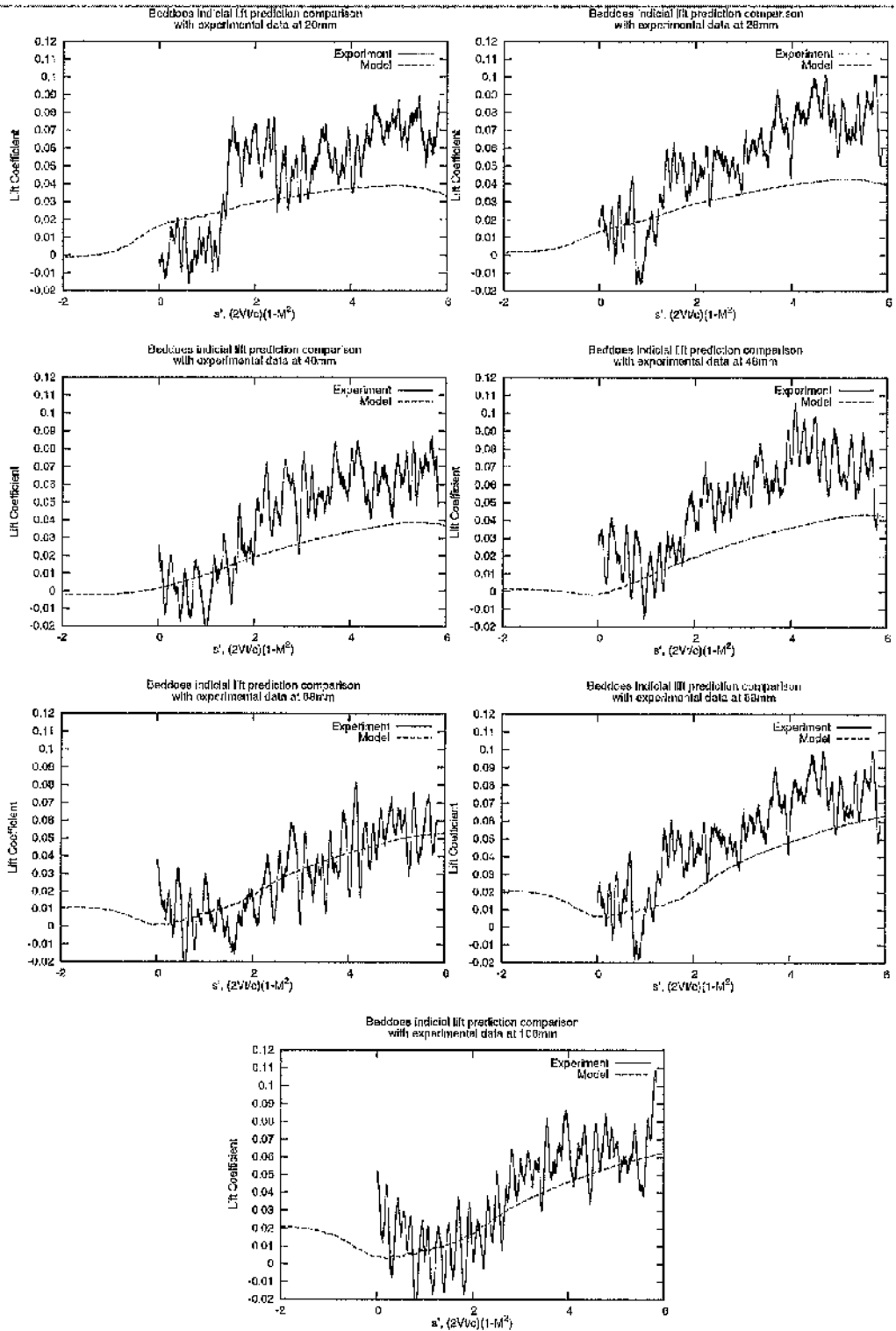
Table C.12: Comparison of peak axial velocity calculated in all test cases at the spanwise location 0.1m below the vortex centre. Freestream velocity = 50 m/s.

Appendix D: Comparison of indicial predictions with experimental data

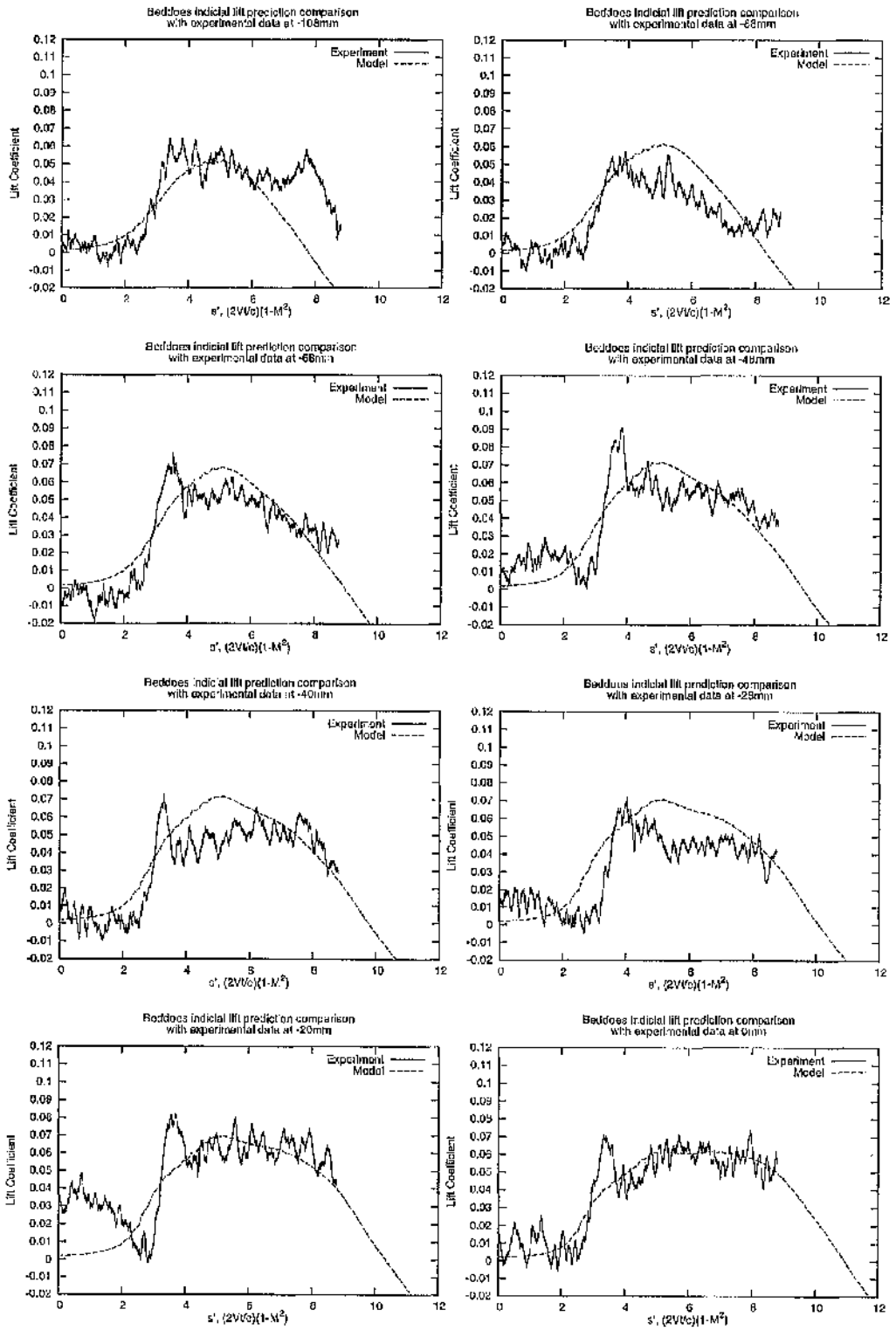
These comparisons show indicial predictions based on the horizontal cross flow extracted from the numerical simulation. In the cases presented below, the angle of incidence of the vortex generator has been reduced so that the circulation over the interacting blade is similar to the experimentally measured circulation.

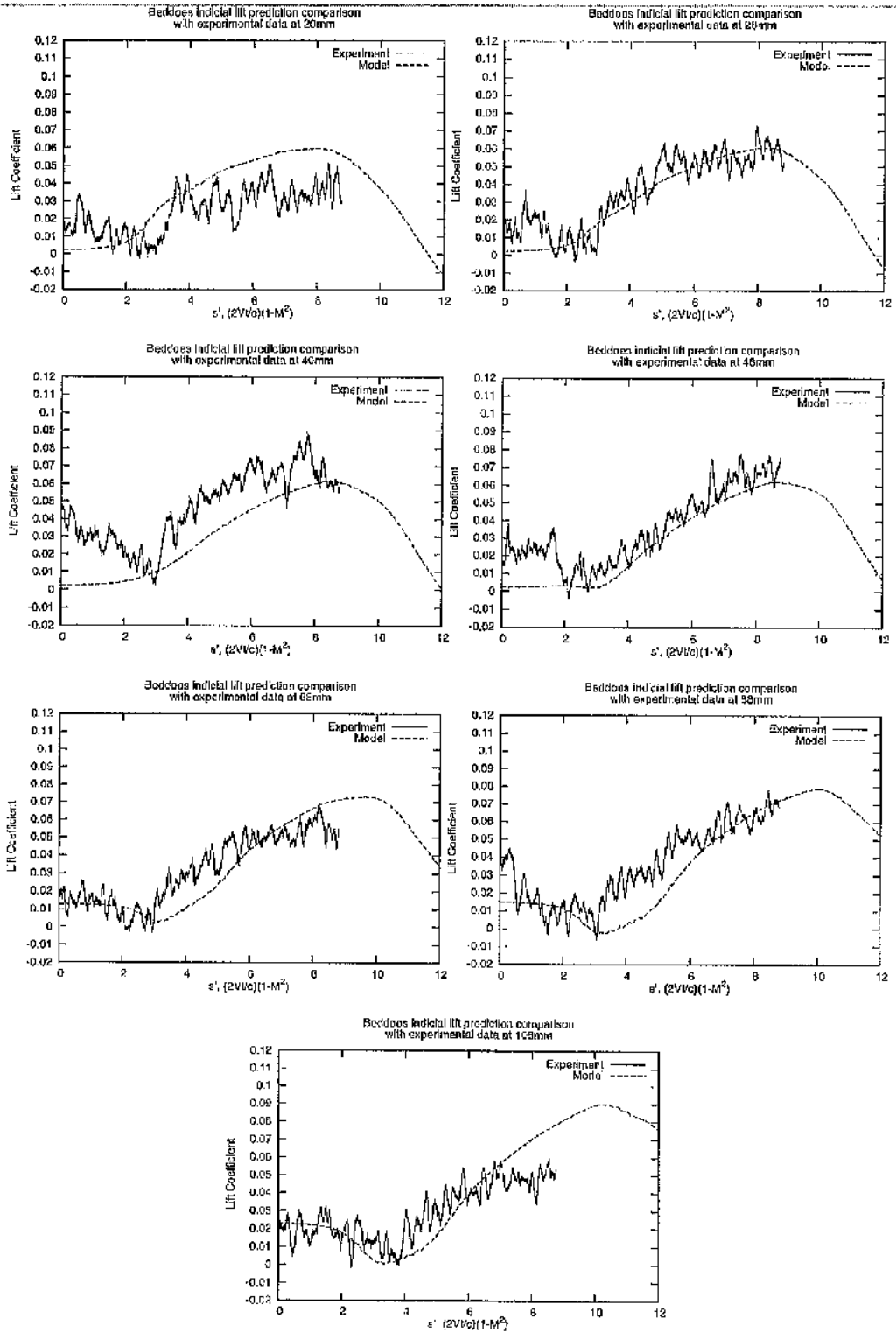
Velocity 20 m/s



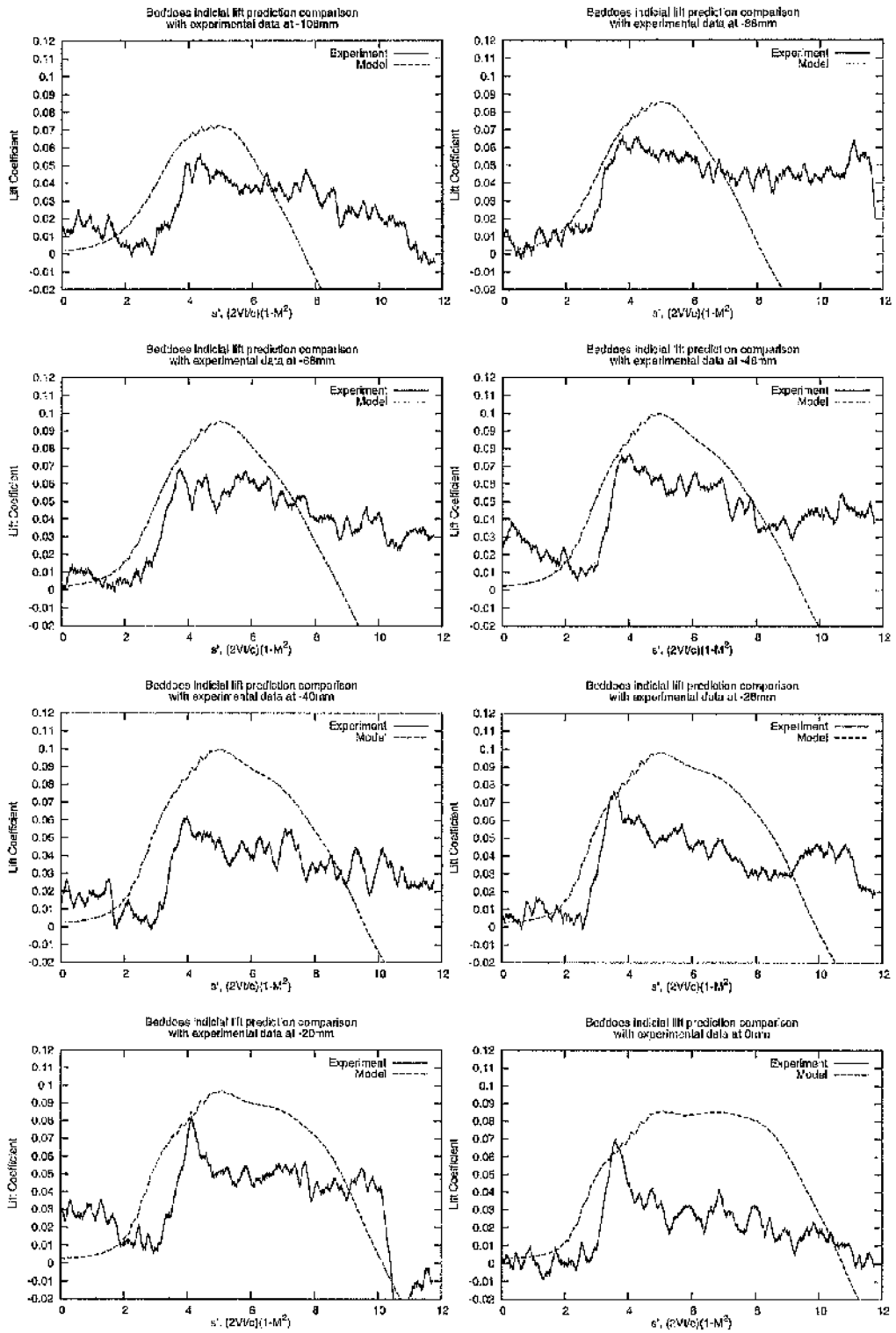


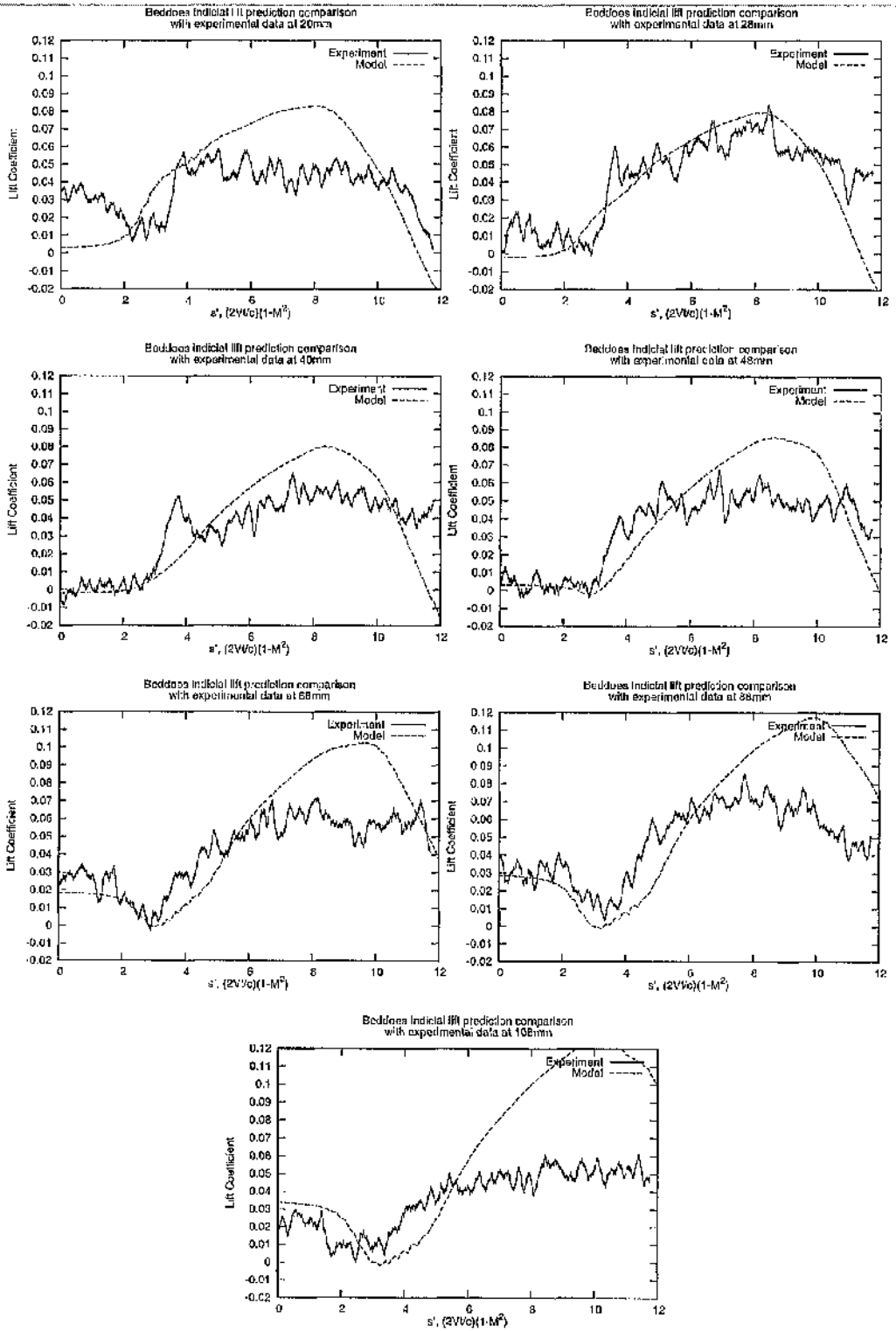
Velocity 30 m/s



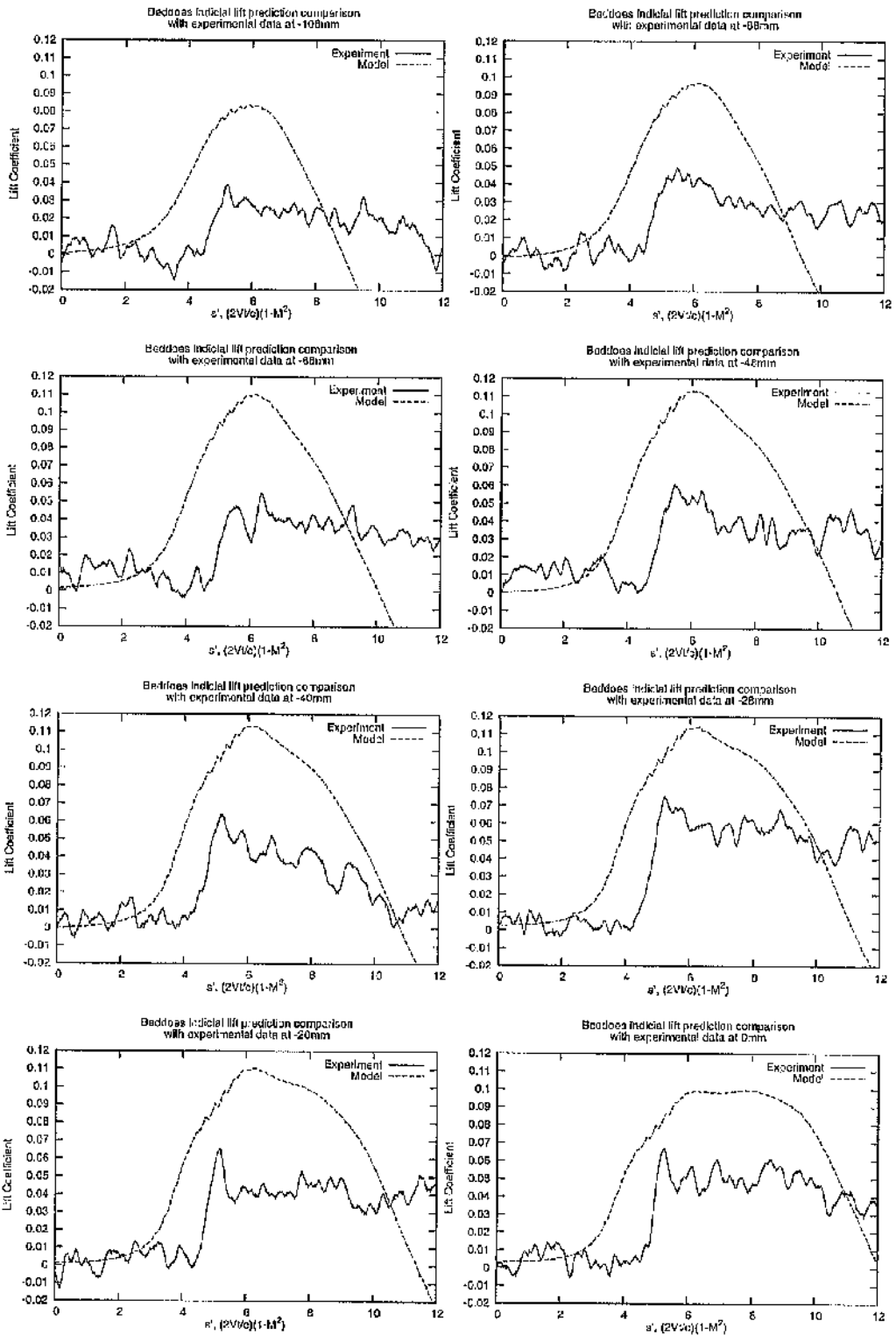


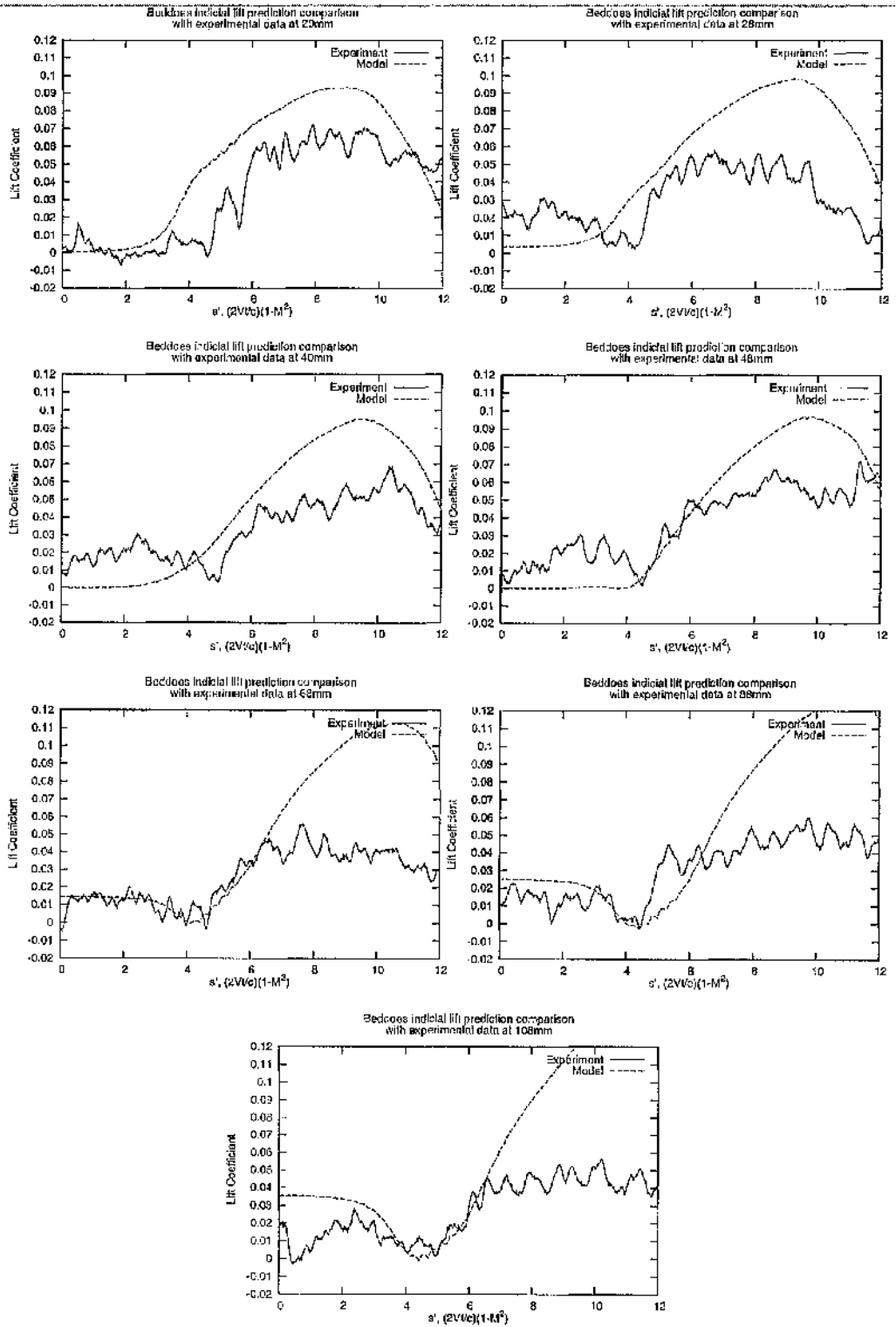
Velocity 40 m/s





Velocity 50 m/s

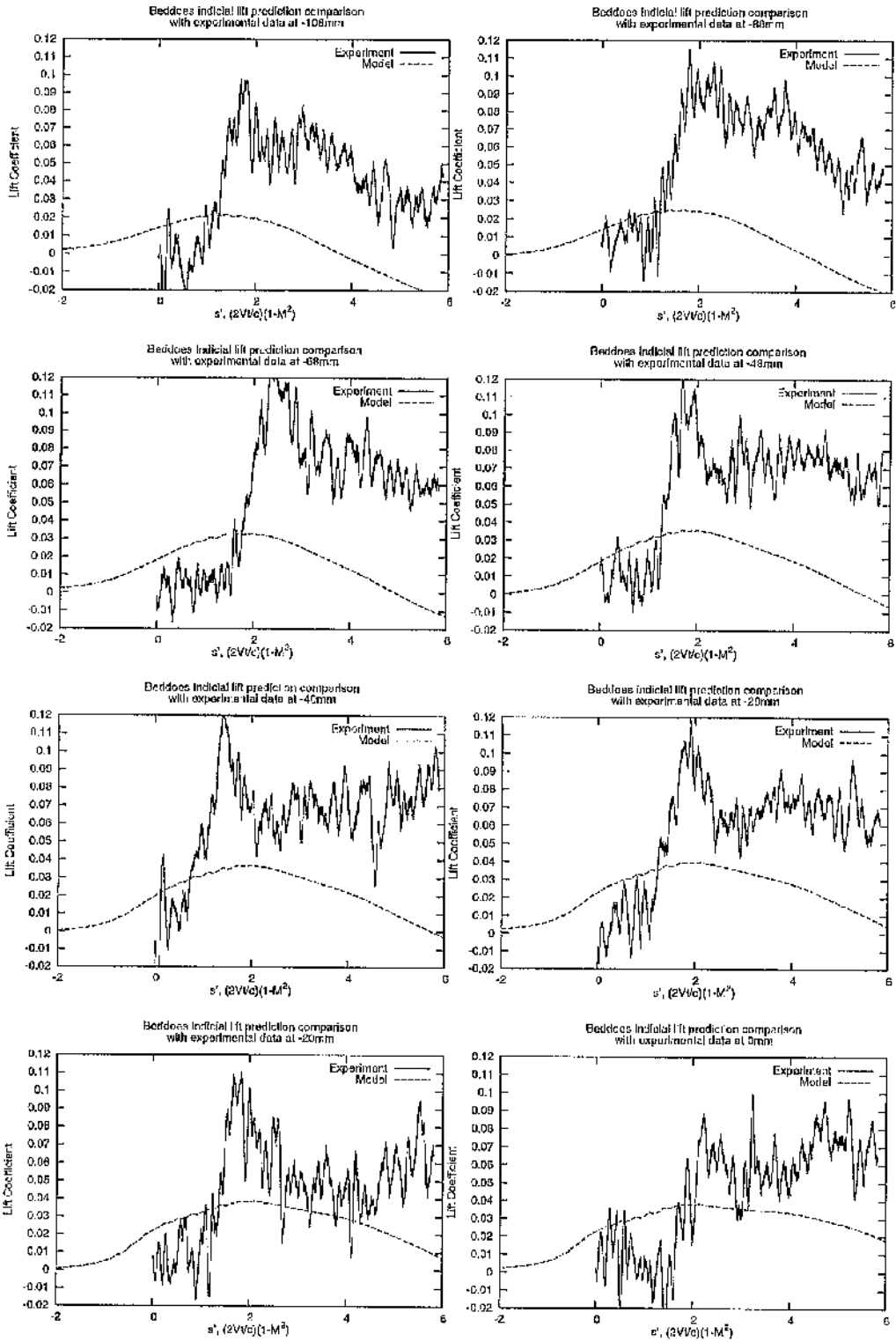


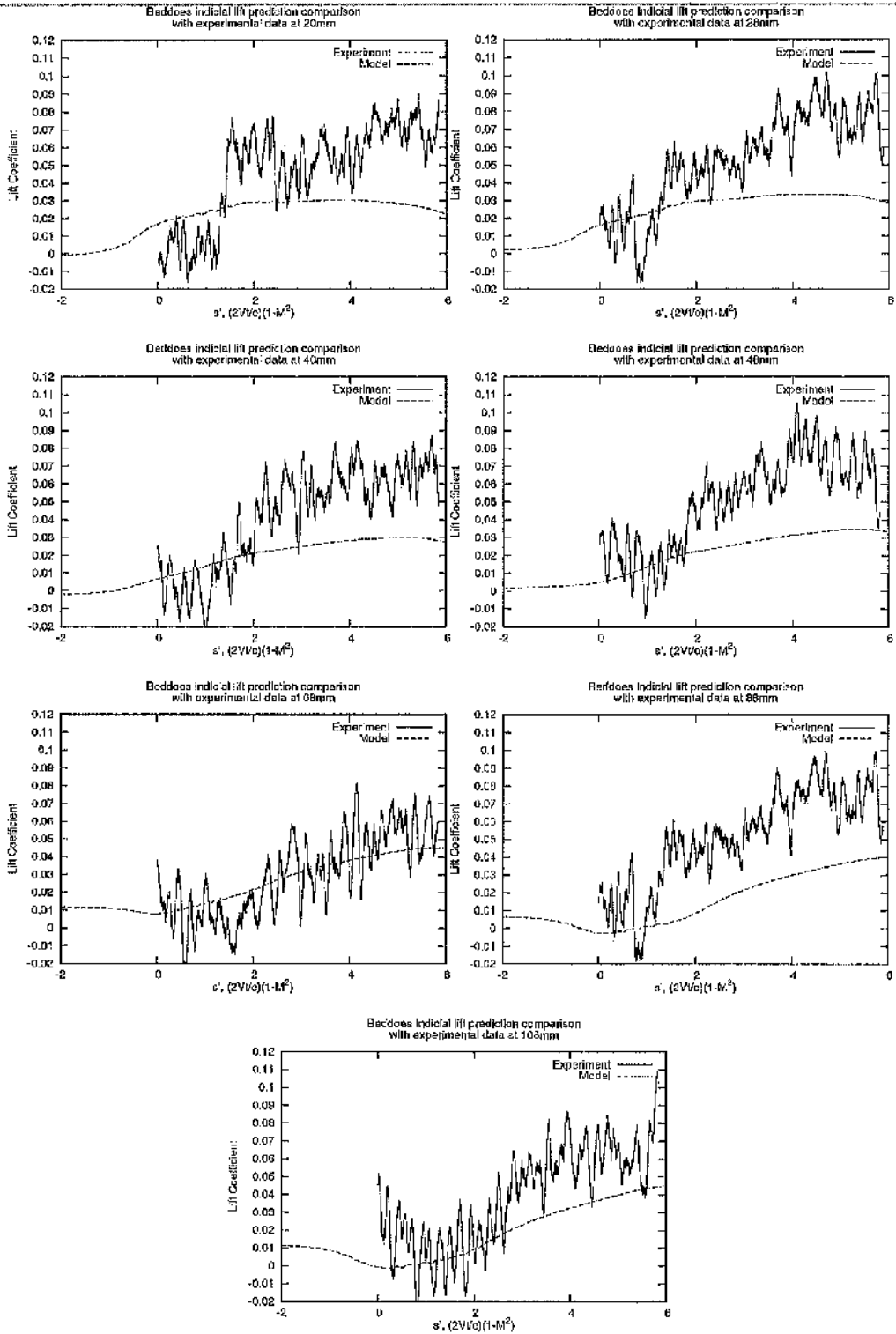


Appendix E: Comparison of indicial predictions with experimental data

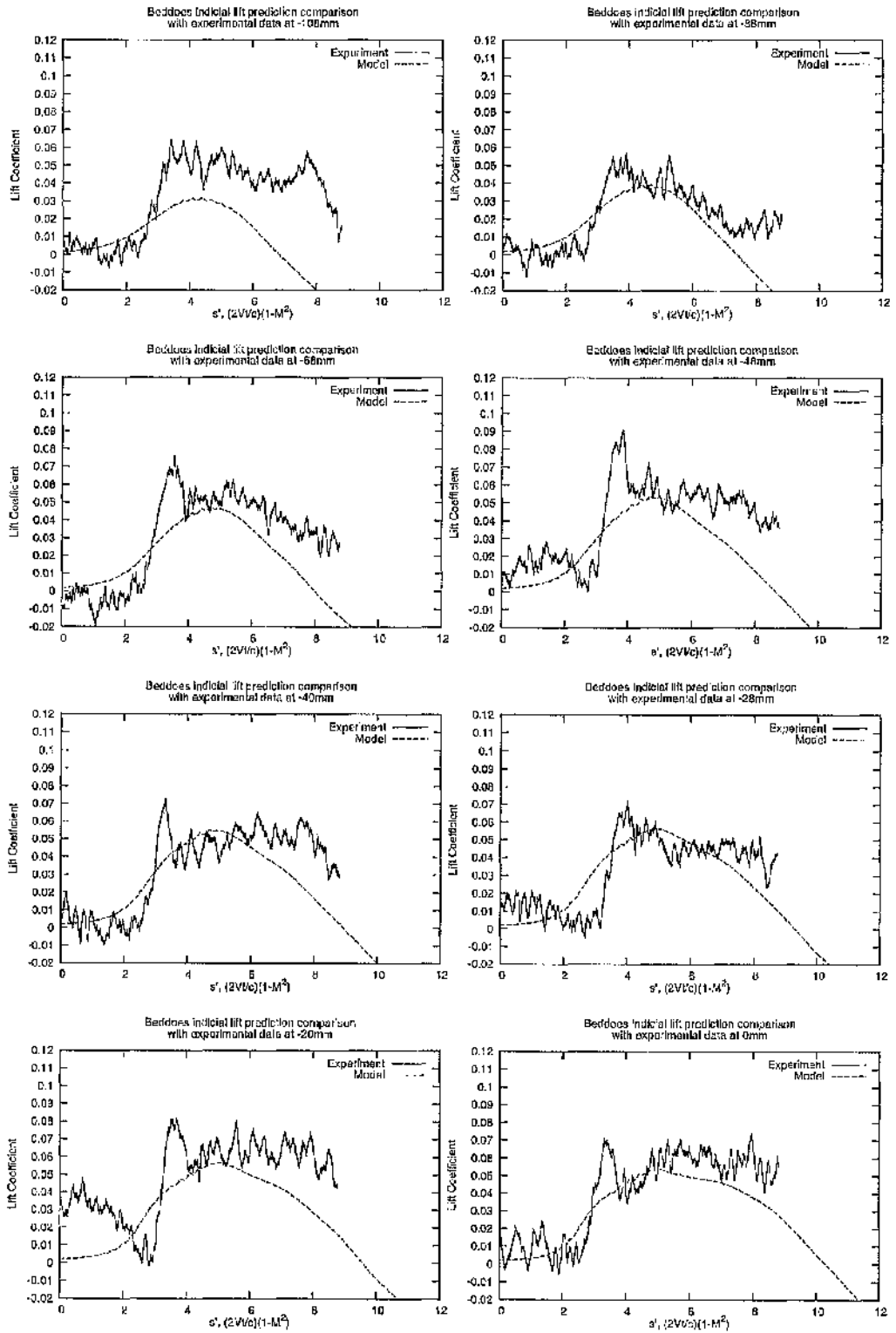
These comparisons show indicial predictions based on the horizontal cross flow extracted from the numerical simulation. In the cases presented below, the angle of incidence of the vortex generator has been reduced so that the circulation over the interacting blade is similar to the experimentally measured circulation.

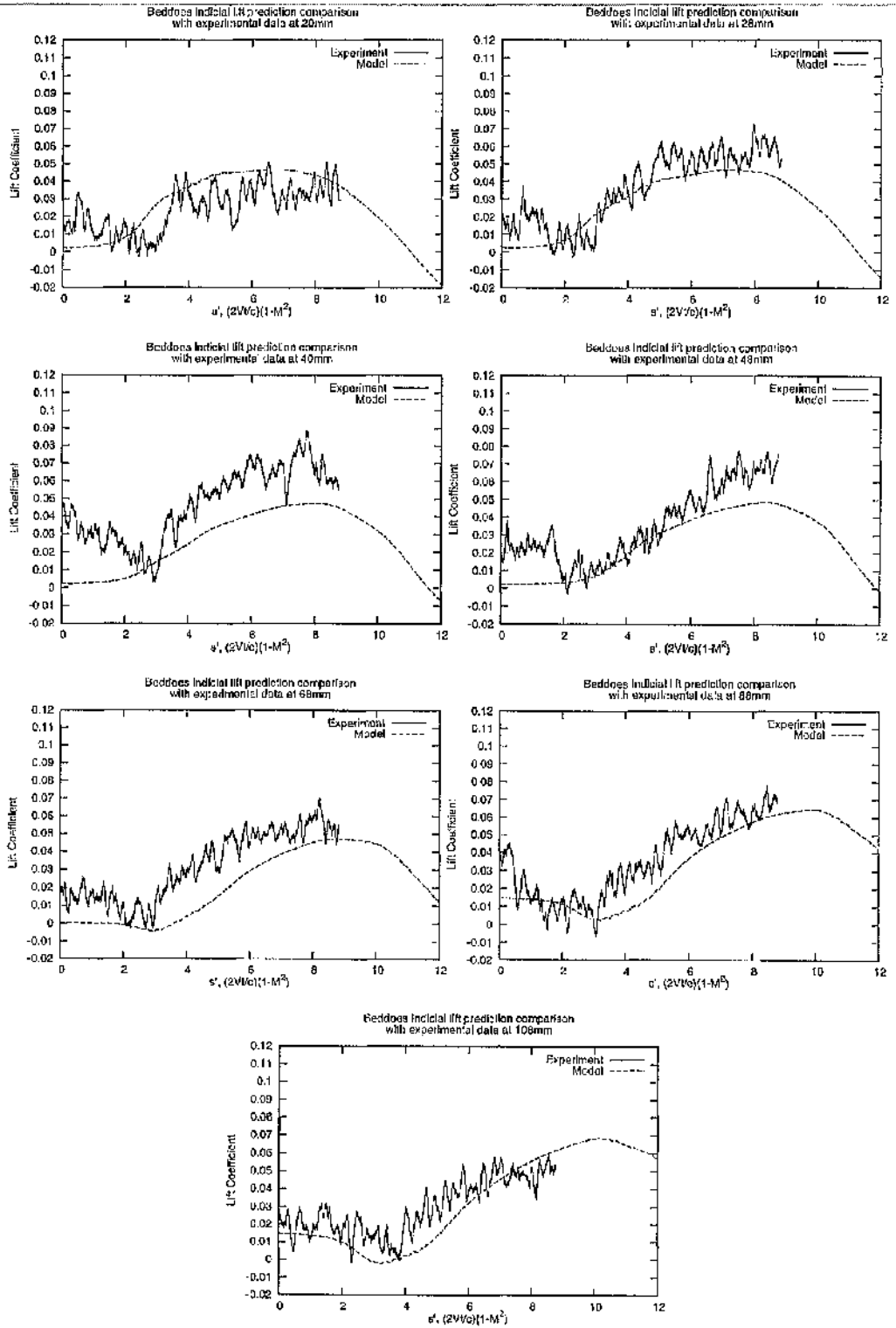
Velocity 20 m/s



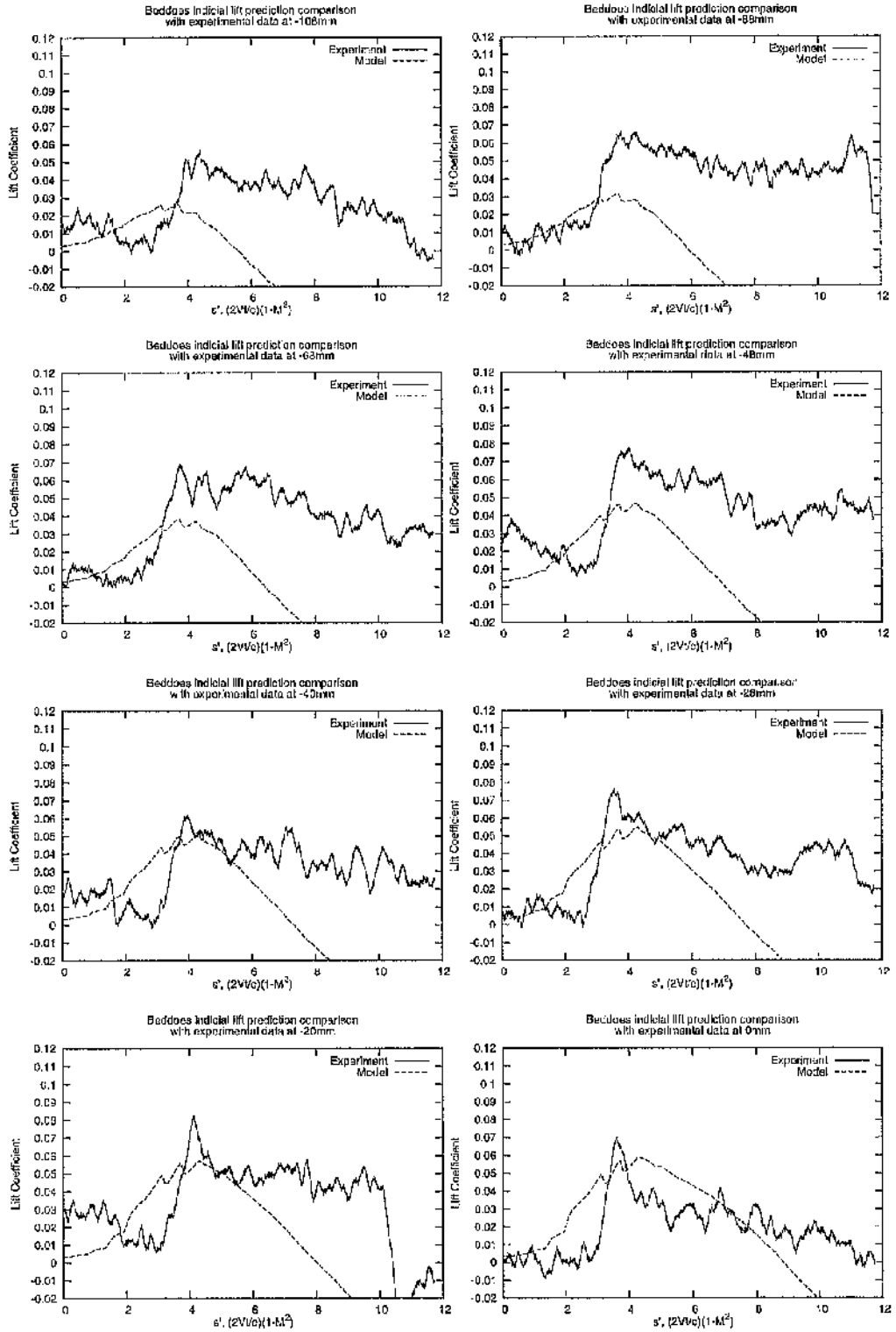


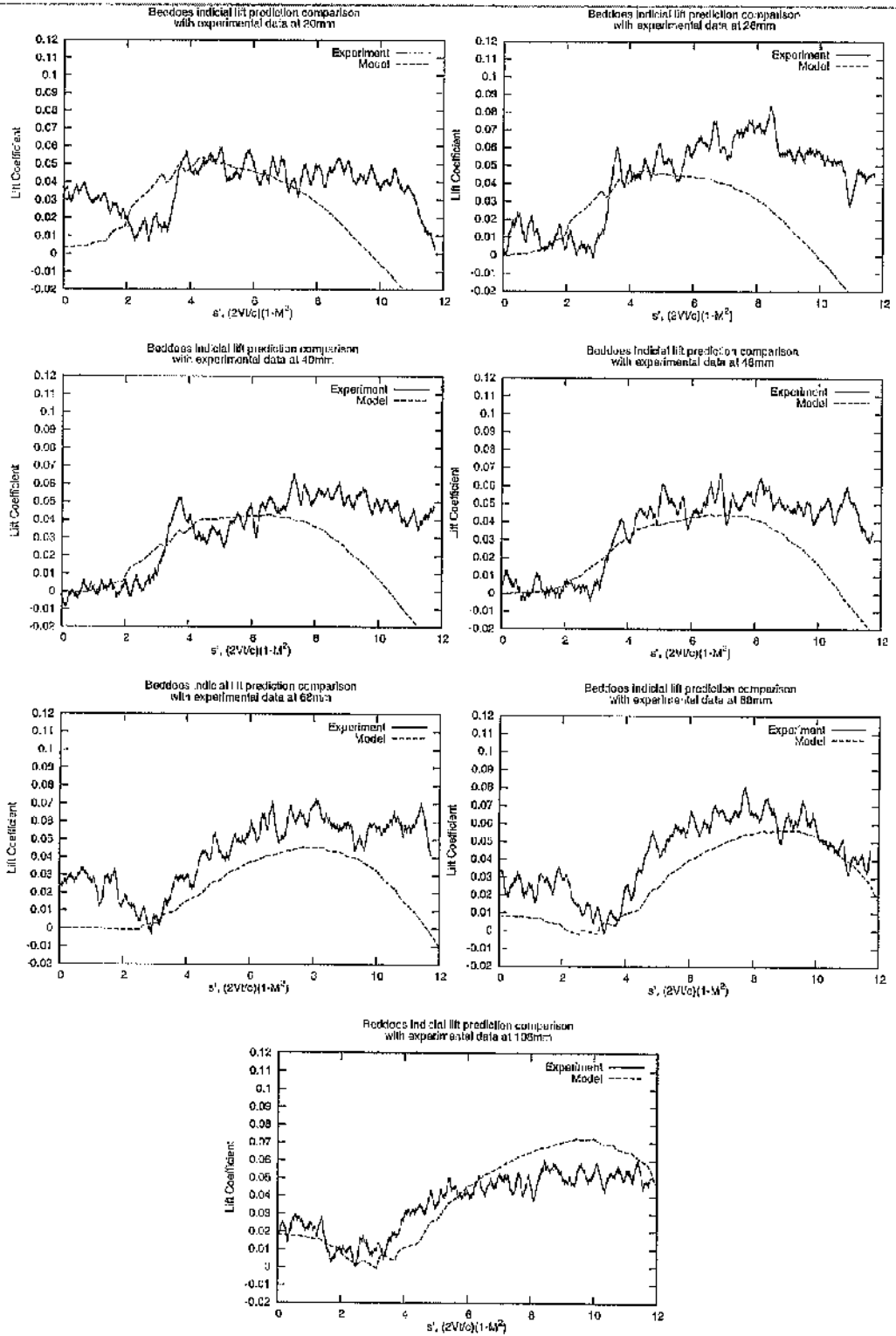
Velocity 30 m/s



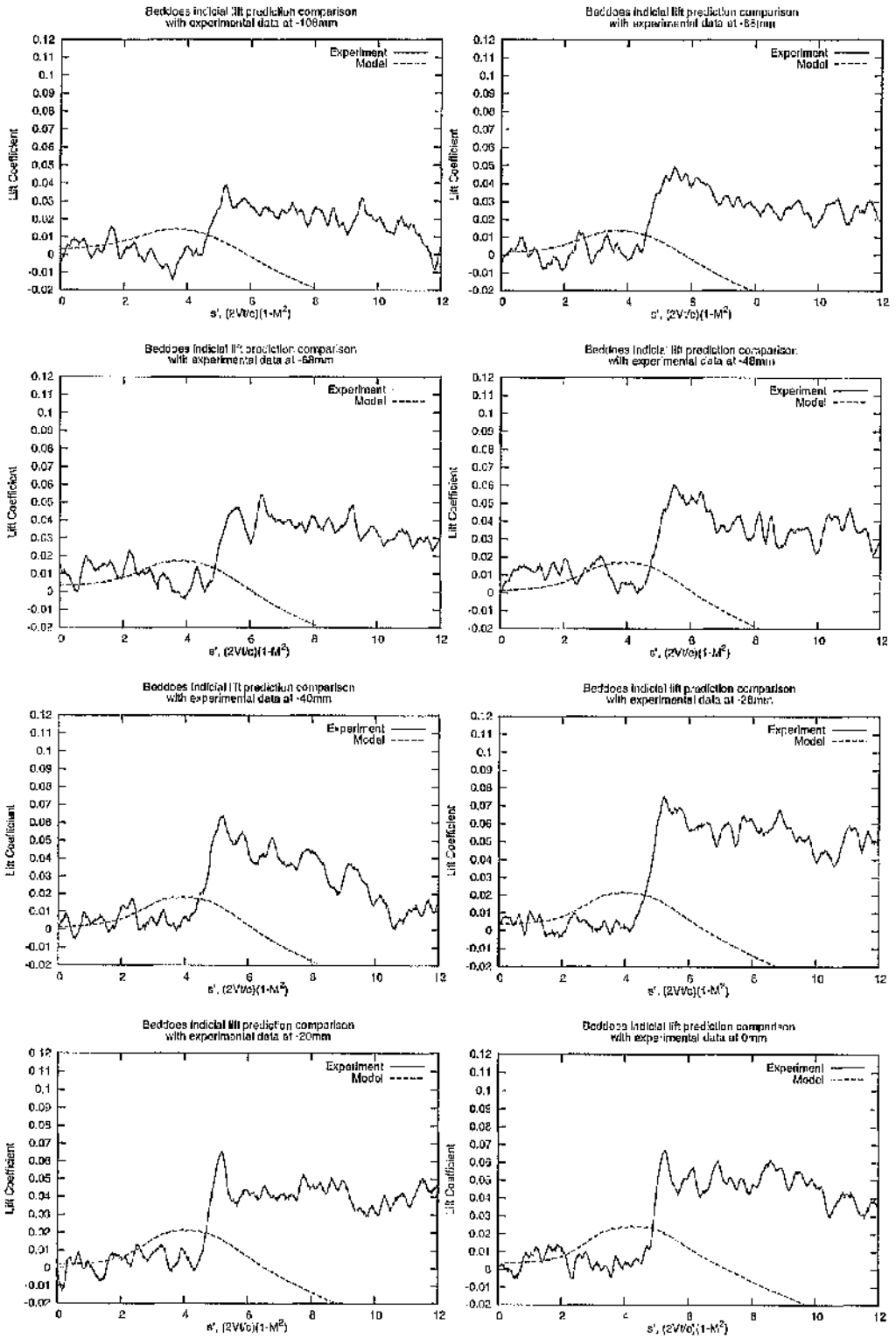


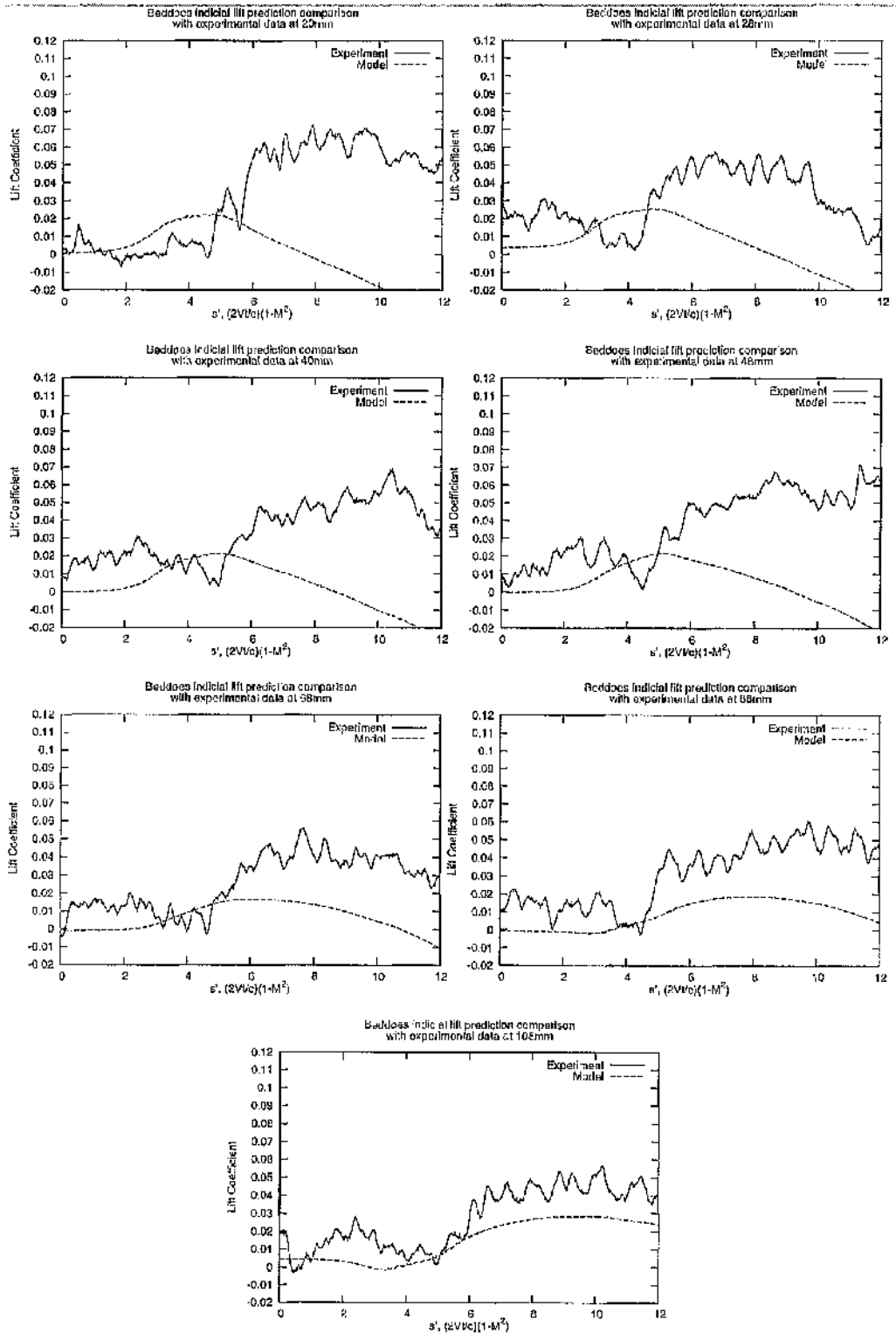
Velocity 40 m/s





Velocity 50 m/s





Appendix F: Parameters Calculated For B-cases Defined in Liu and Marshall (2004)

SET X

Case	IP	TP	ReV	AFP	ReB	Kinematic Viscosity	Velocity [m/s]	Chord [m]	Rc [m/s]	Wo [m/s]	Circulation [m ² /s]
B1	4	0.78	488	0.51	2000	6.875E-03	50	0.275	0.0423	6.375	3.323
B2	10	0.56	45	0.85	1000	1.375E-02	50	0.275	0.0589	4.250	1.851
B3	41	0.42	44	1.8	1000	1.375E-02	50	0.275	0.0786	2.195	0.602
B4	4	0.78	488	3.8	2000	6.875E-03	50	0.275	0.0423	47.500	3.323
B5	4	0.78	245	3.8	1000	1.375E-02	50	0.275	0.0423	47.500	3.323
B6	4	0.78	73	3.8	300	4.588E-02	50	0.275	0.0423	47.500	3.323
B7	4	0.78	488	3	2000	6.875E-03	50	0.275	0.0423	37.500	3.323
B8	16	0.37	250	3	2000	6.875E-03	50	0.275	0.0892	9.375	1.751
B9	33	0.37	125	3	2000	6.875E-03	50	0.275	0.0892	4.545	0.849
B10	4	0.39	966	3.8	2000	6.875E-03	50	0.275	0.0846	47.500	6.646

SETY

Case	IP	TP	ReV	AFP	ReB	Kinematic Viscosity	Velocity [m/s]	Chord [m]	Rc [m/s]	Wo [m/s]	Circulation [m ² /s]
B1	4	0.78	488	0.51	2000	1.45E-05	50	5.800E-04	8.923E-05	6.375	7.008E-03
B2	10	0.56	45	0.85	1000	1.45E-05	50	2.900E-04	6.214E-05	4.250	1.952E-03
B3	41	0.42	44	1.8	1000	1.45E-05	50	2.900E-04	8.266E-05	2.195	6.349E-04
B4	4	0.78	488	3.8	2000	1.45E-05	50	5.800E-04	8.923E-05	47.500	7.008E-03
B5	4	0.78	245	3.8	1000	1.45E-05	50	2.900E-04	4.462E-05	47.500	3.504E-03
B6	4	0.78	73	3.8	300	1.45E-05	50	8.700E-05	1.338E-05	47.500	1.051E-03
B7	4	0.78	488	3	2000	1.45E-05	50	5.800E-04	8.923E-05	37.500	7.008E-03
B8	16	0.37	250	3	2000	1.45E-05	50	5.800E-04	1.881E-04	9.375	3.693E-03
B9	33	0.37	125	3	2000	1.45E-05	50	5.800E-04	1.881E-04	4.545	1.791E-03
B10	4	0.39	966	3.8	2000	1.45E-05	50	5.800E-04	1.785E-04	47.500	1.402E-02

SETZ

Case	IP	TP	ReV	AFP	ReB	Kinematic Viscosity	Velocity [m/s]	Chord [m]	Rc [m/s]	Wo [m/s]	Circulation [m ² /s]
B1	4	0.78	488	0.51	2000	1.45E-05	0.105	0.275	0.0423	1.345E-02	7.008E-03
B2	10	0.56	45	0.85	1000	1.45E-05	0.0527	0.275	0.0589	4.482E-03	1.952E-03
B3	41	0.42	44	1.8	1000	1.45E-05	0.0527	0.275	0.0786	2.315E-03	6.349E-04
B4	4	0.78	488	3.8	2000	1.45E-05	0.105	0.275	0.0423	1.002E-01	7.008E-03
B5	4	0.78	245	3.8	1000	1.45E-05	0.0527	0.275	0.0423	5.009E-02	3.504E-03
B6	4	0.78	73	3.8	300	1.45E-05	0.0158	0.275	0.0423	1.503E-02	1.051E-03
B7	4	0.78	488	3	2000	1.45E-05	0.105	0.275	0.0423	7.909E-02	7.008E-03
B8	16	0.37	250	3	2000	1.45E-05	0.105	0.275	0.0892	1.977E-02	3.693E-03
B9	33	0.37	125	3	2000	1.45E-05	0.105	0.275	0.0892	9.587E-03	1.791E-03
B10	4	0.39	966	3.8	2000	1.45E-05	0.105	0.275	0.0846	1.002E-01	1.402E-02

References

Papers

Affes, H., Conlisk, A.T., "Model for Rotor Tip Vortex-Airframe Interaction, Part 1: Theory", AIAA Journal, Vol. 31, no. 12, 1993, pp. 2263-2273.

Affes, H., Conlisk, A.T., Kim, J.M., Komerath, N.M., "Model for Rotor Tip Vortex-Airframe, Part 2: Comparison with Experiment", AIAA Journal, Vol. 31, No. 12, 1993, pp. 2274-2282.

Affes, H., Xiao, Z., Conlisk, A.T., "The boundary-layer flow due to a vortex approaching a cylinder", Journal of Fluid Mechanics, Vol. 275, 1994, pp. 33-57.

Affes, H., Xiao, Z., Conlisk, A.T., Kim, J.M., Komerath, N.M., "Model for Rotor Tip Vortex-Airframe, Part 3: Viscous Flow on Airframe", AIAA Journal, Vol. 36, No. 3, 1998, pp. 409-415.

Ahmadi A.R., "An Experimental Investigation of Blade-Vortex Interaction at Normal Incidence", Journal of Aircraft, Vol. 23, No. 1, Jan 1986, pp. 47-55.

Amiet, R.K., "Airfoil Gust Response and the Sound Produced by Airfoil-Vortex Interaction", Journal of Sound and Vibration. Vol. 107, 22 June, 1986, pp. 487-506

Beddoes, T.S., "A Synthesis of Unsteady Aerodynamic Effects Including Stall Hysteresis", Vertica, Vol 1, 1976, pp113-123.

Beddoes, T.S., "Representation of Airfoil Behaviour", Vertica, Vol 7 No 2, 1983, pp 183-197.

Beddoes, T.S., "Practical Computation of Unsteady Lift", Vertica, Vol 8 No 1, 1984, pp 55-71.

Beddoes, T.S., "A Near Wake Dynamic Model", in proceedings of the American Helicopter Society National Specialists Meeting on Aerodynamics and Acoustics, February, 1987.

Beddoes, T.S., "Two and Three Dimensional Indicial Methods for Rotor Dynamic Airloads", presented at AHS/National Specialist's Meeting on Rotorcraft Dynamics, Arlington, Texas, Nov 1989.

Beddoes, T.S., "A 3-D Separation Model for Arbitrary Planforms", presented at 47th Annual Forum of the American Helicopter Society, Phoenix, Arizona, May 1991.

Bhagwat, M.J., Leishman, J.G., "Generalized Viscous Vortex Model for Application to Free-Vortex Wake and Aeroacoustic Calculations", AHS International, 58th Annual Forum Proceedings, Volume II, Montreal, Canada, June 2002, pp. 2042-2057.

Bi, N-B., Leishman, J.G., Crouse, G.L. Jr., "Investigation of Rotor Tip Vortex Interactions with a Body", Journal of Aircraft, Vol. 30, No. 6, 1993, pp. 879-888.

Boxwell, D.A., Schmitz, F.H., Spletstoesser, W.R., Schultz, K.J., "Helicopter Model Rotor-Blade Vortex Interaction Impulsive Noise: Scalability and Parametric Variations", Journal of American Helicopter Society, January, 1987, pp. 3-12.

Brooks, T.F., Marcolini, M.A., Pope, D.S., "Main Rotor Broadband Noise Study In the DNW", Journal of American Helicopter Society, Vol. 34, No. 2, 1989, pp. 3-12.

Caradonna, F.X., Strawn, R.C., Bridgeman, J.O., "An Experimental and Computational Study of Rotor-Vortex Interactions", Vertica, Vol. 12, No. 4, 1988, pp. 315-327.

Caradonna, F.X., Lautenschlager, J.L., Silva, M.J., "An Experimental Study of Rotor-Vortex Interactions", AIAA Paper 88-0045, 1988.

Cary, C.M., "An Experimental Investigation of the Chopping of Helicopter Main Rotor Tip Vortices by the Tail Rotor", NASA CR-177457, 1987.

Cook, C.V., "A Review of Tail Rotor Design and Performance", Vertica, Vol. 2, 1979, pp. 163-181.

Copland C.M., Coton FN, Galbraith R.A.McD., "A Study of Helicopter Tail Rotor Interaction: Phase 1 - Proof of Concept", 24th European Rotorcraft Forum, 1998.

Copland, C.M., Coton, F.N., Galbraith, R.A.McD., "Use of a Numerical model in the Conceptual Design of a New Blade Vortex Interaction Facility", Internal Report, University of Glasgow, Report No. 9509, 1995.

Copland, C.M., "The Generation of Transverse and Longitudinal Vortices in low Speed Wind Tunnels", PhD Thesis, Department of Aerospace, University of Glasgow, 1997.

Coton, F.N., Iglesia Moreno, F., Galbraith, R.A.McD., "A Three-Dimensional model of Low Speed Blade-Vortex Interaction", 20th European Rotorcraft Forum, Paper 18, October 1994

Coton, F.N., Galbraith, R.A.McD., Copland, C.M., "A Feasibility Study into the Generation of Transverse and Longitudinal Vortices in Low Speed Wind Tunnels", Departmental Report 9509, Aerospace Department, University of Glasgow, 1995.

Coton, F.N., Galbraith, R.A.McD., Wang, T., Newman, S.J., "A Wind-Tunnel Based Study of Helicopter Tail Rotor Blade Vortex Interaction", The Aeronautical Journal, May, 2004, pp.237-244.

Devenport, W.J., Glegg, S.A.L., Sharma, G., "Turbulence Measurements in Trailing Vortex for B.W.I. Noise Prediction", Report to NASA Langley, Grant NAG-1-1119, 1992.

Doolan, C.J., Coton, F.N., Galbraith, R.A.McD., "Three-dimensional vortex interactions with a stationary blade", The Aeronautical Journal, Dec 1999a.

Doolan, C.J., Coton, F.N., Galbraith, R.A.McD., "Normal vortex interaction with a loaded symmetrical blade", 25th European Rotorcraft Forum, Rome, 1999b.

Doolan C.J., Coton, F.N., Galbraith R.A.McD., "Measurement of Three-Dimensional Vortices using a Hot Wire Anemometer", 30th AIAA Fluid Dynamics Conference, Norfolk, VA, July, 1999c.

Doolan, C.J., Coton, F.N., Galbraith, R.A.McD., "The Effect of Preceding Blade on Orthogonal Blade Vortex Interaction", AHS 56th Annual Forum, May 2000, Accepted March 2001a.

Doolan, C.J., Coton, F.N., Galbraith, R.A.McD., "Surface Pressure Measurements of the Orthogonal Vortex Interaction", AIAA Journal, Vol. 39, No. 1, 2001b, pp. 88-95.

Early, J.M., Green, R.B., "Phenomena observed during the Orthogonal Blade-Vortex Interaction", 4th International Symposium on Particle Image Velocimetry, Gottingen, Germany, Sept 17-19, 2001.

Early, J.M., Green, R.B., Coton, F.N., "Flow visualization of the orthogonal blade-vortex interaction using particle image velocimetry", *The Aeronautical Journal*, March 2002.

Ellin, A.D.S., "Lynx main rotor/tail rotor interactions: mechanisms and modelling", *Journal of aerospace Engineering, Proceedings of the Institute of Mechanical Engineers*, Vol.208, 1994.

Fitzgerald, J, Kohlhepp, F., "Research Investigation of Helicopter Main Rotor/Tail Rotor Interaction Noise", NASA Report 4143, 1986.

George, A.R., Chou, S.T., "Helicopter Tail Rotor Blade-Vortex Interaction Noise", NASA Contractor Report, Grant NAG 2-379, March 1987.

Glegg, S.A.L., "Significance of Unsteady Thickness Noise Sources", *AIAA Journal*, Vol. 25, No. 6, June, 1987, pp. 839-844.

Glegg, S.A.L., "The Prediction Blade-Wake Interaction Noise Based on a Turbulent Vortex Model", *AIAA Paper 89-1134*, April 1989.

Glegg, S.A.L., "The Prediction of Blade-Vortex Interaction Noise Based on a Turbulent Vortex Model", *AIAA Journal*, Vol. 29, No. 10, 1991, pp. 1545-1551.

Green, R.B., Doolan, C.J., "PIV Measurements of the Orthogonal Blade-Vortex Interaction", 3rd International Workshop on PIV, Paper 136, Santa Barbara, USA, 1999.

Green R.B., Doolan, C.J., Cannon, R.M., "Measurements of the Orthogonal Blade-Vortex Interaction using a Particle Image Velocimetry Technique", *Experiments in Fluids*, Vol. 29, 2000, pp. 369-379.

Ham, N.D., "Some Conclusions from an investigation of Blade-Vortex Interaction", *Journal of American Helicopter Society*, Oct 1975, pp. 26-31.

Hancock, G.J., "Aerodynamic Loading Induced on a Two-Dimensional Wind by a Free Vortex in Incompressible Flow", *The Aeronautical Journal*, Vol. 75, June 1971, pp. 413-416.

Hawkings, D.L., "Theoretical Models of Helicopter Rotor Noise", NASA Langley Res. Center Helicopter Acoustics see N78-32816 23-71, 1978, pp. 89-108.

Hess, J.L., Smith, A.M.O., "Calculation of Nonlifting Potential Flow About Arbitrary Three-Dimensional Bodies", *Journal of Ship Research*, September, 1964, pp. 22-44.

Horner, M.B., Saliveros, E., Galbraith, R.A.McD., "An Experimental Investigation of the Oblique Blade-Vortex Interaction", *Aeronautical Journal*, May 1992, pp. 184-191.

Horner, M.B., Saliveros, E., Kokkalis, A., Galbraith, R.A.McD., "Results from a Set of Low Speed Blade-Vortex Interaction Experiments", *Experiments in Fluids*, 14, 1993, pp.341-352.

Horner, M.B., Galbraith, R.A.McD., Coton, Stewart, J.N., Grant, I, "Examination of Vortex Deformation During Blade-Vortex Interaction", *AIAA Journal*, Vol. 34, No. 6, 1996, pp. 1188-1194.

Jacobs, E.W., Mancini, J., Visintainer, J.A., Jackson, T.A., "Acoustic Flight Test Results for the Sikorsky S-76 Quiet Tail Rotor at Reduced Tip Speed", Presented at the American Helicopter Society 53rd Annual Forum, April, 1997.

Johnston, R.T, Sullivan, J.P., "Unsteady Wing Surface Pressures in the Wake of a Propeller", *AIAA Aerospace Sciences Meeting and Exhibit*, 30th, Reno, NV, USA, Jan, 1992.

Jones, R. T., "The Unsteady Lift of a Wing of Finite Aspect Ratio," *NACA Report 681*, 1940.

von Karman, Th., and Sears, W.R., "Airfoil Theory for Non-Uniform Motion," *Journal of the Aeronautical Sciences*, Vol. 5, No. 10, 1938, pp. 379-390.

Kim, J.N., Komerath, N.M., "Summary of the Interaction of a Rotor Wake with a Circular Cylinder", *AIAA Journal*, Vol. 33, No. 3, 1995, pp.470-478.

Kokkalis, A., Galbraith, R.A.McD., "Results from the Glasgow University Blade-Vortex Interaction Facility", 13th European Rotorcraft Forum, Arles, France, 1987.

Krisnamoorthy, S., Marshall, J.S., "Three-Dimensional Blade-Vortex Interaction in the Strong Vortex Regime", *Physics of Fluids*, Vol. 10, no. 11, 1998, pp. 2828-2845.

Kussner, H.G., "Zusammenfassender Bericht über den instationären Auftrieb von Flügeln", *Luftfahrtforschung* Bd. 13, 1936, pp. 410-424.

Lee, D.J., Smith, C.A., "Distortion of the Vortex Core During Blade-Vortex Interaction", AIAA Paper 87-1243, 1987.

Lee, D.J., Smith, C.A., "Effect of Vortex Core Distortion on Blade-Vortex Interaction", AIAA Journal, Vol. 29, No. 9, 1991, pp.1355-1362.

Leishman, J.G., Beddoes, T.S., "A Semi-Empirical Model for Dynamic Stall", presented at 42nd Annual Forum of the American Helicopter Society, Washington, D.C., June 1986

Leishman, J.G., Bi, Nai-pei, "Aerodynamic Interactions Between a Rotor and a Fuselage in Forward Flight", Journal of the American Helicopter Society, July 1990, pp.22-31.

Leishman, J.G., "Indicial Lift Approximations for Two-Dimensional Subsonic Flow as Obtained from Oscillatory Measurements", Journal of Aircraft, Vol. 30, No. 3, May-June 1993, pp. 341-351.

Leishman, J.G., "Challengers in modelling the unsteady Aerodynamics of Wind Turbines", 21st ASME Wind Energy Symposium and the 40th Aerospace Sciences Meeting, Reno, NV, AIAA 2002-0047, 2002.

Leverton, J.W., Pollard, J.S., Will, C.R., "Main Rotor Wake/Tail Rotor Interaction", Vertica, Vol. 1, 1977, pp. 213-221.

Leverton, J.W., Pike, T.C., "The Importance of Tail Rotor Interaction as an Acoustic Source", Presented at AHS 49th Annual Forum, Missouri, May, 1993.

Lighthill, M. J. "On sound generated aerodynamically I. General theory", Proc. Royal Society London, 1952.

Liou, S., Komerath, N., McMahon, H., "Measurement of Transient Vortex-Surface Interaction Phenomena", 27th Aerospace Sciences Meeting, January 9-12, Reno, Nevada, 1989.

Liu X, Marshall JS. Blade penetration into a vortex core with and without axial core flow. *Journal Fluid Mechanics*, 519:81–103, 2004.

Lorber, P.F., "Aerodynamic results of a pressure instrumented model rotor test a DNW", 4th AHS Forum, Washington D.C., USA, 1990

Lowson, M.V., "The Sound Field Singularities in Motion", Wyle Laboratories -- Huntsville, Report WR 64-10, Dec. 1964.

Lundgren, T.S., Ashurst, W.T., "Area-varying waves on curved vortex tubes with application to vortex breakdown", *Journal of Fluid Mechanics*, Vol. 200, 1989, pp.283-307.

Marshall, J.S., "Vortex Cutting by a Blade, Part I: General Theory and a Simple Solution", *AIAA Journal*, Vol. 32, No. 6, pp. 1145-1150, 1994a.

Marshall, J.S., Yalamanchili, R., "Vortex Cutting by a Blade, Part II: Computation of Vortex Response", *AIAA Journal*, Vol. 32, No. 7, 1994b, pp. 1428-1436.

Marshall, J.S., Krisnamoorthy, S., "On the instantaneous cutting of columnar vortex with non-zero axial flow", *Journal of Fluid Mechanics*, Vol. 351, 1997, pp. 41-74.

Martin, R.M., Burley, C.L., Elliott, J.W., "Acoustic Test of a Model Rotor and Tail Rotor: Results for the Isolated Rotors and Combined Configuration", *NASA Technical Memorandum 101550*, February 1989.

McCroskey, W.J., "Some rotorcraft applications of computational fluid dynamics", *NASA TM 100066*, 1988.

Mazelsky, B., "Numerical Determination of Indicial Lift of a Two-Dimensional Sinking Airfoil at Subsonic Mach Numbers From Oscillatory Lift Coefficients With Calculations for Mach No. 0.7", *NACA Technical note 2562*, Dec 1951.

Pegg, R.J., Shidler, P.A., "Exploratory Wind Tunnel Investigation of the Effect of the Main Rotor Wake on Tail Rotor Noise", *NASA CP-2052*, Pt. 1, 1978, pp. 205-219.

Quakenbush TR, Bliss DB, Mahajan A. "High resolution flow field prediction for tail rotor aeroacoustics". *Proceedings of the 45th American Helicopter Society Forum*, Boston, May 1989.

Resienthel, P.H., "Development of a Nonlinear Indicial model for Maneuvering Fighter Aircraft", *AIAA 96-0896*, 1996.

Reisenthel, P.H., Bettencourt, M.T., "Extraction of Nonlinear and Critical State Responses from Experimental Data", AIAA 99-0764, 1999.

Renzoni, P., Mayle, R.E., "Incremental Force and Moment Coefficients for a Parallel Blade-Vortex Interaction", AIAA Journal, Vol. 29, No. 4, 1991, pp. 6-13.

Rockwell, D., "Vortex-Body Interactions", Annual Review of Fluid Mechanics, Vol. 30, 1998, pp.199-229.

Schlinker, R. H. Amiet, R. K., "Rotor-vortex interaction noise", AIAA, Aeroacoustics Conference, 8th Atlanta, GA, Apr. 11-13, 1983.

Schultz, K.-J., Splettstoesser, W.R., "Model Tail Rotor Noise Study in the DNW – Measured Acoustics, Blade Pressures, Noise Predictions –", 18th European Rotorcraft Forum, paper no. 78, Avignon, France, September 15-18, 1992.

Schultz, K.-J., Splettstoesser, W.R., "Helicopter Main Rotor/Tail Rotor Noise Radiation Characteristics from Scaled Model Rotor Experiments in DNW", American Helicopter Society 49th Annual Forum, St. Louis, Missouri, May 19-21, 1993, pp. 89-99.

Sears, W., "Operational Methods in the Theory of Airfoils in Non uniform Motion," Journal of the Franklin Institute, Vol. 230, 1940, pp. 95–111.

Sears, W. R., and Sparks, B. O., "On the Reaction of an Elastic Wing to Vertical Gusts," Journal of the Aeronautical Sciences, Vol. 9, No. 2, 1941, pp. 64–51.

Sears, W.R., "Aerodynamics, Noise, and the Sonic Boom", AIAA Journal, Vol. 7, No. 4, April, 1969.

Sheridan, P.F., Smith, R.P., "Interactional Aerodynamics – A New Challenge to Helicopter Technology", Presented at 35th Annual National Forum of the American Helicopter Society, May, 1979.

Shiekh, A.H., Hillier, R., "The Compressible Perpendicular Interaction of a Columnar Vortex-Jet with a Flat Plate", 31st Fluid Dynamics Conference and Exhibit, Anaheim, California, A01-31272, 11-14 June, 2001.

Srinivasan, G.R., McCroskey, W.J., Baeder, J.D., "Aerodynamics of Two-Dimensional Blade-Vortex Interaction", AIAA Journal, Vol. 24, No. 10, October, 1986, pp. 1569-1576.

Straus, J., Ludi, L.H., "Airfoil Pressure Measurements during a Blade-Vortex interaction and Comparison With Theory," AIAA Paper 88-0069, 1988.

Straus, J., Renzoni, P., Mayle, R.E., "Airfoil Pressure Measurements During a Blade Vortex Interaction and a Comparison with Theory", AIAA Journal, Vol. 28, No. 2, 1990, pp. 222-228.

Surendraiah, M., "An Experimental Study of Rotor Blade-Vortex Interaction," M.S. Thesis, University of Pennsylvania, USA, 1969.

Tadghighi, H., Cheeseman, I.C., "A Study of Helicopter Rotor Noise, with Special Reference to Tail Rotors using an Acoustic Wind Tunnel", Vertica, Vol. 7, No. 1, 1983, pp. 9-32.

Theodorsen, T., "General Theory of Aerodynamic Instability and the Mechanism of Flutter," NACA Report 496, 1935.

Van der Wall, B.G., Leishman J.G., "On the Influence of Time-Varying Flow Velocity on Unsteady Aerodynamics", American Helicopter Society Journal (0002-8711). Vol. 39, no. 4. Oct. 1994, pp. 25-36.

Wagner, H., "Über die Entstehung des dynamischen Auftriebes von Tragflügeln", Zeitschrift für Angewandte Mathematik und Mechanik, Vol. 5, No. 1, 1925.

Wang, T., Doolan, C.J., Coton, F.N., Galbraith, R.A.M. "An Experimental Study of the Three Dimensionality of Orthogonal Blade-Vortex Interaction", AIAA Journal, Vol. 40, No. 10, 2002, pp. 2037-2046.

White, R.P., Balcerak, J.C., Pegg, R.J., "A Parametric Model Study of the Noise Generated by the Aerodynamic Interaction of the Tail Rotor with the Wake of the Main Rotor", AHS Mid-East Region Symposium on Rotor Technology, Essington, 1976.

Widnall, S., "Helicopter Noise due to Blade-Vortex Interactions", Journal of the Acoustical Society of America, Vol. 50, No. 1, 1971, pp. 354-365.

Wittmer, K.S., Devenport, W.J., Rife, M.C., Glegg, S.A.L., "Perpendicular Blade Vortex Interaction", AIAA Journal, Vol. 33, No. 9, 1995a, pp. 1667-1674.

Wittmer, K.S., Devenport, W.J., "Interaction of a Streamwise Vortex with a Full-Span Blade", 26th AIAA Fluid Dynamics Conference, June 19-22, San Diego CA, AIAA-95-2214, 1995b.

Wittmer, K.S., Devenport, W.J., "Effects of Perpendicular Blade-Vortex Interaction, Part 1: Turbulence Structure and Development", AIAA Journal, Vol. 37, No. 7, 1999a, pp. 805-812.

Wittmer, K.S., Devenport, W.J., "Effects of Perpendicular Blade-Vortex Interaction, Part 2: Parameter Study", AIAA Journal, Vol. 37, No. 7, 1999b, pp. 813-817.

Yang, C., Aoyama, T., Saito, S., "Numerical Analysis of Interaction Noise Between Main Rotor and Tail Rotor of Helicopter", 24th International Congress of the Aeronautical Sciences, 2004

Yin, J.P., Ahmed, S.R., "Helicopter main-Rotor/Tail-Rotor Interaction", Journal of American Helicopter Society, October, 2000.

Ziada, S., Rockwell, D., "Vortex-leading-edge interaction", Journal of Fluid Mechanics, Vol. 118, 1982, pp. 79-107.

Bibliography

Anderson, J.D., "Fundamentals of Aerodynamics", 3rd Edition, McGraw-Hill International Edition, 2001

Bisplinghoff, R.L., Ashley, H., "Principles of Aeroelasticity", Dover Publications, Inc., 1962.

Golten, Jack, "Understanding Signals and Systems", McGraw-Hill, 1997.

Katz, J., Plotkin, A., "Low-speed Aerodynamics", 2nd Edition, Cambridge University Press, 2001.

Kuethe, A.M., Chow, C-Y., "Foundations of Aerodynamics: Bases of Aerodynamic Design", 5th Edition, John Wiley & Sons, Inc., 1998.

Lynn, Paul A., Fuerst, Wolfgang, "Introductory Digital Signal Processing with Computer Applications", 2nd Edition, John Wiley and Sons, 1994

Oppenheim, Alan, V., Willsky, Alan, S., "Signals & Systems (Second Edition)", Prentice Hall, 1997.

Prouty, R. W., "Helicopter aerodynamics", PJS Publications, 1985.

Taylor, Fred, J., "Principles of Signals and Systems", McGraw-Hill, 1994.

